



**HAL**  
open science

# Microfluidic approach to Circulating Tumor Cells response to fast flow-induced deformations

Emile Gasser

► **To cite this version:**

Emile Gasser. Microfluidic approach to Circulating Tumor Cells response to fast flow-induced deformations. Cancer. Université Paris sciences et lettres, 2024. English. NNT: 2024UPSLS005 . tel-04842229

**HAL Id: tel-04842229**

**<https://theses.hal.science/tel-04842229v1>**

Submitted on 17 Dec 2024

**HAL** is a multi-disciplinary open access archive for the deposit and dissemination of scientific research documents, whether they are published or not. The documents may come from teaching and research institutions in France or abroad, or from public or private research centers.

L'archive ouverte pluridisciplinaire **HAL**, est destinée au dépôt et à la diffusion de documents scientifiques de niveau recherche, publiés ou non, émanant des établissements d'enseignement et de recherche français ou étrangers, des laboratoires publics ou privés.



**THÈSE DE DOCTORAT**  
**DE L'UNIVERSITÉ PSL**

Préparée à l'Institut Curie

**Microfluidic approach to Circulating Tumor Cells response  
to fast flow-induced deformations**

***Approche microfluidique de la réponse des Cellules Tumorales  
Circulantes aux déformations rapides sous écoulement***

Soutenue par

**Emile Gasser**

Le 29 Mars 2024

École doctorale n°564

**Physique Ile-de-France**

Spécialité

**Physique**

Préparée au

Laboratoire Physique des  
Cellules et du Cancer - UMR168

Composition du jury :

Olivia **Du Roure**  
ESPCI - PSL

*Présidente du jury*

Emmanuèle **Helfer**  
CINaM - Aix-Marseille Université

*Rapporteuse*

Julien **Husson**  
LadHyX - Institut Polytechnique de Paris

*Rapporteur*

Matthieu **Piel**  
Institut Curie - PSL

*Examineur*

Pierre **Joseph**  
LAAS CNRS

*Examineur*

Catherine **Villard**  
LIED - Université Paris Cité

*Directrice de thèse*

Jean-Yves **Pierga**  
Institut Curie - Université Paris Cité

*Co-Directeur - Invité*





## REMERCIEMENTS

A ceux qui liront cette thèse, il me paraît important de commencer par rappeler qu'elle ne serait pas ce qu'elle est sans l'aide et l'accompagnement de nombreuses personnes. Je prends ici l'occasion de les remercier.

Aux membres du jury, et particulièrement aux rapporteurs Emmanuèle Helfer et Julien Husson, je vous remercie d'avoir pris le temps d'évaluer mon travail. Vos nombreuses remarques et conseils m'ont été précieux et permettront à ce projet de progresser encore pour les années à venir.

A Catherine, pour m'avoir guidé au cours de ces 3 années et demi, et avoir su t'adapter à mes besoins au fur et à mesure que j'ai progressé. Je te remercie pour la confiance et l'autonomie que tu m'as accordé sur ce projet. Même si par moment j'ai eu des doutes, je suis satisfait de ce qu'on a pu produire pour ce projet.

A Jean-Yves, malgré ton emploi plus que chargé, tu as toujours trouvé le temps de nous conseiller. Ton regard de clinicien aura été un des atouts de ce projet. J'ai particulièrement apprécié ta manière de mettre en regard les résultats de recherche, souvent abstraits, à la réalité clinique.

A toutes les personnes avec qui j'ai pu collaborer sur ce projet. En particulier Matthieu, et son équipe, je vous remercie pour l'écoute et les conseils que vous avez su m'apporter. Pour les nombreuses interactions que nous avons pu avoir durant ces années, Kotryna, tu mérites mes remerciements les plus chaleureux. Travailler avec toi a été un réel plaisir, et je pense aussi une réussite. A nos collaborateurs de l'Institut Curie, François-Clément et l'équipe BTC ; et du CHU de Montpellier, Catherine et Keerthi, et leurs CTCs. Je vous remercie pour vos conseils et nos discussions lors des réunions autour du projet.

A Arthur et Domenico, qui chacun reprennent une partie de ce projet, je vous remercie pour votre aide pour avancer ce projet. J'espère vous avoir laissé de bonnes bases pour continuer et je vous souhaite le meilleur pour la suite, et de la patience surtout.

A Stéphanie et son équipe à l'IPGG, avec qui j'ai partagé le plus de temps au quotidien. Tu as su créer un environnement de travail agréable pour tous, qui sera compliqué à remplacer. Jean-Louis, qui le premier m'a accueilli en stage, merci de m'avoir orienté vers cette thèse. Claire et Aurore, merci pour vos conseils et votre enthousiasme. Et évidemment l'ensemble des thésards,

post-docs, ingénieurs et stagiaires qui ont foulé le 4ème étage au cours de ces 4 années. A Noam, Juliette, avec qui j'ai partagé mon bureau, je vous laisse le contrôle du volet. A Moencopi et son incomparable passion pour le cheval (et le ski maintenant), Brice, son flegme et ses gâteaux, Charlotte et son énergie, merci d'avoir soutenu avant moi et montré que ce n'est pas si terrible. Eliot, tu le découvriras bientôt, courage! Merci à Giacomo pour son aide sur tout les sujets, Vivian pour le terroir ardéchois et le départ à la cantine. Ainsi que tous les autres : Anastasiia, Guilhem, Caroline, Maxime, Elliot et Elliot, Efra, Alberto, Solène et Lucas, et ceux qui sont déjà partis vers d'autres aventures : Manh, Monica, Fahima, Lucile, Simon, Elodie, Mathilde, Charles, Ismail et Laurianne.

A Jean-Baptiste, et par extension l'ensemble de l'équipe Physique du Vivant au MSC, qui m'a accueilli avec ma manip en cours de thèse. Merci pour l'aide que vous m'avez apporté et qui m'a permis de compléter ce projet.

Aux stagiaires qui m'ont apporté leur aide sur ce projet, et se sont cassés les dents sur les puces microfluidiques ou l'analyse de données : Cyril, Jules, Emilie et Nassiba.

A Bertrand ainsi que son équipe à la plateforme de l'IPGG pour leur support technique, que ce soit en microfabrication ou en microscopie. Merci à la MJB4 et la  $\mu$ PG d'avoir été plus ou moins coopératives aux cours des manips.

A Fluigent pour leurs conseils en microfluidique et pour Omi. J'espère qu'il facilitera la tâche pour Arthur.

Enfin, puisque le travail n'est pas tout, je voudrais remercier encore plus chaleureusement ceux qui m'ont entouré en dehors : Aux amis que je me suis fait en prépa, à l'ESPCI ou en Master. Même si je ne vous vois que rarement, je chéris d'autant plus ces moments. A mon coloc Gasch (et Faust sa plante de compagnie), merci pour m'avoir supporter et pour avoir fait semblant de m'écouter râler lorsque tout n'allait pas dans le bon sens. Ce fut un plaisir de partager cet appartement avec toi.

A ma mère et mon père pour m'avoir supporter et encourager depuis ma naissance, et m'avoir de si nombreuses fois déposer/chercher à la gare.

A mes frères, qui doutent toujours que je travaille réellement, j'espère que vous aurez presque compris ce à quoi je passe mes journées.

A ma grand-mère, pour ses bons petits plats qui ont fait jalouser mes collègues toutes ces années et pour prendre si bien soin de nous.

Ce sont les dernières lignes que j'ajoute ce manuscrit, et comme ont dit chez moi "Isch güet"! Il ne me reste plus qu'à vous souhaiter "a güetes laasa" (i.e. bonne lecture)!

Tumors are often referred to as solid mass, thus highlighting a first argument towards the difference in mechanics of a tumor. In fact, early diagnosis of cancer was achieved through palpation. Traces of this detection technique go back a long time before our understanding of cell and cancer biology : In the 18th century, a French clinician from Besançon reportedly extracted a "solid mass" from the breast of a woman, which prompt other women to ask for palpation. X-rays were first used by German surgeon Albert Salomon to differentiate between benign and malignant tumors. The technique was then improved in 1949 by Raul Leborgne in Uruguay by compressing the breast between two plates to produce better quality images, thus developing the mammography as it is still performed today [Gold, 1990].

Abnormal growth of cells and an overproduction of extra-cellular matrix components make the tumor environment denser and stiffer than the original tissue [Gkretsi, 2018]. Interestingly, even though the tumor is more rigid than its environment, the tumor cells are often softer than their non-malignant homologous [Alibert, 2017; Fuhs, 2022].

We believe the mechanical properties to play a role in the development of tumors and its progression through the metastatic cascade. Indeed, in order to reach distant organs to colonize, the tumor cell has to breach several barriers, some of them being literally barriers (such as the endothelial vascular barrier), others harsh mechanical conditions.

Blood circulation is the main and most effective way to disseminate cells throughout the body. As they travel with the blood flow, tumor cells experience conditions like they have never encountered before. The majority of them originate from a tissue, where they grew adhering to the extra-cellular matrix. Here in suspension, there is nothing to adhere to, and worse there is a lot of stress produce by the flow. As the cells circulate through the capillary bed, they encounter constrictions with diameters smaller than the cells, as can be seen in the electron micrograph of Fig.1a. As the cells are being pushed through these narrow spaces by the flow, they have to deform. If the cell is not well adapted to undergo deformation, it may result in damages and cell death. The ability of cells to navigate the circulation and the capillary bed thus depends highly on their mechanical properties and the molecular players of these properties.

How circulating tumor cells (CTCs) manage to survive to such extreme conditions is still unsettling and misunderstood. However, here may lie the key to prevent the formation of metastases.

If we consider the cancer cells as a new organism, which aim is to grow, to proliferate and to metastasize, then surviving the blood circulation becomes a cause of "natural selection". In the framework of the "survival of the fittest", only cells with the best characteristics, or the ones with the higher adaptability, will be able to continue their journey. The selective pressure of the blood circulation will drive changes in the CTCs population towards characteristics which are the best suited to survive the blood circulation. We believe the mechanical properties of the cell to be one of these characteristics.

Using Drake equation<sup>1</sup> to investigate relative importance of the different steps in the metastatic cascade, [Dujon, 2021] identified that the most essential parameter to the success of metastasis, by far, is the life-expectancy of CTCs during their journey in the bloodstream. This finding suggests that therapies reducing the survival of those cells in the vascular system could significantly reduce the risk of metastasis.

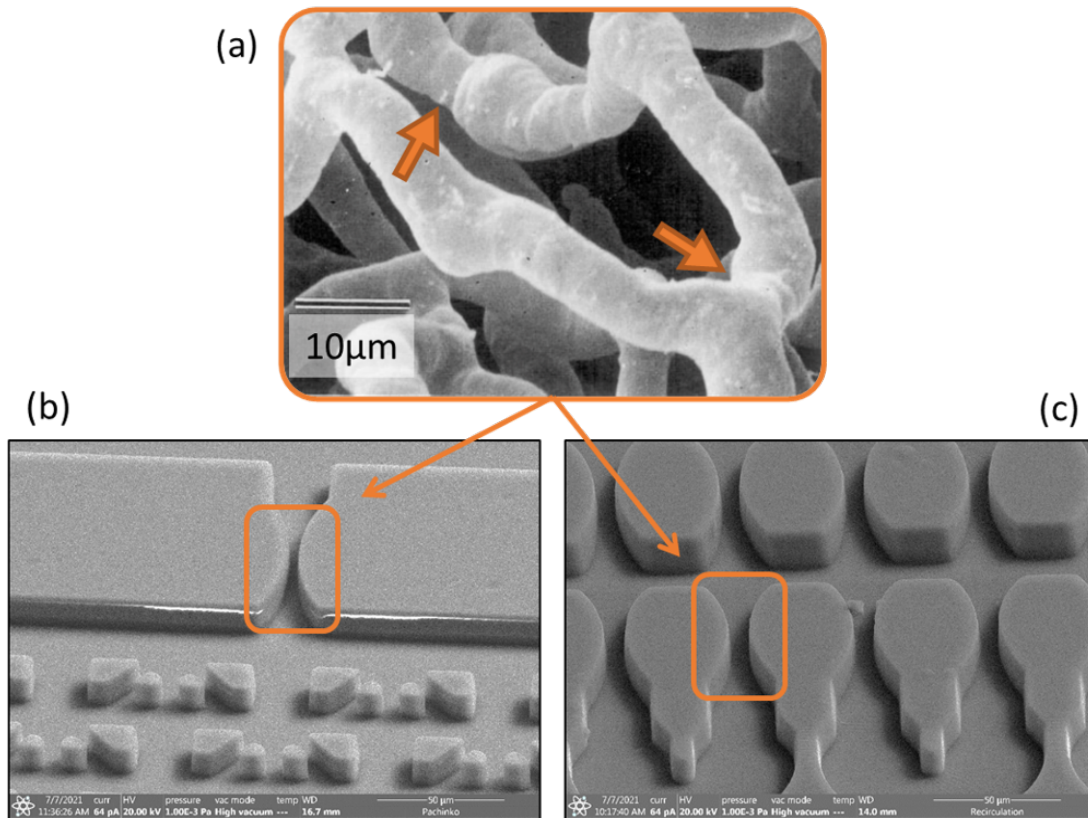


**Figure 1** – *In vitro* reconstruction and microfluidic reproduction of blood capillary constrictions. (a) Scanning electron micrograph of corrosion cast showing capillaries in exocrine pancreas of mouse. Arrows denote several prominent constrictions (adapted from [MacDonald, 1995]). (b) Scanning electron microscope image of the capillary-like constriction in the Pachinko device (with single cell nests to capture the cells), scale bar = 50 µm. (c) Scanning electron microscope image of a capillary-like constriction in the recirculation device, scale bar = 50 µm.

1. Proposed by astrophysicists in the 1960's to evaluate the probability of another complex phenomenon occurring, the emergence of intelligent civilizations in the Milky Way. Here the complex phenomenon occurring is the apparition of metastasis

---

In this study, we have chosen to investigate the relation between a circulating tumor cell mechanical properties and its ability to withstand fast flow-induced deformations and survive the blood circulation. We have used the microfluidic technology to reproduce the blood circulation harsh conditions and mimic the capillary constrictions.

To that aim, we developed two complementary microfluidic devices. The first one, named Pachinko by analogy with a popular Japanese game, aims at studying the dynamics of fast flow-induced deformation and recovery. The device is composed of a capillary-like constriction (see Fig.1b) to deform the cell, and an array of single cells nests to trap the cell and study its recovery. The device allows to study the morphological characteristics of the CTC at the single cell level.

The second device aims at studying the long-term consequences of repeated flow-induced deformations at the cell population level. The microfluidic chip is composed of an array of capillary-like constrictions (see Fig.1c), through which the CTCs are recirculated over several hours. The cells can be collected throughout and at the end of the recirculation in order to characterize their number, viability and other characteristics.

The current manuscript will present the development and use of these microfluidic chips to the study the biomechanics of several cancer cell lines, following the outline presented below :

- **Chapter 1** will provide an introduction and literature review to the subject. We introduce first concepts of cell mechanics, then their relevancy in the context of cancer biology and metastasis, and finally microfluidics and its use to study the biomechanics of cells.
- **Chapter 2** will present the first microfluidic device, named Pachinko, developed to study the short-term dynamics of deformation and recovery of single cells. As a proof of concept, we'll focus at the whole cell level to establish the viscoelastic behavior of several cell lines of breast and colon cancer.
- **Chapter 3** will focus on the dynamics of the nucleus in the Pachinko device. We'll show the particular elastic behavior of the nucleus, and the role of vimentin in this behavior.
- **Chapter 4** will present the second microfluidic device developed to study the long-term effect of repeated deformations on cancer cells. We'll compare the overall survival, damages accumulation but also vesicles production of two breast cancer cell lines.
- **Chapter 5** will provide the materials and methods used in this study.

# TABLE OF CONTENTS

<b>Remerciements</b>	<b>i</b>
<b>Preamble</b>	<b>iii</b>
<b>1 General Introduction</b>	<b>1</b>
1 Cell mechanics . . . . .	1
1.1 Rheology . . . . .	1
1.2 The cell, its components and their mechanics . . . . .	2
1.2.1 Nucleus . . . . .	2
1.2.2 Cytoskeleton . . . . .	4
1.2.3 Plasma membrane . . . . .	6
1.2.4 Comparison and orders of magnitude . . . . .	7
1.3 Experimental approaches to rheological measurements . . . . .	8
1.3.1 Micropipette aspiration . . . . .	8
1.3.2 Optical stretcher and tweezers . . . . .	8
1.3.3 AFM . . . . .	10
1.3.4 Microfluidics and microsystems . . . . .	10
1.3.5 Rheological values reported for cells . . . . .	11
1.4 Impact of mechanics on cell biology . . . . .	13
1.4.1 Interaction with the extracellular environment . . . . .	13
1.4.2 Relevance of mechanics in cancer . . . . .	13
2 Cancer and Metastasis . . . . .	14
2.1 Introduction to cancer . . . . .	14
2.1.1 Breast cancer . . . . .	16
2.1.2 Colon cancer . . . . .	17
2.2 The metastatic cascade . . . . .	18
2.2.1 Tumor growth . . . . .	19
2.2.2 Migration and Intravasation . . . . .	19
2.2.3 Passage in the blood circulation . . . . .	20
2.2.4 Extravasation . . . . .	21
2.2.5 Epithelial to mesenchymal transition (EMT) . . . . .	22
2.3 Focus on the blood circulation . . . . .	22
2.3.1 Topology . . . . .	22
2.3.2 Cells in the circulation . . . . .	24

2.4	Liquid biopsy . . . . .	25
2.4.1	CTCs & ctDNA . . . . .	25
2.4.2	CTCs capture devices . . . . .	25
2.4.3	Clinical relevance . . . . .	27
3	Microsystems and microfluidics . . . . .	28
3.1	General knowledge . . . . .	28
3.1.1	History . . . . .	28
3.1.2	Theory . . . . .	28
3.2	Microfluidics in biology . . . . .	29
3.2.1	Droplets microfluidics . . . . .	29
3.2.2	NGS, FACS . . . . .	29
3.2.3	Organ-on-chips . . . . .	30
3.3	The study of cell mechanics in microfluidics . . . . .	31
3.3.1	Confinement . . . . .	31
3.3.2	Free migration in confined space . . . . .	33
3.3.3	Forced migration through confined space . . . . .	35
3.3.4	Focus on cancer cells . . . . .	37
4	Scope of the PhD project . . . . .	38
4.1	MecaCTC project . . . . .	39
4.2	My Project specifically . . . . .	40
<b>2</b>	<b>Pachinko : Design and results at the cell level</b>	<b>41</b>
1	Introduction to the paper . . . . .	42
1.1	Working principle of the Pachinko device . . . . .	42
1.2	Short summary of the paper . . . . .	43
2	Paper draft "Deformation under flow and morphological recovery of breast cancer cells" . . . . .	44
3	Comments on the paper . . . . .	68
3.1	Analysis workflow . . . . .	68
3.2	About segmentation . . . . .	69
3.3	About shape descriptors . . . . .	69
4	Fast deformation of colon cancer cells and morphological recovery . . . . .	71
4.1	Focus on the arrest time . . . . .	71
4.2	Cell deformation in the constriction . . . . .	73
4.3	From deformation to recovery . . . . .	76
4.4	Recovery of colon cells display two regimes . . . . .	77
5	Discussion & Perspectives . . . . .	81
5.1	About the design and experiment . . . . .	82
5.2	About the rheology . . . . .	87
5.3	About the cytoskeleton . . . . .	91
6	Short Conclusion . . . . .	92
<b>3</b>	<b>Pachinko : Focus on the nucleus</b>	<b>93</b>
1	About the arrest time . . . . .	93
1.1	Link with diameter . . . . .	93
2	Deformation of nuclei in the constriction . . . . .	95
2.1	Deformation curves and fits . . . . .	95
2.2	Nucleus positioning through the constriction . . . . .	97
3	From deformation to recovery . . . . .	99
4	Results : Nucleus recovery is mostly elastic . . . . .	101

TABLE OF CONTENTS

---

4.1	Recovery curves and fits . . . . .	101
5	Link with cancer aggressiveness . . . . .	103
5.1	EMT and vimentin . . . . .	103
6	Role of vimentin filaments . . . . .	106
6.1	Vimentin knockdown in SW-620 cells . . . . .	106
6.1.1	Protocol optimisation . . . . .	106
6.1.2	Change to 3x15 $\mu\text{m}^2$ constrictions . . . . .	107
6.1.3	Recovery of siVim SW-620 nuclei . . . . .	108
6.2	Expression in HT-29 cells . . . . .	109
6.2.1	Transfection protocol . . . . .	111
6.2.2	Recovery of trVim HT-29 nuclei . . . . .	111
7	Discussion . . . . .	112
7.1	Nuclear damages and Viability . . . . .	112
7.1.1	DNA damages and nucleus envelope rupture? . . . . .	112
7.1.2	Long term viability after fast deformation . . . . .	113
7.2	About the rheology . . . . .	114
7.3	Validation of rheological models . . . . .	117
7.3.1	Micro Hydrogel Beads . . . . .	117
7.3.2	Oil Droplets . . . . .	118
8	Perspectives . . . . .	118
9	Short Conclusion . . . . .	119
<b>4</b>	<b>Recirculation : Effect of repetitive deformations</b>	<b>121</b>
1	Experiment design . . . . .	121
1.1	Microfluidic chip . . . . .	122
1.1.1	First design . . . . .	122
1.1.2	Second design . . . . .	123
1.1.3	Numerical simulations . . . . .	123
1.1.4	Experimental considerations . . . . .	124
1.2	Implementation of the recirculation fluidic system . . . . .	125
1.2.1	Back and forth using pressure controllers . . . . .	125
1.2.2	Omi recirculation instrument by Fluigent . . . . .	126
1.2.3	Use of a peristaltic pump . . . . .	128
2	Study of circulated breast cancer cells . . . . .	128
2.1	Viability of recirculated cells . . . . .	129
2.2	Vesicles production under stress and deformation . . . . .	131
2.3	Nuclear damages accumulation . . . . .	133
3	Discussion . . . . .	135
3.1	About the microfluidic chip and recirculation setup . . . . .	135
3.2	About vesicles . . . . .	136
3.3	About what happens in the cell . . . . .	137
3.4	About metastasis . . . . .	138
4	Perspectives . . . . .	139
5	Short Conclusion . . . . .	140
<b>5</b>	<b>Materials and Methods</b>	<b>142</b>
1	Microfabrication . . . . .	142
1.1	Chrome mask fabrication . . . . .	142
1.2	Photolithography . . . . .	142
1.3	Soft lithography . . . . .	144

---

2	Cell Biology . . . . .	144
2.1	Cell culture . . . . .	144
2.1.1	Cell staining . . . . .	145
2.2	Treatments . . . . .	146
2.2.1	Vimentin silencing . . . . .	146
2.2.2	Vimentin transfection . . . . .	146
2.3	Cell preparation . . . . .	147
2.4	Biochemistry . . . . .	148
2.4.1	Live/Dead imaging . . . . .	148
2.4.2	Immunofluorescence . . . . .	148
2.4.3	Immunoblotting . . . . .	148
2.4.4	Vesicles collection . . . . .	150
3	Experiments . . . . .	150
4	Data Analysis . . . . .	151
4.1	ImageJ . . . . .	151
4.2	Matlab . . . . .	152
4.3	Python . . . . .	152
4.4	GraphPad Prism . . . . .	152
	<b>Conclusion</b>	<b>154</b>
	<b>Résumé en français</b>	<b>158</b>
	<b>Appendixes</b>	<b>168</b>
A	Notions of rheology . . . . .	168
B	Matlab App code . . . . .	173
C	Data and fits . . . . .	178
D	Improvement on the Pachinko device . . . . .	187
	<b>References</b>	<b>188</b>

In this first chapter, I'll introduce notions of mechanics, cell and cancer biology, and microfluidics that will help apprehend my project. All of these fields may individually require too many pages to be described thoroughly. I'll thus focus my interest on their relevancy to the study of cell mechanics, and how each of these fields rely on each other to reach the understanding that we have today on the mechanics of cells.

## 1 Cell mechanics

As cells are inherently made of matter, they don't escape the laws of physics. We'll first rapidly put aside that cells are "active" matter and study them with concepts and laws that were initially developed for soft matter. Though their organization is complex, as we'll describe it, we'll show that major cellular components can be understood and combined in an attempt to recreate the behavior of the whole object.

### 1.1 Rheology

Having a look at the literature, one might find that the cells are regularly described as "soft" or "stiff", sometimes "deformable", without a proper definition of what these terms refer to. Rheology, the study of how materials deform when forces are applied to them, is the field that deals with these concepts. Though this field is often not familiar to biologists, it has brought key experimental results and concepts from mechanics to cell biology. The concept of viscoelasticity that is often used to describe cells draws from theories describing ideal materials, namely the Hookean elastic solid [*True Theory of Elasticity*, Robert Hooke (1678)] and the Newtonian viscous liquid [*Principia*, Isaac Newton (1687)] [Barnes, 1989].

We'll provide in Appendix A a short summary of rheological concepts that will be used in this work. In brief, the extension of an Hookean solid is instantaneous and proportional to the load (Hooke's law). A Hookean solid in a deformed state will remain deformed as long as the applied stress persists. In contrast, Newton's theory describes ideal liquid states, in which the

flow will persist as long as a stress is applied. The flow rate will be proportional to the applied stress. These proportionality laws allow to define the concepts of "elasticity" and "viscosity" respectively. Combination of these elements create viscoelastic models, such as Kelvin-Voigt viscoelastic solid, the Maxwell viscoelastic liquid, and more complex ones [Lim, 2006].

There exist a variety of rheological moduli, as each depends on the design of the experiment used to measure it. The most well-known Young modulus  $E$  specifically refers to a force applied perpendicularly to the surface of the object resulting in an uniaxial deformation in the same direction. If the stress is applied tangentially to the surface, the modulus measured resulting from the deformation is the shear modulus  $G$ . Though these moduli are related, their values differ, so one must be careful in comparing experiments in the literature. Finally, the extent of deformation can strongly depend on how long and how quickly the force is applied, making it even harder to compare different experimental designs.

The property that rheological studies are designed to quantify is conceptually simple, namely a value that predicts how a material will deform when a force of a certain magnitude is applied to it in a defined geometry for a given amount of time [Janmey, 2007]. Yet, one must be precise about its measurement. In this work, the use of "soft" and "stiff" will refer to comparison of elastic moduli, while "deformable" will refer to a lower viscosity.

## 1.2 The cell, its components and their mechanics

The cellular composition of eukaryotic cells is a complex assembly of various organelles, filaments, vesicles, etc. (see Fig.1.1a), some of them playing a central role in cell mechanics. These mechanical properties sustain vital cellular functions such as shape maintenance, division, motility, and mechanotransduction. Key components that may exert notable influence over the mechanical characteristics of a cell include the nucleus, the cytoskeleton, and the cellular membrane We'll describe these ones in particular.

### 1.2.1 Nucleus

As the cells biggest organelle, the nucleus plays a determinant role in cell mechanics. Its size, shape, and position within the cell impact the overall cell morphology and stiffness.

The nucleus compartmentalizes the chromatin from the cytosol, thus protecting the genetic information inscribed within the chromatin. The nuclear envelope is composed of an inner and outer bilayered lipidic membrane (INM and ONM), pierced by several nuclear pores which allow exchange of small molecules ( $< 60$  kDa) with the cytosol. The outer nuclear membrane extends into the endoplasmic reticulum, where messenger RNA is transcribed into proteins. The inner nuclear membrane is supported by a meshwork of intermediate filaments named lamins (60-70 kDa, see Fig.1.1b), which gives the nuclear membrane structural integrity, contributes to its mechanical resistance [Turgay, 2017; Malashicheva, 2021] and binds to the chromatin. Lamin meshworks have been reported to be highly elastic and exhibit limited compressibility, thus

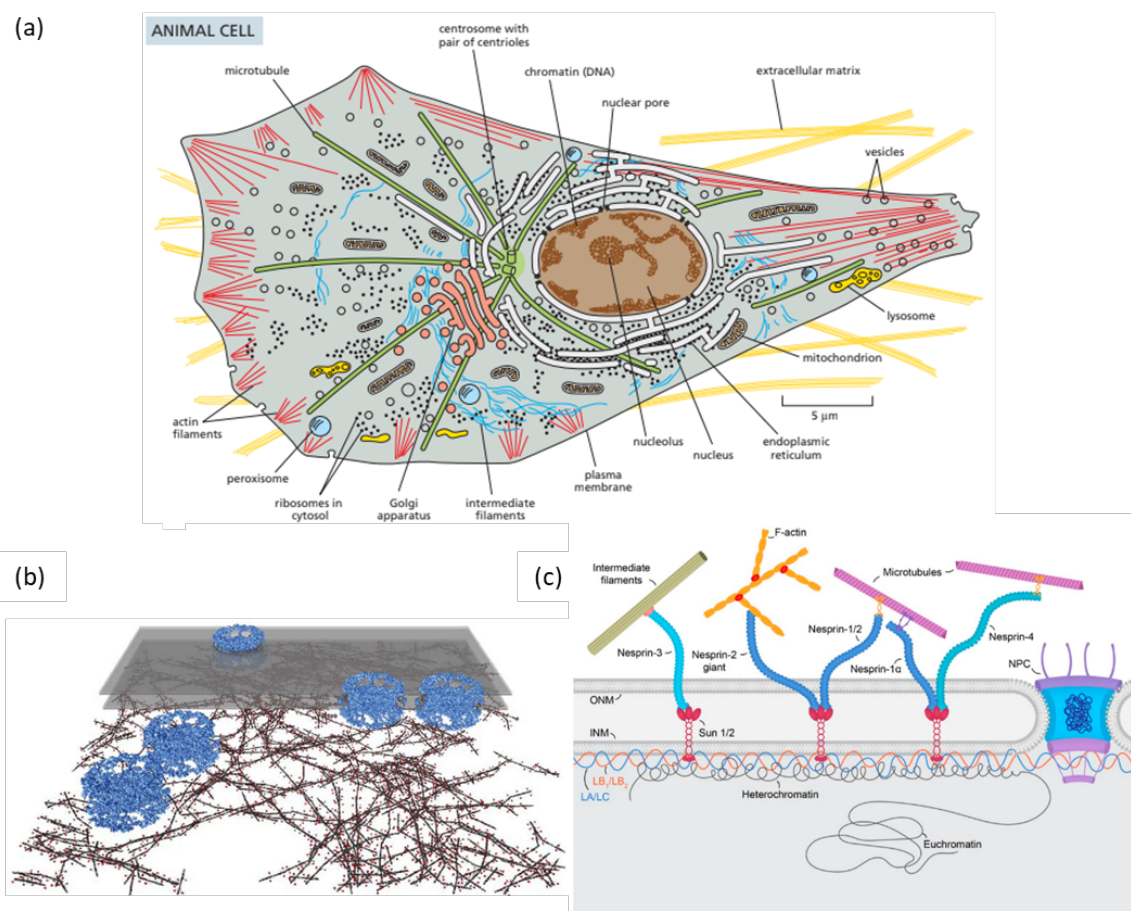


**Figure 1.1** – organization of the cell and its nucleus (a) Drawing of the major features of eucaryotic cells organization (adapted from [Alberts, 2019]). (b) The nuclear envelope (INM and ONM in transparent grey) with underlying lamins meshwork (rod-domain in dark grey and Ig-domain in red) and NPCs (blue), were modeled into a region of a cryo-tomogram (adapted from [Turgay, 2017]). (c) Schematic illustration of the nuclear envelope in mammalian cells. The interplay between lamins and LINC complexes at the nuclear envelope has been proposed to facilitate coupling of the nucleus to the cytoskeletal systems in the cytoplasm. Lamins further interact with peripheral heterochromatin to regulate chromatin organization within the cell nucleus (adapted from [Vahabikashi, 2022]). INM, inner nuclear membrane; NPC, nuclear pore complex; ONM, outer nuclear membrane.

acting as a "shock absorber" to protect the nucleus [Dahl, 2004]. Among the four types of lamins (A/C, B1 and B2), only Lamin A/C seems to contribute to nuclear mechanics [Lammerding, 2006].

The chromatin is organized in regions of open chromatin (euchromatin, which is accessible for genes transcription) and dense chromatin (heterochromatin, which is repressed). It is often referred to as a complex viscoelastic material [Vries, 2007; Stephens, 2017; Keizer, 2022]. Additionally, chromatin compaction affects its mechanical properties [Stephens, 2017].

Both the bulk (chromatin) and the shell (lamins) contribute nuclear rheology. [Stephens, 2017] reported that they each respond to different regimes. Chromatin elasticity governs small nuclear deformation ( $< 3 \mu\text{m}$ ), whereas lamin A/C levels control nuclear strain stiffening at

large extensions ( $> 3 \mu\text{m}$ ).

The volume of the nucleus is regulated by the "pump and leak" model : the difference in protein concentration inside the nucleus results in an osmotic pressure which drains water inside and inflates it. This force is balanced by the nuclear envelope tension [Rollin, 2023b]. In normal conditions, the nucleus envelope displays wrinkles. These folds originate from the difference of elastic modulus of the stiff nuclear membrane (supported by the lamina) and the soft inner nucleoplasm it relies on [Brau, 2011].

The nucleus is anchored to the cytoskeleton through the LINC (LInker of Nucleoskeleton and Cytoskeleton) complex (see Fig.1.1c), which facilitates force transmission between the nucleus and cytoskeleton, and governs its positioning [Lee, 2018]. These complexes are composed of 2 parts positioned on either side of the nuclear membrane : SUN proteins anchored in the INM and binding to lamins on the inside of the nucleus ; and nesprins embedded in the ONM and binding to filaments of the cytoskeleton [Tapley, 2013]. Thus, this structure allows for a mechanical transmission between the cytoskeleton and the nucleus [Lombardi, 2011]. As we'll see later, mechanotransduction (process by which external forces are sensed by the cell, transmitted to the cell interior and converted into a cellular response) can affect the nucleus mechanics as it can alter gene expression, and induce formation of heterochromatin thus increasing chromatin rigidity [Stephens, 2019].

### 1.2.2 Cytoskeleton

The cytoskeleton, as its name hints at, brings structural integrity to the cell. It is composed of filaments of different polymers (see Fig.1.2a), each of which have their specific organization and functions.

- **Actin** : The actin cytoskeleton, an intricate network of actin filaments, is pivotal in cellular mechanics. It confers shape and maintains mechanical stability through dynamic remodeling. Actin-driven processes such as lamellipodia formation, cell adhesion, and contractility influence cell stiffness, migration, and deformation responses. The mechanical properties of actin filaments are regulated by crosslinking proteins, motor proteins, and polymerization dynamics.

The actin filaments are highly dynamics. They are constantly extending as monomers (G-actin) are incorporated into the polymeric filament (F-actin). Disassembly events brings the length of filaments down, thus creating an equilibrium [Blanchoin, 2014].

The cell is layered with actin stress fibers that run through the cell (see Fig.1.2b) and create tension. Anchored below the cellular membrane, the actin cortex brings structural integrity to the fluid plasma membrane.

Its combination with the molecular motor myosin II allows for cell contractility, as the two filaments slides upon one another bringing their ends closer upon ATP consumption. This assembly can generate forces ( $\approx 3 \text{ pN}$  per myosin molecule [Morris, 2001]), and drive change in the cell shape. When coordinated at the scale of the cell (sarcomere organization)

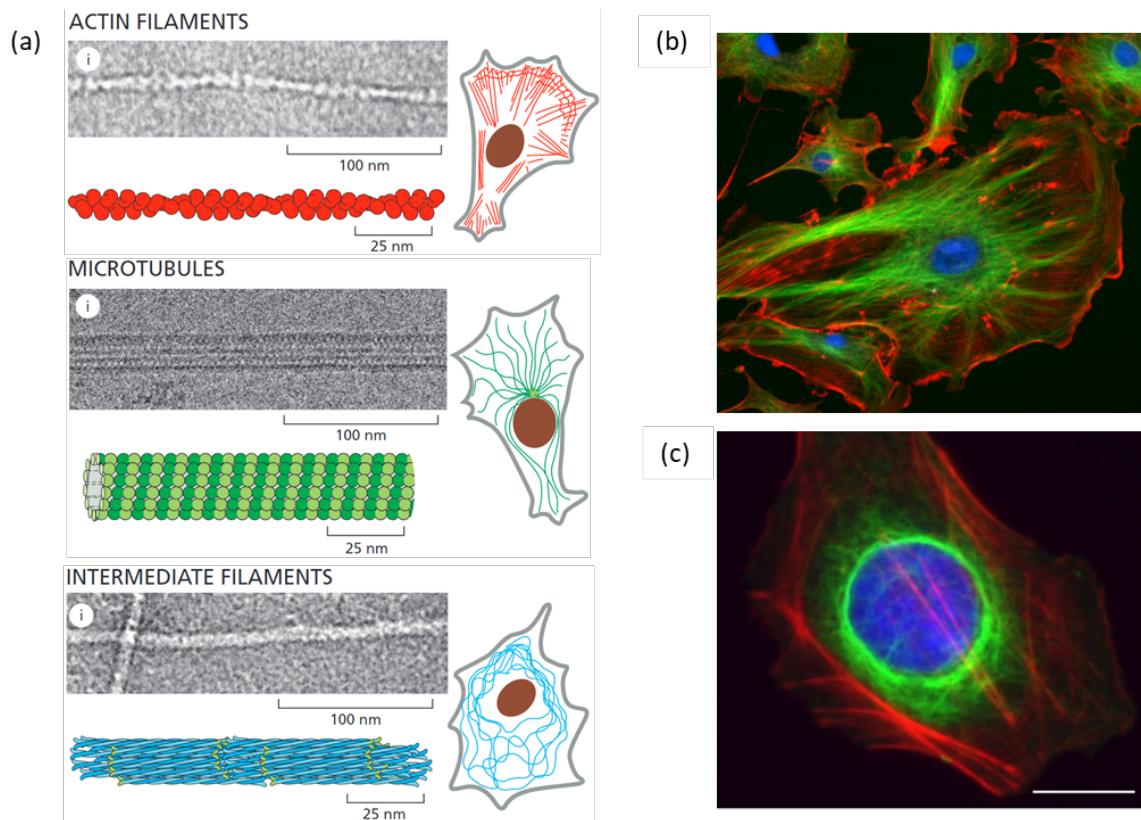


**Figure 1.2** – organization of the cytoskeleton (a) Main components of the cytoskeleton : actin, microtubules and intermediate filaments. TEM images, scheme of filaments and distribution in the cell (adapted from [Alberts, 2022]). (b) Actin (red) and microtubules (green) organization in a pulmonary artery endothelial cell. Scale bar = 15  $\mu\text{m}$  (example image from the ImageJ-Programmpaket (public domain)). (c) Intermediate filament networks and the cell nucleus. The greater localization of vimentin intermediate filaments juxtaposed to the nucleus is indicative of a distinct cage. Immunofluorescence image of a HUH7 (liver tumor) cell marked for vimentin (green), actin (red), and DNA (blue). Scale bar = 15  $\mu\text{m}$  (adapted from [Patteson, 2020]).

and the tissue (muscle cells fibers), this mechanism allows for muscle contraction [Murrell, 2015].

Reconstituted *in vitro* actin-and-membrane systems display either buckling or wrinkling upon reduction of the volume, which is characteristic of an elastic network [Kusters, 2019].

- **Microtubules** : Microtubule filaments, composed of tubulin subunits, form dynamic networks. The microtubules network originates from nucleation centers (MTOCs microtubule-organizing centers), the main one being the centrosome. Microtubules grow from these centers towards the boundary of the cell. They support the organization of the cell, and define for instance the shape of axons, cilia and flagella.

They serve as tracks for intracellular transport. Microtubule filaments act as pathways for proteins motors (such as kinesins, and dyneins) to allow for intracellular cargo transport. They also play a role in processes like cell division, orienting the chromosomes during mitosis and pulling cellular components into each daughter cells.

Compared to actin and others filaments, microtubules filaments are large (25 nm diameter),

hollow but rigid structures. When under cycles of bending and release, microtubule stiffness decreases incrementally with each 10s cycle. Strikingly, in a process of self-healing, damaged microtubules were able to incorporate new tubulin dimers into their lattice and recover their initial stiffness after a 100 s rest [Schaedel, 2015].

- **Intermediate Filaments** : Intermediate filaments constitute a class of structural proteins contributing significantly to cell mechanics. They impart mechanical resilience and stability to cells by resisting tensile forces [Bodegraven, 2021]. Keratins (in epithelial cells), vimentin (in mesenchymal cells), and neurofilaments (in neuronal cells) are examples of intermediate filaments found in different cell types. Their expression patterns and mechanical contributions vary, affecting cell stiffness and resistance to mechanical stress. Unlike actin and microtubules which undergo rapid growth and disassembly, the intermediate filaments are much more stable.

Only present in cells with a mesenchymal phenotype, vimentin has been reported to act as a "shock absorber", by dissipating energy upon unfolding of the filament structure [Block, 2017]. Its mechanical response is non-linear and depends strongly on the loading rate : they are soft during a slow deformation, and stiffen under a fast deformation. Repeated stretching of the filaments leads to a softening due to irreversible conformations changes, which doesn't seem to recover after 1h [Forsting, 2019].

These three main types of filaments interact with each others, as exemplified by the variety of cytolinker proteins that binds different filaments together in many configurations (spectraplaklin, formin, APC, Tau, ... [Dogterom, 2019]). They are responsible for interactions in actin-microtubules crosslinking, guidance of microtubules by actin bundles, anchoring of microtubules in the cortical actin network... Similar proteins exists with intermediate filaments : Plectin, for instance, binds intermediate filaments to actin microtubules, actin filament bundles, and filaments of the motor protein myosin II [Svitkina, 1996]. In reconstituted *in vitro* system, vimentin intermediate filaments were able to stabilize microtubules against depolymerization and support microtubule rescue [Schaedel, 2021].

As we'll see later in more details, the cytoskeleton transmits external forces, from focal adhesion and cell-cell junctions to the nucleus. these forces are transformed into biomechanical cues that regulates cell expression (mechanotransduction) [Mathieu, 2019].

### 1.2.3 Plasma membrane

The plasma cellular membrane, composed of a bilayer of phospholipids embedded with proteins, functions as a semi-permeable barrier. Membrane tension and fluidity impact cell shape and deformability. Membrane receptors and adhesion proteins play vital roles in mechanotransduction, cell adhesion and migration, among others.

In a mammalian cell, the tension in the membrane is of the order of  $10^{-5}$  N/m [Hochmuth, 2000; Morris, 2001], which is lower than the tension in the underlying cortical actin network ( $\approx 10^{-4}$  N/m during interphase,  $\approx 10^{-3}$  N/m during mitosis) [Fischer-Friedrich, 2014]. The

contribution of the membrane to the cell mechanics results mostly from the underlying actin cortex. The lysis tension (required to break the membrane) is of the order of  $10^{-2}$  N/m [Gauthier, 2012].

The membrane is permeable to water and has dedicated channels to accelerate the transport of water and other ions. These channels can either be passive (if the transport follows the concentration gradient) or active (against the gradient), and are affected by membrane tension [Cox, 2019]. The exchange of water allows to regulate the volume of the cell according to the "pump and leak" model (equilibrium between osmotic pressure and cell membrane tension) [Tosteson, 1960].

Cells undergo slow deformation at constant volume, while fast deformation leads to volume loss [Venkova, 2022], in response of the increase of membrane tension when the rate of deformation is faster than the relaxation time of the actin cortex and membrane ensemble.

Similarly to the nucleus, the cell membrane presents invaginations, named caveolae, that unfold and act as membrane reservoirs upon rapid stretching of the membrane, then reforms upon stress release [Sinha, 2011]. For instance, the absence of a functional caveola reservoir in myotubes from muscular dystrophic patients enhanced membrane fragility under mechanical stress. As lymphocytes are deformed within capillary, these reservoirs allow to extend the membrane surface and prevent rupture [Guillou, 2016a].

#### 1.2.4 Comparison and orders of magnitude

The persistence length, defined as the length over which correlations in the direction of the tangent are lost, can be used to compare the strength of the different polymers that compose a cell (DNA, actin, microtubules, intermediate filaments). The typical order of magnitude of the persistence length is 50 nm for DNA (very flexible),  $\approx 600$  nm for lamins,  $15 \mu\text{m}$  for actin (typically the size of a cell) and a few millimeters for microtubules (much larger than a cell, microtubules are very stiff and rigid) [Blanchoin, 2014].

The persistence length  $l_p$  can be expressed using the bending stiffness of the polymer  $B$  through  $l_p = \frac{B}{k_B T}$  where  $k_B$  is the Boltzmann constant and  $T$  is the temperature. The bending stiffness itself depends on the Young modulus  $E$  and radius  $r$  of the polymer filament :  $B = E \frac{\pi r^4}{4}$ . We can then deduce a measure of the Young modulus :

$$E = \frac{4k_B T}{\pi} \frac{l_p}{r^4} \quad (1.1)$$

The Young modulus has then been estimated to 300 MPa for the lamins network. F-actin is 2 GPa, and vimentin is 6 MPa, as reported in Table 1.1.

Among the cytosolic filaments, intermediate filaments are the most extensible, while microtubules are the more rigid.

Filament	Persistence length	Radius	Young modulus
Chromatin	50 nm	2 nm	300 Pa (metaphase)
Lamins	600 nm	3.5 nm	300 MPa
Vimentin	1 $\mu\text{m}$	10 nm	6 MPa
F-actin	15 $\mu\text{m}$	8 nm	2 GPa
Microtubules	> 1 mm	25 nm	1.2 GPa

**Table 1.1** – Mechanical parameters for different types of filaments in the cell. Values are extracted from [Gittes, 1993; Wen, 2011; Blanchoin, 2014; Turgay, 2017]

---

### 1.3 Experimental approaches to rheological measurements

To access and measure rheological moduli, one should be able to apply a controlled force or deformation on the object, and to measure the resulting other one. To that aim, several types of devices have been developed, as presented in Fig.1.3a. Some of these techniques quantify mechanical properties at the scale of the whole cell (micropipettes, optical stretcher, microfluidics), while others focus on the local scale (AFM, optical tweezers, particle tracking microrheology).

#### 1.3.1 Micropipette aspiration

Micropipette aspiration works by gently applying suction to a small section of a cell membrane using a fine glass pipette. This controlled suction causes the cell membrane to deform and enter the pipette (see Fig.1.3b). The dynamics of this deformation and subsequent relaxation, once suction is stopped, allows to access the cell’s mechanical properties. These properties include its elasticity and viscosity. Using low pressure difference and a small tip diameter, micropipettes aspiration allows to probe the membrane tension only. Increasing the pressure difference, more of the cell will enter in the pipette and properties of the cytoplasm and/or nucleus will be probed.

This technique has been widely used to study properties of many cell types (see [Xie, 2019] for a comparison of 8 cancer cell lines). It is for instance appropriate for the measurement of membrane tension [Hochmuth, 2000] or cell adhesion forces [Hogan, 2015]. This device also allows to study the properties of the nucleus, either within an intact cell through staining [Booth, 2015], or on isolated nuclei [Dahl, 2004] to characterize its properties independent of the surrounding environment. As an example, [Pajerowski, 2007] reported that nuclei in human embryonic stem cells are highly deformable and stiffen 6-fold through terminal differentiation.

Micropipettes can also be used to hold suspended cells by applying a low suction, which also to perform rheological measurements (microindentation) by applying forces with a probe [Husson, 2023].

#### 1.3.2 Optical stretcher and tweezers

Optical stretchers and tweezers rely on the principles of laser light manipulation to trap and precisely control tiny particles, including cells. By focusing a highly focused laser beam onto a cell, the refractive forces exerted by the beam trap the cell in three dimensions and deform it (see Fig.1.3c). By focusing on organelles or artificially injected microbeads, the forces can be applied

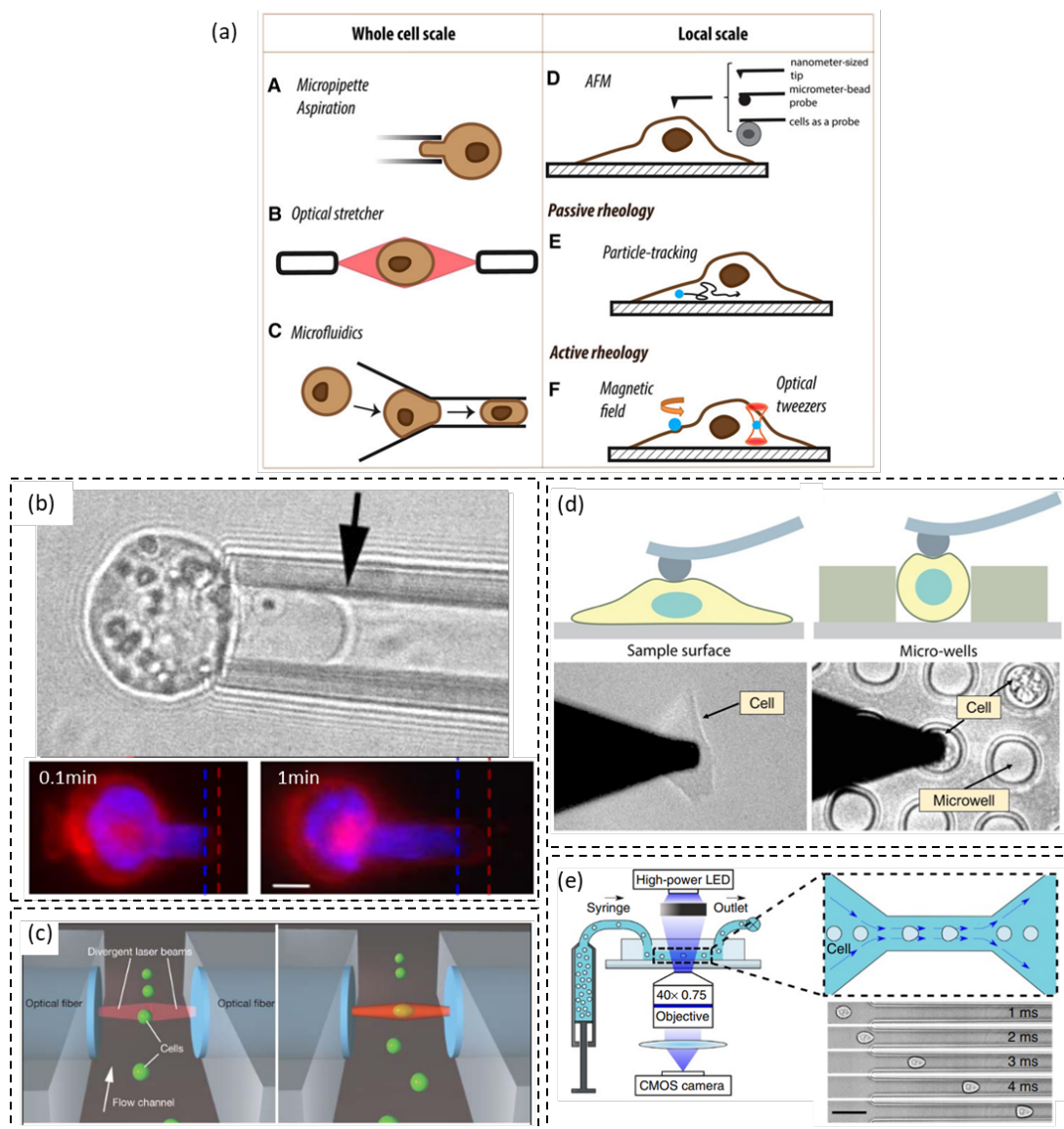


**Figure 1.3** – Summary of experiments designed to access cells rheological properties (a) Overview of experimental techniques used to compare the rheological properties of cells at the whole cell scale or local scale (adapted from [Alibert, 2017]) (b) Micropipette aspiration principle, and human Embryonic Stem Cells in the device (red : cell membrane, blue : DNA) (adapted from [Pajerowski, 2007]). (c) Optically induced surface forces lead to trapping and stretching of cells (adapted from [Guck, 2005]) (d) AFM indentation on adhered and suspended cells (adapted from [Nematbakhsh, 2017]). (e) Real-Time Deformability Cytometry (adapted from [Otto, 2015]).

on subcompartments of the cells. The trapped cell's or organelle's position can be manipulated, and its response to controlled forces can be measured.

As an example, [Mandal, 2016] were able to map the intracellular mechanics of cells on micropatterned substrates, by studying the position of an internalized bead. They were able to show that the shear modulus decreases from the cell center to the periphery and from the cell rear to the front along the polarity axis of the micropattern.

Similar techniques use magnetic forces to control the displacement of injected microbeads, and

thus applying forces. Using two mutually attracted magnetic beads, one inside the cell and the other in the extracellular medium, the cortex can be pinched to provide an accurate and time-resolved measure of its thickness [Laplaud, 2021].

### 1.3.3 AFM

Atomic Force Microscopy (AFM) offers a precise and finite control of stresses and deformations locally applied on the cell. It operates on the principle of a small cantilever armed with a sharp tip that scans the cell's surface. As the tip approaches the cell, it experiences forces arising from interactions with the surface. These forces induce deflections in the cantilever, which are then used to generate nanoscale-resolution images of the cell's topography. Moreover, AFM goes beyond mere imaging as it can quantitatively assess mechanical properties. By applying controlled forces and measuring the resulting cantilever deflections, AFM can determine parameters like cell stiffness, elasticity, and adhesion forces.

However, AFM relies on the cell being immobile during the measurement, which is easy with adherent cells and require more complex geometries with suspended cells (see Fig.1.3d). The measure obtained depends on the geometry of the tip used on the cantilever, and the depth and speed of the indentation. Thus, one should carefully choose these parameters in accordance to the investigated characteristics. For instance, a sharp tip used with a small indentation will probe only the cell membrane mechanics, while a larger tip with a bigger indentation will mobilize the bulk of the cell.

Some variants like flat AFM or microplate rheometers allow to apply large uniaxial deformations [Hosseini, 2022], and/or to submit cells to more complex patterns of deformations (sinusoidal solicitation) [Mitrossilis, 2010].

### 1.3.4 Microfluidics and microsystems

These systems rely on microfabrication technics which allow to design structures at the micron scale. As the devices that we use in this work belong to this group of microfluidic systems, we will describe microfluidics and the related devices more thoroughly in a following section 3.

By designing specific geometries, and using properties of the laminar flow, these devices are able to exert forces on flowing cells. In deformability cytometry experiments, a rapid narrowing in a microfluidic channel leads to an increased velocity, and thus increased shear stress, which deforms the cells flowing in the narrow channel (see Fig.1.3e). Using different velocities or channels dimensions will results in different shear stresses being apply to the cells. Alternatively, cells can be deformed between two opposing flow in cross-slots devices [Guillou, 2016b]. In these kinds of devices, the suspended cell and its properties are treated as a continuum [Gerum, 2022]. Indeed, these devices do not allow to decipher the contribution of different parts of the cell. Additionally, the pattern of forces applied on the object is complex and make the extraction of parameters difficult.

Microsystems allows to drastically increase the throughput of experiments, either using high throughput technics (up to 1000 cells analyzed per seconds in deformability cytometry [Otto,

2015]) or through parallelization and simultaneous characterization of measurements (see [Davidson, 2019] for a parallelized microfluidic implementation of micropipettes aspiration experiment).

### 1.3.5 Rheological values reported for cells

Several studies have focused on the same cells using different technical approaches. We report in Table 1.2 a few studies comparing the rheological properties of cell lines of breast tissue : non-cancerous MCF-10A and cancerous MCF-7 and MDA-MB-231.

Experimental technic	Rheological Parameters			Reference
	Non-cancerous MCF-10A	Cancerous MCF-7	Cancerous MDA-MB-231	
	Cell			
Micropipettes	E = 0.21 kPa			[Tabatabaei, 2019]
AFM	adherent cells : E = 0.56 kPa $\eta = 69$ Pa.s suspension cells : E = 0.21 kPa $\eta = 47$ Pa.s	adherent cells : E = 0.43 kPa $\eta = 50$ Pa.s suspension cells : E = 0.18 kPa $\eta = 29$ Pa.s	adherent cells : E = 0.32 kPa $\eta = 38$ Pa.s suspension cells : E = 0.15 kPa $\eta = 33$ Pa.s	[Nematbakhsh, 2017] (Hertz model)
		E = 1.04 kPa	E = 0.62 kPa	[Omidvar, 2014] (Hertz model)
Optical Stretcher and Tweezers	OD = 10.5	OD = 21.4	OD = 33.7	[Guck, 2005]
	$G_0 = 3.7$ Pa $G' = 3.3$ Pa $G'' = 1.4$ Pa		$G_0 = 1.7$ Pa $G' = 1.7$ Pa $G'' = 0.3$ Pa	[Mandal, 2016] (SLL model)
Microsystems and Microfluidics	E1 = 12.3 kPa E2 = 10.0 kPa $\eta = 1.89$ kPa.s	E1 = 14.5 kPa E2 = 7.0 kPa $\eta = 1.64$ kPa.s	E1 = 22.4 kPa E2 = 5.9 kPa $\eta = 2.56$ kPa.s	[Hu, 2017] (Hertz and Tataru's model)

**Table 1.2** – Comparison of rheological values for breast cancer cell lines MCF-10A (non-cancerous), MCF-7 (cancerous, lowly metastatic) and MDA-MB-231 cells (cancerous, highly metastatic).

Depending on the experiments, the elasticity moduli reported were in the range of 0.1-10 kPa, and viscosity in the range of 0.01-10 kPa.s. This illustrates the complexity of rheological measurements in heterogeneous soft objects such as cells, as discussed below.

**Rheological values depend on experimental designs.** The wide range of values reported in Table 1.2 highlights the importance of the choice of parameters (deformation level, loading rate, etc...) used for the experiments. As the measurements depend of the magnitude the forces, and how quickly they are applied, one should be careful when interpreting and comparing results, as reported values may vary up to a 1000 fold [Wu, 2018].

In the microfluidic system presented in [Hu, 2017], deformation levels reached a few micrometers (up to 70% of the cell size, likely integrating the properties of the nucleus as well) while maximal indentation in both AFM experiments were 600 nm. Thus, the elasticity and viscosity

values reported were an order higher in the microfluidic experiment. Indeed, using micropipette aspiration on whole cells and isolated nuclei, the nucleus has been reported to be 3-4 times stiffer than the cytoskeleton and twice as viscous [Guilak, 2000]. Following relaxation of a bead injected into the cytoplasm of cells, [Mandal, 2016] reported that the shear modulus of the cytoplasm is of the order 1 Pa, approximately a 100 to 1000 times less than the cytoskeleton and nucleus.

Using the same AFM technic, [Nematbakhsh, 2017] and [Omidvar, 2014] reported slightly different values (within a factor 2-3), though using cantilever with the same rigidity and indentation with the same speed, maximal force and maximal depth. However, while [Nematbakhsh, 2017] used a microsized-bead (4.5  $\mu\text{m}$  diameter) probe for attached to the tip, in [Omidvar, 2014] cantilevers were functionalized with cells to probe cell-cell adhesion at the same time as the mechanical properties. Similarly, [Li, 2008] reported the dependency of apparent Young moduli measurements with the loading rate during AFM indentation : Young moduli measured at 1 Hz were in average twice bigger than when measured at 0.03 Hz.

**Cancer cells are softer.** In all experiments though, it can be noted that MDA-MB-231 cells have the lowest elasticity and viscosity of all three lines. Values for MCF-7 are always similar or lower than the ones for MCF-10A cells. These experiments underline that cancer cells appear softer and more fluid-like than their non-malignant counterparts.

Using micropipettes aspiration, [Tabatabaei, 2021] reported that MDA-MB-231 cells were more deformable reaching the equilibrium length faster than MCF-7 cells, though rheological parameters were not extracted. The same trend was observed in the optical deformability reported in [Guck, 2005], though modelization was too complex to extract rheological parameters from the experiment.

This trend for reduced elasticity and viscosity in cancer cells compared to their non-malignant counterparts seems to be a conserved characteristics, and have been reported in other cell lines from other cancers (colon [Pachenari, 2014], ovarian [Xu, 2012]), and in primary cells (breast [Plodinec, 2012], thyroid [Prabhune, 2012], oral [Remmerbach, 2009]).

However, tumors are highly heterogeneous in their mechanical properties on all scales from the tissue level down to individual cells. This results in a broad rigidity distribution, from very stiff cells to cells softer than those found in healthy tissue [Fuhs, 2022].

It is worth noting that nuclei mechanics highly depends on the cell cycle. The nucleus architecture that we have described is valid for the G1/S state (meaning in non-dividing cells). Notably during mitosis chromatin compacts into chromosomes and the nuclear envelope disappears, thus allowing the two copies of the genome to be separated into the two daughter cells. During this phase (G2/M), the cells are then much softer. In a deformation-based quantification, cancers cells in G2/M state showed an  $\approx 45\%$  reduction in steady-state viscosity and a more than 60% decrease in both transient elasticity and viscosity [Teng, 2018].

## 1.4 Impact of mechanics on cell biology

Mechanics is of importance in many biological processes. The cytoskeleton is able to transmit forces from the exterior of the cell to the nucleus. In a process call mechanotransduction, cells convert mechanical signals conveyed by the microenvironment into biochemical signals to adapt their behavior to the environment.

### 1.4.1 Interaction with the extracellular environment

Thanks to the acto-myosin coupling at the site of focal adhesions, cells are able to sense and exert forces. In particular, they are sensible to the rigidity of their surrounding environment. Solid tissues exhibit a range of stiffness in the body. In the brain, a very soft tissue, the Young modulus  $E$  is approximately 0.1-1 kPa, and can reach up to 100 kPa in bones. In muscles, the ECM reach intermediate values of approximately 10 kPa [Guimarães, 2020]. It has been shown that the substrate elasticity is able to direct stem cell lineage specification [Engler, 2006]. Naive mesenchymal stem cells grown on a soft matrix (0.1-1 kPa) will differentiate into neurons, while if grown on intermediate (8-17 kPa) or stiff (25-40 kPa) matrix will differentiate into muscle cells or osteoblasts respectively, the specificity being Myosin II dependent. The transcription factors YAP and TAZ (mediators of Hippo signaling, powerful regulators of cell proliferation and survival, playing critical roles in organ growth) were identified as nuclear relays of mechanical signals exerted by ECM rigidity and cell shape [Dupont, 2011]. They are localized in the cytoplasm in cells experiencing low levels of mechanical signaling, such as in rounded cells attached to a soft ECM (typically  $< 1.5$  kPa for epithelial cells); they are instead nuclear in cells perceiving high levels of mechanical signaling, such as cells cultured on rigid substrates (typically at  $> 5-10$  kPa) or experiencing deformation and cytoskeletal tension (for example, cells stretching over an area of  $> 3000 \mu\text{m}^2$ ) [Helvert, 2018]. When adherent cells are detached and unable to sense the rigidity of their environment, the lack of proliferative signal through the Hippo pathway leads them to apoptosis (anoikis, detachment-induced death).

Elasticity of the extracellular matrix also influences protein expression. For instance, lamin A levels scaled with tissue elasticity (correlated with levels of collagen in the extracellular matrix) [Swift, 2013]. Indeed, lamin A/C transcription levels were similar to those of mechanosensitive proteins (Vinculin, Yap1, and Piezo1), thus indicating regulation by both matrix elasticity and externally imposed tissue strain, while lamin B levels align with and predict regulation by the cell cycle transcription factor, FOXM1 [Wang, 2022].

Reciprocally, cells are able to modulate the stiffness of their environment, either stiffening it through production of collagen and other matrix proteins, or softening through expression of matrix metalloproteinases [Winkler, 2020].

### 1.4.2 Relevance of mechanics in cancer

It is well accepted that tumor tissues are stiffer than their normal surrounding environment. Indeed, palpation remains one of the ways to detect tumors. In the mammary gland,

the elastic modulus of the tissues has been showed to increase with tumorigenesis [Levental, 2009]. This observation has been the rationale for the development of elastography in addition to ultrasonography. Some recent studies have shown the stiffness of the tissue surrounding of the malignant breast lesions to be higher than that of benign breast lesions [Xiao, 2016 ; Yang, 2020b]. Cancer-associated fibroblasts (CAFs) are the main contributors to ECM stiffness and degradation [Najafi, 2019]. Extensive remodeling of ECM during cancer progression causes alterations in its density and composition [Gkretsi, 2018]. Cancer cell proliferation, migration, and invasion as well as angiogenesis are consequences of ECM stiffness and degradation. A stiff or rigid ECM is for instance capable of stimulating epithelial cell transformation from normal cells to malignant cancer cells [Katara, 2018].

In their transformed state, cancer cells seems to escape anoikis death, probably linked to a malfunction in the rigidity-sensing structure at focal adhesions or in the cytoskeletal organization [Sheetz, 2019]. Indeed, modulating the absence or presence of mechanosensory modules, cancer cells from different tissues can be toggled between rigidity dependent and independent growth rate, respectively [Yang, 2020a]. Mechanical stretching of adherent cancer cells inhibited growth and activated cell apoptosis. However, when rigidity sensing was restored in cancer cells, they grew better with mechanical stretch, like normal cells [Tijore, 2018]. Thus, the mechanical differences in transformed cells may make them more sensitive to mechanical damage.

As we'll see later when we'll focus on the impact of the blood circulation on cancer cells (section 2.3), shear stress produced by the flow proves to be harmful for most cancer cells. However, in the surviving cells, shear stress promote adaptation in the cell phenotype (epithelial to mesenchymal transition, stemness).

## 2 Cancer and Metastasis

Having described the typical tools and experiments to address the mechanics of cells, we considered the cells as passive objects, which they are not. We thus must not forget that the cells are alive, and thus active objects, which properties may change as the cell adapts.

In this work, we'll focus particularly on a subset of cells : the cancer cells, for they are of particular importance as cancer remains among the highest mortality cause in the world. According to estimates from the World Health Organization (WHO) in 2019 [WHO, 2020], cancer is the first or second leading cause of death before the age of 70 years in 112 of 183 countries and ranks third or fourth in a further 23 countries.

### 2.1 Introduction to cancer

Worldwide, an estimated 19.3 million new cancer cases and almost 10.0 million cancer deaths were reported by the International Agency for Research on Cancer in 2020 (see Fig.1.4a)[Sung, 2021]. Female breast cancer has surpassed lung cancer as the most commonly diagnosed cancer, with an estimated 2.3 million new cases (11.7%), followed by lung (11.4%), colorectal (10.0%), prostate (7.3%), and stomach (5.6%) cancers. Lung cancer remained the leading cause of cancer

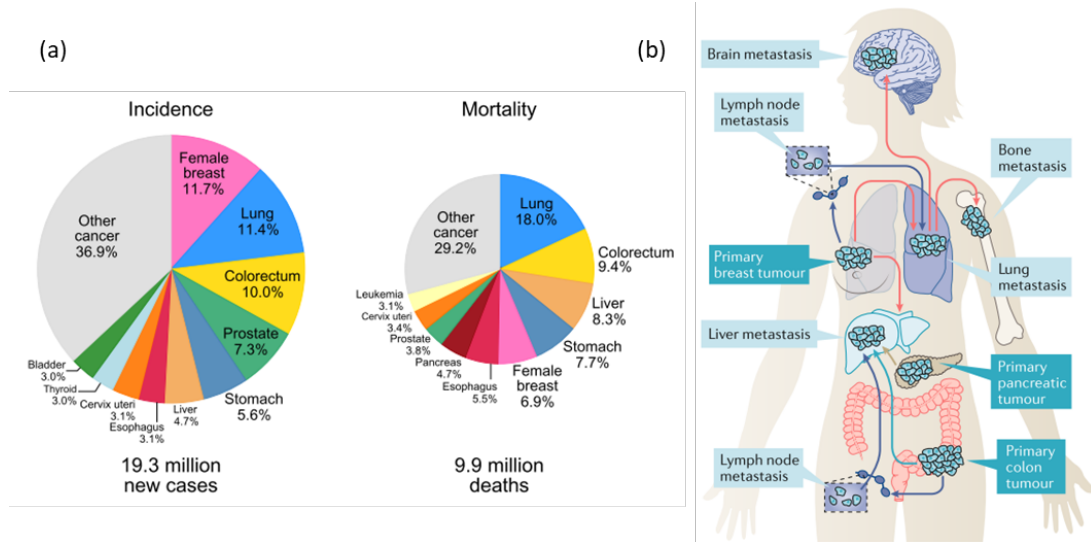


**Figure 1.4** – Introduction to cancer (a) Distribution of Cases and Deaths for the Top 10 Most Common Cancers in 2020 [Sung, 2021]. (b) Metastatic dissemination is a non-random process based on biological and mechanical cues. The anatomical plan and corresponding vascular pathways depict how circulating tumor cells (CTCs) use blood, as well as the lymphatic circulation (purple arrows), to reach distant organs, highlighting the common metastatic patterns for colon cancer (blue arrows), breast cancer (red arrows) and pancreatic cancer (brown arrows). Adapted from [Follain, 2020].

death, with an estimated 1.8 million deaths (18%), followed by colorectal (9.4%), liver (8.3%), stomach (7.7%), and female breast (6.9%) cancers.

Cancer is characterized by the unregulated proliferation and invasive behavior of abnormal cells in the body. Cancer can affect any part of the human organism, originating from a variety of factors, including genetic mutations, epigenetic alterations, exposure to carcinogens (cancer-causing substances), and lifestyle choices. The hallmark feature of cancer is the ability of these deviant cells to grow uncontrollably, eventually spreading to nearby tissues and disrupting normal bodily functions. While the term "cancer" encapsulates a diverse range of individual diseases, each with its own distinct characteristics and behaviors, they all share the fundamental trait of unregulated cell growth. This uncontrolled growth can result in the formation of a mass of cells, referred to as a tumor, which can be categorized as benign (non-cancerous) or malignant (cancerous) [Hanahan, 2011; Hanahan, 2022].

With some exceptions, most tumors are classified into four major groups according to their origin (epithelial, mesenchymal, hematopoietic, and neuroectodermal). Virtually all cell types can give rise to cancer, but the most common human cancers are of epithelial origin, the carcinomas. Most carcinomas fall into two categories: squamous cell carcinomas arise from epithelia that form protective cell layers, while adenocarcinomas arise from secretory epithelia [Weinberg, 2014]. Tumors that breach the basement membrane and invade underlying tissue are malignant. An even further degree of abnormality is metastasis, the seeding of tumor colonies to other sites in the body. Metastasis requires not only invasiveness but also such newly acquired traits as motility and adaptation to foreign tissue environments.

The work presented here was realized using models of breast and colon cancer. We'll rapidly describes these two specific cancers here.

### 2.1.1 Breast cancer

Breast cancer occurs when cells in the breast begin to grow out of control. Many breast cancers are diagnosed based on a mammogram (specialized x-ray scan), or when a woman or her doctor finds an abnormal lump in her breast.

Worldwide, breast cancer is the leading type of cancer in women, accounting for 25% of all cases. Five-year survival rate is between 80-90%, though lower in developing countries.

At diagnosis, breast cancer cells may be found in the breast tissue only, in the axillary lymph nodes under the armpit, or in more distant sites in the body. Based on where the cancer is found, breast cancer is assigned a stage, from I to IV. Stage IV breast cancer, also called metastatic breast cancer, has spread to a distant place in the body.

- **Classification** Breast cancer is divided into 3 types based on the presence or absence of different proteins in the breast cancer cells [Waks, 2019].
  - Hormone receptor–positive breast cancer (also referred to as luminal) makes up 70% of breast cancer cases and has either estrogen receptor (ER) or progesterone receptor (PR) protein expressed in the cancer cells.
  - HER2-positive (also known as ERBB2-positive), characterized by cells displaying a high level of the HER2 protein due to HER2 gene amplification, makes up 15% to 20% of breast cancer cases
  - Triple-negative breast cancer makes up 15% of breast cancer cases and does not have ER, PR, or HER2 protein expression in the cancer cells.

Luminal tumors have a better prognosis, and are less aggressive than that in triple negative tumors which have a higher metastatic rate [Kast, 2015]. Identifying a patient cancer stage and subtype is important as prognosis and treatments differ for each.

- **Treatments** For patients with stage I to III, usual treatment consists of surgery to remove the breast tumor and possibly the whole breast (mastectomy), in combination with systemic treatments, and possibly radiation therapy to the breast +/- lymph node area. Hormone receptor–positive breast cancer is best treated with anti-estrogen drugs, while HER2-positive breast cancer is treated with intravenous antibodies that specifically attack the abnormal HER2 protein, both in combination with intravenous chemotherapy. Triple-negative breast cancer is treated with intravenous chemotherapy [Waks, 2019], and more recently immunotherapy [Loibl, 2024].
- **Risk factors** On top of the usual ones (obesity, alcohol, lack of physical exercise, older age ...), other risk factors may include exposition to estrogen (early menarche, late menopause, late pregnancy or endocrine treatments) and familial history of breast cancer [NCI, 2023]. About 5-10% of all cases are from genetic origin. Among mutated genes that are associated with breast cancer, BRCA1 and BRCA2 are the predominant. These genes belong to a

class of tumor suppressors, expressed in the breast and other tissues where they help DNA repair or cells death if DNA cannot be repaired.

- **Models** Several models of cells are available from commercial cell lines, to patients derived primary xenografts.

Among cell lines, some of them are widely used in laboratories including MCF-7, MDA-MB-231, MDA-MB-468... In this study we choose to focus on three cell lines : MCF-7, SK-BR-3 and MDA-MB-231. Each of these lines present markers that represent the three main types of breast cancer : MCF-7 present receptors for estrogen (ER) and progesterone (PR), SK-BR-3 are positive for HER2, and MDA-MB-231 present none of these markers (triple negative) [Dai, 2017].

Though cell lines provide unlimited homogenous materials for tumor studies and are relatively easy to culture, they are known to accumulate mutations during the initial establishment and subsequent series of cultivations. Thus, whether breast cancer cell line heterogeneity reflects that of carcinoma remains an important issue to resolve before drawing any reliable conclusion at the tumor level using cell lines. In that regard, more elaborate models can be used, including patient derived xenografts (resected human tumors engrafted into mice). These models allow to better conserve the original human tumor characteristics [Woo, 2021].

### 2.1.2 Colon cancer

Colon (or colorectal cancer) is the development of cancer from the colon or rectum (parts of the large bowel). It affects both men and women equally, and represent approximately 10% of all cases. More than 1.9 million new colorectal cancer (including anus) cases and 935'000 deaths were estimated to occur in 2020, representing about one in 10 cancer cases and deaths. Overall, colorectal ranks third in terms of incidence, but second in terms of mortality [Morgan, 2023].

It can be detected through colonoscopy, possibly coupled with medical imaging to determine if the disease has spread.

- **Pathogenesis** Colon cancer exemplifies stepwise progression as it develops initially as a benign precursor lesion from the epithelial cells lining the colon or rectum, which can progress to an invasive lesion with the capacity to metastasize. The lesion arises from an intestinal clonogenic precursor cell (crypt base stem cell) through the accumulation of multiple genetic abnormalities, most notably in the Wnt pathway (inactivating mutations of APC, activating mutations of KRAS, and subsequent mutations of TP53 and of genes in the TGF- $\beta$  pathway) which confer invasive and metastatic capacity [Tabibzadeh, 2020]. The Wnt signaling pathway normally plays an important role for normal function of these cells, as the intestinal epithelium is the most rapidly self-renewing tissue in adult mammals.
- **Risk factors** Most colon cancers are due to old age and lifestyle factors, with only a small number of cases due to underlying genetic disorders. Risk factors include diet, obesity, smoking, and lack of physical activity, dietary factors (red meat, processed meat, alcohol)

or some inflammatory bowel diseases (includes Crohn's disease, ulcerative colitis) [Stewart, 2014].

- **Treatments** At an early stage, colon cancer may be removed through surgery, with possible resection of parts of the intestinal tracts. If there are only a few metastases in the liver or lungs, these may also be removed. Chemotherapy, radiotherapy and immunotherapy may come in combination with surgery.
- **Models** Similarly to breast cancer, commercially available cells lines originating from colon cancer exists : Caco-2, HT-29, SW-620... In this work, we'll use HT-29 and SW-620s as models of primary and metastatic tumors respectively. HT-29 originates from a primary tumor, while SW-620s was isolated in a lymph node metastasis [Ahmed, 2013].

What makes these diseases even more deadly is the fact they can metastasize. Primary tumors can be reasonably well treated and removed surgically as long as they remain localized. However, it is much more difficult once it has spread through the body. Metastatic potential varies between cancers, and within each cancer subtypes. For instance, metastasis incidence is more common in patients with a triple negative breast cancer than the other two subtypes [Zagami, 2022]. Additionally, metastasis establish preferentially in different organs depending on the type of cancer. Where breast cancer can give rise to lymph node, bone, liver, lungs and brain metastasis [Harbeck, 2019], colon cancer preferentially extends to lymph node and liver metastasis (see Fig.1.4b) [Follain, 2020]. These preferences may arise from cell markers affinity [Ganesh, 2021], and/or topological cues : the lymphatic system locally drains tissues, while the portal vein drains blood from the gastrointestinal tract to the liver.

The "seed and soil" hypothesis in cancer metastasis was proposed by British surgeon Stephen Paget in 1889. Paget's hypothesis suggests that just as a seed (the cancer cell, or "the seed") needs a fertile environment (the tissue, or "the soil") to grow, certain cancer cells have a predilection for specific target organs or tissues when they metastasize [Paget, 1889]. This hypothesis highlights the non-random nature of cancer metastasis and the role of the microenvironment in facilitating the colonization of secondary sites by metastatic cancer cells.

We will then focus on the metastatic process.

## 2.2 The metastatic cascade

As primary tumor gets better treated, metastasis (the development of secondary tumors in distant organs) amount to approximately 90% of cancer-related deaths [Chaffer, 2011].

Metastasis is a complex multi-step process, in which cancer cell will escape the primary tumor, migrate through the surrounding tissue, invade a blood or lymph vessel (intravasation) where it will circulate for a certain amount of time before escaping (extravasation) and colonizing a distant organ, thus giving rise to a secondary tumor [Fidler, 2003 ; Lambert, 2017]. In all of these steps, the cancer cell experiences different levels of stresses and confinement. We'll rapidly describe these different steps, then we'll focus on the passage in the blood circulation that this present work addresses.

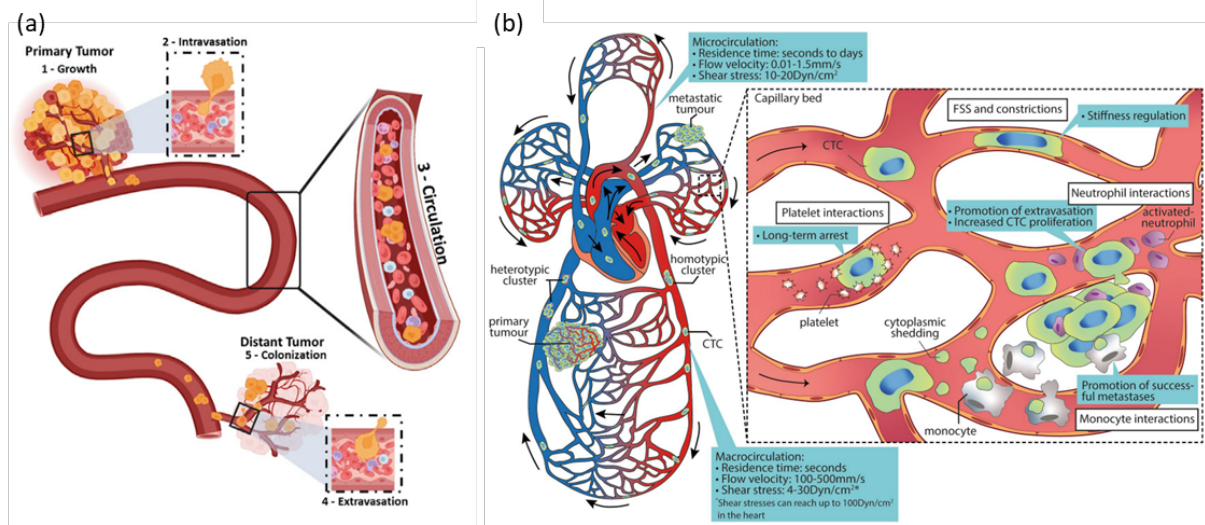


**Figure 1.5** – The metastatic cascade - (a) The different metastatic cascade steps : (1) tumor growth, (2) intravasation of cancer cells into the circulation, (3) survival in the blood circulation as CTCs, (4) extravasation at distant sites, and (5) subsequent organ colonization (adapted from [Kurma, 2023]). (b) tumor cell adaptations and interactions within the microcirculation. Cancer cells escape from primary tumors and are shed into the circulation, where they eventually arrest in capillary beds. Inset : Transit through the microcirculation alters CTC behaviors. Cell deformation due to biomechanical forces (FSS, constrictions) may induce phenotypic changes on CTCs, such as adaptations in cellular stiffness. Moreover, interactions of CTCs with immune cells, endothelium and platelets also take place, leading to stable arrest (platelets, neutrophils), extravasation (neutrophils) and colonization (monocytes and neutrophils) (adapted from [Varotsos Vrynas, 2021]).

### 2.2.1 Tumor growth

As cancer cells undergo uncontrolled proliferation during the initial tumor growth, a favorable microenvironment is created through neovascularization, inflammatory-like immune response, and extracellular matrix remodeling. Some cells may undergo changes and acquire stem-cell features (self-renewing) during a process called epithelial-to-mesenchymal transition (EMT), that we'll detail in a later section 2.2.5.

However, cells in the tumor will still experience high levels of confinement resulting from tumor expansion, and hypoxia as the tumors expands faster than new vessels. Confinement can induce DNA damages mediated by ruptures in the nuclear envelope, which in turn is able to promote tumor cell invasion [Nader, 2021b] As the cells acquire migratory characteristics, they are then able to escape the primary tumor and migrate through tissues.

### 2.2.2 Migration and Intravasation

The mechanisms that individual cells, including non-malignant ones such as immune cells, use to migrate can be divided into two distinct types, known as mesenchymal migration and amoeboid migration. Cells migrating in a mesenchymal fashion typically adopt an elongated, spindle-like shape and exert traction on their substrates via focal adhesions associated with actin rich protrusions, such as lamellipodia or filopodia [Abercrombie, 1980]. In contrast, cells undergoing amoeboid migration adopt round or irregular shapes. They undergo cycles of expansion

and contraction, which allow them to squeeze through gaps in the extracellular matrix. The velocity of amoeboid migration is often higher than that of mesenchymal migration [Paňková, 2010]. This free migration can be guided by chemical gradients (chemotaxis) or mechanical gradients (durotaxis).

The gain in migratory properties also allows cells to cross the endothelial barrier and enter the blood of lymph circulation, referred to as intravasation. Intravital microscopy studies have shown that cancer cells generate protrusions (invadopodia) that are first aligned along endothelial cell–cell junctions through contact guidance, and then inserted in between endothelial cells [Roh-Johnson, 2014]. Interestingly, the protrusions formation is enhanced upon physical contact with macrophages. Both single cells and clusters of cancer cells together with partnering cells from the microenvironment can intravasate into blood [Aceto, 2014]. Intrinsic properties of cancer cells (genetic mutations, gene expression, metabolism ...), signals from the tumor microenvironment (interaction with immune cells, pericytes), and mechanical cues (tissue stiffness, interstitial fluid pressure) have been hypothesized to promote intravasation [Sznurkowska, 2022].

### 2.2.3 Passage in the blood circulation

Once in the blood circulation, cancer cells are exposed to very harsh conditions, including high shear stress and deformations, due to the flow and topology of the capillaries [Follain, 2020]. These stresses and deformation are harmful for the cancer cells of epithelial origin. A majority of the cells entering the blood circulation will die from exposition to the stresses. However, a small fraction of these cells survives, and may give rise to metastasis [Weiss, 1990]. This metastatic inefficiency has been characterized very early by Zeidman in 1950 who observed that only tens of lung tumors resulted from  $> 10^5$  cancer cells injected intravenously [Zeidman, 1950]

This deleterious effect on cancer cells has been observed *in vivo*, following radioactive marked melanoma tumor cells, [Fidler, 1970] reported that only 1% of cells survived 24h after intravenous injection in immunodeficient mice. However, these few remaining cells were sufficient to establish metastasis proliferation.

The causes of CTCs deaths are still unclear. Hypothesized destructive mechanisms include anoikis (programmed cell death due to detachment), though cancer cells often have some intrinsic resistance to this [Sheetz, 2019], exposure to immune system-mediated destruction when separated from the immune privileged microenvironment of the primary tumor [Labelle, 2012], and mechanical destruction due to hemodynamic forces including deformation in the microvasculature [Weiss, 1985].

Thus, the outcome for cancer cells becomes either death or escape the circulation. It has also been reported than cells can enter a dormancy state [Luzzi, 1998].

Then comes the question of how long does a cancer cell remain circulating in the blood circulation, before stopping, dying or extravasating. *In vivo*, CTCs half-life have been estimated to the order of an hour. [Meng, 2004] reported a half-life of 1 to 2.4 h in patients whose primary breast cancer was just removed while searching for  $CD45^- CK^+$  cells. [Stott, 2010] reported a short ( $< 24$  h) half-life for CTCs post surgical removal of the primary tumor in 6 out of 8

prostate cancer patients, while the remaining 2 patient presented persistent CTCs for up to 3 months. [Aceto, 2014] reported that clusters of CTCs are cleared faster from the blood circulation (6-10 min) compared to single CTCs (25-30 min) following injection in immunosuppressed mice, as these clusters are more likely to be trapped in small capillaries.

As CTCs navigate the circulation, biomechanical forces and blood cell-CTC interactions play a crucial role in shaping CTCs during their transit through capillaries [Varotsos Vrynas, 2021]. Biomechanical adaptations, facilitated by the activation of the RhoA-ROCK pathway, allow tumor cells to withstand frictional forces and survive hemodynamic forces, promoting metastasis. Additionally, platelets contribute to the protection and facilitation of metastasis by forming heterotypic aggregates with CTCs. Neutrophils also enhance the metastatic ability of tumor cells and promote their proliferative ability.

As cells can remain stuck in the blood microcirculation, it is unclear what is the proportion of free cells moving through the capillaries during transit in the blood circulation. Thus, cells could spend most of the time trapped, and exposition to fluid shear stress could be very short (a few seconds) [Krog, 2018].

We'll focus more on the description of the blood circulation, its topology and stresses in a later section 2.3.

#### 2.2.4 Extravasation

In order to escape the blood circulation, CTCs have to interact with and attach to the endothelial cells of the vessel, either through cell arrest in constrictions, or through interaction with the endothelial wall under favorable flow patterns.

Using the zebrafish embryo, [Follain, 2018] show that arrest of CTCs occurs in vessels with favorable flow profiles where flow forces control the adhesion efficacy of CTCs to the endothelium. They identified a threshold of hemodynamic profiles (mean velocity in the range 400–600  $\mu\text{m/s}$ ) that participates in the stable arrest of CTCs in permissive vascular regions. These permissive flow profiles promote the formation of transient protrusions, establishing integrin-dependent adhesion of CTCs to the endothelium. This fast and weak adhesion is then quickly stabilized to reach adhesion forces exceeding the shear forces generated by such permissive flow values.

Even if the cells manage to extravasate and form micrometastasis, these do not necessarily develop to form macroscopic metastases. Indeed [Luzzi, 1998] reported only 0.02% of melanoma cells injected intraportally in mice livers gave rise to macroscopic metastasis after 13 days, while after day 3 more than 80% of the cells had extravasated. In this study, only 10% of the injected cells died within the microcirculation. Similar results were found following injection in the lung of mice, where 74% of cells managed to extravasate after 3 days but only a small proportion started to form metastasis [Cameron, 2000].

### 2.2.5 Epithelial to mesenchymal transition (EMT)

Cancer cells are able to adapt to the environmental changes encountered during the different steps of the metastatic cascade through a process called the Epithelial to mesenchymal transition (EMT). It characterizes the cells change in phenotype from epithelial (from a tissue, typically adherent) to mesenchymal (similar to immune cells, ability to migrate). It also contributes to cell growth, cell survival, and the reemergence of stem cell characteristics [Thiery, 2009].

EMT is characterized by a loss of polarity and cell-cell adhesion and a gain of migratory and invasive properties. Loss of E-cadherin (cell-cell junction) is considered to be a fundamental event in EMT. Cellular mechanics is also affected as EMT influences actin cortex regulation. Additionally, transition from keratin filaments (epithelial phenotype) to vimentin (mesenchymal) guides transformation to motile cells [Lorenz, 2019].

Studies have shown that EMT can be induced through many transcription factors (SNAI1/2, ZEB1/2, Twist, ...) and signaling pathways (TGF- $\beta$ , Wnt, Notch). EMT can also be induced in response to hypoxia, which is characteristic of tumor environments [Zhang, 2013].

Microfluidic approaches were able to show that flow forces increase the EMT of tumor cells and favor their motility and aggressiveness [Rizvi, 2013]. Changes in the morphological, genetic, and protein profiles of biomarkers associated with aggressive disease were evaluated in ovarian cancer 3D cultures grown under controlled and continuous laminar flow. A modulation of biomarker expression and tumor morphology consistent with increased epithelial–mesenchymal transition, a critical step in metastatic progression and an indicator of aggressive disease, is observed because of hydrodynamic forces. Similar effect was observed in breast MDA-MB-221 cell lines where EMT genes overexpression was induced in response to flow-induced deformation in a microfluidic device [Ahmad-Cognart, 2020].

## 2.3 Focus on the blood circulation

In a cylindrical blood vessel, the pattern of velocity  $u$  is given by the Poisson flow : velocity is maximal at the center ( $r = 0$ ) and zero at the walls ( $r = d/2$ ) of the vessel :  $u(r) = u_{max}(1 - (\frac{2r}{d})^2)$ . As the velocity decreases from the center to the walls, it creates a gradient between fluid layers of different radial coordinate, namely the shear rate  $\gamma(r) = |\frac{\partial u(r)}{\partial r}| = u_{max} \frac{4r}{d}$ . The shear stress  $\tau$  is the product of the shear rate  $\gamma$  by the viscosity  $\mu$  of the fluid  $\tau(r) = \mu\gamma(r)$ . The shear stress is homogeneous with a force per unit area, and is traditionally expressed in dyn/cm<sup>2</sup> (even though the corresponding unit in the international system is the Pa : 1 Pa = 10 dyn/cm<sup>2</sup>).

The viscosity of blood is about 4 centipoise (cP), which is considerably greater than the viscosity of water (0.7 cP at 37 °C), primarily owing to the presence of red blood cells.

### 2.3.1 Topology

During their journey in the blood circulation, CTCs experience a huge variety of hemodynamic conditions. Typical values are given in Table 1.3. In the heart and the aorta, the velocity is very high (around 1m/s), thus giving rise to high shear stress. As the diameters of the vessels decreases (arteries and veins), the velocity and shear stress decreases as well. In the capillary bed,

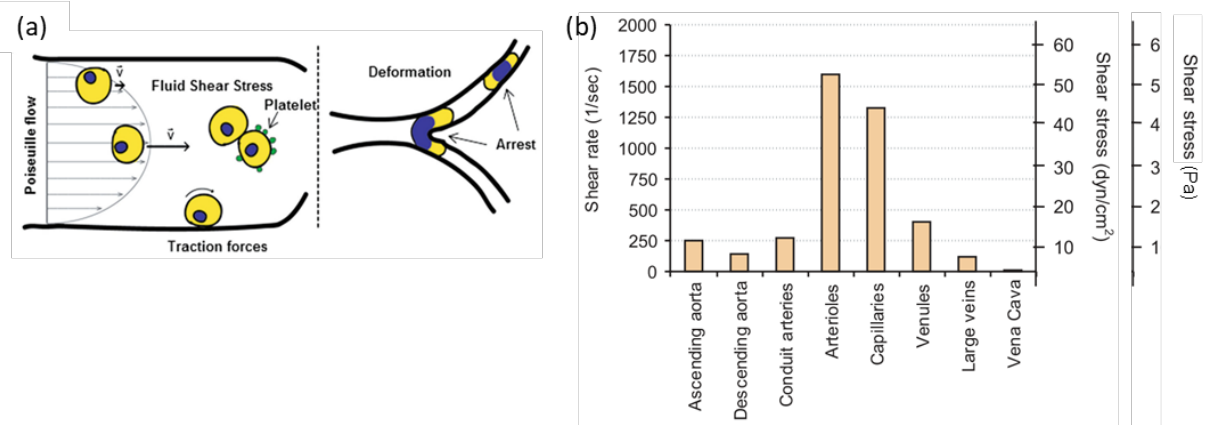


**Figure 1.6** – Stresses and Deformations in the blood circulation - (a) Representation of different hemodynamic forces encountered by CTCs. Fluid shear stress (FSS) can be calculated under conditions of Poiseuille flow where the maximum is at the vessel wall and the minimum is at the vessel axis (adapted from [Krog, 2018]). (b) Shear stress values in various vessels (adapted from [Papaioannou, 2005])

System	Radius	Fluid Velocity	Shear stress	Reynolds number
Interstitial fluid		0.001-0.004 mm/s	0.1-1 dyn/cm <sup>2</sup>	0.00005-0.0002
Lymphatic system	15-75 $\mu\text{m}$	0.02-1 mm/s	0.64-12 dyn/cm <sup>2</sup>	0.000033-0.002
Arteries	0.1-5 mm	100-500 mm/s	4-30 dyn/cm <sup>2</sup>	1-5000
Veins	0.2-1 mm	1-200 mm/s	1-4 dyn/cm <sup>2</sup>	0.006-100
Capillaries	5-20 $\mu\text{m}$	0.01-1.5 mm/s	10-20 dyn/cm <sup>2</sup>	0.003-0.004

**Table 1.3** – Key features of different fluid systems involved in cancer cell transport (Velocity, shear stress and Reynolds values reproduced from [Follain, 2020])

velocity is small (from 0.01 to 1.5 mm/s). However, as the diameters of capillaries are extremely small as well, the shear stress increases again (10-20 dyn/cm<sup>2</sup>, see Fig.1.6).

The blood flow, driven by contractions of the heart, is thus pulsatile. It can be turbulent in the heart and arteries, whereas it is mostly laminar in veins and capillaries. This is characterized by the Reynolds number  $Re = \frac{\rho u L}{\mu}$ , where  $\rho$  is the density,  $u$  is the flow velocity,  $L$  the characteristic length of the vessel and  $\mu$  the dynamic viscosity of the system.  $Re$  greater than 2000 suggests transition to turbulent flow, while  $Re$  is less than one within the microcirculation where viscous forces dominate.

In the capillary bed, vessels are relatively simple, composed only of a layer of endothelial cells that allow for exchange with the tissue. Vessel diameters are small (typically a few microns [Müller, 2008; MacDonald, 1995]) and present branching and constrictions (down to 3-4  $\mu\text{m}$ , see Fig.1.7a) These constrictions induce strong deformations on cells (see intravital imaging Fig.1.7b) and their nuclei, which modify various cell properties and behaviors (through mechanotransduction or damages, see Fig.1.7c) and may contribute to CTCs arrest in the blood circulation.

It is worth noting that red blood cells (RBCs) and leukocytes have relatively small diameters (6-8  $\mu\text{m}$  for RBCs, 6-7  $\mu\text{m}$  for lymphocytes, 12-15  $\mu\text{m}$  for neutrophils for instance) and are

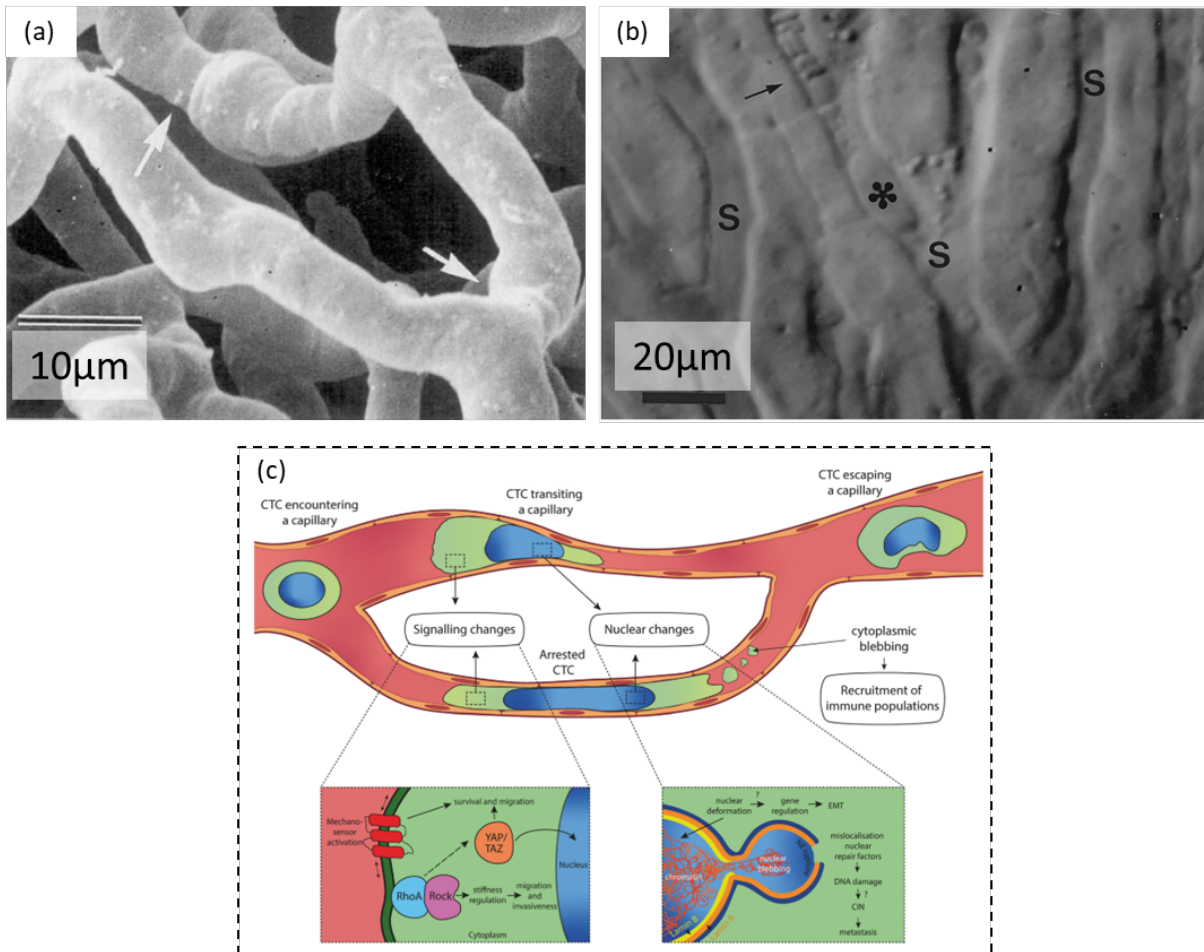


**Figure 1.7** – Stresses and Deformations in the blood circulation - (a) Scanning electron micrograph of corrosion cast showing capillaries in exocrine pancreas of mouse. Arrows denote several prominent constrictions (adapted from [MacDonald, 1995]). (b) Intravital videomicroscopic view of a B16F1 melanoma cell (\*) arrested due to size restriction within a sinusoid (S) of mouse liver, shown 45 minutes after injection. Blood flow is blocked (→) in the region immediately downstream from the cell (adapted from [Luzzi, 1998]). (c) Circulating tumor cell (CTC) encountering a capillary constriction and the possible adaptations that may increase its metastatic potential (adapted from [Perea Paizal, 2021]).

highly deformable [Shaw Bagnall, 2015]. Their small size helps navigate the microcirculation, RBCs for instance cross capillaries in seconds,  $\approx 300$  times faster than leukocytes [Chien, 1987].

### 2.3.2 Cells in the circulation

**Fluid shear stress reduce cancer cells viability.** Though malignant cells appear to resist short high shear stress ( $> 600 \text{ dyn/cm}^2$ ) pulses better compared to non-transformed epithelial cells [Barnes, 2012], prolonged exposition to high shear stress still remains deleterious to cancer cells.

Indeed, in an *in vitro* circulation device, high shear stress ( $60 \text{ dyn/cm}^2$ , comparable to those induced by an intensive exercise) caused necrosis in over 90% of MDA-MB-231 cells within the first 4 h of circulation in suspension, while low shear stress ( $15 \text{ dyn/cm}^2$ , resting state) had low

impact [Regmi, 2017]. More importantly, the cancer cells that survived the first 4 h of circulation underwent apoptosis during 16–24 h of post-circulation incubation.

**Stress induce EMT and promote stemness.** In a parallel plate experiment, fluid shear stress on the order of 10 dyn/cm<sup>2</sup> promoted EMT (upregulation of Vimentin and Snail, both at the gene and protein expression levels) and adhesion of breast cancer cells to an endothelial monolayer [Fuh, 2021]. Upregulation of EMT was more pronounced in MDA-MB-231 and MCF-7 compared to SK-BR-3 cell lines. Up regulation of cell motility and cell-cell adhesion was more pronounced in MDA-MB-231 cells than MCF-7 and SK-BR-3.

HeLa cells cultured under different shear stress levels showed increased cell proliferation with medium to low FSS (10 to 100 mPa), whereas high shear (1 Pa) had a suppressing effect, along with increase in stemness-related gene (Sox2, N-cadherin) expression in a magnitude-dependent manner [Dash, 2022].

## 2.4 Liquid biopsy

Liquid biopsy consists in using blood samples to look for tumor markers. In blood targets are CTCs, but also their subproducts, namely ctDNA (circulating tumor DNA), EVs (Extracellular Vesicles) and proteins.

### 2.4.1 CTCs & ctDNA

The first description of CTCs by Thomas Ashworth dates back to 1869 [Ashworth, 1869]. Since then, this specific subset of cancer cells has been thoroughly described and studied by many [Bidard, 2016 ; Keller, 2019].

Accessing these markers remains complicated due to the low number of CTCs and small amount of ctDNA in circulation [Pantel, 2019].

Circulating cell-free DNA in blood plasma is highly fragmented DNA mainly derived from apoptotic cells. The total amount of ctDNA might be <0.01% of the total circulating DNA concentration. Detection technics include targeted DNA sequencing (relies on the knowledge of a single mutation to be targeted) or non-targeted sequencing (genome-wide analysis, but less sensitive). Apart from detection, interest in these tumor subproducts (ctDNA, EVs) exists as they may transfer information and signals between cells.

### 2.4.2 CTCs capture devices

The isolation and capture of CTCs in the blood can be done in a variety of ways, that can be summarized in two categories : label-dependent and label-independent methods [Kumar, 2022] (see Fig.1.8). Several commercially available devices have been developed to detect and isolate CTCs from blood samples.

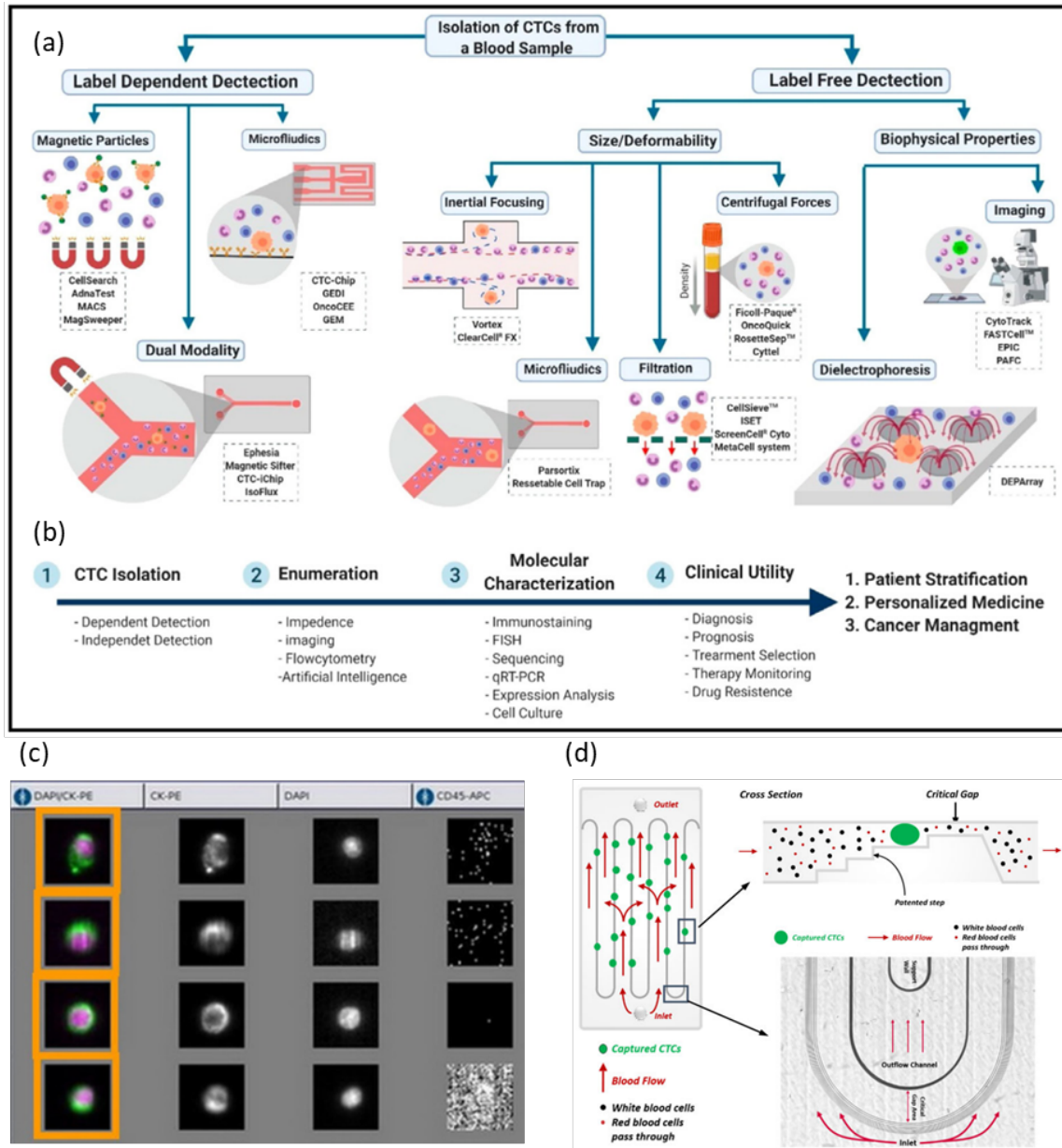


**Figure 1.8** – Schematic representation of the CTCs isolation and detection techniques, (a) various mechanisms for the isolation/detection; (b) overview of different steps and their associated techniques for CTCs isolation/detection (adapted from [Kumar, 2022]). (c) Identification of cytokeratin positive cells through CellSearch (adapted from [Riethdorf, 2007]). (d) Diagram of a Parsortix GEN3 Cell Separation Cassette showing how the blood flows into the cassette, over the step structures and through the critical gap (adapted from [Miller, 2018]).

**Label dependent methods** for positive CTC isolation depend on specific CTC cell surface markers, such as EpCAM, EGFR, HER2, etc. Conversely negative selection include CD45 (leukocytes) and CD66b (granulocytes).

The antibodies can be coupled to magnetic nanoparticles to allow for magnetic sorting, as it is the case for the CellSearch® system (Menarini Silicon Biosystems), the first FDA-approved CTCs isolation product and considered as the gold standard method of CTCs isolation. It is

intended for enumeration of CTCs of epithelial origin (characterized as CD45-, EpCAM+, and cytokeratins 8, 18+, and/or 19+) in whole blood (see Fig.1.8c) [Riethdorf, 2007].

Other methods target interaction between the CTC and ligand-tagged surfaces of microfluidic channels and their adhesion to them through lateral passive rolling to capture the CTC [Choi, 2014].

However, these methods yield may vary a lot as expression levels of the target markers may vary. For instance, some CTCs display low levels of EpCAM and are thus hard to detect in the CellSearch system [Andree, 2016].

**Label independent methods** rely on specific physical properties of CTCs to capture them, for instance larger cell size or enhanced mechanical plasticity of CTCs compared to normal blood cells.

Several devices employ high flux membrane (microsieve technology), pillars, cross flow to achieve mechanical filtration of larger CTCs. As larger objects also exert higher inertial forces, microfluidics can be used to separate cells of different size. The same is true with electrokinetics or acoustophoresis whose applied forces vary with the size of the object, thus allowing separation.

Parsortix® (ANGLE plc) is a recently FDA-approved microfluidic devices that captures CTCs based on their less deformable nature and larger size compared to other blood cells. The cells are flown through separation structure laid out in a “step” configuration yielding a final “critical gap” where the cells are captured (see Fig.1.8d) [Miller, 2018]. As a result, cells of interest are preferentially captured based on their size and resistance to compression.

However, size and mechanical properties may be heterogeneous within a CTC population, or may be too similar to the ones of blood cells to allow for separation.

### 2.4.3 Clinical relevance

CTCs have been detected in the blood already at early stages of tumor developments.

The presence of CTCs in the blood was shown to be a marker of poor prognosis in many studies. The presence of  $\geq 5$  CTCs per 7.5 mL of whole blood in patients with metastatic breast cancer was an independent predictor of shorter median progression-free survival (2.7 months vs. 7.0 months) and shorter overall survival (10.1 months vs.  $> 18$  months) [Cristofanilli, 2004]. Similarly in metastatic colon cancer, a meta-analysis including 11 studies ( $n = 1847$  patients) showed that an elevated CellSearch based baseline CTC count (using various cutoffs ranging from 1 to 5 CTCs/7.5 mL) was a strong and independent prognostic factor for progression-free survival and overall survival [Huang, 2015]. The presence of CTCs in the circulation after treatment can be a sign of minimal residual disease [Pantel, 2019].

Utility of CTCs into treatments decision are discussed in two major axes : either treatment based on CTCs count or CTCs variations; or based on the molecular characteristics of CTCs [Vasseur, 2021]. Current clinical trials demonstrated that the inclusion of CTCs count in therapy choice would help improve treatment. For instance, CTC count was shown to be a reliable biomarker method for guiding the choice between chemotherapy and endocrine therapy as the first-line treatment in ER metastatic breast cancer [Bidard, 2021]. In a phase II study

on metastatic colon cancer, [Krebs, 2015] found that patients with a high baseline CTC count ( $\geq 3$  CTCs/7.5 mL) could benefit from an intensive chemotherapy regime (four drugs), unlike patients with low CTC counts.

However, in metastatic breast cancer, clinical practice guidelines still currently do not recommend the use of CTCs for treatment decisions [Van Poznak, 2015], while results from several CTC-based interventional clinical trials are still pending.

With that in mind, these cells may prove relevant object of analysis in the study of metastasis [Cayrefourcq, 2015 ; Koch, 2020].

## 3 Microsystems and microfluidics

### 3.1 General knowledge

#### 3.1.1 History

Microfluidics is undergoing fast development over the last 20 years. Similarly to microelectronics which controls electrical current at the microscale, microfluidics allows for control of fluids at the micrometer scale [Whitesides, 2006]. The first applications of microfluidic technologies have been in analysis, for which they offer a number of useful capabilities : the ability to use very small quantities of samples and reagents (femto to nanoliters), and to carry out separations and detections with high resolution and sensitivity ; low cost ; short times for analysis ; and small footprints for the analytical devices. Microfluidics exploits both its most obvious characteristic — small size — and less obvious characteristics of fluids in microchannels, such as laminar flow.

This expansion has been made possible by the generalization of microfabrication, including the introduction of soft-lithography by the group of Whitesides in 1998 [Xia, 1998] : this technique has enabled simplified fabrication, and fast prototyping of elastomer-based, transparent and biocompatible microfluidic devices. The gold standard material used in microfluidic chips is PDMS (polydimethylsiloxane). PDMS is an optically transparent, gaz permeable, biocompatible, soft elastomer (Young modulus  $\approx 2$  MPa). Its ease of use contributed to the explosion of microfluidics.

#### 3.1.2 Theory

In fluid mechanics, the velocity field  $\mathbf{u}$  of an incompressible fluid is given by the Navier-Stokes equation :

$$\frac{\partial \mathbf{u}}{\partial t} + (\mathbf{u} \cdot \nabla) \mathbf{u} = -\frac{1}{\rho} \nabla p + \nu \nabla^2 \mathbf{u} + \mathbf{f}$$
$$\nabla \cdot \mathbf{u} = 0$$

where  $\mathbf{u}$  represents the velocity vector field,  $t$  is the time variable,  $p$  the pressure,  $\rho$  the fluid volumic mass,  $\nu$  its kinematic viscosity ( $\nu = \frac{\mu}{\rho}$  with  $\mu$  the dynamic viscosity).  $\mathbf{f}$  represents external body forces, such as gravity.

In this equation, the term  $(\mathbf{u} \cdot \nabla)\mathbf{u}$  represents inertial forces, while  $\nu\nabla^2\mathbf{u}$  represents viscous forces. We introduce the Reynolds number  $Re = \frac{\rho UL}{\mu}$ , where  $\rho$  is the fluid density,  $\mu$  its dynamic viscosity,  $U$  is the characteristic velocity,  $L$  is a characteristic length of the system. The Reynolds number can be seen as the magnitude ratio of inertial over viscous forces. In the case of microfluidics, the magnitude of  $L$  and  $U$  is small enough so that  $Re \ll 1$ , thus inertial forces can be neglected. Similarly, gravity can be neglected as well, and in absence of any other external forces, the equation then becomes :

$$\frac{\partial\mathbf{u}}{\partial t} = -\frac{1}{\rho}\nabla p + \nu\nabla^2\mathbf{u}$$

In the stationary regime ( $\frac{\partial\mathbf{u}}{\partial t} = 0$ ), we obtain the simplified form of the equation :

$$\nu\nabla^2\mathbf{u} = \frac{1}{\rho}\nabla p$$

The flow described by this equation, also referred to as Stokes flow, is laminar (smooth and orderly fluid motion characterized by parallel layers of fluid moving in the same direction). Oppositely, in the regime of high Reynolds number ( $Re > 2300$ ), the flow is turbulent.

## 3.2 Microfluidics in biology

The development of microfluidics has contributed to huge progresses in the domain of biology. Microfluidics is now part of many standard experiments.

### 3.2.1 Droplets microfluidics

Droplet microfluidics enables the manipulation of micro-droplets of a volume ranging from femto to microliter in an immiscible phase. The phase constituting the droplets and the one surrounding them are respectively referred to as “dispersed” and “continuous” phases. Although both water-in-oil and oil-in-water droplets can be generated, most applications involve water-based droplets in an immiscible carrier oil, in a way that each droplet can be considered as a small reactor in which controlled reactions can occur. Offering the possibility to manipulate extremely small volumes of fluid, droplet microfluidics has emerged as a powerful tool for high throughput bioanalytical experiments such as drug screening or single-cell analysis.

### 3.2.2 NGS, FACS

From the first genome sequencing of a bacteriophage by F.Sanger and others in 1977 [Sanger, 1977], to the Human Genome Project who mapped the entire human genome in a ten-years worldwide effort [Lander, 2001], sequencing in the past have proved to be a long, expensive and complicate work. The development of microfluidics allowed for the emergence of next-generation sequencing (NGS) techniques in the mid-2000s, more cost-effective and high-throughput methods which resulted in significantly lowered costs and expedited sequencing. Currently, the gold standard in genome sequencing is a combination of long-read sequencing (e.g., PacBio or

Nanopore) and short-read sequencing (e.g., Illumina) [Slatko, 2018].

The use of droplets microfluidics has allowed to compartmentalize individual cells into droplets, thus allowing the analysis of each of them individually. One of the pivotal applications of droplet-based single-cell analysis is single-cell RNA sequencing (scRNA-seq)[Jiang, 2023]. Here, each droplet serves as a miniature reaction vessel for cell lysis, reverse transcription, and cDNA amplification. This methodology allows for the simultaneous profiling of thousands of individual cells, thereby elucidating cellular heterogeneity within tissues and biological systems. Beyond transcriptomics, droplet microfluidics has been applied to single-cell proteomics and epigenomics. By integrating various analytical modules within a microfluidic chip, researchers can perform multi-omic analyses on single cells, unraveling the intricate connections between genomic, epigenomic, and proteomic information at the single-cell level.

### 3.2.3 Organ-on-chips

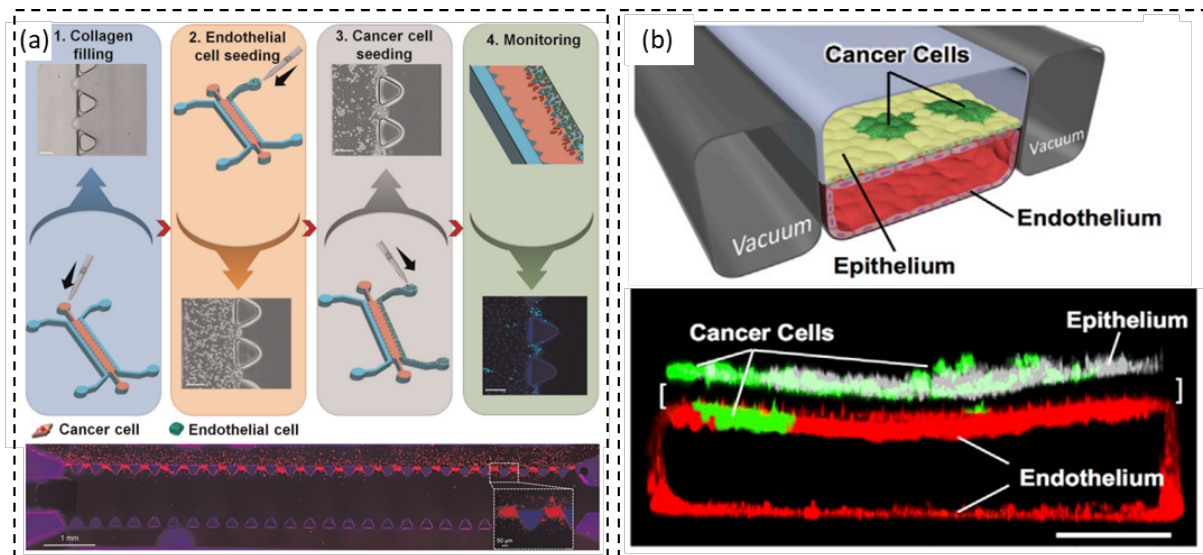


**Figure 1.9** – Tumor-on-Chip models (a) A 3D model of cancer cell migration on a microfluidic platform. A multistep process was followed to incorporate collagen, endothelial cells (green), and cancer cells (red) into the target channels. (adapted from [Azadi, 2021]). (b) Human Orthotopic Lung Cancer-on-a-Chip Models. 2-channel microfluidic chip containing human lung epithelial cells and a low density of NSCLC tumor cells cultured on the upper surface of a porous ECM-coated membrane (brackets) with human lung microvascular endothelial cells cultured on all four walls of the lower channel, forming a hollow vascular lumen. Scale bar = 200µm (adapted from [Hassell, 2017]).

Microfabrication and microfluidics opened new perspectives to recapitulate organs architecture with organs-on-chip (OOC). They allow to better reproduce 3D organization of organs which cannot be achieved with conventional 2D cell culture, while still being simpler and more accessible than *in vivo* animal models.

OOC are an integration between 3D tissue engineering with microfluidic systems. These platforms raise hopes for the study of drug delivery and drug screening, and for the development of controlled environments for cell culture, including the development of a complex model of organs with organoids and spheroids, and the growth of self-organizing stem cells in a controlled

environment with a high temporal and spatial resolution. In this way, OOC can be considered as an alternative or complement to animal models [Verhulsel, 2014].

The first organ-on-chip was developed in 2010 in the team of D.E. Ingber (Wyss Institute, Boston, USA) : a breathing lung-on-chip device to reconstitute an alveolar-capillary interface [Huh, 2010]. Many models of many organs have been developed on chips since, and the bridge to a human-on-chip model will soon be crossed. Among these, we'll focus on a subset which aim at reproducing the tumor microenvironment, namely tumors-on-chip (TOC) [Bouquerel, 2023]. The main challenge of these devices is to integrate *in vivo*-like extracellular matrix composition (collagen and other proteins) and stiffness [Azadi, 2021], multi-cellular constructs (including endothelial cells, fibroblasts, immune cells) [Bersini, 2014] and hypoxia [Bouquerel, 2022], among other characteristics to increase the biomimicry of these reconstituted systems.

In a 3D microenvironment model containing cancer cells, endothelial cells, and the biological matrix, the extravasation of tumor cells was studied, focussing on the effect of substrate stiffness on the invasion ability of breast cancer cells (see Fig.1.9a) [Azadi, 2021]. MCF-7 and MDA-MB-231 cancer cells were cultured among substrates with different stiffness, and showed reduced invasion in softened substrates.

By introducing mechanical stimulation, the interaction of a tumor with an endothelium barrier was reproduced in a human orthotopic models of non-small-cell lung cancer (NSCLC) that recapitulate organ microenvironment-specific cancer growth, tumor dormancy, and responses to therapy observed in human patients *in vivo* (see Fig.1.9b) [Hassell, 2017]. The use of mechanical actuation functionalities revealed a previously unknown sensitivity of lung cancer cell growth, invasion, and therapeutic responses to physical cues associated with breathing motions.

### 3.3 The study of cell mechanics in microfluidics

In the body, cells can be exposed to a variety of confinements. During solid tumor growth, cancer cells gets compressed [Nader, 2021b]. Migrating cells gets deformed as they migrate through the extracellular matrix. As presented above, cells in the blood circulation experience fast deformation as they flow through the capillary bed.

Using the technology aforementioned, several microfabricated devices have been fabricated to study the dynamics of cells under confinement. In this section we'll review the devices that allow to deform cells under confinement, then devices that allow to reproduce cell free migration through confined space, and finally forced migration through constrictions.

#### 3.3.1 Confinement

This first category of device allows placing cells in a deformed state similar to what they may encounter *in vivo* as the tumor expands for instance.

Using microfabrication technics described above, a multiwell confiner was developed in the team of M.Piel (Institut Curie). Cells can be confined to a chosen height under microfabricated pillars, as described in Fig1.10a. Upon confinement, the cell membrane expands (to conserve the cell volume) and gets tensed. Upon a threshold specific to each cell line, the cell membrane is able

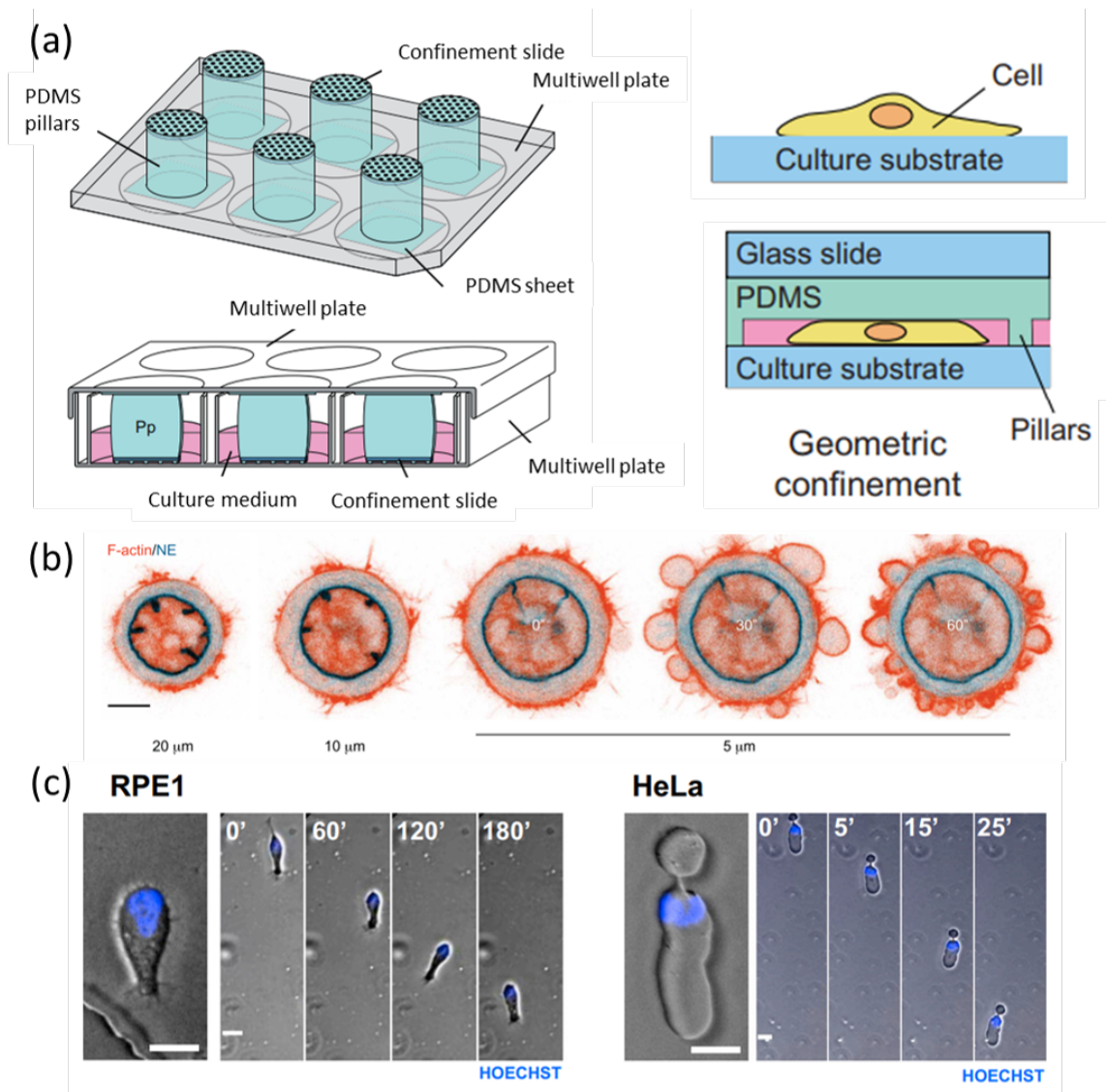


**Figure 1.10** – Uniaxial confinement of cells. (a) Multiwell plate confiner design. Cells are squeezed under a PDMS ceiling, which height is given by the height of designed PDMS pillars, adapted from [Le Berre, 2014]. (b) Representative graph of temporal evolution of nuclear envelope unfolding (blue) and plasma membrane blebbing (red) under confinement, adapted from [Lomakin, 2020] (c) Two modes of amoeboid migration, either through formation of local protrusions (RPE1) or through cortex instability ("stable bleb", HeLa), adapted from [Liu, 2015].

to detach from the cortex to form blebs (see Fig1.10b). These structures are largely unstable and will collapse as actin polymerization within will bring the membrane back [García-Arcos, 2022].

Similarly at the nucleus level, the nucleus membrane unfolds upon confinement and gets tensed (see Fig1.10b). If tension increases, the nuclear membrane will detach from the lamina, creating a bleb. This bleb can then rupture, putting in direct contact the content of the nucleus with the cytosol.

The nucleus is able to sense its confinement and respond to it [Venturini, 2020]. Upon stretching of the membrane, the calcium- dependent phospholipase cPLA2 is recruited at the mem-

brane and acts as a membrane tension sensor, which triggers a pathway leading to the production of aradonic acid and subsequent increase in cell contractility [Lomakin, 2020]. Other proteins have been reported to be recruited at the nuclear membrane upon mechanical stress, for instance ATR which is a kinase known to protect the chromatin from mistakes during replication [Kumar, 2014].

Nuclear envelope ruptures induce DNA damage. For instance, TREX1 (a cytosolic endonuclease) causes DNA damage in deformed nuclei upon nuclear envelope rupture events. Interestingly, TREX1 drives senescence in normal cells and an invasive phenotype in cancer cells [Nader, 2021b].

Under confinement and in the absence of focal adhesions, mesenchymal cells can spontaneously switch to a fast amoeboid migration phenotype [Liu, 2015]. In this state, they can adopt two main types of fast migration: one involving a local protrusion and a second involving a myosin II dependent mechanical instability of the cell cortex that leads to a global cortical flow (see Fig1.10c). The choice depends on both the cell type and the level of confinement, for instance epithelial RPE1 cells form protrusions, while tumoral HeLa cells form a stable bleb in the direction of migration. The formation of stable blebs requires actomyosin contractility, and thus can be prevented by inhibition of myosin II (Y27632).

This increase in motility can be observed in cell migration through the dense extracellular matrix environment. The cells establish cell-fiber attachment sites that are needed to either push or pull the cell body forward [Brábek, 2010], which is faster than the regular crawling movement motion [Abercrombie, 1980]. If the mesh size is too large, the migration speed decreases due to a loss of these cell-fiber attachments. If the mesh size becomes too small, the migration speed decreases and the cells may get trapped. Then the cell can either force the network fibers apart where it can remodel its shape until it can pass through the pore, or it can degrade the fiber matrix with the help of proteolytic enzymes.

Confinement and migration are closely connected, as cells experience confinement during migration and that confinement can alter, and even promote, migration. Hence the following devices focus on the free migration of cells through small confined spaces such as microchannels.

### 3.3.2 Free migration in confined space

As cells migrate through tissues, or through epithelial barriers with pores smaller than the cell itself, the whole cell and its nucleus have to squeeze in. Due to its relatively large size and relative rigidity as an organelle (2-10 times stiffer than the cytoplasm [Friedl, 2011b]), it has been hypothesized that the nucleus can impact the cell's ability to migrate. Thus, the nucleus acts as a "physical barrier to migration" [McGregor, 2016].

To study migration, one can use different designs such as microfabricated confined channels of a desired width, or transwell assays (migration through pores in a membrane). Migration of cells can be either free or directed along a gradient of chemicals (chemotaxis). These devices

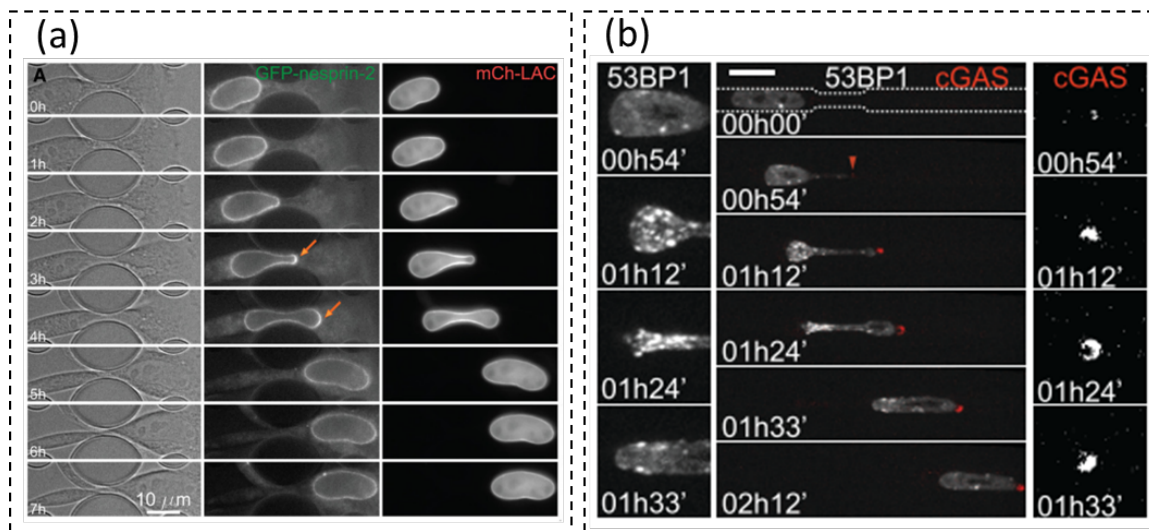


**Figure 1.11** – Free migration of cells through constrictions. (a) Nesprin-2 but not Lamins accumulates at the front of the nucleus as it is deformed through the constriction (adapted from [Davidson, 2020]) (b) Representative RPE-1 cell expressing 53BP1-GFP (gray levels) and RFP-cGAS (red) migrating through a constriction ( $L = 15 \mu\text{m}$ ,  $w=2 \mu\text{m}$ ). Red arrow shows first RFP-cGAS entry at nuclear tip ; scale bar= $20 \mu\text{m}$  (adapted from [Raab, 2016])..

allow to gain insight into the organization and dynamics of the cell's components and proteins during deformation.

As nucleus is being deformed, all associated proteins are reorganized. For instance, nesprin-2 (a protein which anchors actin filaments to the nucleus as part of the LINC complex) accumulates at the front of the nucleus during confined cell migration of NIH-3T3 through  $2 \mu\text{m}$  wide constrictions [Davidson, 2020] (see Fig.1.11a). Movement of the nucleus through the constriction was sustained from the front of the cell by an actomyosin- dependent pulling force on the nucleus. Actin filaments, organized in a barrel structure around the nucleus in the direction of movement, in concert with myosin, were able to redistribute nesprin-2 toward the front of the nucleus and contribute to pull the nucleus through narrow constrictions.

Migration of dendritic cells or HeLa cells were followed through a  $2 \mu\text{m}$ -wide confined channel. At the tip of the nucleus, the nuclear membrane can detach from the lamina and form a bleb. This conformation is unstable and the bleb ends up breaking, which allows for cytosolic proteins to enter the nucleus and chromatin to escape the nucleus into the cytoplasm [Raab, 2016] (see Fig.1.11b). This transient opening caused by nuclear deformation was rapidly repaired in an ESCRT (endosomal sorting complexes required for transport)-dependent manner. DNA double-strand breaks coincided with nuclear envelope opening events. As a consequence, survival of cells migrating through confining environments depends on efficient nuclear envelope and DNA repair machineries.

These devices can also be used to characterize cell phenotypic characteristics. For instance, transwell ( $8 \mu\text{m}$  pores in a membrane) assays were used to separate highly from weakly migratory cells within a population of MDA-MB-231 cells [Hapach, 2021]. When injected orthotopically into immunocompromised mice, both subpopulations formed primary tumors that grew steadily

over the course of 4 weeks. However, distal metastatic spread was observed in all mice injected with weakly migratory MDAs, whereas minimal distal signal was observed in mice injected with highly migratory MDAs. Difference was explained by the fact that weakly migratory cells were found as clusters in the blood, while the others remain as single cells. These weakly migratory cells retained an epithelial phenotype, including E-cadherin expression, which enables successful distal metastasis in this model.

In experiments presented in this section, cells were left free to migrate through constrictions, either naturally [Raab, 2016 ; Davidson, 2020] or helped with a gradient of serum [Hapach, 2021]. As a results, migration through the constriction span over several hours. In this context, the cell is able to reorganize, may repair any damages that may happen, change its genomic expression, and so on. The cell acts as active matter in this case. When we consider migration through the blood circulation, the motor of migration through the constriction is the blood flow and typical crossing times for red blood cells are on the order of the second to the minute [Blom, 2003]. At this time scale, it is hard to imagine the cell having time to actively respond to the deformation it experiences. Thus, we need specific models to understand the mechanisms involved in flow-induced migration.

### 3.3.3 Forced migration through confined space

To push the cell through confined channels or constrictions, microfluidic devices use flow as a carrier for the cell. The pressure difference used to create the flow will also determine the force applied on the cell :  $F = \Delta P \times S$  where  $\Delta P$  is the pressure difference around the cell, and  $S$  is the surface of the constriction. These devices allow to probe cells with a large range of forces (depending on the pressure difference and confinement level used) with much lower duration (typical duration of applied constrained is milliseconds to seconds). In these conditions, the cell can be considered as inactive matter, meaning that no biological modifications have the time to happen.

The impact of LaminA/C in such condition was studied in the case of laminopathies [Jebane, 2023]. Using a microfluidic device incorporating 6  $\mu\text{m}$  square cross-section constrictions, they were able to probe the deformation mechanics of cells pushed in these constrictions under a pressure difference of 165 mbar (see Fig.1.12a). The deformation of the cells in this device follows the Jeffrey’s rheological model presented section A. Cells affected by lamin A/C alterations display a distinctive increase in long-time viscosity, meaning they deform more slowly in the constriction. These cells include fibroblasts from two patients carrying a R482W mutation on the LMNA gene ; and healthy fibroblasts treated with atazanavir (which impacts lamin A/C maturation), which results in abnormal nuclei shapes. Moreover they have been able to identify that the whole-cell response to mechanical stress is driven not only by the nucleus, but also by the nucleo-cytoskeleton links and the microtubule network, as confirmed by nocodazole-induced destabilization of microtubules.

Similar devices were used to probe leukocyte trafficking through narrow capillaries (entry, transit and shape relaxation) using specific drugs (latrunculin A, jasplakinolide, and blebbista-

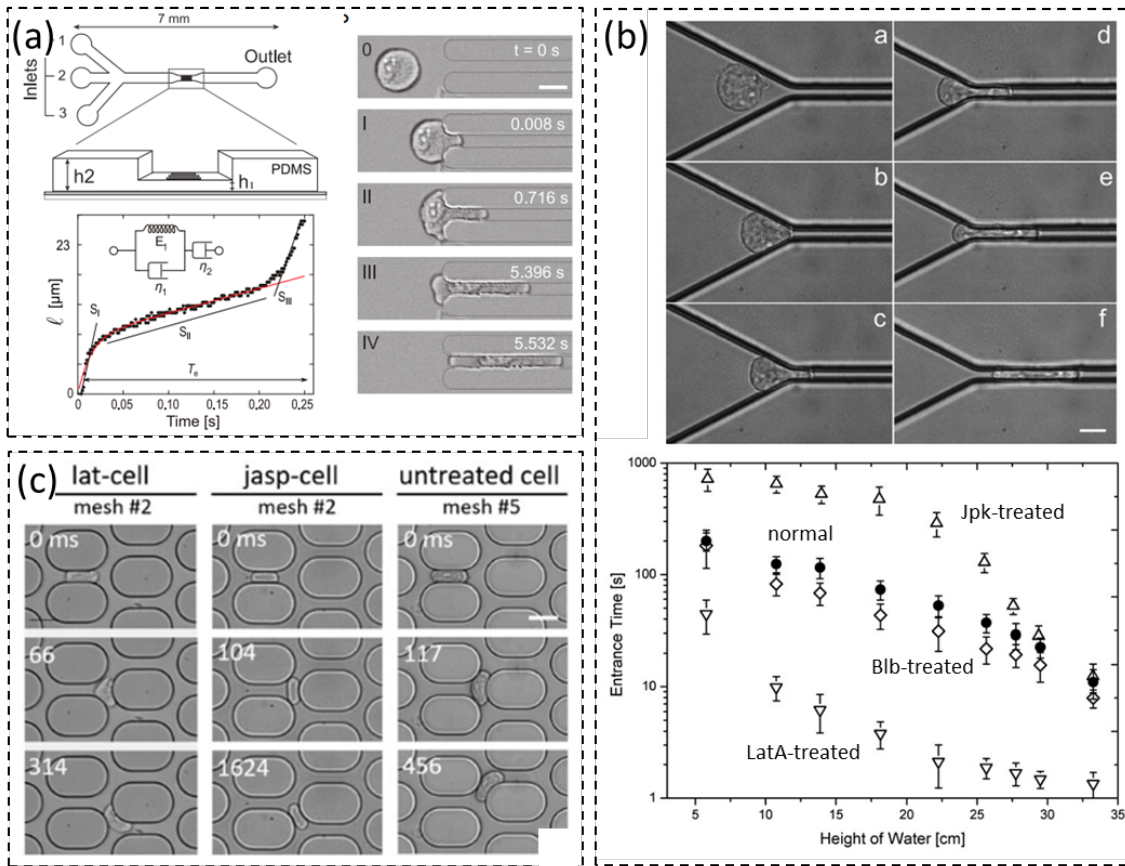


**Figure 1.12** – Forced migration of cells through constrictions. (a) Design of the microfluidic chip with square  $6 \times 6 \mu\text{m}^2$  constrictions. The cells enters the constriction under pressure ( $\Delta P = 165 \text{ mbar}$ ). The cell tongue length increase follows Jeffrey’s rheological model (adapted from [Jebane, 2023]). (b) Entry of a leukocyte in a  $4 \mu\text{m}$  wide channel. Entrance time as function of the pressure difference applied on the device for ( $\bullet$ ) normal, ( $\diamond$ ) blebbistatin-treated, ( $\triangle$ ) jasplakinolide-treated, and ( $\nabla$ ) latrunculin A-treated cells (adapted form [Gabriele, 2009]). (c) Selected images from timelapses of lat-cells, jasp- cells, and untreated THP1 cells ; scale bar :  $15 \mu\text{m}$  (adapted from [Dupire, 2020])

tin) [Gabriele, 2009]. As circulating cells in the blood, leukocytes have to cross the capillaries constrictions, including the lung, where they can remain trapped and cause acute lung injury. A microfluidic device was constructed to deform leukocytes (THP1 monocytes) gradually down to a  $4 \mu\text{m}$  wide channel (see Fig.1.12b). The deformation rate during entry reveals that cell stiffness depends strongly on F-actin organization and hardly on myosin II activity, supporting a actin cytoskeleton role in leukocyte sequestration. In the transit stage, cell friction is influenced by stiffness, demonstrating that the actin network is not completely broken after a forced entry into a capillary. Finally, cell shape relaxation was largely independent of both actin organization and myosin II activity, whereas a deformed state was required for normal trafficking through capillary segments.

In a microfluidic device mimicking the pulmonary capillary bed, the dynamics of THP1 monocytes evolved along successive capillary-like channels, from a nonstationary slow motion with hops to a fast and smooth efficient one [Dupire, 2020]. Here a very finely tuned cortical

tension combined with a high cell viscosity governs the fast transit through the network while preserving cell integrity, as demonstrated using drugs targeting the actin cytoskeleton. In this study, cortical tension controls the steady-state cell velocity via the viscous friction between the cell and the channel walls.

### 3.3.4 Focus on cancer cells

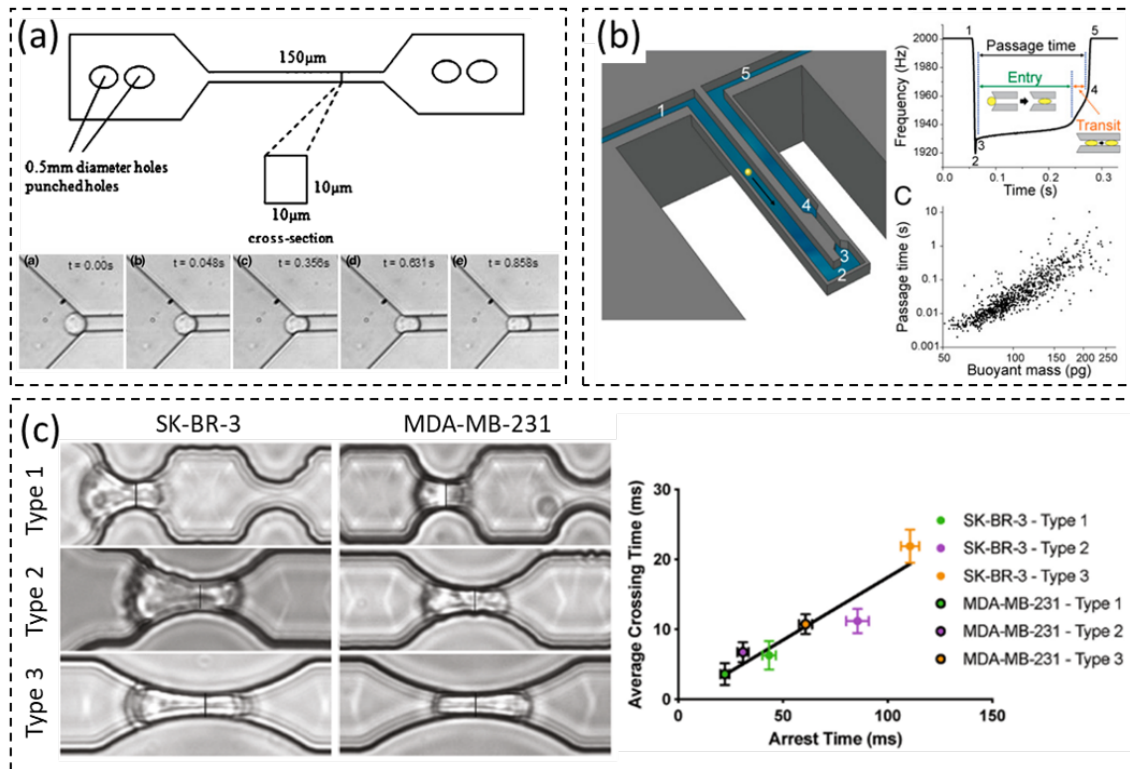


**Figure 1.13** – Focus on cancer in forced migration of cells through constrictions devices. (a) Optical images showing the entry of a single MCF-7 cell into a 10 by 10  $\mu\text{m}$  microchannel (adapted from [Hou, 2009]). (b) Suspended microchannel resonator (SMR) with a constriction (6  $\mu\text{m}$  wide, 15  $\mu\text{m}$  deep, and 50  $\mu\text{m}$  long under 124 mbar) located at the apex (adapted from [Byun, 2013]). (c) Brightfield images of SK-BR-3 and MDA-MB-231 cells three geometries of micro constrictions ( $6 \times 15 \mu\text{m}^2$ ) at a constant applied pressure of 100 mbar (adapted from [Ahmad-Cognart, 2020]).

Finally, we'll present here examples in the literature which focused on cancer cells in forced migration through confined spaces devices.

The devices are similar to the ones presented above. For instance, in a  $10 \times 10 \mu\text{m}^2$  micro channel, [Hou, 2009] compared the properties of breast tumor MCF-7 cells to their non-malignant MCF-10A counterpart (see Fig.1.13a). In this device, tumor cells crossed the constriction faster than normal cells, which is coherent with regarding the higher deformability of cancer cells reported in the literature presented above. This type of experiments based on optical acquisition of cells through a single confined microchannel has been performed in several studies with different cell types of different cancers [Byun, 2013; Khan, 2013; Nath, 2018], different pressure

[Xia, 2018], different levels of confinement [Nath, 2019] and sometimes focusing on the crossing of cells clusters [Au, 2016].

[Byun, 2013] embedded a microfluidic channel and  $6 \times 15 \mu\text{m}^2$  constriction in a suspended microchannel resonator (SMR) (see Fig.1.13b), which resonance frequency depends on the mass of the resonator. As a cell passes through the constriction, the mass of the resonator changes because of the difference in density with water. Thus, the cell passage through the constriction can be recorded, and its buoyant mass estimated from the shift in frequency. When accounting for cell buoyant mass, they found that cells possessing higher metastatic potential exhibit faster entry and transit velocities, thus hypothesizing increased deformability and reduced friction as markers of more invasive cells.

In a rare example, [Yan, 2022] approached the study of cell recovery following deformation with a manually actuated valve to stop the flow following each cell escape of a constriction. These experiments confirmed the viscoelastic nature of cells. More interestingly, cells of from more aggressive lineage exhibited higher irreversible plastic deformation as compared with less aggressive ones, highlighting the potential of focusing on recovery as a marker for cells metastatic potential.

In these devices, the constrictions are generally abrupt, either with a sharp change in width, or with a narrowing at a constant angle. In a previous work in the team, [Ahmad-Cognart, 2020] investigated the effect of constriction geometry on the transit of breast cancer cells through multiple successive  $6 \times 15 \mu\text{m}^2$  constrictions. Constrictions profiles were made of circle arcs with increasing diameters, leading to a less abrupt entry in the constriction. The sharper constrictions (type 1,  $10 \mu\text{m}$  diameter) resulted in a faster transit of the cells through the entire channel with its many narrowings than the softer ones, highlighting the need to be careful about the constriction geometry in designing experiments. Cells were able to be collected at the outlet in the chip, revealing changes in gene expression and damages accumulation in response to flow-induced deformations.

Thus, constriction-based microfluidic devices allow to discriminate between different cancer cell lines of different origins and metastatic potential. By doing so, they correlate the potential aggressiveness of a cancer cell with its mechanical properties. The devices presented here, and in the literature, almost exclusively use a single deformation to extract these properties. We'll propose to complete this bundle of knowledge by studying the often disregarded recovery of cells following deformation, as well as the impact of repetitive deformations. This complementary approach will give us insight on the behavior of the single cell as well as of the cell population, at the short and long timescale, following a single or repetitive deformations.

## 4 Scope of the PhD project

Having described the interest of the study of mechanics of cancer cell deformation, I'll present here the framework of the project I collaborated to.

#### 4.1 MecaCTC project

MecaCTC is an INSERM supported project, led by Catherine Villard, which aim is to understand the biomechanics of circulation cancer cells under flow. The partners of the project are the following :

- team of Catherine Villard, Institut Curie UMR168 then LIED CNRS UMR8236, Univ. Paris Cité.
- team of Matthieu Piel, Institut Curie UMR144.
- team of François-Clément Bidard, Laboratory of Circulating Tumor Biomarkers, Institut Curie & Dep. Oncologie Médicale.
- team of Catherine Alix-Panabières, Laboratoire des Cellules Circulantes Rares Humaines (LCCRH), CHU Montpellier.

The objective of the consortium is the following : We showed that cancer cell lines flown in microfluidic systems mimicking the blood circulation may undergo DNA damage and modify their expression of mechanosensitive pathways. The central hypothesis of this project is thus that the circulation has in itself a significant impact on various facets of circulating tumor cells (CTCs) physiology and fate, and consequently on the metastatic process as a whole. This project gathers physicists, biologists and clinicians to develop the potential of this hypothesis in oncology. We shall first explore the role of pathways previously identified as being affected in cells under static or quasi-static confinement, associated e.g., with nuclear membrane tension and rupture (leading to DNA damage), or volume regulation at the whole cell level (targeting cell survival). This exploration will use state-of-the-art cell biology methods, e.g., live imaging, pharmacology or KO of specific genes. In parallel, we will implement a general transcriptomic approach to identify pathways specifically affected by the circulation stimuli. We shall first use cell lines, including CTC lines established in this consortium, then primary cells from patients “naïve” to circulation (ascites).

The consortium benefits from an expertise in microfabrication and microfluidics developed in the Institut Pierre-Gilles de Gennes building, where the team of Catherine Villard and Matthieu Piel are located. All partners have an extensive understanding of cell and cancer biology, specifically under confinement. The consortium will benefit from the use of interesting cell lines established in the team of Catherine Alix-Panabières, in complement to the use of commercially available cell lines. These models will be completed by clinical sample (ascites), obtained from Institut Curie hospital with the help of the team of François-Clément Bidard.

The experimental work was distributed between :

- Kotryna Vaidžiulytė (post-doc), under the supervision of Matthieu Piel and Catherine Villard. Her work consisted in the study of the CTCs lines under conditions of static confinement.
- Keerthi Kurma (post-doc), under the supervision of Catherine Alix-Panabières. Her work consisted in the multi-omic analysis of the colon CTCs lines developed in their team under conditions of flow-induced deformation in microfluidic chips that I developed.

- Myself, under the supervision of Catherine Villard and Jean-Yves Pierga. I will describe the aim of my work just below.

## 4.2 My Project specifically

Within this framework, my work consisted in the development and use of microfluidic devices to study the response of CTCs to flow-induced deformations :

- The first device focuses on the short-term dynamics of flow-induced deformation and recovery. I screened several cell lines in this device, including three cell lines of breast cancer (MCF-7, SK-BR-3 and MDA-MB-23, and 4 lines of colon cancer (commercial HT-29 and SW-620, and two lines from the collection isolated by the CHU Montpellier partners, namely CTC-41 and CTC-41.5A). I focused on the morphological changes at the whole cell level (see **Chapter 2**) and at the nucleus level (see **Chapter 3**). I investigated the role of nucleus and cytoskeleton in the deformation and recovery dynamics, with a special focus of vimentin filaments. Additionally, I also explored cell viability and DNA damages, cell volume, and cell blebbing in these Pachinko devices.
- The second device aims at understanding the long-term consequences of repeated flow-induced deformations on CTCs lines. I developed the microfluidic chip and a first recirculation set-up. I performed proof of concept experiments with two lines of breast cancer (MCF-7 and MDA-MB-231) demonstrating loss of viability, increase in vesicles production and accumulation of nuclear damages (see **Chapter 4**). The analysis of the colon CTCs lines in this device was entrusted to Keerthi Kurma in Montpellier.

During this project, I had the opportunity to supervise four interns who helped with the experiments of the time : Cyril Bonhomme (M2, 3 months, back and forth recirculation), Jules Edwards (M1, 2 months, Pachinko experiments), Emilie Su (M2, 6 months, Pachinko experiments and analysis) and Nassiba Abbade (M2, 6 months, Pachinko experiments and analysis, vimentin silencing and transfection).

## CHAPTER 2

### PACHINKO : DESIGN AND RESULTS AT THE CELL LEVEL

In this chapter, I'll present the design and use of the microfluidic device named Pachinko. This device allows the study of the fast dynamics of deformation and subsequent recovery in the milliseconds to seconds range. We'll use this device to sort the cell lines by their rheological behavior.

The main question we address is : Does the mechanical properties of the cell correlate with its aggressiveness/ metastatic potential at the clinical level? The literature we presented in the introduction points in this direction [Alibert, 2017], including a few studies on the widely used MCF-7 and MDA-MB-231 cell lines [Guck, 2005 ; Hou, 2009 ; Omidvar, 2014 ; Hu, 2017 ; Ahmad-Cognart, 2020]. The present study addresses this question by including an analysis of the cell recovery after deformation. To this aim, we will study seven cell lines : three breast cancer lines (MCF-7, SK-BR-3 and MDA-MB-231) and four colon cancer lines (CTC41, CTC41.5A, HT-29 and SW-620).

- The breast cancer cell lines are each representative of the three subtypes of breast cancer, as defined in section 2.1.1, which present different metastatic potential. Tumors from basal origin present a higher risk of metastasis formation than luminal tumors. We'll see if these differences can be expressed at the rheological level.
- The colon CTC41 and CTC41.5A cell lines were obtained from CTCs collected at different instants of the disease progression in a single patient : cells at the origin of the CTC41 lineage were isolated before the lines of treatment, and CTC41.5A after the last relapse before death. We'll investigate how the mechanical properties of the cells evolved as the cancer progresses, and compare them with reference lines for primary (HT-29) and metastatic (SW-620) colon cancer.

In this chapter, we'll include the accepted version of a paper written to demonstrate the use of Pachinko devices to study the mechanics of fast flow-induced deformation and subsequent recovery on breast cancer cells. We'll then complete the analysis with similar results obtained

with cell lines of colon cancer. Finally we will comment on the common features and differences between the two different types of cancer.

## 1 Introduction to the paper

### 1.1 Working principle of the Pachinko device

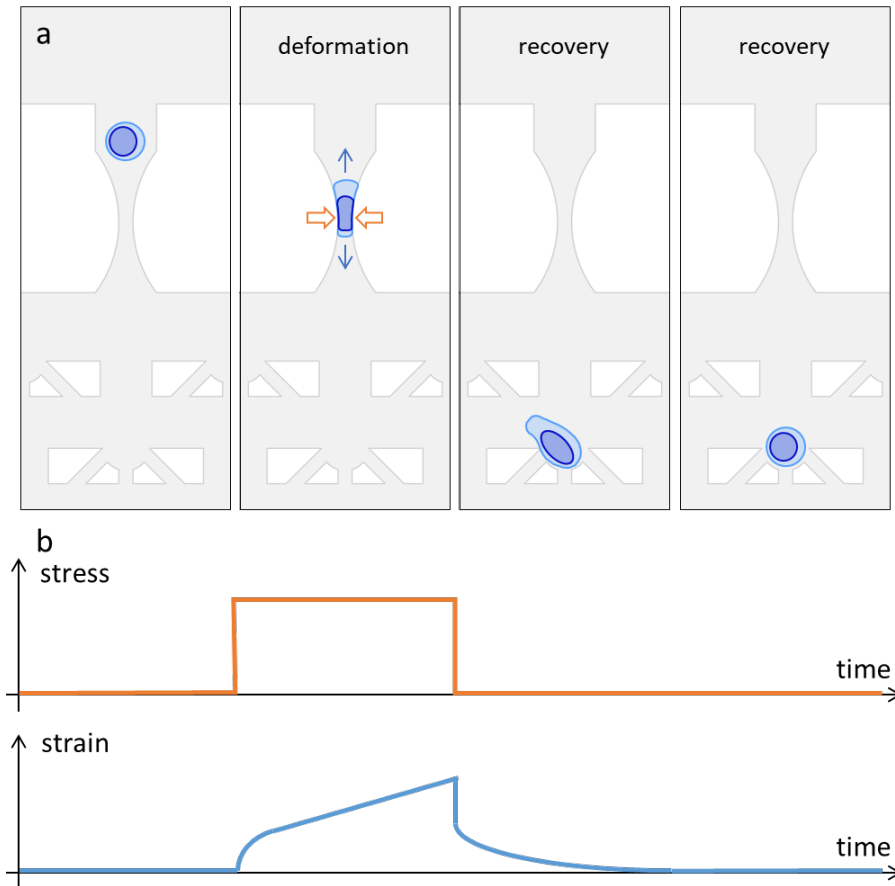


**Figure 2.1** – Schematic working principle of Pachinko device. (a) Application of stress (orange arrows) and resulting strain (blue arrows) under pressure difference in the constriction. (b) Schematic stress and strain curves.

The Pachinko device gets its name for its shape analogy with a popular Japanese game. The device is constructed to push cells through a capillary-like constriction using flow (see Fig.2.1a). There, each cell will deform under the pressure difference, and will then be trapped in a single-cell nest after its escape.

In a microfluidic channel of dimensions in the micrometer range, the resulting Reynolds number is small enough so that the flow can be considered as laminar (Stokes flow). We'll confirm this hypothesis by quantifying it in the channel. We'll take  $u = 0.003 \text{ m}\cdot\text{s}^{-1}$  as the flow speed (in the main channels before the constrictions, see later Comsol Simulations),  $L = 15 \text{ }\mu\text{m}$  as the smallest dimension (height of the channel) and  $\nu = 0.7 \times 10^{-6} \text{ m}^2\cdot\text{s}^{-1}$  (kinematic viscosity

of water at 37°C).

$$Re = \frac{uL}{\nu} \approx \frac{3 \times 10^{-3} \cdot 15 \times 10^{-6}}{0.7 \times 10^{-6}} \approx 0.06 \ll 2300$$

The Reynolds number is largely small enough to confirm the flow within the chip is laminar (i.e. there is no turbulence).

Similarly to what we described in the section 2.3, the velocity profile follows here a Poiseuille distribution, which is maximal at its center and null on the walls. More precisely, as the height of the channel ( $h = 15 \mu\text{m}$ ) is much smaller than the other dimensions (in the main channel  $w \approx 250 \mu\text{m}$ ), the Poiseuille gradient is mainly present in the vertical direction, and the velocity is constant across the width of the channel (also known as Hele-Shaw flow approximation). The resulting flow  $Q$  (in  $\text{m}^3 \cdot \text{s}^{-1}$ ) depends on the applied pressure difference  $\Delta P$  (in Pa) and the hydraulic resistance of the channel  $R_h$  :

$$Q = \frac{\Delta P}{R_h}$$

In a channel of rectangular section  $w \times h$  and length  $L$ , the resistance is  $R_h = \mu \frac{12L}{w \times h^3}$  where  $\mu$  is the fluid dynamic viscosity (in Pa.s). Thus a sudden decrease in channel width  $w$  leads to an increase of resistance.

The negligible width of the three constrictions ( $w = 6 \mu\text{m}$ ) compared to the main channel before ( $200 \mu\text{m}$ ) and trap chamber region ensures the resistance of the constriction is large in front of the ones of the main channel and trap chamber. It thus ensures that the majority of the pressure difference applied between the inlets/outlets is located within the constriction. Numerical simulations show that the pressure drop applied on a cell in a constriction is  $\approx 6 \text{ mbar}$  (see simulations in the Supplementary Materials of the paper).

The cells are pushed by the flow against the walls of the constriction. The resulting force from the walls compresses the cells, which then elongates in the perpendicular direction (see Fig.2.1a). To quantify the cell strain, we measure the elongation of the cell along its major axis in the direction of the constriction (Fig.2.1b).

## 1.2 Short summary of the paper

In the paper included in the following section and recently accepted for publication in Lab on Chip, we demonstrate the use of the microfluidic-based fast induced deformations in the Pachinko device to compare and characterize the rheological properties of three breast cancer cell lines : MCF-7, SK-BR-3 and MDA-MB-231.

We first characterized the deformation of the cells within the capillary-like constriction. We show that SK-BR-3 cells are able to cross the constriction faster due to their smaller size in general. We then show that the less metastatic MCF-7 cells are less deformable, and thus take a longer time to deform and cross the constrictions.

We then analyzed the recovery dynamics once the cells escaped the constriction, and the applied stress is released. We show that for each cell lines, the recovery is composed of two regimes : a fast elastic regime, followed by a slower viscoelastic regime. We show that two characteristic times appear in the viscoelastic regime, of the order of 1 s and 10 s. Using the generalized Kelvin-Voigt formalism, we extracted rheological parameters, including elastic and viscous moduli for the different regimes. We calculated the MDA-MB-231 cells to have a smaller elastic modulus (= 0.79 kPa vs  $\approx$  1 kPa for the SK-BR-3 and MCF-7 lines) overall, while the MCF-7 cells display higher viscous moduli ( $\approx$  2.9 kPa.s) than the other two lines .

Using treatments to perturb the cytoskeleton we show that the integrity of the cell cortex was required to observe recovery. Inhibiting actomyosin contractility lead to a slower partial recovery of the deformation.

The originality of this approach resides in the implementation of a recovery chamber with traps allowing to capture and observe the cell recovery after flow-induced deformations. Indeed, if several devices have been developed to study cell deformation (as recapitulated in section 3.3.3), none are able to study cell recovery over several minutes. Though the use of high speed camera allows to capture first instants of the cell recovery, the cell rapidly escapes the field of view of the camera.

## **2 Paper draft "Deformation under flow and morphological recovery of breast cancer cells"**

In the following pages you'll find the draft of the paper accepted for publication in Lab on Chip on June 10th, 2024, followed by the associated Supplementary Informations.

## Journal Name

## ARTICLE TYPE

Cite this: DOI: 00.0000/xxxxxxxxxx

Deformation under flow and morphological recovery of cancer cells <sup>†</sup>Emile Gasser<sup>a,b</sup>, Emilie Su<sup>b,c</sup>, Kotryna Vaidziulytė<sup>d</sup>, Nassiba Abbade<sup>a,d</sup>, Hamizah Cognart<sup>a</sup>, Jean-Baptiste Manneville<sup>c</sup>, Jean-Louis Viovy<sup>a</sup>, Matthieu Piel<sup>d</sup>, Jean-Yves Pierga<sup>e</sup>, Kyohei Terao<sup>\*f</sup>, and Catherine Villard<sup>\*b‡</sup>Received Date  
Accepted Date

DOI: 00.0000/xxxxxxxxxx

## Abstract

The metastatic cascade includes a blood circulation step for cells detached from the primary tumor. This stage involves significant shear stress as well as large and fast deformations as the cells circulate through the microvasculature. These mechanical stimuli are well reproduced in microfluidic devices. However, the recovery dynamics after deformation is also pivotal to understand how a cell can pass through the multiple capillary constrictions encountered during a single hemodynamic cycle. The microfluidic system developed in this work allows to study single cell recovery in flow-free conditions following pressure-actuated cell deformation inside constricted microchannels. We used three breast cancer cell lines - namely MCF-7, SK-BR3 and MDA-MB231 - as cellular models representative of different cancer phenotypes. Changing the size of the constriction allows to explore moderate to strong deformation regimes, the latter being associated to the formation of plasma membrane blebs. In the regime of moderate deformation, all cell types display a fast elastic recovery behavior followed by a slower viscoelastic regime, well described by a double exponential decay. Among the three cell types, cells of the mesenchymal phenotype, i.e. the MDA-MB231 cells, are softer

and the most fluid-like, in agreement with previous studies. Our main finding here is that the fast elastic recovery regime revealed by our novel microfluidic system is under the control of cell contractility ensured by the integrity of the cell cortex. Our results suggest that the cell cortex plays a major role during the transit of circulating tumor cells by allowing their fast morphological recovery after deformation in blood capillaries.

## Introduction

The role of cell mechanics in the successive steps leading to metastatic cancers<sup>1</sup> is more and more documented<sup>2</sup>. Migrating cells from a primary tumor experience strong deformations in their path toward the blood vessels<sup>3</sup>. The environment of the bloodstream is then a source of shear stress and confinement<sup>4,5</sup>. Finally, the step of extravasation requires cell squeezing across the endothelial barrier<sup>6</sup>.

*In vitro* approaches using microfluidic tools have highlighted the transformation and sorting effects of blood stream mechanical stressors on circulating tumors cells (next referred to as CTCs). Cells exposed to shear stress display subsequent increased migration capabilities<sup>7,8</sup> and over-expression of epithelial-mesenchymal transition<sup>9,10</sup> or stemness<sup>11</sup> genes. Furthermore, shear stress applied during hours favors the survival of soft, stem cell like phenotype showing high metastatic potential compared to stiffer cells<sup>12</sup>.

Mechanical stimuli encountered into the blood circulation are however not limited to shear stress. Because the diameters of vessels in the capillary bed are much smaller than cell and even nucleus sizes<sup>13,14</sup>, circulating cells are repetitively squeezed in the microvasculature (see<sup>15</sup> for a review). Eventually, capillary occlusion through cell arrest may occur. Interestingly, the mechanics of CTCs opens a new field of mechanobiology addressing strong and fast flow-induced deformations, distinct from the phenomenon of spontaneous migration under confinement which has been studied for a decade<sup>16,17</sup>. This regime of large

<sup>a</sup> Université PSL, Institut Curie and Institut Pierre Gilles de Gennes, Physico-Chimie Curie, CNRS UMR168, F-75005 Paris, France.

<sup>b</sup> Université Paris Cité, Laboratoire Interdisciplinaire des Energies de Demain, CNRS UMR 8236, F-75013, Paris, France.

<sup>c</sup> Université Paris Cité, Laboratoire Matière et Systèmes Complexes (MSC), CNRS UMR 7057, 10 rue Alice Domon et Léonie Duquet, F-75013 Paris, France.

<sup>d</sup> Université PSL, Institut Curie and Institut Pierre Gilles de Gennes, CNRS UMR144, F-75005 Paris, France.

<sup>e</sup> Département d'Oncologie Médicale de l'Institut Curie et Université Paris Cité.

<sup>f</sup> Kagawa University, Nano-Micro Structure Device Integrated Research Center, 2217-20 Hayashi-cho, Takamatsu 761-0396, Japan.

<sup>†</sup> Electronic Supplementary Information (ESI) available: Fig. S1-S9 and Table S1. See DOI: 00.0000/00000000.

\* Corresponding authors. E-mail: catherine.villard@u-paris.fr and terao.kyohei@kagawa-u.ac.jp

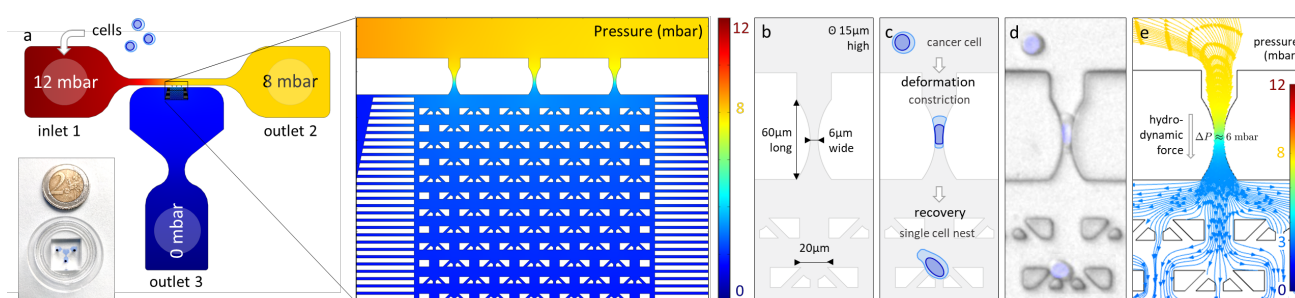


Fig. 1 - Design and operating principle of the Pachinko device. (a) Image and overall design of the microfluidic device. The simulated pressure profile (values in mbar) in the microfluidic device is indicated (b) Constrictions and cell nests dimensions. (c) Principle of cell deformation and recovery in the device. (d) Reconstructed representative image of a cell in different parts of the device (light blue overlay: cell nucleus stained with Hoechst). (e) Pressure profile with simulated streamlines through a single constriction and adjacent nests. Most of the pressure gradient is located in the constriction (pressure drop  $\Delta P \approx 6$  mbar), ensuring cell recovery under negligible hydrodynamic forces (due to a pressure drop of about 0.1 mbar across a trapped cell, see Fig. S2).

deformation under flow has been studied using microfluidic-based models including constricted microchannels<sup>18–21</sup>. We have reported in a previous study that the time required for a cell to cross multiple successive constrictions was mainly determined by the time needed to enter through the first constriction<sup>22</sup>. This observation is a consequence of the finite time of cell shape recovery, higher than the time necessary to reach the next constriction. Quite importantly, the viscoelastic relaxation time of CTCs might influence the transit and arrest of CTCs in capillaries<sup>4</sup>, a phenomenon essential for extravasation. By devising a device including 80  $\mu\text{m}$  long relaxation chambers in-between constrictions, Kamyabi et al.<sup>23</sup> were able to follow cell shape relaxation occurring in an about 10ms duration, thanks to the use of a high speed camera (1000 fps). This relaxation step occurs however under shear stress and cell motion. More recently, Yan et al.<sup>24</sup> succeeded in monitoring cell recovery under free-flow conditions by manually stopping the flow each time a cell escaped from the constrictions.

The present work focuses on new methodological developments for the study of cell morphological relaxation. The novelty of our work lies in the immediate release of hydrodynamic stresses after flow-induced deformation, together with cell immobilization in traps, providing unprecedented access to cell morphological recovery. This new methodology is then applied, in a proof-of-concept approach, to circulating cancer cells of three different types, to demonstrate the potential and limitations of this new system. Finally, this work highlights the role of the actomyosin cortex in cell recovery, which appears to be responsible for their initial elastic behavior.

Specifically, the journey of a cell in our original device occurs in several steps. Cells are first pushed by a pressure gradient into constrictions in which they next progress by deforming. They are then released into a relaxation chamber characterized by uniform pressure and filled with nest-like traps to immobilize them and track their morphological relaxation by fast camera imaging. Importantly, we designed the constrictions as slits in order to achieve significant cell deformation while avoiding cell blebbing. We will

refer to this device as Pachinko in the following, by analogy with a popular Japanese game.

## Design and running principle of the Pachinko microfluidic system

### The Pachinko microfluidic chip

The overall design of the microfluidic device is described in Fig.1a. It includes three inlet/outlet ports and three main compartments: a flowing channel between inlet 1 and outlet 2, a recovery chamber connected to the outlet 3, and a set of three identical microchannels (constrictions) connecting the main channel to the recovery chamber. Each constriction is composed of a 60  $\mu\text{m}$ -long narrowing of the channel with a circle arc profile. This shape was selected on the basis of a previous work<sup>22</sup> to produce a smooth deformation profile, similar to what is observed at the level of mural cells (e.g. pericytes) in both static and dynamic conditions (during e.g. capillary diameter regulation for cerebrovascular blood flow control)<sup>25,26</sup>. At the narrowest part of the constriction, the cross section is a 6  $\mu\text{m}$ -wide and 15  $\mu\text{m}$ -high rectangle (Fig.1b and Suppl. Information, section 2, Fig.S1). This characteristic lowest dimension falls in the range of typical diameters found in the microvasculature of various mammals<sup>26,27</sup>, including humans<sup>28</sup> while providing a significant deformation of the cell. It is in addition achievable using standard microfabrication techniques in contrast to circular channels which would require more sophisticated methods<sup>29</sup>.

Cell suspension is injected into the device through inlet 1, thus establishing a flow of cells in the main channel. The pressure difference between the main channel and the recovery chamber creates a pressure profile that drives cells to enter constrictions. There, they will undergo flow-induced deformation before crossing the constriction and getting trapped into one of the nests arranged in a staggered pattern. We set the pressure difference between the main channel and outlet to 10 mbar, in order to achieve cell arrest time in the range of seconds, i.e. close to the order of magnitude of arrest time reported for CTCs in blood capillaries *in vivo*<sup>30</sup>.

Pressure and velocity profiles in the microfluidic chip have been

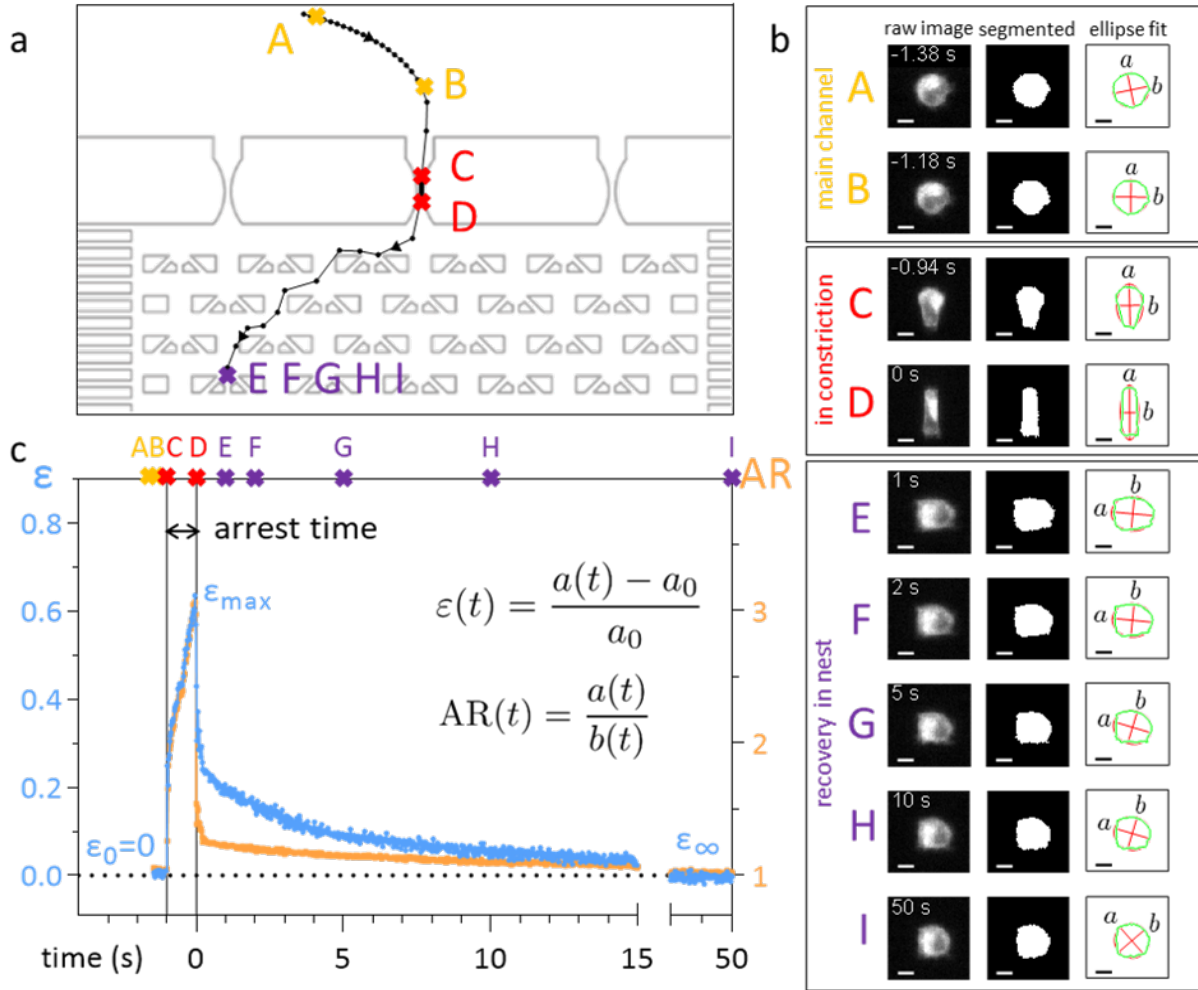


Fig. 2 - Cell trajectory and morphological analysis in the Pachinko device. (a) Trajectory of a representative cell. Cell initially flowing in the main channel (A) is deviated (B) into the constriction where it is pushed and deformed under flow-induced forces (C-D) before a final recovery step in a nest (E-I). (b) Representative images of the cell (DIL staining) at the different A-I time points shown in (a) (scale bar =  $10\mu\text{m}$ ). Images display the raw and segmented shapes as well as the corresponding elliptic fit (major axis  $a$ , minor axis  $b$ ). (c) Cell elongation  $\epsilon(t)$  (blue) and aspect ratio  $AR(t)$  (orange) versus time as the cell flows through the microfluidic device, highlighting the time points A-I. The arrest time of the cell inside the constriction is defined as the duration between C and D.

determined by numerical simulations. Due to the negligible size of the three constrictions in parallel compared to the main channel and the recovery chamber, the majority of the pressure drop is located at the constrictions level, thus ensuring the cell is free of any significant pressure gradient in the main channel and in the recovery chamber (Fig.1e and Suppl. Information, section 3, Fig.S2 and Table S1). The pressure drop applied along the narrowest part of the constriction, estimated to approximately  $\Delta P_h = 6 \text{ mbar}$ , creates a hydrodynamic force that will push the cell, squeezing it between the channel walls (see Fig.1d), until the cell reaches a deformation high enough to be released in the recovery chamber. Note that the surface of channels is passivated using pLL-PEG to minimize the friction between the cells and the PDMS surface. The cell will then follow the streamlines and end up in one of the single cell nests where it can recover from the

deformation. The pressure difference applied on the cell in a trap is estimated to  $0.1 \text{ mbar}$  (Fig.S2) and is thus negligible compared to  $\Delta P_h$ ). Note that as the cell membrane is being curved in the constriction, a pressure difference  $\Delta P_c$  is created which opposes cell deformation and counteracts the hydrostatic pressure difference  $\Delta P_h$ . Laplace law gives the equation which relates  $\Delta P_c$  with the cell membrane cortical tension  $\tau_0$  and the front and back radius of the cell ( $R_{front}$  and  $R_{back}$ , respectively) in the constriction:  $\Delta P_c = \tau_0(1/R_{front} - 1/R_{back})$ <sup>31,32</sup>. Taking an estimate of  $\tau_0 \approx 50 \text{ pN}/\mu\text{m}$ <sup>33</sup> for cancer cells, we found that  $\Delta P_c \approx 0.05 \text{ mbar}$  at the cell entry and decreases as the cell progresses in the constriction (Suppl. Information, section 4 and Fig.S3). Thus we can neglect the membrane curvature induced pressure difference and consider that cells experience in the constriction a pressure drop of  $\Delta P \approx 6 \text{ mbar}$ .

### Dynamics of cell morphology upon flow-induced deformation

Briefly, cells are stained with a membrane dye (DIL) to detect the outline of the whole cell (see Material and Method section). The trajectory of a cell can be divided into three parts (see Fig.2a): travel in the main channel (points A-B), then deformation and transit through the constriction (points C-D), followed by recovery in the single cell nest (points E-I). In each frame, a region of interest around the cell is segmented to reveal the shape of the cell (represented by its 2D projection). The segmented image properties are measured to determine the cell deformation versus time, which is computed from the elliptical fit of the segmented shape (Fig.2b, see Suppl. movie). As a proxy for cell deformation and shape recovery, we use the elongation parameter  $\varepsilon$  defined as the length of the ellipse major axis  $a$  normalized to its initial value  $a_0$  before the cell entry into the constriction:

$$\varepsilon(t) = \frac{a(t) - a_0}{a_0}$$

We also measure the aspect ratio  $AR(t) = \frac{a(t)}{b(t)}$ , with  $a(t)$  and  $b(t)$  the major and minor axis lengths, which increases from 1 for a spherical cell to values above 1 for elongated cells. Fig.2c displays an example of the dynamics of both parameters during the journey of a typical cell in the Pachinko device. The main regimes of  $\varepsilon(t)$  variation defined by yellow, red and purple letters, reflect the history of the cell in the three compartments of the device. In the main channel (points A-C),  $\varepsilon = \varepsilon_0$  is constant and equal to 0 by definition. Similarly,  $AR = AR_0$  is constant and close to 1, which reflects that a spherical floating cell displays a projected shape close to a perfect circle. In the constriction (points C-D), the deformation increases rapidly as the cell is pushed in-between the walls, reaching the maximum  $\varepsilon_{max}$  (equivalently  $AR_{max}$ ) value. In the cell nest (points E-I), the deformation relaxes toward an asymptotic  $\varepsilon_{\infty}$  (equivalently  $AR_{\infty}$ ) value. To capture all of the recovery, we record for a duration of 50s after the cell exits the constriction. Above this time, we noticed that the cell shape no longer evolve.

Finally, let's note that approximately 30% of cells ended up alone in a nest. Cells escaping the nest array chamber, or multiple cells ending up in a single cell nest were discarded from the analysis.

## Results

The method described above has been applied to three breast cancer cell lines: SK-BR-3, MCF-7 and MDA-MB-231. Each cell lines represents one of the three main subtypes of this disease: SK-BR-3 cells originate from a HER2+ cancer<sup>34</sup>, MCF-7 from estrogen and progesterone receptors positive tumor while MDA-MB-231 cells display none of these markers and are therefore categorized as "triple-negative". These subtypes correlate with different levels of aggressiveness, with the triple-negative breast cancer being the most aggressive, and more prone to induce metastasis<sup>35</sup>.

### Deformation regime

Our device has been mainly designed for the study of the recovery regime. The circle arc shape of the constriction, in contrast to long and uniform deformation channels as developed in<sup>20,36-38</sup>,

involves complex deformation and friction force patterns whose modeling would deserve specific mathematical treatment. However, temporal monitoring of cell deformations in these constrictions may provide useful comparisons between cell lines.

We first consider the cell arrest time, defined as the residence time within the constriction. It should be noted that, due to the double flared shape of our constriction and its short length (relative to the cell diameter), this arrest time differs from the entry or the transit time as defined in the literature for funnel-shaped constrictions opening onto a long and narrow channel<sup>20,36-38</sup>. Actually, our arrest time is a combination of both, reflecting the fact that cells are never arrested in the constriction but move slowly until their velocity displays an abrupt change upon cell release.

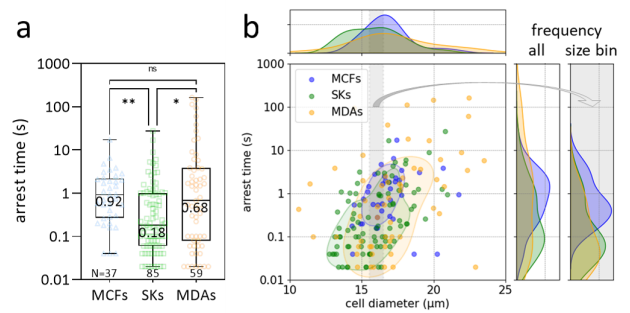


Fig. 3 - Cell arrest in the constriction displays high variability within each cell line. (a) Box plot of the arrest time for each cell line. The indicated value refers to the cell line median arrest time. (b) Scatter plots of the arrest time as a function of cell diameter. Contours of highest point density are represented for each cell line (MCFs n=37, SKs n=85, MDAs, n=59). Top and side plots around the central scatter plot represent the density of cell diameters (top) or arrest times (right, 'all'). The gray-shaded side plot (right, 'size bin') represents the density of cell arrest times selected within the size bin 15.5-16.5  $\mu\text{m}$  (highlighted in gray in the central plot) for whole cells.

For each cell line, arrest times range from around 100s for the slowest cells, down to 20ms for the fastest (Fig.3 and Methods). A large variability in arrest time is observed for all the three cell lines analyzed, in particular for MDA-MB-231 cells.

### Arrest time is firstly correlated to cell diameter

The median arrest time of SK-BR-3 cells is 180 ms, which is significantly smaller than median arrest time of MDA-MB-231 (680 ms) and MCF-7 cells (920 ms), without any significant difference between the latter two (Fig. 3a).

The arrest time correlates with cell size at the population level as SK-BR-3 cells are on average smaller compared to the other two cell lines. The median diameter for SK-BR-3 cells is 15.9  $\mu\text{m}$ , while MDA-MB-231 and MCF-7 median diameters have both been measured at 16.8  $\mu\text{m}$  (Suppl. Information, section 5 and Fig.S4). On average, the larger the cell is, the longer it takes to cross the constriction (Fig. 3b).

Other studies using flow-induced deformation in constrictions of similar dimensions have reported a correlation between cell size and arrest time<sup>39</sup>, or between cell buoyant mass, (which is related to its volume), and arrest time<sup>36</sup>. Our results therefore

confirm previous data.

#### Arrest time is a read-out of cell mechanical properties

The scatter plot of Fig3b indicates however that cell size is not the only relevant parameter to determine the arrest time. Indeed, some of the bigger cells can cross the constriction very rapidly, and inversely small cells can spend up to a few seconds in the constriction.

To compare between cells of a given size, we binned the data of Fig3b by cell size, performing a sliding 1  $\mu\text{m}$  bin size (Suppl. Information, section 6 and Fig.S5). Interestingly, a hierarchy between cell types emerges. A typical example of such window is shown on the right of Fig3b. The arrest time for MDA-MB-231 and SK-BR-3 cells distribute over the lowest values, conversely the MCF-7s over the highest ones. In other terms, MDA-MB-231 and SK-BR-3 cells appear to be more deformable than MCF-7 cells. Our results are in line with other studies comparing the deformability of circulating MCF-7 and MDA-MB-231 cells<sup>40-42</sup>. Although the mechanical properties of SK-BR-3 cells are less documented, our results confirm a previous work from our group, showing no significant difference between the arrest time of SK-BR-3 and MDA-MB-231 cells in an identical constriction geometry<sup>22</sup>.

#### Cells progress linearly through the constriction

We next examined the position of the center of mass and longitudinal extent of cells during their journey into the constriction (Fig. 4a). To compare cells of different arrest times, we normalized the time spent in the constriction by their arrest time, so that each cell enters the constriction at time 0 and exits at time 1. Overall, the cell rapidly enters the constriction, then they linearly progress through the narrow 6  $\mu\text{m}$  wide opening until most of the cell has crossed the neck of the constriction (Fig. 4b).

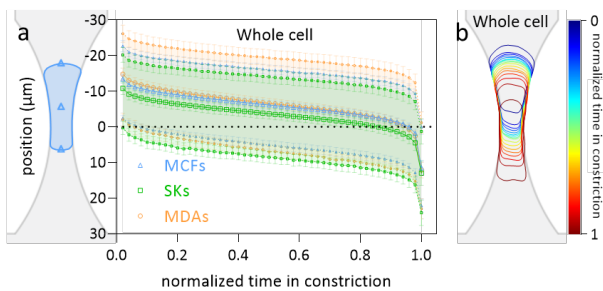


Fig. 4 - Spatio-temporal dynamics of cells during their passage through the constriction. (a) Position of the cell center ( $\pm$  95% CI) relative to the center of the constriction as the cell crosses the constriction. Upper and lower curves represent respectively back and front position of the cell. For each cell, time has been normalized by 1/arrest time to overlay curves. Only curves with at least 50 points were considered for this graph (MCFs  $n=17$ , SKs  $n=20$ , MDAs  $n=24$ ). (b) Outline of a whole cell (the same as represented in Fig.2) at different time points as it progresses through the constriction.

The arrest of the cell in the constriction is thus a continuous transit and not a full stop. Remarkably, for all cell lines, cell release from the constriction occurred as soon as the center of mass of the cell has passed the neck of the constriction (Fig. 4a).

	MCF-7	SK-BR-3	MDA-MB-231
$\tau$	0.28 s [0.24-0.32]	0.36 s [0.32-0.40]	0.66 s [0.56-0.77]
$E$	1.90 kPa [1.74-2.06]	1.15 kPa [1.08-1.22]	1.16 kPa [1.10-1.22]
$\eta_1$	0.056 kPa.s [0.045-0.068]	0.044 kPa.s [0.037-0.051]	0.081 kPa.s [0.068-0.095]

Table 1 - Parameters obtained from Jeffrey's model fits, using  $R_{eff} = 6.27 \mu\text{m}$  and  $\Delta P = 6 \text{ mbar}$ . Values represent fitting parameters and 95% confidence interval.

#### The rheological analysis of the deformation regime reveals that MCF-7 cells are less deformable

We next studied the rheological parameters of cell deformation. We consider these objects as viscoelastic, meaning they can be modeled by the association of elastic "springs" and viscous "dashpots" (see for instance<sup>43</sup> for an overview of these rheological models). The simplest combination of springs and dashpots that allows to adequately fit our data is the serial association of a Kelvin-Voigt element, built from a spring (Young modulus  $E$ ) and a dashpot (viscosity  $\eta_1$ ) in parallel, and a pure viscous regime (viscosity  $\eta_2$ ). This combination of mechanical elements also known as the Jeffreys model is described in Fig.5a. Short-time scale deformation is governed by the viscoelastic deformation of the Kelvin-Voigt element, while long-time scale deformation is governed by the linear elongation of the dashpot element. In this framework, the elongation  $\varepsilon(t)$  (see Fig.5a) is ruled by the following equation<sup>44</sup>:

$$\varepsilon(t) = \frac{R_{eff}\Delta P}{a_0} \frac{1}{E} \left[ \left( 1 - e^{\left( \frac{-E}{3\pi\eta_1} t \right)} \right) + \frac{E}{3\pi\eta_2} t \right]$$

where  $a_0$  is the initial major axis length,  $R_{eff}$  is the equivalent radius of the constriction (see Suppl. Informations, section 1),  $\Delta P$  is the pressure difference applied on the constriction, and  $E$ ,  $\eta_1$ ,  $\eta_2$  the rheological parameters described in Fig.5a.

It is important to note that most of the cells cross the constrictions in less than a few seconds. In other terms, the number of cells which can be analyzed decreases dramatically beyond a 5s window. We have thus decided to confine our analysis on the viscoelastic regime at short time scale by fitting the data with the Kelvin-Voigt model on time scales below 2 sec (Fig.5b).

The parameters deduced from this analysis are reported in Table 1. They are characterized by a low viscosity and an elastic modulus on the order of the kPa, in agreement with other works dealing with flow-induced deformations<sup>32,42,45</sup>.

Overall, Table1 and Fig. 5 indicate that MCF-7 cells are relatively less deformable than SK-BR-3 and MDA-MB-231 cells, as indicated by their larger Young modulus  $E$  (Table 1) and lower maximal deformation (Fig. 5b). These observations are consistent with other results in the literature<sup>40</sup> and with the larger arrest time of MCF-7 cells measured with our Pachinko device (Fig.3).

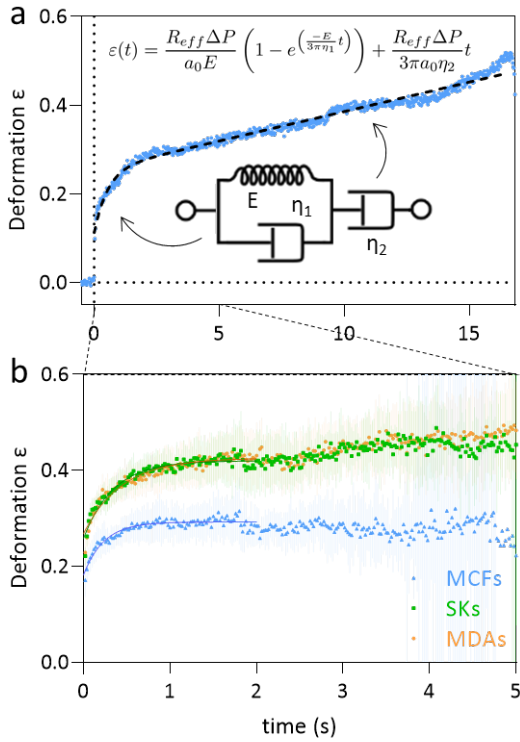


Fig. 5 - Deformation curves. (a) Deformation curves are well described by the Jeffreys model (see the main text for a description). The graph shows an example of the time variation of the elongation  $\epsilon$  obtained for a cell arrested a few seconds in the constriction, highlighting the viscous regime. (b) Mean curves for the three cell lines and fits of the viscoelastic regime set over a time range of 2s. The viscous regime was not fitted as the majority of the cells escaped before reaching this regime. Error bars represent 95% confidence intervals (MCFs  $n=31$ , SKs  $n=46$ , MDAs  $n=29$ ).

### Recovery regime

We then turned our attention to the morphological fate of cells when trapped in the nests of the recovery chamber after their passage through the constrictions.

In order to compare cells of different size and different maximal elongation, we normalize the elongation by its maximal value for each cell (Fig.6a) to define the normalized deformation as

$$\epsilon_{Norm}(t) = \frac{\epsilon(t) - \epsilon_{\infty}}{\epsilon_{max} - \epsilon_{\infty}} = \frac{a(t) - a_{\infty}}{a_{max} - a_{\infty}}$$

The starting time  $t = 0$  of the recovery regime corresponds to the last frame before the cell exits the constriction i.e. in most case to the maximum deformation  $\epsilon_{max}$ . Fig.6a displays a typical example of the variation of  $\epsilon_{Norm}(t)$ . It can be decomposed into an almost instantaneous recovery, happening faster than our frame rate of observation ( $\leq 20$ ms), followed by a slower shape relaxation. To identify the time constants governing cell recovery, we here chose to describe this slow decay as a viscoelastic (VE) regime according

to a generalized fractional Kelvin-Voigt model<sup>43,46</sup>:

$$\epsilon_{Norm}(t) = \sum a_i e^{(-t/\tau_i)}$$

Alternatively, fitting with a timescale-free power law model was also performed (Suppl. Info section 7) according to<sup>47</sup>

$$\epsilon_{Norm}(t) = \left(\frac{t}{t_0}\right)^{-n} + C$$

with  $C$  a constant.

### Cells recover almost entirely from the deformation

Although recovery from the deformation induced in the constriction is almost complete, the mean values of  $\epsilon_{\infty}$  show a small but significant difference with the initial value  $\epsilon_0 = 0$  (Fig.6b). The observation may be attributed to cell plasticity, a behavior already reported after similar deformation under flow for SK-BR-3 and MDA-MB-231 cell lines<sup>22</sup>. Assuming an elastic modulus of  $\approx 1$  kPa for the softer cells, the small pressure difference of 0.1 mbar across a trap (Fig. S2) would result in a deformation of  $\approx 1\%$  through Hooke's law. The remaining pressure difference that cells undergo in the recovery chamber is thus not able to explain alone the magnitude of their residual deformation.

### Cell recovery displays two regimes of different nature

As described previously in Fig6a, each cell recovery curve can be divided in an instantaneous recovery occurring in less than 20 ms, followed by a slower shape relaxation. This was observed for the three cell lines analyzed here (Fig.6d). We want to emphasize here that the instantaneous recovery does not originate from an eventual flipping of the cell at the exit of the constriction which would anyway yields the same maximal elongation. Only a tilt of the cell over the height of the recovery chamber could affect this parameter. But a simple geometric calculation would then show that this would minimize  $\epsilon_{max}$  by only around 10%. Finally, we performed experiments with an isotropic square constrictions of similar section area as  $6 \times 15 \mu\text{m}^2$  constrictions (i.e.  $9 \times 9 \mu\text{m}^2$ ) and observed again this instantaneous recovery (Fig. S8).

At the whole cell level, the latter regime appears to be best described with a three-phase exponential decay equation (Suppl. Information section 7 and Fig.S6 for a comparison with one-phase, two-phase decay and power law fits) corresponding to a viscoelastic behavior (Fig.6a). The addition of more phase decay did not improve the quality of the fits, we thus chose to limit the fit to a sum of three exponential decays labelled as fast, medium and slow. The general form of the equation thus becomes:

$$\epsilon_{Norm}(t) = a_{fast} e^{(-t/\tau_{fast})} + a_{medium} e^{(-t/\tau_{medium})} + a_{slow} e^{(-t/\tau_{slow})}$$

with  $a_i$  the amplitudes of the three exponential decays and  $\tau_i$  ( $i = fast, medium, slow$ ) their characteristic times. The order of magnitude of about 100 ms obtained for the fast exponential decay for all cell lines (i.e. 110ms for MCF-7, 113ms for SK-BR-3 and 56ms for MDA-MB-231 cells) has led us not to distinguish it from the recovery phase that takes place in less than 20 ms at the exit of the constriction, and to associate these two phases of recovery with an elastic regime. We then define  $\Phi_{VE} = a_{medium} + a_{slow}$  as

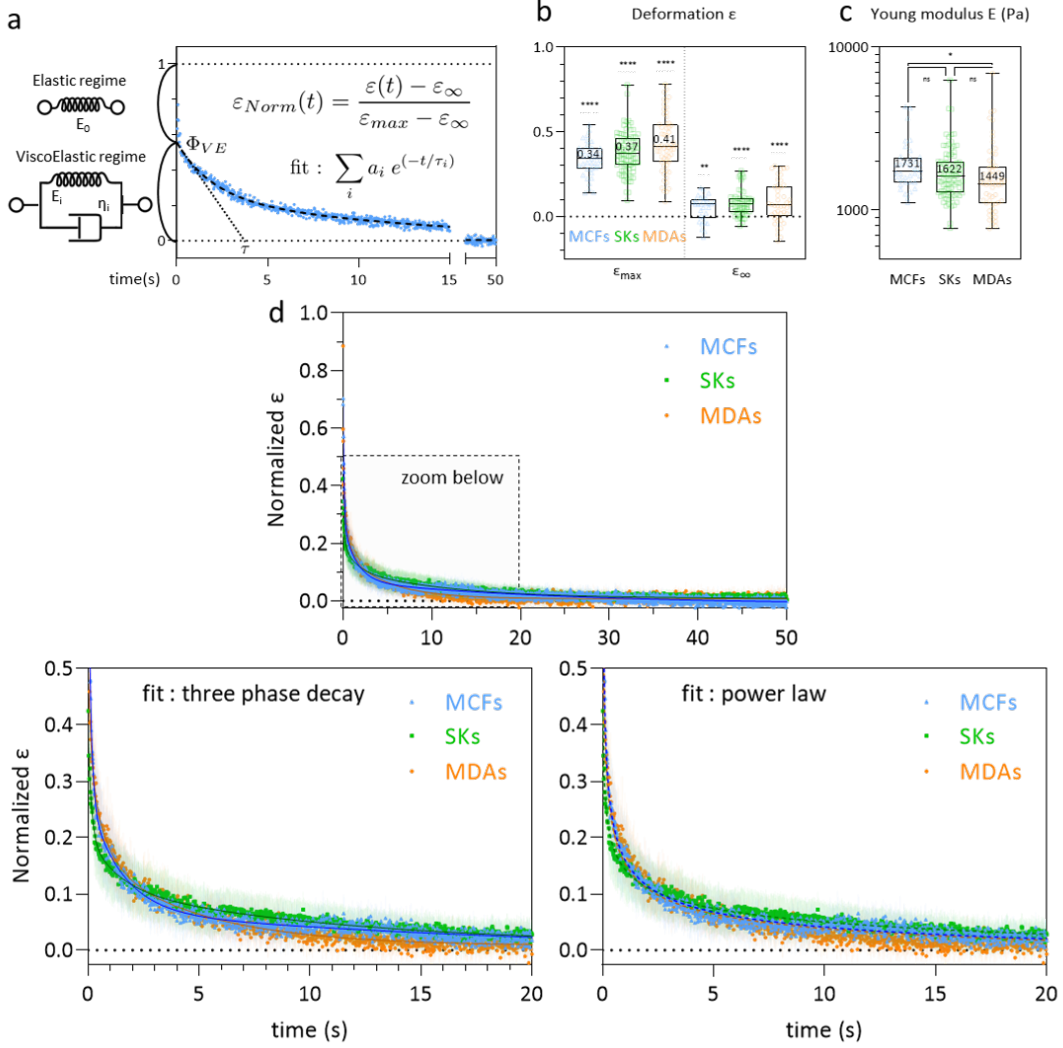


Fig. 6 - Recovery at the whole cell level. (a) The graph shows the time variation of the normalized deformation  $\epsilon_{Norm}(t) = (\epsilon(t) - \epsilon_{\infty}) / (\epsilon_{max} - \epsilon_{\infty})$  during recovery, which can be modeled by an instantaneous elastic regime, followed by a slower regime of total amplitude  $\Phi_0$ . The latter can be described by a sum of Kelvin-Voigt elements of characteristic decay time  $\tau_i$ . (b) Cell deformation measured in the constriction ( $\epsilon_{max}$ , MCFs n=36, SKs n=85, MDAs n=59) and after recovery ( $\epsilon_{\infty}$ , MCFs n=30, SKs n=56, MDAs n=44). Statistical difference to  $\epsilon_0 = 0$  is shown. (c) Distribution of  $E_{tot} = E_0 + E_{fast} + E_{medium} + E_{slow}$  for the three cell lines. Statistical comparison between each cell lines is represented (MCFs n=36, SKs n=85, MDAs n=59). (d) Mean normalized  $\epsilon$  curves after exiting the constriction (taken as starting point t=0). Bottom graph displays zoom over the first 20 seconds. Error bars represent confidence interval at 95% (MCFs n=25, SKs n=51, MDAs n=37). Fitting curves represent three-phases decay (bottom left) or power law (bottom right) fits of the mean curves. Corresponding parameters (with confidence interval at 95%) are reported in Table 2.

the fraction of the viscoelastic (VE) regime in the total recovery. Table 2 displays the results of these fits for each cell lines.

The graphs of Fig.6d does not show striking differences between cell lines. However we observe that the viscoelastic regime contributes more to the recovery in MDA-MB-231 cells ( $\Phi_{VE} = 37\%$  of the whole recovery compared to 29% and 20% for MCF-7 and SK-BR-3 cells, respectively), almost equally distributed along the medium and slow decay. The characteristic decay times are also lower in MDA-MB-231 indicating that MDA-MB-231 relaxes faster towards their equilibrium shape.

The power law fits (Suppl. Info section 7 and Fig.6d) overlap

nically with the three phases decay fits. They allow for an overall fit of the curves, without any distinction between elastic and viscoelastic regimes. The power law exponents obtained for each cell lines are  $n_{MCFs} = 0.35$ ,  $n_{SKs} = 0.18$  and  $n_{MDAs} = 0.33$  for MCF-7, SK-BR-3 cells and MDA-MB-231 cells, respectively. The lower value for SK-BR-3 cells reflects the lower contribution of the viscoelastic regime to the relaxation of SK-BR-3 cells, consistent with the lower value of  $\Phi_{VE}$  in these cells.

To go deeper into the analysis of the whole cell recovery, we sought to deduce the rheological parameters of the three cell types. Assuming that in the constriction, cells experience a stress

Three phase decay fit			
	MCF-7	SK-BR-3	MDA-MB-231
$a_{medium}$	20.4 % [19.7-21.1]	9.49 % [8.89-10.1]	20.3 % [18.8-21.8]
$\tau_{medium}$	1.46 s [1.38-1.55]	1.23 s [1.11-1.38]	0.58 s [0.52-0.66]
$a_{slow}$	8.24 % [8.04-8.44]	10.6 % [10.3-10.9]	16.5 % [15.8-17.2]
$\tau_{slow}$	24.0 s [21.6-27.0]	10.8 s [10.5-11.3]	4.68 s [4.49-4.87]
$R^2$	0.968	0.977	0.962
$\Phi_{VE}$	28.6 % [27.7-29.5]	20.1 % [19.2-21.0]	36.8 % [34.6-39.0]
$E_{tot}$	1.76 kPa [1.57-1.96]	1.62 kPa [1.45-1.78]	1.45 kPa [1.19-1.62]
$E_{elastic}$	1.26 kPa [1.12-1.40]	1.30 kPa [1.15-1.42]	0.92 kPa [0.75-1.03]
$E_{viscoelastic}$	0.50 kPa [0.45-0.56]	0.33 kPa [0.29-0.36]	0.53 kPa [0.43-0.60]
$\eta_{medium}$	0.53 kPa.s [0.46-0.60]	0.19 kPa.s [0.16-0.22]	0.17 kPa.s [0.13-0.20]
$\eta_{slow}$	3.48 kPa.s [2.96-4.07]	1.87 kPa.s [1.65-2.07]	1.12 kPa.s [0.91-1.27]
Power law fit			
	MCF-7	SK-BR-3	MDA-MB-231
$n$	0.35 [0.345-0.355]	0.18 [0.174-0.186]	0.33 [0.327-0.342]
$R^2$	0.962	0.971	0.925

Table 2 - Parameters obtained from the three phase decay and power law fits of the cell recovery and deduced rheological parameters. Values represent median and [95% confidence intervals].

of magnitude  $\Delta P \approx 6$  mbar, the Hooke's law leads to the relation  $\Delta P \approx E_{tot} \epsilon_{max}$  where  $E_{tot} = E_0 + E_{fast} + E_{medium} + E_{slow}$  and  $\epsilon_{max}$  is the maximal longitudinal deformation. Though it was defined *ad hoc* for elastic materials only, we'll use it here to give an approximation of the apparent Young modulus  $E_{tot}$  of our viscoelastic cells. Fig.6c shows a trend in the distributions of  $E_{tot}$ : MCF-7 cells have the highest median value and the MDA-MB-231 the lowest, all of the order of 1 kPa and not significantly different from each other. From the value of  $E_{tot}$ , we could deduce the values of the Young modulus associated with the elastic and viscoelastic regimes (i.e.  $E_{elastic} = E_0 + E_{fast}$  and  $E_{viscoelastic} = E_{medium} + E_{slow}$ , see Table 2). The elastic regime (values of the Young modulus of the order of 1 kPa) is the most discriminant between cell types in terms of Young modulus, with again MDA-MB-231 cells showing the lowest values. Oppositely,  $E_{viscoelastic}$  is similar for the three cell lines and of the order of a few hundred of Pa, i.e. much lower than  $E_{elastic}$  except for MDA-MB-231 cells.

More generally, the cell viscosity in recovery can reach very large values, in particular for the slowest decay  $\eta_{slow}$  (i.e. 3.48 kPa.s for MCF-7 cells). Strikingly, MDA-MB-231 cells exhibit the lowest viscosity, the lowest recovery elastic modulus and the lowest relaxation times among the three cell lines, which underlines their relatively high deformability, as expected from their mesenchymal phenotype and their higher metastatic potential.

### Role of the cell cortex integrity in shape recovery

The results shown so far have been obtained under moderate deformations, with no detectable cell damage such as blebbing of the plasma membrane. We focus here on the role played by the cell acto-myosin cortex underlying the plasma membrane during the elastic recovery highlighted in the previous sections. We address this question through mechanical and pharmacological perturbations of the acto-myosin cortex. As all cells display an elastic regime, with no striking differences between cell types, we choose to perform these experiments on the MDA-MB-231 cell line.

### The occurrence of membrane blebs in a large deformation regime suppresses the elastic recovery regime

To induce larger cell deformation, we used constrictions with a  $6 \times 6 \mu\text{m}^2$  square cross-section. The higher mechanical constraints induced membrane blebbing (Fig. 7a), suggesting that the deformation is here strong enough to disrupt the attachment of the cell cortex to the membrane. In a first set of experiments, we observed the presence of membrane blebs in 43 out of the 51 cells (84%) recorded going through the  $6 \times 6 \mu\text{m}^2$  square constriction. Cells which did not present blebs were among the smallest cells observed. Strikingly, the elastic recovery regime was lost in these conditions. Instead, we observe a slow healing of blebs, compatible with the timescale of a few minutes associated with bleb retraction<sup>48</sup>.

### Actin depolymerization prevents cell recovery

To further investigate the role of the cell cortex integrity on elastic recovery, we applied pharmacological perturbation on the cell cortex to depolymerize actin or impairing cell cortex contractility.

MDA-MB-231 cells were treated with 0.5  $\mu\text{M}$  of Latrunculin A (LatA) for 30min. This concentration induces a partial F-actin depolymerization on adherent MDA-MB-231 cells (Suppl. Info section 8 and Fig.S7), in agreement with other works<sup>49</sup>. LatA treated cells display shorter arrest time (median 300 ms, i.e. less than half the median value observed in the control condition, see Fig.S9), thus supporting the role of the actin cytoskeleton in the resistance to deformation. Then, instead of progressively recovering their initial disc-shaped appearance into the nest, LatA treated cells tend to spread between trap structures, adopting indented shapes (see Fig.7b). This prevented us to perform elliptical fits, hence to compute recovery curves. This observation highlights the need for an intact actin cytoskeleton to observe recovery following induced deformation.

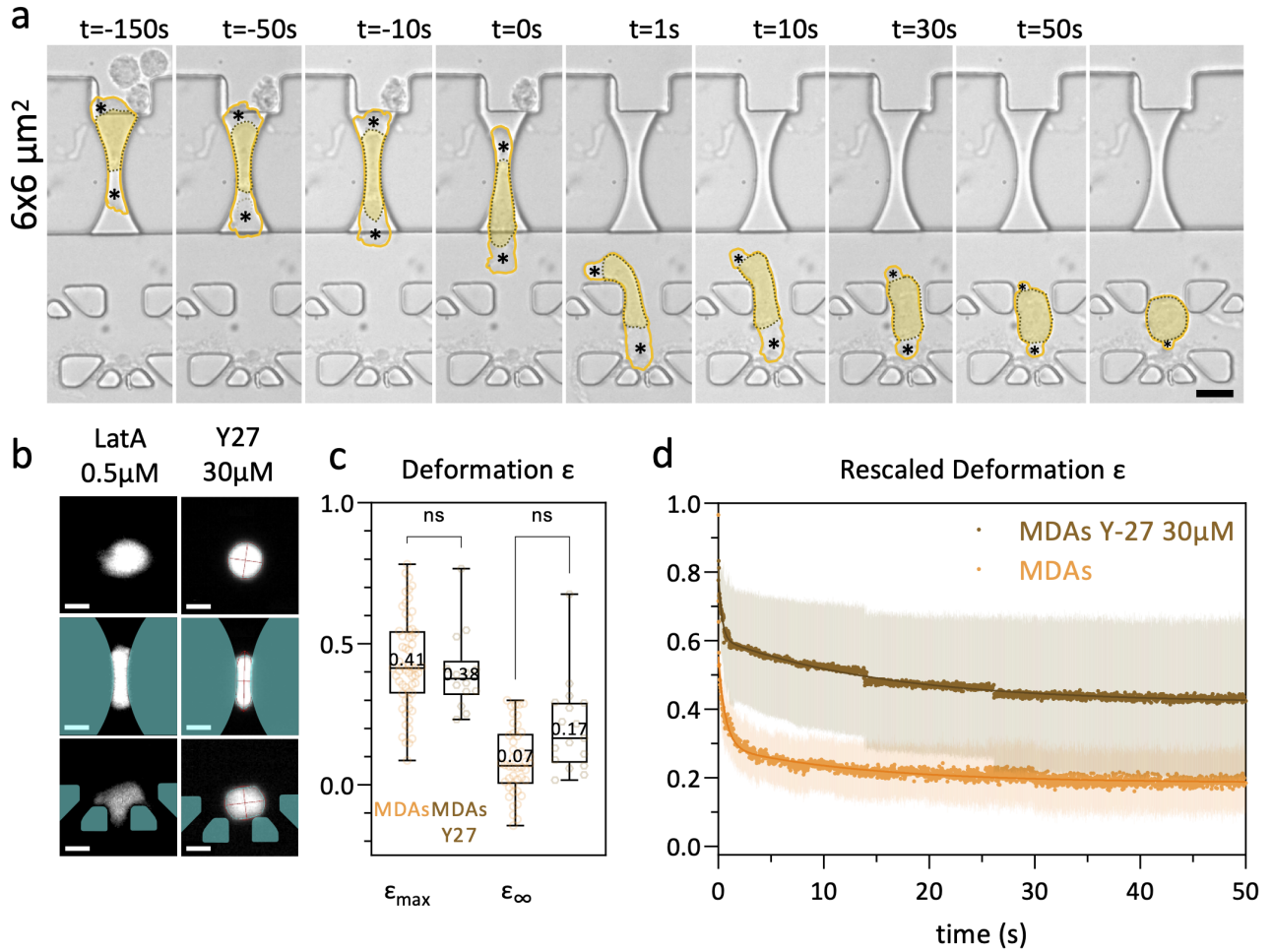


Fig. 7 - Role of the actin cytoskeleton and acto-myosin contractility in cell shape recovery following large deformation. (a) Images of a MDA-MB-231 cell through a square 6x6 μm<sup>2</sup> constriction (scale bar = 20 μm). The overall contour of the cell is delimited in yellow and encompasses the area of membrane blebs (\*) located beyond the dark dotted line. (b) Representative images of cells treated with either 0.5 μM Latrunculin A or 30 μM Y-27632 (scale bar = 10 μm). (c) Cell deformation measured in the constriction ( $\epsilon_{max}$ , MDAs Y-27 n=14, non-treated MDAs n=59) and after recovery ( $\epsilon_{\infty}$ , MDAs Y-27 n=17, non-treated MDAs n=44). Data were statistically different to  $\epsilon_0 = 0$  (not shown, with at least \*\*\*). (d) Mean rescaled  $\epsilon$  curves after exiting the constriction (taken as starting point t=0). Error bars represent confidence interval at 95% (MDAs Y-27 n=14, non-treated MDAs n=34).

### MyosinII inhibition leads to partial recovery

We next explored whether contractility was required using the ROCK inhibitor Y-27632 (Y-27). MDA-MB-231 cells were treated with 30 μM Y-27632 for 30min. This condition is associated with an increase in the spreading area of cells (see Fig.S7), which suggests a significant inhibition of acto-myosin activity, as expected in this range of concentrations<sup>50</sup>.

Even though maximal deformation levels were similar, the remaining deformation  $\epsilon_{\infty}$  was higher for Y-27 treated cells (though not significant) compared to the control condition. Y-27 treated cells kept an elongation of 0.17, against 0.07 for non-treated cells (Fig. 7c). The higher residual deformation observed in Y-27 treated cells suggests that acto-myosin contractility participates in cell shape recovery.

To highlight long-term differences in the recovery we define the

rescaled deformation as

$$\epsilon_{Resc}(t) = \frac{\epsilon(t)}{\epsilon_{max}} = \frac{a(t) - a_0}{a_{max} - a_0}$$

The mean recovery curves are shown in Fig.7d for treated and control cells. Both curves are composed of a first elastic regime followed by a viscoelastic regime, but Y-27 treated cells display lower and incomplete recovery. A three-phase exponential decay fit, as presented previously, yields a slow characteristic time of  $\tau_{slow} = 9.91$  s for Y-27 treated cells, emphasizing a slower viscoelastic recovery than observed for non-treated MDA-MB-231 cells ( $\tau_{slow} = 4.68$  s).

## Discussion and Conclusion

The present study demonstrates the ability of a custom-made device, including constricted micro-channels and single cell traps placed in a flow-free recovery chamber, to study the morphological recovery of cells after fast deformation under flow. Using this device, we obtained new insights into the morphological adaptation of cancer cells to mechanical stressors and physical constraints such as those encountered in the blood circulation. Most of our study was performed using a constriction geometry leading to a significant cell deformation of about 40% but without observable disruption of the attachment of the cell cortex to the plasma membrane.

Even if the principle of the operating mode of the Pachinko device is simple, obtaining the recovery mechanical parameters of cells meets several challenges. We first need to image individual cells during their entire journey from the inlet to the traps, i.e. before entering the constriction, inside the constriction, and within a trap after their escape from the constriction. Those multiple requirements are particularly challenging as many events can occur to lead us to discard a cell: first the cell must not flow too rapidly (leading to a blurred image in the main channel, or to an arrest time below our framerate in the constrictions), it should not be attached to another cell before and within the constriction, and finally the cell must recover in an empty trap that should remain as such for 50 s while many other cells continue to flow into our device. We estimate that less than 30 % of cells are exploitable. On top of that, track's reconstruction, segmentation and fitting procedure require manual reviewing and adjustments (e.g. of initial fitting parameters) when necessary, as mentioned in the dedicated Material and Method sub-sections. It is why this system could be qualified as moderate-throughput, which is nevertheless sufficient to obtain about 10-15 exploitable cells per experiment, which typically lasts around 1 hour.

We have shown that MCF-7, SK-BR-3 and MDA-MB-231 breast cancer cells mostly recover their spherical shape after deformation, with a residual deformation more pronounced in SK-BR-3 and MDA-MB-231 as compared to MCF-7 cells. Let's note that plastic deformation has also been reported in breast cancer lines after deformation<sup>24</sup>, and was associated to cytoskeletal damages accumulation particularly in high metastatic potential cancer cells. Strikingly, the major part of this recovery takes place within 100 ms. It is followed by a slower recovery regime, well described by a two exponential decay expressing the visco-elastic behavior of cells on a time scale of tens of seconds. The order of magnitude of about 1 mm/s of the speed of circulating blood cells<sup>51</sup> would result in a full recovery length in the centimeter range. Such a slow recovery might avoid repetitive, large amplitude cycles of deformation-relaxation for cells encountering successive capillary constrictions, while the elastic-like relaxation occurring on much shorter lengths would on the contrary relax partly and almost instantaneously the cell strain. Both effects might contribute to protect cells during their transit in the circulation.

Our main finding is that cell recovery relies on the presence of

actin filaments as well as on the integrity of the acto-myosin cortex lining the inside of the plasma membrane. We indeed found that (i) depolymerizing F-actin filaments using Latrunculin A suppresses the process of recovery itself, leading to plastic cell behavior, and (ii) inhibition of the myosin light chain phosphorylation using the ROCK inhibitor Y-27632 limits the amplitude of the elastic regime, restraining in turn the amplitude of the total recovery. Our observations are in line with evidences that the elastic modulus dominates over the viscous modulus at high frequency<sup>52</sup> due to cortical tension. The acto-myosin cortex, an active gel responsible for the most part of the tension of the cell envelope<sup>53</sup>, ensures the storage and relaxation of elastic energy<sup>32,54</sup>. We thus cannot totally exclude the contribution of active mechanisms in the regime of elastic recovery. Similarly, and although the passive viscous properties of the cytoplasm<sup>55</sup> and of the entangled cytoskeleton<sup>56</sup> alone could account for the post-elastic regime of recovery, we cannot rule out from our experiments an active contribution of the cell cortex in the viscoelastic recovery regime of amplitude  $\Phi_{VE}$ .

The approach followed in this study has considered cell recovery independently of their prior deformation. A more elaborate analysis could however consider the entirety of the cell history (deformation and recovery), similarly to the work of Bonakdar et al.<sup>57</sup>. The time constants of the viscoelastic regimes are much higher in recovery than in deformation. These differences might be interpreted by considering the role of the nucleus, whose diameter is larger than the smallest size of our constrictions. The nucleus is expected to resist deformation in the constrictions, while it should interfere less with cell recovery. It would be interesting in future studies to monitor the deformation and recovery of isolated nuclei, enucleated cells and nuclei in their natural cellular environment. However, beyond these differences, MDA-MB-231 cells are, among the three cell lines, the softer and most fluid-like in both deformation and recovery<sup>58,59</sup>. Increase in softness is a recognized signature of tumorigenesis<sup>12,43</sup>, and a fluid-like behavior might be an asset for survival in the circulation, enhancing the probability of the occurrence of metastasis<sup>60</sup>. Our study deals with originally adherent cells which we have detached from their substrate and suspended to mimic the behavior of circulating tumor cells. It has been reported that suspended cells display significant differences regarding elasticity<sup>61</sup>, myosin II activity<sup>62</sup> and lamin A/C posttranscriptional level<sup>63</sup> as compared to their adherent counterparts. In line with these results, we have established that the level of p-MLC (phospho MyosinII Light Chain) in our 3 breast cell lines was lower in suspended cells, which seems to indicate a decrease in their contractility (Fig.S10).

A remaining open question is that of a possible change in volume of cells in the regime of fast deformation studied here. Some recent results obtained on the volume monitoring by fluorescence exclusion method (FXm) on a time scale of tens of milliseconds suggest that cells can reduce their volume on these time scales (see Fig.7G of Venkova et al.<sup>50</sup>). This volume loss is associated to an increase in membrane tension as well as to the loss of water and small solutes. The recovery rate expected from volume loss is on the order of minutes<sup>50</sup>, i.e. well beyond the recovery characteristic times measured in the present study. However, volume

loss could contribute also to shorter timescales in both deformation and recovery by e.g. reducing the cell apparent modulus. Further technological developments would be necessary to address the important question of suspended cell volume adaptation to fast deformation and release.

Overall, our work gives new insights not only into flow-induced deformation of suspended cells but also into their shape recovery, which are both critical cellular events during the journey of CTCs in the blood circulation. A natural extension of our work, which would initially avoid the challenges raised by the rarity of CTCs among an overwhelming quantity of surrounding normal blood cells -requiring advanced sorting techniques<sup>64</sup>- will be to flow CTC cell lines<sup>65</sup> into our Pachinko device.

### Materials and Methods

#### Photolithography

The microfluidic device layout was etched on a photosensitive resin-coated chrome-glass substrate (Nanofilm) following standard technics to obtain the adequate mask of the device. A thin 15  $\mu\text{m}$  layer of negative photoresist SU-8 (SU-8 2015, Kayaku Advanced Materials) was spin-coated on a silicium wafer (3000 g, 30 s), baked rapidly (3 min, 90°C), then exposed through the chrome mask (140  $\text{mJ}/\text{cm}^2$ ). The wafer was baked (4 min, 90°C), developed in PGMEA to dissolve unexposed resin, then baked once more at 200°C. Exact height of the device was measured with a mechanical profilometer (Dektam 6M profilometer, Veeco). Wafer surface was rendered hydrophobic by silanization under vacuum with (tridecafluoro-1,1,2,2-tetrahydrooctyl)trichlorosilane (AB111444, abcr) after activation via plasma cleaning.

#### Soft lithography and microfluidic chip coating

PDMS mix (10:1 base:curing agent, Sylgard 184, Don Corning) was prepared, degassed, and poured over the resin structures of the silanized silicium wafer (height  $\approx$  5 mm). PDMS was degassed under vacuum for 15 min so that it perfectly matches the resin structures, then cured at 70°C for 3 h. PDMS was removed from the wafer mold, and individual chips were cut apart. Inlets and outlets were punched out at a 1.5 mm diameter. PDMS was cleaned using 70% Ethanol and Isopropanol, then dried with a nitrogen air gun. PDMS chips and fluorodishes were plasma-cleaned then immediately bonded together to seal the microfluidic chip. On the day of the experiment, microfluidic chips were washed with 70% Ethanol then PBS, then passivated by injecting 100  $\mu\text{L}$  of 1 mg/mL solution of pLL-PEG (pLL(20)-g[3.5]-PEG(5), Susos) for 30 min, then rinsed with PBS.

#### Numerical simulations

Simulations were performed using the Microfluidics module of COMSOL Multiphysics 5.5. Device geometry was imported and meshed finely (minimal element size 0.172  $\mu\text{m}$ , Suppl. FigS2). Navier-Stokes equation was applied to simulate fluid behaviour in the microfluidic chip. Laminar flow was assessed due to the characteristic dimensions of the system. Channel height was taken into consideration using the shallow channel approximation of

the laminar flow module. Pressure and velocity field distribution were exported to confirm hypothesis that the pressure drop is located at the constrictions (see Fig.1e and Figs. S2 and S3).

#### Cell culture

All three MDA-MB-231, SK-BR-3 and MCF-7 cell lines were cultured in Dulbecco's Modified Eagle Medium (DMEM GlutaMax, ThermoFisher 10566016), supplemented with 10% of Foetal Bovine Serum (FBS, Gibco 10270-106) and 1% of Penicillin-Streptomycin (10 000 U/ml penicillin, 10 000  $\mu\text{g}/\text{mL}$  streptomycin, Gibco 151140-122). Cells were maintained in growth-enhanced treated culture flasks at 37°C under 5%  $\text{CO}_2$  atmosphere. Cells were passaged routinely before reaching confluency, and media was renewed every couple of days.

#### Cell staining and treatments

Cells were plated in a 6well plate so that they reach 70-90% confluency on the day of the experiment. The culture medium was removed and replaced with 1 mL of 20  $\mu\text{g}/\text{mL}$  lipophilic tracer DIL (1,1'-Dioctadecyl3,3',3'-Tetramethylindocarbocyanine Perchlorate, ThermoFisher D3911) or in culture media, and left to incubate for 1 hour at 37°C. Alternatively, cells were stained with 5  $\mu\text{M}$  CalceinAM (Invitrogen C3099) in culture media for 30 min at 37°C. Dye containing medium was removed and cells washed with 1mL PBS before being harvested with 500  $\mu\text{L}$  Trypsin (Gibco 12605) for at 37°C. Cells suspension was spun at 500 g for 5 min, then resuspended at  $\approx$  400 000 cells/mL in serum-free DMEM supplemented with 25 mM HEPES (Sigma H0887) and 2 000 U/mL DNase (Sigma D4513). Optionally, either 30  $\mu\text{M}$  Y-27632 (Tocris 1254) or 0.5  $\mu\text{M}$  Latrunculin A (Sigma L5163) was added to the preparation. Cells were left to incubate for 30 min at 37°C before being injected into the microfluidic Pachinko device.

#### Cell injection in the Pachinko device

The cell suspension was placed in an Eppendorf tube mounted with a p-cap (Fluigent) connected to the inlet 1 of the microfluidic chip through a fluidic tubing (ID .02 in, OD .06 in, Tygon ND-100-80, Cole-Parmer). Outlets 2 & 3 were connected to Eppendorf tubes containing experiment media without cells. The cell suspension and media were kept at 37°C on a hot plate for the whole duration of the experiment. Inlet 1 and outlet 2 pressure were set to 12 and 8 mbar respectively to initiate a flux of cells in the device main channel. The pressure in outlet 3 was initially kept at 10 mbar to prevent cells from entering constrictions then decreased to 0 mbar to allow cells to enter (Fig.1a.).

#### Acquisition

Cell fluorescence as the cell moves through the device were recorded through a 10x objective on an inverted microscope mounted with a CMOS camera (acA1920-150um Basler AG, pixel size 4.8  $\mu\text{m} \times 4.8 \mu\text{m}$ ) to record. Stained cells were acquired at 50 Hz with a 5 ms exposition for at least 50 s. Exposure times and frame rates were adjusted to maximize the contrast of the fluorescent object while minimizing the blur due to cell motion at

high speed through the device. The framerate was increased as much as possible within the limits of the camera to achieve the highest temporal resolution possible for each fluorescent marker, i.e. 20 ms for whole cell fluorescence.

### Cell trajectory reconstruction

Sequences of fluorescent cell or nucleus moving through the device were binned on ImageJ. Cell tracks were reconstructed using the TrackMate plugin on ImageJ<sup>66</sup> (see an example on Fig2a). Briefly, cells were detected with a threshold based method, then detected spots were linked on each successive images (linear motion LAP tracker) to reconstruct tracks. Parameters of the detection and tracking algorithms were adjusted to each sequence. Tracks were manually reviewed and corrected for punctual errors in track reconstruction. Track coordinates were exported to Matlab (R2020a, MathWorks) for downstream analysis.

### Cell arrest time determination

Only complete tracks (i.e. with images before and after deformation in the constriction) were selected for the analysis. Entry and exit time points were defined as the index of the first image where the cell y-position exceeds respectively the constriction entry and exit y-coordinate. The arrest time of a cell was determined as elapsed time between entry and exit time points. For the fastest cells which can cross the constriction in less than 1 frame, we attribute to these cells an arrest time corresponding to the inverse of the acquisition frame rate, i.e. 20 ms.

### Image analysis and segmentation

For each cell track, for each time point in the cell track, a region of interest around the cell position was drawn in the original images. The selected section of the image was binarized: DIL-stained membrane images were segmented with 2 thresholds calculated using Otsu's method, to account for fluorescent intensity heterogeneity in the cell. Non-background layers were merged together to recreate cell binarized region. Images were filtered to keep the biggest structure in the image. Major and minor axes of the ellipse that have the same normalized second central moments as the binarized region were measured (see an example on Fig2b).

### Cell parameters extraction

The diameter of the cell can be estimated by measuring the average area of the shape in the main channel assuming that the 2D projection of the cell is a circle through the relation  $a_0 = \sqrt{\frac{4A}{\pi}}$  between the cell diameter  $a_0$  and the binarized region area  $A$ . Elongation  $\epsilon$  and aspect ratio  $AR$  of the cell or nucleus were defined with major axis  $a$  and the minor axis length  $b$  as  $\epsilon(t) = \frac{a(t)-a_0}{a_0}$  and  $AR(t) = \frac{a(t)}{b(t)}$  where  $a_0$  is the average value of the diameter measured in the main channel. Maximal  $\epsilon_{max}$  and end value  $\epsilon_{\infty}$  were determined for each cell using Matlab Cftool application interface, and used to compute the normalized deformation  $\epsilon_{Norm}(t) = \frac{\epsilon(t)-\epsilon_{\infty}}{\epsilon_{max}-\epsilon_{\infty}}$ . Incomplete and blurry images were manually excluded from the analysis based on visual examination of corre-

sponding images.

### Contour plots

Contour and density plots were generated for each cell lines data sets using Python gaussian kernel density estimation. For better visualization, one density level was overlaid on scatter plots to indicate region of highest points density. Kernel density plots for each parameter was added right and on top of the graph to represent this parameter distribution.

### Mean recovery curves and fits

For each cell, normalized elongation values of the cell during recovery were imported on Graphpad Prism9 software (GraphPad Software Inc., USA) (with time  $t=0s$  taken as the last image of the cell in the constriction). For each cell lines, mean curves and corresponding 95% confidence interval were plotted. These mean curves were used to fit according to the developed models described in the text and in the Supplementary Information section 7.

### Statistical analysis

All statistical evaluations were conducted using the Graphpad Prism9 software (GraphPad Software Inc., USA). Independent groups were compared using the non-parametric Mann-Whitney test (arrest times, diameters, Young modulus), or Wilcoxon matched-pairs rank test in the case of paired data ( $\epsilon_{max}$  vs  $\epsilon_{\infty}$ ). Significance is reported as the following: \* :  $p \leq 0.05$ , \*\* :  $p \leq 0.005$ , \*\*\* :  $p \leq 0.0005$ , \*\*\*\* :  $p \leq 0.0001$ .

### Western blotting

Cells were collected, lysed with RIPA buffer (RIPA Lysis and Extraction Buffer, Thermo Fischer Scientific) supplemented with Protease and Phosphatase inhibitor cocktail (Halt™ Protease and Phosphatase Inhibitor Cocktail (100X), Thermo Fischer Scientific) and EDTA solution (0.5 M EDTA (100x), Thermo Fischer Scientific), incubated on ice for 5 min, passed through a 1 mL syringe (Terumo) with 25G needle (Terumo) ten times, incubated on ice for another 5 min and centrifuged at 16 000 g for 5 min at 4°C. Equal amounts of the supernatant was then mixed with 2x Laemmli sample buffer (Sigma) and boiled at 95°C for 10 min. Proteins were then separated using sodium dodecyl sulfate polyacrylamide gel electrophoresis (SDS-PAGE, 4%-12% Bis-Tris gel, Life Technologies) and transferred onto a nitrocellulose membrane using dry transfer Trans-blot Turbo Transfer System (Bio-Rad). Membranes were blocked with 5% BSA (Euromedex) in Tris-buffered saline (Interchim) containing 0.1% Tween (Sigma) (TBS-Tween) for 1 h at room temperature, after which primary antibodies diluted in TBS-Tween 5% BSA were added for overnight incubation at 4°C. The membranes were subsequently washed in TBS-Tween after which secondary horseradish peroxidase (HRP) conjugated antibodies were added in 5% BSA in TBS-Tween and incubated for 2 h at room temperature. After extensive washing in TBS-Tween, SuperSignal West Pico PLUS (Thermo Fgischer Scientific) reagent was used and chemiluminescence sig-

nal was recorded on a ChemiDoc Touch 2 Imager (BioRad). The primary antibodies used for p-MLC2 detection were Phospho-Myosin Light Chain 2 (Thr18/Ser19) (polyclonal rabbit, Cell Signaling, #3674S), and for GAPDH - GAPDH (14C10) (monoclonal rabbit, Cell Signaling, #2118S). Secondary antibodies used were Goat anti-Rabbit IgG (H+L), HRP (polyclonal goat, Invitrogen, #65-6120).

### Conflicts of interest

There are no conflicts to declare.

### Author contributions

J.-L.V., H.C., K.T. and C.V. conceived the principle of the presented device. K.T. produced a set of preliminary experiments that form the basis of this paper. E.G. performed all experiments and analysed the data, helped by E.S. and N.A.. E.G. set up the mathematical modeling and conceptual framework of data analysis, while C.V., J.-B. M. and M.P. provided critical feedback. K.V. provided support to E.G. and N.A. regarding pharmacological experiments, immunostaining and immunoblotting. E.G. and C.V. wrote the manuscript. All authors discussed the results and contributed to the final manuscript. C.V. supervised the project and the findings of this work.

### Acknowledgements

This work benefited from the technical contribution of the joint service unit CNRS UAR 3750. The authors would like to thank the engineers of this unit for their advice during the development of the experiments. This work was supported by the European Research Council Advanced Grant 321107 "Cello", the Institut Pierre-Gilles de Gennes ("Investissements d'avenir" program ANR-10-IDEX-0001-02 PSL and ANR-10-LABX-31, and ANR-10-EQPX-34), the ITMO Cancer PCSI 2020 program (grant number 20CP101-00), the ITMO Cancer PCSI 2022 program (grant number 22CP073), JST FOREST Program (Grant Number JP-MJFR212D) and "Ligue Contre le Cancer" for the 4th year PhD funding of Emile Gasser.

### Notes and references

- 1 S. Valastyan and R. A. Weinberg, *Cell*, 2011, **147**, 275–292.
- 2 V. Gensbittel, M. Kräter, S. Harlepp, I. Busnelli, J. Guck and J. G. Goetz, *Developmental cell*, 2021, **56**, 164–179.
- 3 G. P. de Freitas Nader, S. Agüera-Gonzalez, F. Routet, M. Gratia, M. Maurin, V. Cancila, C. Cadart, A. Palamidessi, R. N. Ramos, M. San Roman *et al.*, *Cell*, 2021, **184**, 5230–5246.
- 4 J. Perea Paizal, S. H. Au and C. Bakal, *British Journal of Cancer*, 2021, **124**, 58–65.
- 5 B. L. Krog and M. D. Henry, *Biomechanics in Oncology*, 2018, 209–233.
- 6 A. Labernadie and X. Trepast, *Current opinion in cell biology*, 2018, **54**, 57–65.
- 7 S. Ma, A. Fu, G. G. Y. Chiew and K. Q. Luo, *Cancer letters*, 2017, **388**, 239–248.
- 8 S. Ma, A. Fu, S. Lim, G. G. Y. Chiew and K. Q. Luo, *Free Radical Biology and Medicine*, 2018, **129**, 46–58.
- 9 Y. Xin, K. Li, M. Yang and Y. Tan, *International journal of molecular sciences*, 2020, **21**, 8115.
- 10 K. F. Fuh, R. D. Shepherd, J. S. Withell, B. K. Kooistra and K. D. Rinker, *Breast Cancer Research*, 2021, **23**, 1–17.
- 11 S. K. Dash, B. Patra, V. Sharma, S. K. Das and R. S. Verma, *Lab on a Chip*, 2022.
- 12 J. Lv, Y. Liu, F. Cheng, J. Li, Y. Zhou, T. Zhang, N. Zhou, C. Li, Z. Wang, L. Ma *et al.*, *The EMBO journal*, 2021, **40**, e106123.
- 13 I. MacDonald, S. Aharinejad, E. Schmidt and A. Groom, *Microvascular research*, 1995, **49**, 64–77.
- 14 L. Ding, M. Sunamura, T. Kodama, J. Yamauchi, D. Duda, H. Shimamura, K. Shibuya, K. Takeda and S. Matsuno, *British journal of cancer*, 2001, **85**, 431–438.

- 15 A. S. Azevedo, G. Follain, S. Patthabhiraman, S. Harlepp and J. G. Goetz, *Cell adhesion & migration*, 2015, **9**, 345–356.
- 16 P. Vargas, E. Terriac, A.-M. Lennon-Duménil and M. Piel, *JoVE (Journal of Visualized Experiments)*, 2014, e51099.
- 17 P. M. Davidson, J. Sliz, P. Isermann, C. Denais and J. Lammerding, *Integrative Biology*, 2015, **7**, 1534–1546.
- 18 P. Preira, T. Leoni, M.-P. Valignat, A. Lellouch, P. Robert, J.-M. Forel, L. Papazian, G. Dumenil, P. Bongrand and O. Théodoly, *International journal of nanotechnology*, 2012, **9**, 529–547.
- 19 S. H. Au, B. D. Storey, J. C. Moore, Q. Tang, Y.-L. Chen, S. Javaid, A. F. Sarioglu, R. Sullivan, M. W. Madden, R. O'Keefe, D. A. Haber, S. Maheswaran, D. M. Langenau, S. L. Stott and M. Toner, *Proceedings of the National Academy of Sciences*, 2016, **113**, 4947–4952.
- 20 B. Nath, A. Raza, V. Sethi, A. Dalal, S. S. Ghosh and G. Biswas, *Scientific reports*, 2018, **8**, 1–10.
- 21 H. Chen, J. Guo, F. Bian and Y. Zhao, *Smart Medicine*, 2022, **1**, e20220001.
- 22 H. A. Cognart, J.-L. Viovy and C. Villard, *Scientific reports*, 2020, **10**, 1–14.
- 23 N. Kamyabi, Z. S. Khan and S. A. Vanapalli, *Cellular and molecular bioengineering*, 2017, **10**, 563–576.
- 24 Z. Yan, X. Xia, W. C. Cho, D. W. Au, X. Shao, C. Fang, Y. Tian and Y. Lin, *Advanced Healthcare Materials*, 2022, **11**, year.
- 25 C. M. Peppiatt, C. Howarth, P. Mobbs and D. Attwell, *Nature*, 2006, **443**, 700–704.
- 26 S. Grubb, C. Cai, B. O. Hald, L. Khenouf, R. P. Murmu, A. G. Jensen, J. Fordsmann, S. Zambach and M. Lauritzen, *Nature communications*, 2020, **11**, 1–12.
- 27 X. Wang, M. Hossain, A. Bogoslawski, P. Kubes and D. Irimia, *Nature communications*, 2020, **11**, 1–12.
- 28 B. Müller, S. Lang, M. Dominietto, M. Rudin, G. Schulz, H. Deyhle, M. Germann, F. Pfeiffer, C. David and T. Weitkamp, *Developments in X-ray Tomography VI*, 2008, pp. 89–98.
- 29 K. Terao, M. Gel, A. Okonogi, A. Fuke, T. Okitsu, T. Tada, T. Suzuki, S. Nagamatsu, M. Washizu and H. Kotera, *Scientific Reports*, 2014, **4**, 4123.
- 30 G. Follain, N. Osmani, A. S. Azevedo, G. Allio, L. Mercier, M. A. Karreman, G. Solecki, M. J. G. León, O. Lefebvre, N. Fekonja *et al.*, *Developmental cell*, 2018, **45**, 33–52.
- 31 E. Evans and A. Yeung, *Biophysical Journal*, 1989, **56**, 151–160.
- 32 J. Dupire, P. H. Puech, E. Helfer and A. Viallat, *Proceedings of the National Academy of Sciences of the United States of America*, 2020, **117**, 14798–14804.
- 33 K. Tsujita, R. Satow, S. Asada, Y. Nakamura, L. Arnes, K. Sako, Y. Fujita, K. Fukami and T. Itoh, *Nature Communications*, 2021, **12**, 5930.
- 34 D. G. Hicks and S. Kulkarni, *American journal of clinical pathology*, 2008, **129**, 263–273.
- 35 X. Dai, H. Cheng, Z. Bai and J. Li, *Journal of Cancer*, 2017, **8**, 3131–3141.
- 36 S. Byun, S. Son, D. Amodei, N. Cermak, J. Shaw, J. H. Kang, V. C. Hecht, M. M. Winslow, T. Jacks, P. Mallick and S. R. Manalis, *Proceedings of the National Academy of Sciences of the United States of America*, 2013, **110**, 7580–7585.
- 37 H. W. Hou, Q. S. Li, G. Y. H. Lee, A. P. Kumar, C. N. Ong and C. T. Lim, *Biomedical Microdevices*, 2009, **11**, 557–564.
- 38 C. Jebane, A.-A. Varlet, M. Karnat, L. M. Hernandez-Cedillo, A. Lecchi, F. Bedu, C. Desgras, C. Vigouroux, M.-C. Vantyghe, A. Viallat *et al.*, *bioRxiv*, 2022.
- 39 M. Urbanska, H. E. Muñoz, J. Shaw Bagnall, O. Otto, S. R. Manalis, D. Di Carlo and J. Guck, *Nature Methods*, 2020, **17**, 587–593.
- 40 L. Pang, S. Shen, C. Ma, T. Ma, R. Zhang, C. Tian, L. Zhao, W. Liu and J. Wang, *Analyst*, 2015, **140**, 7335–7346.
- 41 Y.-N. Chang, Y. Liang, W. Gu, J. Wang, Y. Qin, K. Chen, J. Li, X. Bai, J. Zhang and G. Xing, *ACS omega*, 2019, **4**, 8318–8323.
- 42 Y. Feng, H. Chai, W. He, F. Liang, Z. Cheng and W. Wang, *Small Methods*, 2022, **6**, 2200325.
- 43 C. Alibert, B. Goud and J. B. Manneville, *Biology of the Cell*, 2017, **109**, 167–189.
- 44 P. M. Davidson, G. R. Fedorchak, S. Mondésert-Deveraux, E. S. Bell, P. Isermann, D. Aubry, R. Allena and J. Lammerding, *Lab on a Chip*, 2019, **19**, 3652–3663.
- 45 S. Hu, R. Wang, C. M. Tsang, S. W. Tsao, D. Sun and R. H. Lam, *RSC advances*, 2018, **8**, 1030–1038.
- 46 A. Bonfanti, J. L. Kaplan, G. Charras and A. Kabla, *Soft Matter*, 2020, **16**, 6002–6020.
- 47 N. Desprat, A. Richert, J. Simeon and A. Asnacios, *Biophysical journal*, 2005, **88**, 2224–2233.
- 48 G. T. Charras, M. Coughlin, T. J. Mitchison and L. Mahadevan, *Biophysical journal*, 2008, **94**, 1836–1853.
- 49 S. Kwon, S. Han and K. Kim, *Oncology Reports*, 2023, **50**, 200.
- 50 L. Venkova, A. S. Vishen, S. Lembo, N. Srivastava, B. Duchamp, A. Ruppel, A. Williart, S. Vassilopoulos, A. Deslys, J. M. Garcia Arcos, A. Diz-Muñoz, M. Balland, J. F. Joanny, D. Cuvelier, P. Sens and M. Piel, *eLife*, 2022, **11**, 1–41.
- 51 U. Baran, L. Shi and R. K. Wang, *Journal of biophotonics*, 2015, **8**, 46–51.
- 52 K. Hosseini, A. Frenzel and E. Fischer-Friedrich, *Biophysical Journal*, 2021, **120**, 3516–3526.
- 53 J. Prost, F. Jülicher and J.-F. Joanny, *Nature physics*, 2015, **11**, 111–117.
- 54 A. X. Cartagena-Rivera, J. S. Logue, C. M. Waterman and R. S. Chadwick, *Biophysical journal*, 2016, **110**, 2528–2539.
- 55 M. I. Arjona, J. Najafi and N. Minc, *Current Opinion in Cell Biology*, 2023, **85**, 102278.

- 56 P. A. Pullarkat, P. A. Fernández and A. Ott, *Physics Reports*, 2007, **449**, 29–53.
- 57 N. Bonakdar, R. Gerum, M. Kuhn, M. SpÄurrer, A. Lippert, W. Schneider, K. E. Aifantis and B. Fabry, *Nature Materials*, 2016, **15**, 1090–1094.
- 58 M. Tabatabaei, M. Tafazzoli-Shadpour and M. M. Khani, *Biorheology*, 2019, **56**, 207–219.
- 59 J. Guck, S. Schinkinger, B. Lincoln, F. Wottawah, S. Ebert, M. Romeyke, D. Lenz, H. M. Erickson, R. Ananthakrishnan, D. Mitchell, J. Kas, S. Ulvick and C. Bilby, *Biophysical Journal*, 2005, **88**, 3689–3698.
- 60 L. Hanin, *Journal of Theoretical Biology*, 2023, **572**, 111582.
- 61 Y. Nematbakhsh, K. T. Pang and C. T. Lim, *Convergent Science Physical Oncology*, 2017, **3**, 034003.
- 62 C. J. Chan, A. E. Ekpenyong, S. Golfier, W. Li, K. J. Chalut, O. Otto, J. Elgeti, J. Guck and F. Lautenschläger, *Biophysical Journal*, 2015, **108**, 1856–1869.
- 63 X. Zhang and Y. Lv, *Biochimica et Biophysica Acta (BBA)-Molecular Cell Research*, 2017, **1864**, 2272–2282.
- 64 M. S. Tretyakova, M. E. Menyailo, A. A. Schegoleva, U. A. Bokova, I. V. Larionova and E. V. Denisov, *International Journal of Molecular Sciences*, 2022, **23**, 15979.
- 65 Y. Shimada, T. Sudo, S. Akamatsu, T. Sunada, A. Myomoto, K. Okano and K. Shimizu, *Journal of Personalized Medicine*, 2022, **12**, 666.
- 66 J.-Y. Tinevez, N. Perry, J. Schindelin, G. M. Hoopes, G. D. Reynolds, E. Laplantine, S. Y. Bednarek, S. L. Shorte and K. W. Eliceiri, *Methods*, 2017, **115**, 80–90.

Supplementary information

1 - Effective radius of the constrictions

The equations used to derive rheological parameters<sup>1</sup> have been established in the case of a cylindrical pipette of radius  $R$ . To be applied to the rectangular constriction of the Pachinko microfluidic device,  $R$  needs to be replaced with an effective radius  $R_{eff}$  that is a function of the constriction width  $w$  and height  $h$ . Referring to the theory for rectangular channels established in<sup>2</sup>, the expression for  $R_{eff}$  is given by:

$$R_{eff}^4 = \frac{2}{\pi} \frac{w \times h^3}{(1 + h/w)^2 \times g^*(h/w)} \quad (1)$$

with  $g^*$  a dimensionless function of the form

$$g^*(x) = \left[ \left(1 + \frac{1}{x}\right)^2 \left(1 - \frac{192}{\pi^5 x} \sum_{i=1,3,5}^{\infty} \frac{\tanh\left(\frac{\pi}{2}ix\right)}{i^5}\right) \right]^{-1} \quad (2)$$

With  $w = 6\mu\text{m}$  the width and  $h = 15\mu\text{m}$  the height of the rectangular channel, applying Eq.1 and Eq.2 yields  $R_{eff} = 6.27\mu\text{m}$ .

2 - Profile of the constrictions

Upon fabrication of the wafer molds, the height of structures were checked using a mechanical profilometer (dektak 6M, Veeco). We also used an optical profilometer (NT9100, Veeco) to obtain 3D imaging of constrictions (Fig. S1a-b). Diffraction during exposure limits the achievable resolution of structures obtained with photolithography. The actual width of the constriction ranges from  $\approx 5\mu\text{m}$  at the top to  $\approx 7\mu\text{m}$  at the bottom of the structure. We consider this distribution to be acceptable, and will refer to the constriction as a rectangle of  $6\mu\text{m}$  width. These results were confirmed by the observation of the structures in the PDMS chip by scanning electron microscopy.

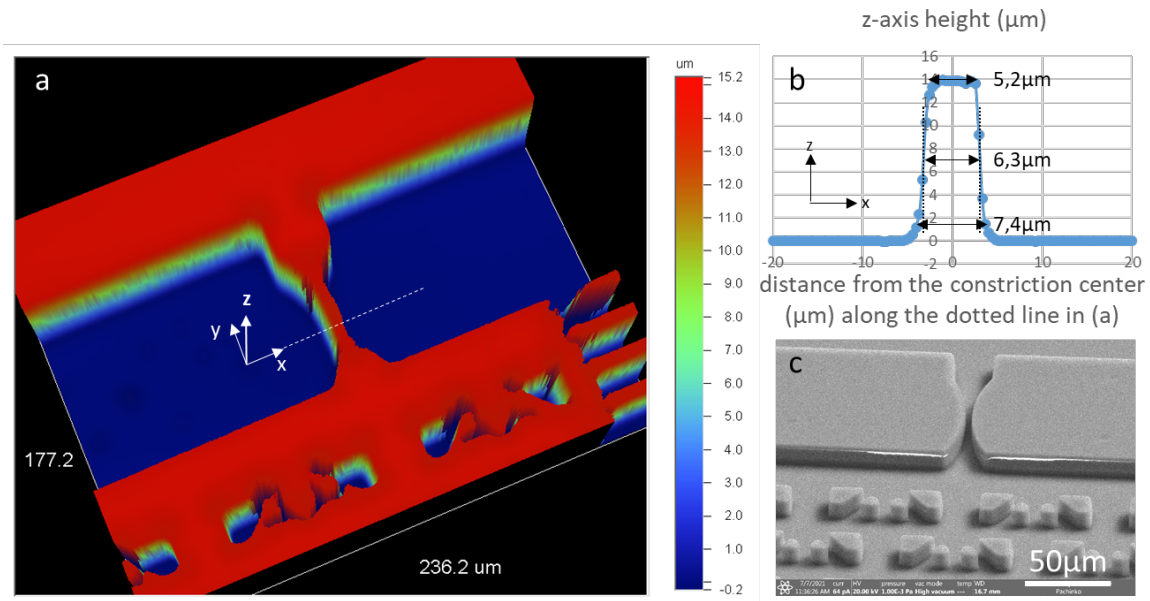


Figure S1 - Detail of a constriction a) 3D visualisation of a constriction height measured on the wafer used to produce the microfluidic chips, using an optical profilometer (NT9100, Veeco). b) Detail of the profile of the cross-section of a constriction at its narrowest point. Due to photolithography limitations, constriction width ranges from  $7\mu\text{m}$  at the base to  $5\mu\text{m}$  at the top. Thus for simplification, the constriction was considered as a rectangle of  $6\mu\text{m}$  width. c) Scanning Electron Microscopy view of the constriction and single cell nests trap chamber, taken on a PDMS chip before bonding to the fluorodish.

3 - Numerical simulations

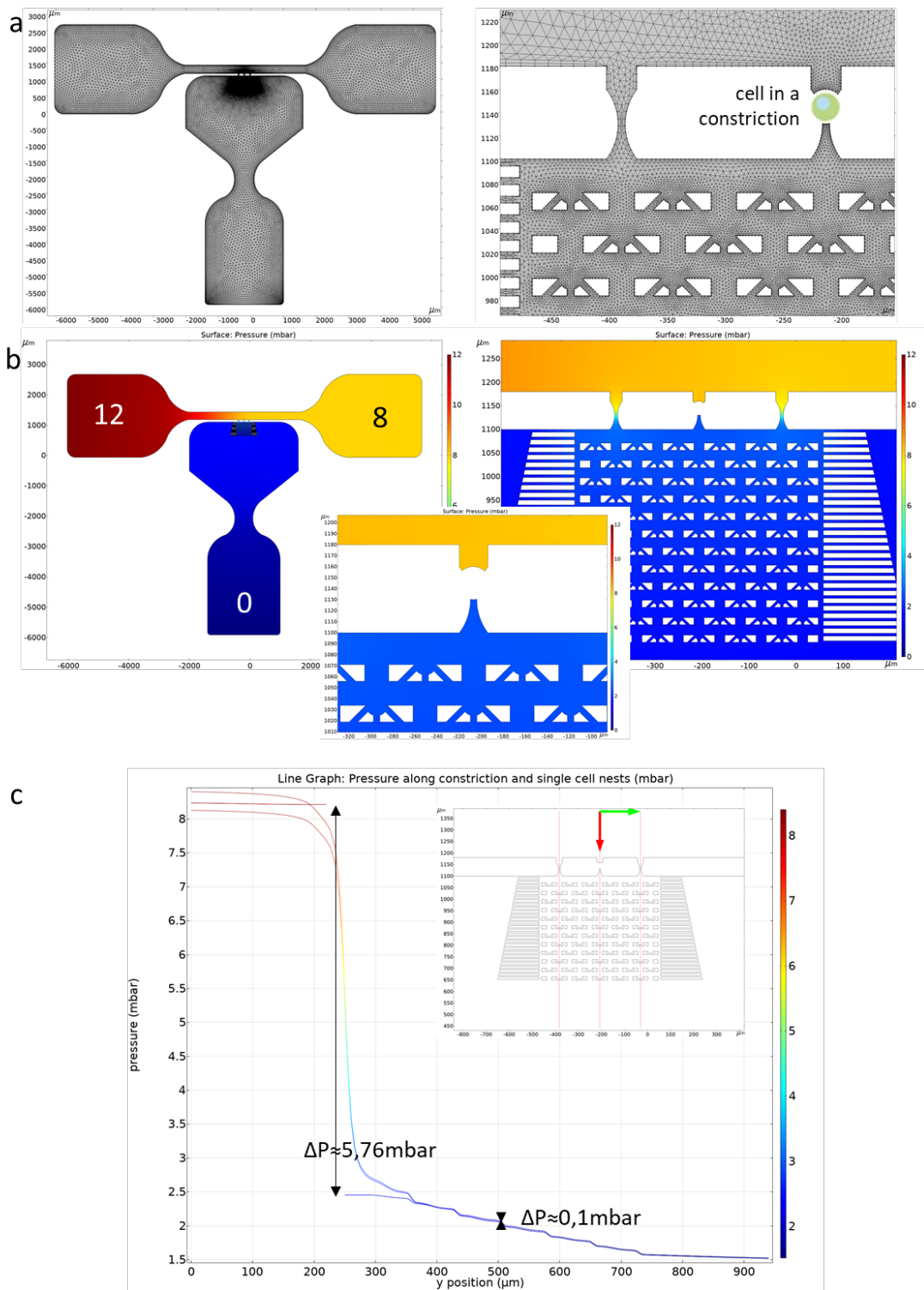


Figure S2 - Numerical simulations performed on the Pachinko device. a) Representation of the mesh used for finite elements calculations. Meshing was refined close to the constriction and single cell nests (minimal element size was set to  $0.172 \mu\text{m}$ ). b) Representation of the pressure profile within the device. Inlet 1, outlets 2 and 3 pressure were set respectively to 12, 8 and 0 mbar. Most of the pressure drop is located on the constrictions. The shallow channel approximation was used to take into account the effect of the channel height on the pressure profile. c) The middle constriction was closed to mimic the effect of a cell within a constriction. The resulting pressure differences applied between the front and back of the cell is approximately  $\Delta P_h \approx 5.76 \text{ mbar}$ . Residual pressure drop located in the single cell nests is  $\approx 0.1 \text{ mbar}$ , and thus can be neglected in front of the pressure drop applied within the constriction.

## 2. Paper draft "Deformation under flow and morphological recovery of breast cancer cells"

Table S2 - Pressure Differences  $\Delta P$  as a function of the possible configurations of constrictions occupancy by cells. Values are obtained through numerical simulations with Comsol (see Fig.S2). The plot for the configuration "1 cell in the middle constriction" is represented on Fig.S2c. Experimentally we observed that in average only one constriction was used at the same time, for calculations purposes we'll then use  $\Delta P = 6 \pm 0.25$  mbar.

$\Delta P$ in constriction	Left	Middle	Right
Nb cells in constrictions			
1 cell	6.19mbar	open	open
	open	5.76mbar	open
	open	open	5.86mbar
2 cells	open	7.35mbar	7.46mbar
	7.50mbar	open	7.22mbar
	7.80mbar	7.40mbar	open
3 cells	10.15mbar	10.0mbar	9.88mbar

### 4 - Membrane curvature-induced pressure differences

As the cell membrane is being curved in the constriction, a pressure difference  $\Delta P_c$  is created which opposes cell deformation and counteracts the hydrostatic pressure difference  $\Delta P_h$ . Laplace law defines the relation between the inside and outside pressures around a curved membrane as:

$$\Delta P = P_{inside} - P_{outside} = \tau_0 \left( \frac{1}{R_1} + \frac{1}{R_2} \right)$$

where  $\tau_0$  is the membrane tension, and  $R_1$  and  $R_2$  are the principal curvature radii. We apply this relation at the back and front of the cell:

$$\Delta P^{back} = P_{inside} - P_{outside}^{back} = \tau_0 \left( \frac{1}{R_{back}} + \frac{1}{R_h} \right) \text{ and } \Delta P^{front} = P_{inside} - P_{outside}^{front} = \tau_0 \left( \frac{1}{R_{front}} + \frac{1}{R_h} \right)$$

where  $R_{back}$  and  $R_{front}$  are the radii of the back and front radii of the cell in an horizontal plane, and  $R_h$  the inverse of the vertical curvature defined between the floor and ceiling of the microchannel of height  $h$ . We define the resulting pressure difference created by the membrane curvatures  $\Delta P_c$  as<sup>3,4</sup>:

$$\Delta P_c = P_{outside}^{back} - P_{outside}^{front} = \tau_0 \left( \frac{1}{R_{front}} - \frac{1}{R_{back}} \right)$$

Tsujita and al. gives values of cortical tensions ranging from  $\approx 50$  pN/ $\mu\text{m}$  for MDA-MB-231 cells to  $\approx 100$  pN/ $\mu\text{m}$  for MCF-7 cells<sup>5</sup>. We take an estimate of  $\tau_0 \approx 50$  pN/ $\mu\text{m}$  for the following calculations. We found that  $\Delta P_c \approx 0.05$  mbar at the cell entry and decreases as the cell progresses in the constriction (Fig.S3). Thus we can neglect in the following the pressure difference induced by membrane curvature and consider that cells experience in the constriction a hydrostatic pressure drop of  $\Delta P_h \approx 6$  mbar. In fact,  $\Delta P_c$  represents the minimal pressure required for the cell to enter the constriction. Slowly increasing the pressure to determine the pressure threshold required for the cell to enter the constriction would result in a measure of the cell cortical tension  $\tau_0$ .

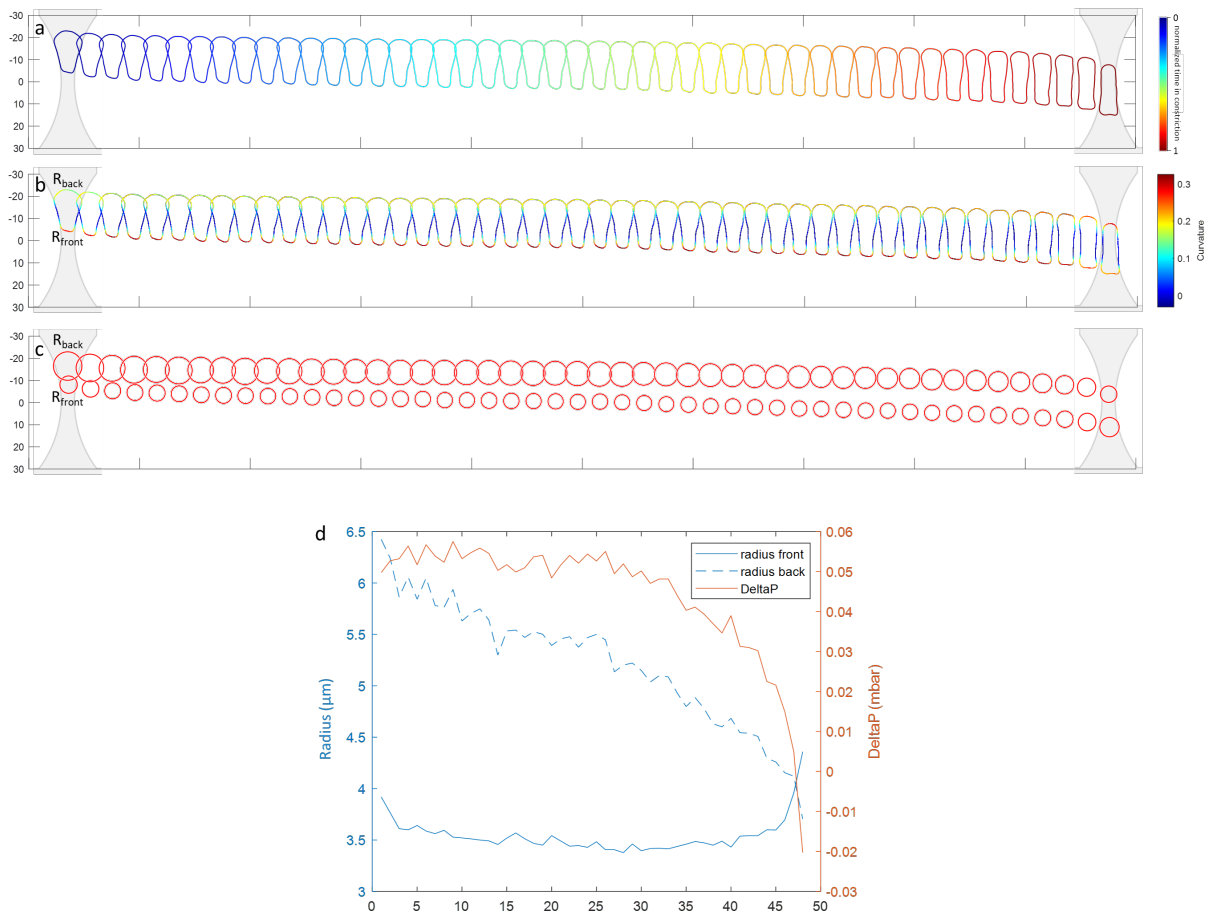


Figure S3 - Evolution of the cell shape as it crosses the constriction and of the pressure difference induced by membrane curvature. a) Outline of the cell presented Fig.2 and Fig.4b as it goes through the constriction. Each image represented here is separated by 20ms. b) The radius of curvature was calculated for each point of the cell outline, using the code developed in Driscoll et al.<sup>6</sup>. The color map represents the curvature  $C = 1/R$  in  $\mu m^{-1}$ . c) Drawing of the front and back curvature radius. The front (resp. back) of the cell was defined as the 10% of the points with the highest (resp. lowest) y-coordinate in the shape outline. Mean over these points was used to determine front and back radii of the cell. d) Front and back radii were plotted as the cell progresses through the constriction (x-axis is the index of the image of the cell represented above). The resulting pressure difference  $\Delta P_c$  induced by membrane curvature is represented on the right y-axis.

## 5 - Cell diameters

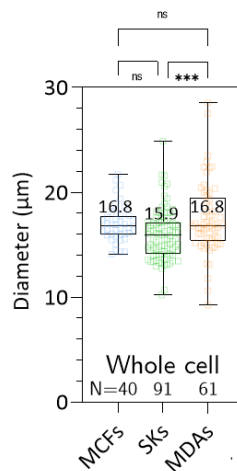


Figure S4 - Cell diameters. The median value is given for each cell line. Interestingly, SK-BR-3 are slightly smaller than the other two cell lines.

## 6 - Scatter and contour plots

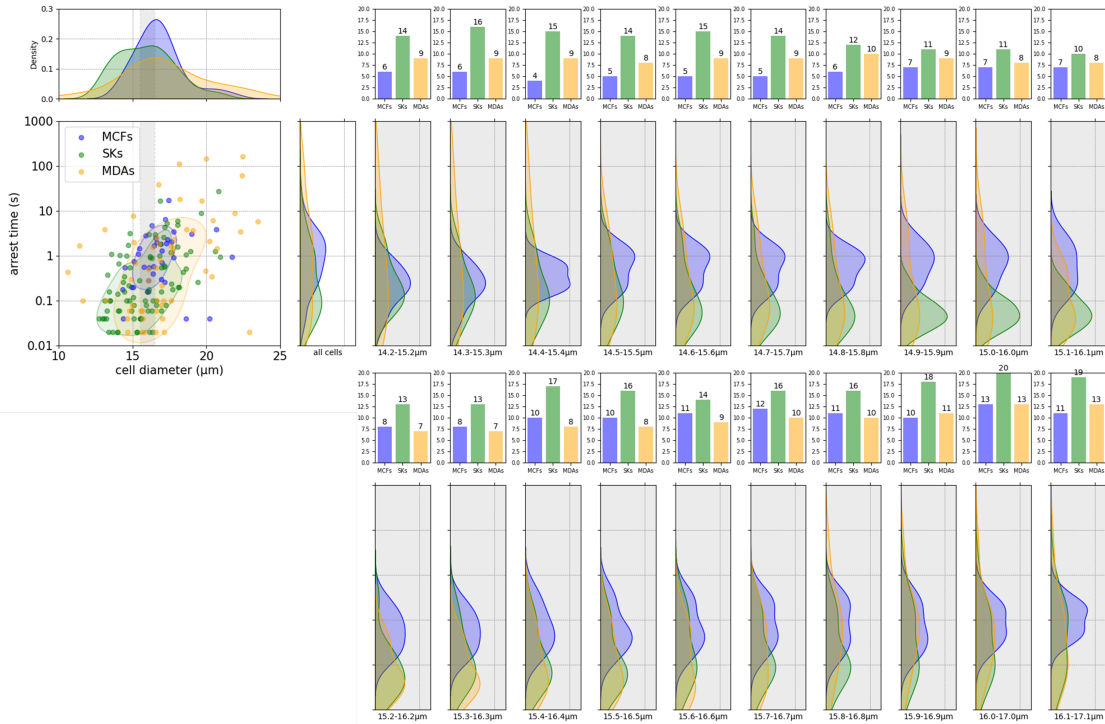


Figure S5 - Scatter plot of arrest time in MCF-7, SK-BR-3 and MDA-MB-231 cell lines. To compare between cell lines independently of size effects, density plots were sampled on a sliding bin of size 1 $\mu$ m.

## 7 - Comparison of fits

The normalized deformation data were fit successively with one, two, and three phase decays fits in order to determine the number of exponential decays to be considered. The corresponding fit equations in GraphPad Prism were the following:

- One Phase Decay:  

$$Y = (Y_0 - \text{Plateau}) * \exp(-X/\text{Tau}) + \text{Plateau}$$
- Two Phase Decay:  

$$\text{SpanFast} = (Y_0 - \text{Plateau}) * \text{PercentFast} * .01$$

$$\text{SpanSlow} = (Y_0 - \text{Plateau}) * (100 - \text{PercentFast}) * .01$$

$$Y = \text{Plateau} + \text{SpanFast} * \exp(-X/\text{TauFast}) + \text{SpanSlow} * \exp(-X/\text{TauSlow})$$
- Three Phase Decay:  

$$Y_{\text{Fast}} = (Y_0 - \text{Plateau}) * \text{PercentFast} * .01 * \exp(-X/\text{TauFast})$$

$$Y_{\text{Slow}} = (Y_0 - \text{Plateau}) * \text{PercentSlow} * .01 * \exp(-X/\text{TauSlow})$$

$$Y_{\text{Medium}} = (Y_0 - \text{Plateau}) * (100 - \text{PercentFast} - \text{PercentSlow}) * .01 * \exp(-X/\text{TauMedium})$$

$$Y = \text{Plateau} + Y_{\text{Fast}} + Y_{\text{Medium}} + Y_{\text{Slow}}$$

Alternatively, a power law fit was considered.

- Power Law:  

$$Y = (X/X_0)^{-n} + C$$

We determined that three phase decay was the best fit to represent the recovery. Addition of more exponential did not increase the quality of the fit, as the software was unable to compute a fourth characteristic time. From the parameters computed here ( $Y_0$ , Plateau, PercentFast, TauFast, PercentSlow, TauSlow, PercentMedium, TauMedium), we define as presented in the main text as the following:

- % slow =  $(\text{PercentSlow}) * (Y_0 - \text{Plateau})$
- % medium =  $(100 - \text{PercentFast} - \text{PercentSlow}) * (Y_0 - \text{Plateau})$
- $\Phi_{VE} = (\% \text{ slow} + \% \text{ medium})$

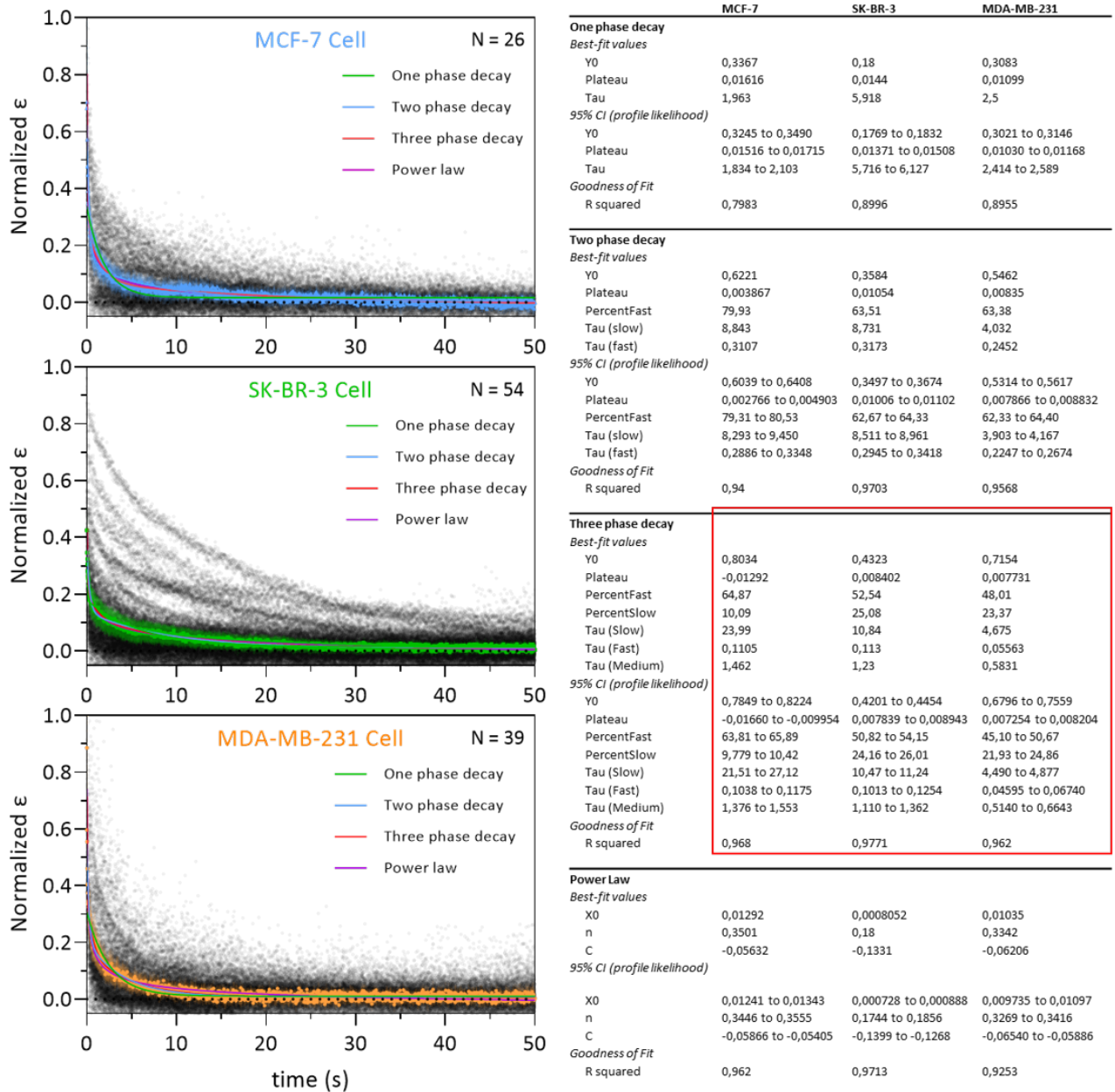


Figure S6 - Fitting of whole cell shape recovery after deformation. For each cell line, the fitting curves obtained with one, two and three phase decays, as well as the fitting curve obtained with the power law were overlaid on the individual cells data points. The parameters obtained for each line are reported in the table on the right. Parameters used in Table 2 are boxed in red.

8 - Treatment of MDA-MB-231 cells with cytoskeletal drugs

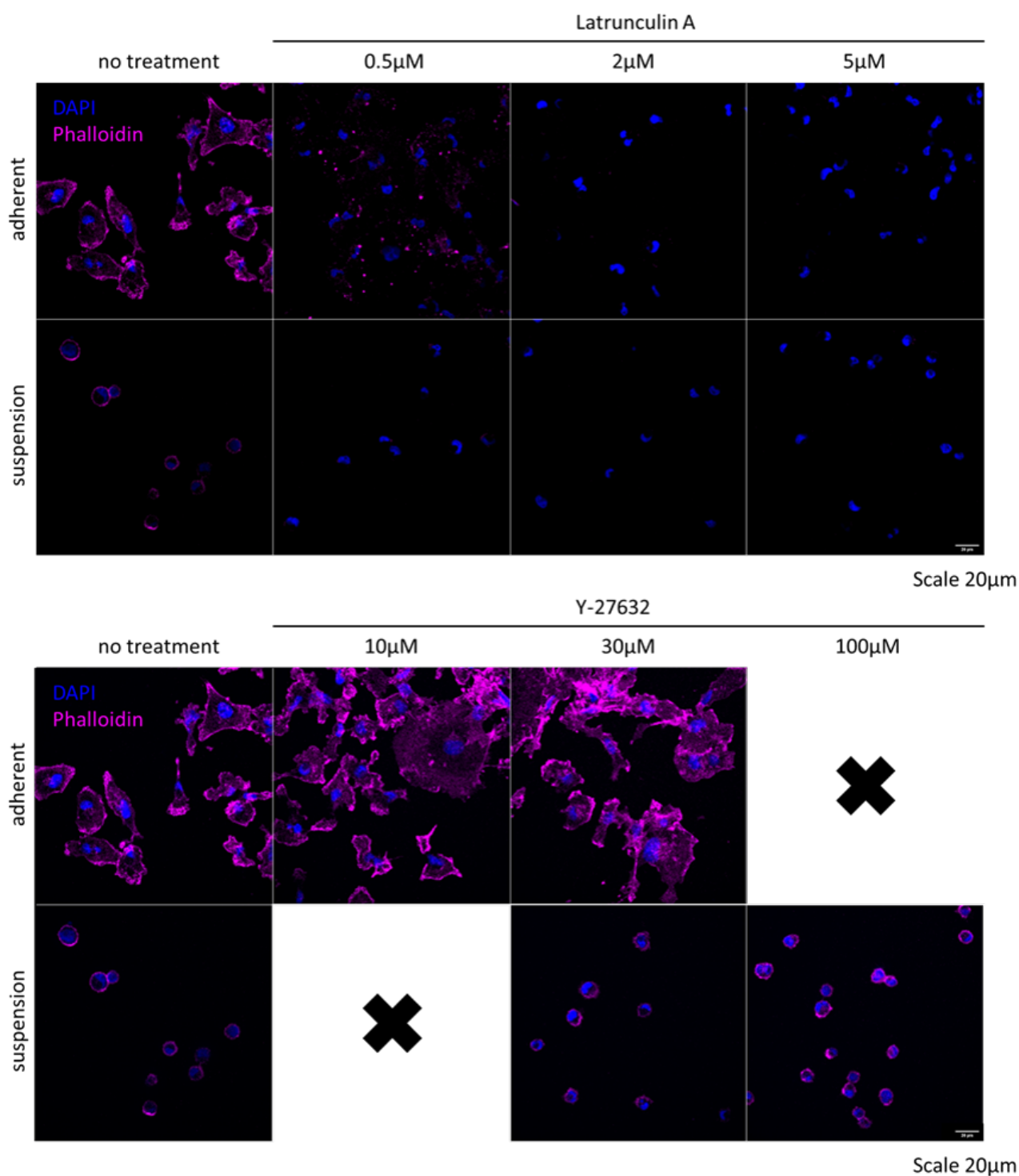


Figure S7 - Treatment of MDA-MB-231 cells with Latrunculin A and Y27632. (top) Treatment with 0.5, 2 and 5 μM LatrunculinA. 0.5 μM was selected as it induced depolymerisation of the actin cytoskeleton in both adherent and suspension conditions. (bottom) Treatment with 10, 30 and 100 μM Y27632. A concentration of 30 μM was selected as it increased adherent cells spreading (a proxy for diminution in contractility and thus acto-myosin activity).

9 - Comparison of the recovery dynamics of MDA-MB-231 cells after passing through 6x15 and 9x9  $\mu\text{m}^2$  constrictions

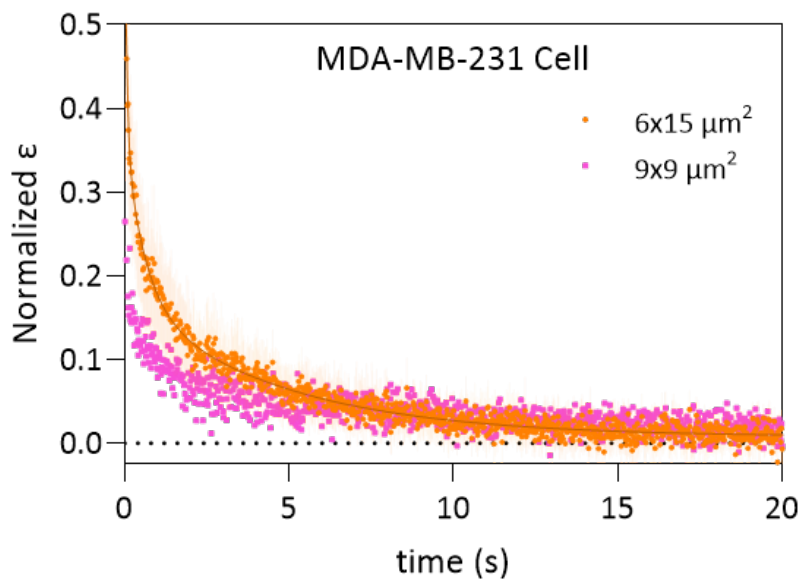


Figure S8 - Recovery of a MDA-MB-231 cell deformed in a square 9x9  $\mu\text{m}^2$  constriction. Elastic recovery is also present in isotropic square constrictions 9x9  $\mu\text{m}^2$  of similar section area as 6x15  $\mu\text{m}^2$  constrictions.

10 - Arrest time of MDA-MB-231 cells submitted to Y-27 and LatA

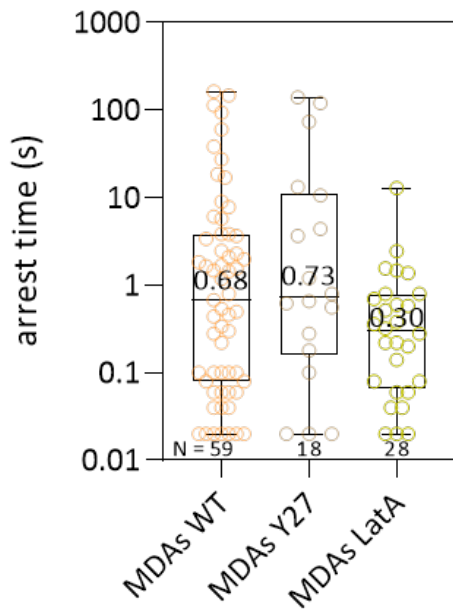


Figure S9 - Box plot of arrest time distribution of WT, Y-27 30  $\mu\text{M}$  and LatA 0.5  $\mu\text{M}$  treated MDA-MB-231 cells. Displayed value represents the median.

## 2. Paper draft "Deformation under flow and morphological recovery of breast cancer cells"

## 11 - Expression levels of p-MLC2 by Western blot

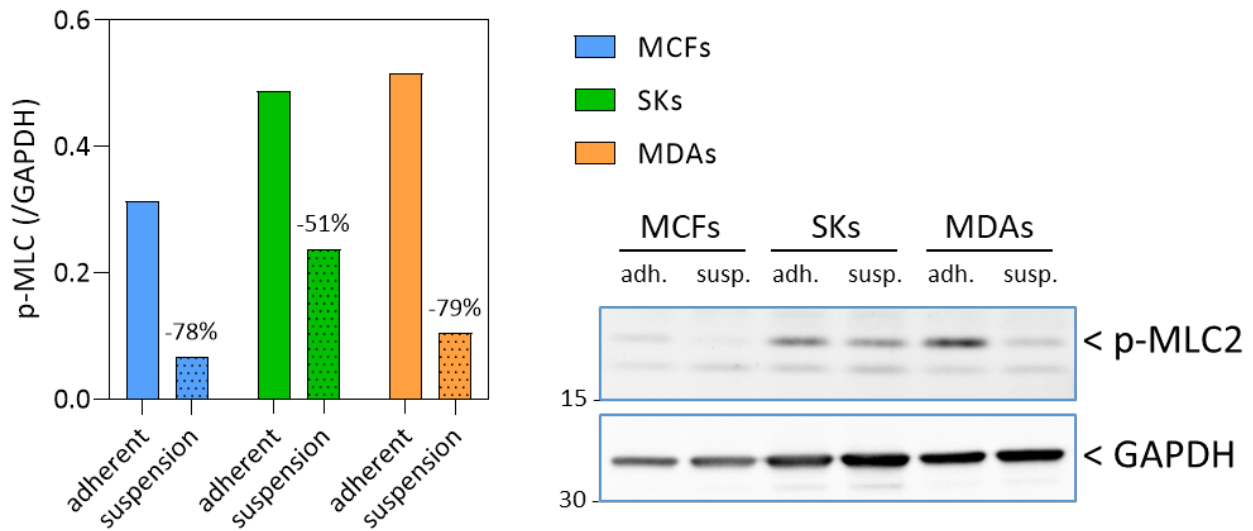


Figure S10 - Western Blots for p-MLC2 (phospho-Myosin Light Chain 2). Adherent (adh.) cells were lysed in the culture dish, while suspended (susp.) cells were lysed 30min after harvesting.

## 12-14 - Raw data files

These files correspond to Fig. 3 and Fig.6c (Supp.12, Data Cells.xlsx), Fig. 5 (Supp. 13, Data Deformation.xlsx) and Fig. 6d (Supp. 14, Data Recovery.xlsx).

## Notes and references

- 1 P. M. Davidson, G. R. Fedorchak, S. Mondésert-Deveraux, E. S. Bell, P. Isermann, D. Aubry, R. Allena and J. Lammerding, *Lab on a Chip*, 2019, **19**, 3652–3663.
- 2 Y. Son, *Polymer*, 2007, **48**, 632–637.
- 3 E. Evans and A. Yeung, *Biophysical Journal*, 1989, **56**, 151–160.
- 4 J. Dupire, P. H. Puech, E. Helfer and A. Viallat, *Proceedings of the National Academy of Sciences of the United States of America*, 2020, **117**, 14798–14804.
- 5 K. Tsujita, R. Satow, S. Asada, Y. Nakamura, L. Arnes, K. Sako, Y. Fujita, K. Fukami and T. Itoh, *Nature Communications*, 2021, **12**, 5930.
- 6 M. K. Driscoll, C. McCann, R. Kopace, T. Homan, J. T. Fourkas, C. Parent and W. Losert, *PLoS Computational Biology*, 2012, **8**, e1002392.

### 3 Comments on the paper

#### 3.1 Analysis workflow

The analysis performed in the paper to extract information from the images is described in the workflow displayed in Fig.2.2.

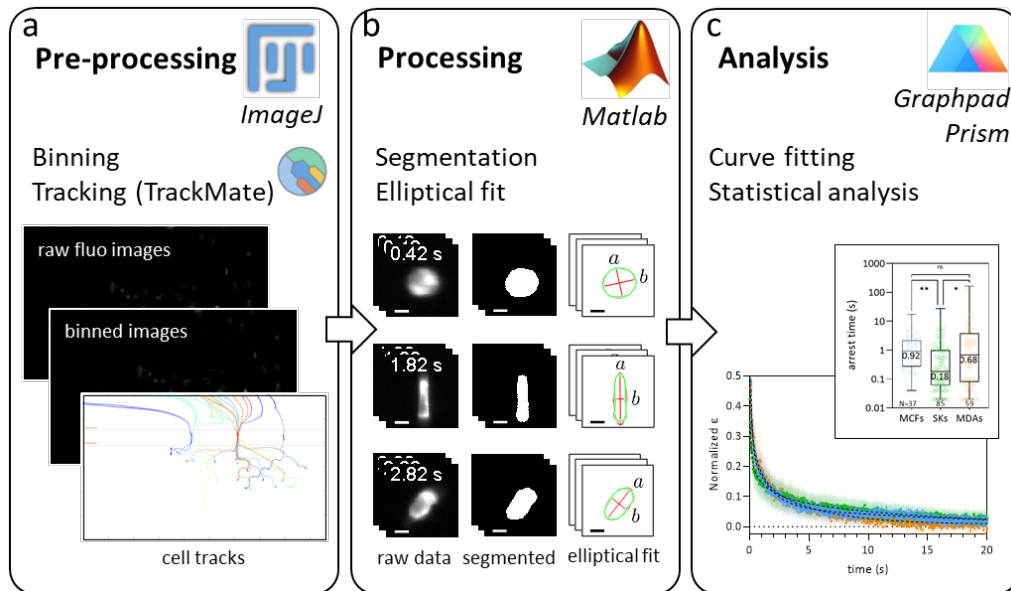


**Figure 2.2** – Data analysis workflow. (a) Binning and tracks reconstruction were performed using ImageJ. (b) Analysis of individual tracks were conducted in Matlab. For each cell at each time point, the cell was segmented and the shape was fitted with an ellipse. Maximal deformation and final deformation were measured and used for normalization. (c) Normalized curves were fitted in Graphpad Prism, and statistical analysis were performed.

Each set of experiments consists of several sequences of a few cells entering the constrictions and the trap chamber. At the end of each sequence, the trap chamber is emptied by increasing the pressure in outlet 3, and a new sequence can be acquired (within a 1 hour window from cell detachment).

**ImageJ :** First step of the analysis is the reconstruction of tracks with the ImageJ plugin TrackMate [Tinevez, 2017] (see Fig.2.2a). The sequences of images recorded were binned by a factor 4, with two aims :

- To reduce the overall memory size and computation times, as all images must be imported into ImageJ memory for tracks reconstruction. A typical sequence of 3 minutes at 50 fps acquisition rate consists of 9000 images of 2.2 Mo; the total amounts to  $\approx 20$  Go which exceeds available memory. Binning in each direction by a factor 4 decreases the size by 16, so that each sequences amounts to  $\approx 1$  Go.
- To act as a filter to reduce background noise and improve cell detection.

Reconstructed tracks need to be manually verified and corrected, as Trackmate reconstruction

algorithm may exchange cells if the two of them come too close to each other. This verification step is the more time consuming, though less than a fully manual tracking.

**Matlab :** The resulting tracks (i.e. positions of each cell in each frame) are imported into Matlab to be analysed. For each cell, movies of a  $100 \times 100$  pixel<sup>2</sup> region centered around the cell as it moves through the device are generated. For each frame, the region is segmented using Otsu’s method [Otsu, 1979] (a two-levels threshold is used to account for heterogeneity in the cell staining, see below). The resulting shape characteristics (area, elliptical fit and related parameters, see section below) are extracted and saved (see Fig.2.2b). Based on movie evaluations, some points are excluded if the segmentation failed (mainly if two cells are touching each other, or when the cells moves extremely rapidly as it enters and/or exits the constriction which results in blurriness). In Matlab we also extract the initial diameter of the cell  $a_0$ , its maximal length  $a_{max}$  and its length after 50 s of recovery  $a_\infty$ . We use these values to define the normalized deformation  $\varepsilon_{Norm}$  that will be then fitted in Graphpad Prism.

Matlab analysis has been implemented as an app that can be shared to other users to analyse data generated in Pachinko experiments. The app has been tested and used by interns and collaborators in the team. In annex B, we include relevant parts of the code used in the app.

**Graphpad prism :** Data analysis was performed in Graphpad Prism. Normalized deformation curves and other parameters were imported. Curves were fitted with the appropriate model in order to extract the parameters. Statistical analysis were performed on other parameters (arrest time, maximal deformation, etc...)

### 3.2 About segmentation

Membrane staining with DIL appear heterogeneous, with regions of higher or lower intensity. Thus, we observed that usual segmentation with a single intensity threshold tends to underevaluate the range of the cell, making it appear smaller than it really is. To overcome this problem, we then turned to a 2-thresholds segmentation (see Fig.2.3a), thus separating the images into three regions : background, low an high intensity (see intensity histogram in Fig.2.3b). We then merged the low and high intensity regions to recreate the shape of the cell, as it can be appreciated in Fig.2.3c.

### 3.3 About shape descriptors

To quantify the deformation, many shape descriptors are available, either based on the shape itself (circularity, solidity, Feret diameters) or its elliptical fit (major  $a$  and minor  $b$  axis, and their combinations). The choice of a descriptor can impact the interpretation of experiments [Fregin, 2022]. We made in the paper the choice of two descriptors based on the elliptical fit : the elongation along the main axis  $\varepsilon = \frac{a-a_0}{a_0}$ , and the aspect ratio  $AR = \frac{a}{b}$ . Though we started using the aspect ratio for its intuitive nature and easiness of understanding, we ended up selecting the elongation  $\varepsilon$  for the analysis. The reasons of this choice are :

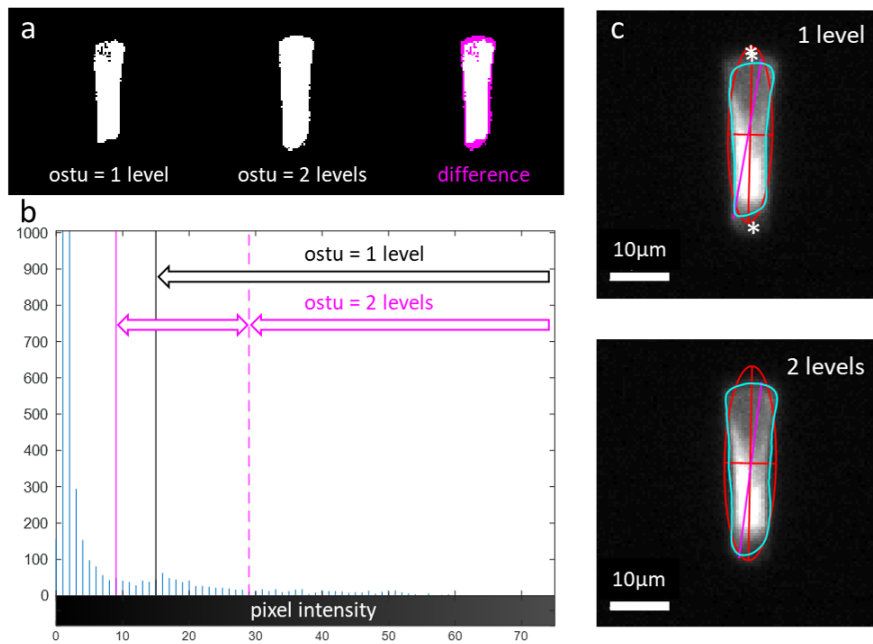


**Figure 2.3** – Segmentation (a) Different segmentation using 1 or 2 thresholds for Otsu’s method (b) Histogram of pixel intensity within the image, and Otsu’s thresholds (1 level in black, two levels in magenta) (c) Segmented shape (cyan) and elliptical fit (red). (\*) denotes regions of low intensity that were lost with a single level segmentation. The max Feret diameter was added (magenta).

- Rheological models in the literature are often developed for an uni-axial deformation. Adapting them for the AR (which simultaneously computes deformation in both the major axis  $a$ , and its perpendicular minor axis direction  $b$ ) would prove difficult.
- The measure of the minor axis may prove unreliable. As the constriction section is a rectangle ( $6 \times 15 \mu\text{m}^2$ ), the deformation is anisotropic. If while exiting the constriction, the cell was to flip around its main axis, the projection of the perpendicular axis in the direction of observation would not reflect the same minor axis as in the constriction. Thus the length of the minor axis may change only due to rotation. This does not concern the cell major axis as it cannot flip due to the confinement provided by the channel ceiling.
- The shape of the cell in the constriction differs from an ellipse, and both major and minor axis are overevaluated in the constriction.

Finally, as we were not satisfied with the elliptical fit for cells stuck in the constriction, we used the measure of the max Feret diameter instead of the major axis to quantify elongation during this stage. The Feret diameter (in magenta in Fig.2.3c) is defined as the longest line that can be drawn in the object, and tend to recapitulate best the elongation of the cell in the constriction while the major axis length (in red in Fig.2.3c) tend to overestimate it.

## 4 Fast deformation of colon cancer cells and morphological recovery

While we focused on the breast cancer lines in the paper, a similar work was also performed on the 4 lines of colon cancer cells presented earlier (CTC41, CTC41.5A, HT-29 and SW-620). We'll refer to CTC41 as primary, as they originate from the primary tumor and present similar phenotype to HT-29s cells [Cayrefourcq, 2015; Alix-Panabières, 2017]; and CTC41.5A as metastatic since they originate from a secondary liver tumor [Soler, 2018]. We'll present here the results for these lines, in the same order as presented in the paper.

### 4.1 Focus on the arrest time

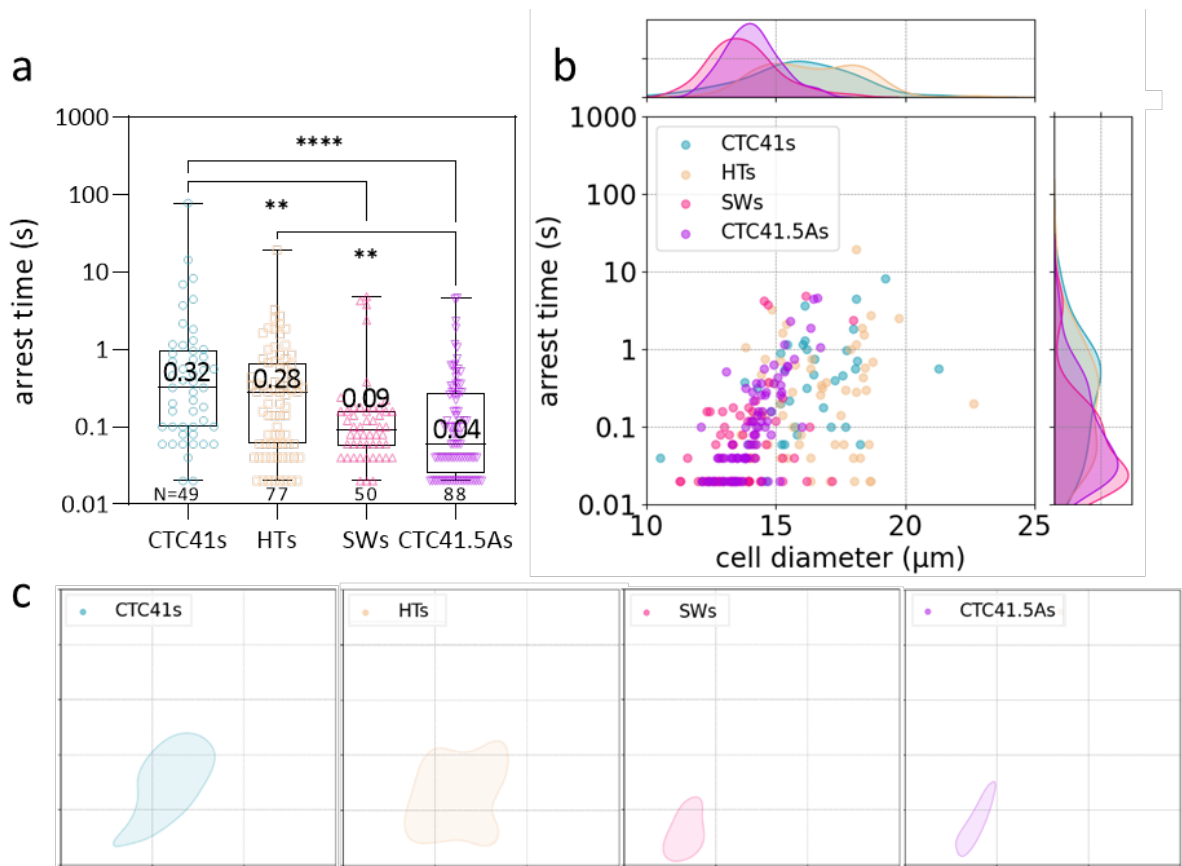


**Figure 2.4** – Cell arrest in the constriction displays high variability within each cell line. (a) Box plot of each cell line arrest time. Written value refers to the cell line median arrest time. (b) Scatter plots of the arrest time as a function of cell diameter. Top and side plots around the central scatter plot represents the density of cell diameters (top) or arrest times (right). (c) Contours of highest points density are represented for each cell line.

We first measured the arrest time, i.e. how long does a cell take to cross the constriction. The arrest time depends on the size of the constriction, the pressure difference and the size and mechanical properties of the cells. As the constriction size is the same for all cells, and the pressure drop is set the same through all experiments, we expect the arrest time to depend only

on the cell size and properties.

**Cell arrest time displays high intra-lines variability.** Similarly to what was observed in the breast cancer lines, the distribution of observed arrest time spans several orders of magnitude, from 20 ms (acquisition framerate) to 10-100 s for the slowest (see Fig.2.4a).

**Colon cell lines display different median arrest time.** We measured median arrest time in the constriction to be 320 ms and 280 ms for the CTC41 and HT-29 cells respectively ; and 90 ms and 40 ms for SW-620 and CTC-41.5A cells respectively. All significant differences are drawn on the plot Fig.2.4a.

**Arrest time is first associated with cell diameter.** We here draw the same conclusion as in the paper on breast cancer cells, which is that the two cell lines with higher median cell diameter (15.3  $\mu\text{m}$  for CTC41 and 15.7  $\mu\text{m}$  for HT-29) are the ones to display a significantly higher arrest time. Median diameters for SW-620 and CTC41.5A lines are respectively 13.5  $\mu\text{m}$  and 13.8  $\mu\text{m}$ . On the plot Fig.2.4b, this translates into the SW-620 and CTC41.5A lines being more grouped in the lower left part of the graph, as it can also be appreciated in the contour of higher density represented Fig.2.4c. However, we do observe cells with a big diameter to go very rapidly through the constriction, and conversely small cells that take longer time to cross than expected, especially for the HT-29 line.

**Mechanical properties of metastatic colon cell lines are more homogeneous.** The spread of the contour plot can be attributed to differences in mechanical properties, as objects with identical properties would organise along a line (meaning that the arrest time would depend only through the objects diameter). Qualitatively we observe that the CTC41 and HT-29 cells spread over a larger area than the two metastatic cell lines, which would characterize a larger heterogeneity of properties within the cells at the beginning of the disease. As the diseases progresses and the most efficient clones are selected, their properties become more homogeneous. Interestingly, the data points for CTC41.5As organize almost perfectly onto a line, which could be explained by their clonal origin from a liver metastasis.

We note that this line would intersect the x-axis around 12.5  $\mu\text{m}$ . Interestingly, this diameter corresponds to the effective radius  $R_{eff}$  that was calculated in the paper ( $R_{eff} = 6.27 \mu\text{m}$ ) in order to adapt the equations developed for cylindrical pipette aspiration to our rectangular constriction. Below  $2R_{eff}$ , cells would go instantly through the constriction without stopping. It is worth noting that this value is way different that the width of the constriction  $w = 6 \mu\text{m}$ , though we would have expected the threshold to be close to it. Thus, for a range of diameters (between  $w = 6 \mu\text{m}$  and  $2R_{eff} = 12.5 \mu\text{m}$ ), cells are deformed though it doesn't result in the cell stopping in the constriction (or for a duration lower than our acquisition framerate 20 ms).

**Link between arrest time and metastatic potential.** In breast cancer lines, we showed that arrest time distribution of cells with similar sizes (within a 1  $\mu\text{m}$  range) recapitulated the expected order of metastatic potential, with MCF-7 cells being less deformable (i.e. having a

higher arrest time) compared with SK-BR-3 and MDA-MB-231 cells. In colon cancer cells, we are unable to draw the same conclusion as primary and metastatic lines have more different diameters distributions. Analysis of 1  $\mu\text{m}$ -wide sliding bins (not represented here) does not return any particular order between the cell lines.

## 4.2 Cell deformation in the constriction

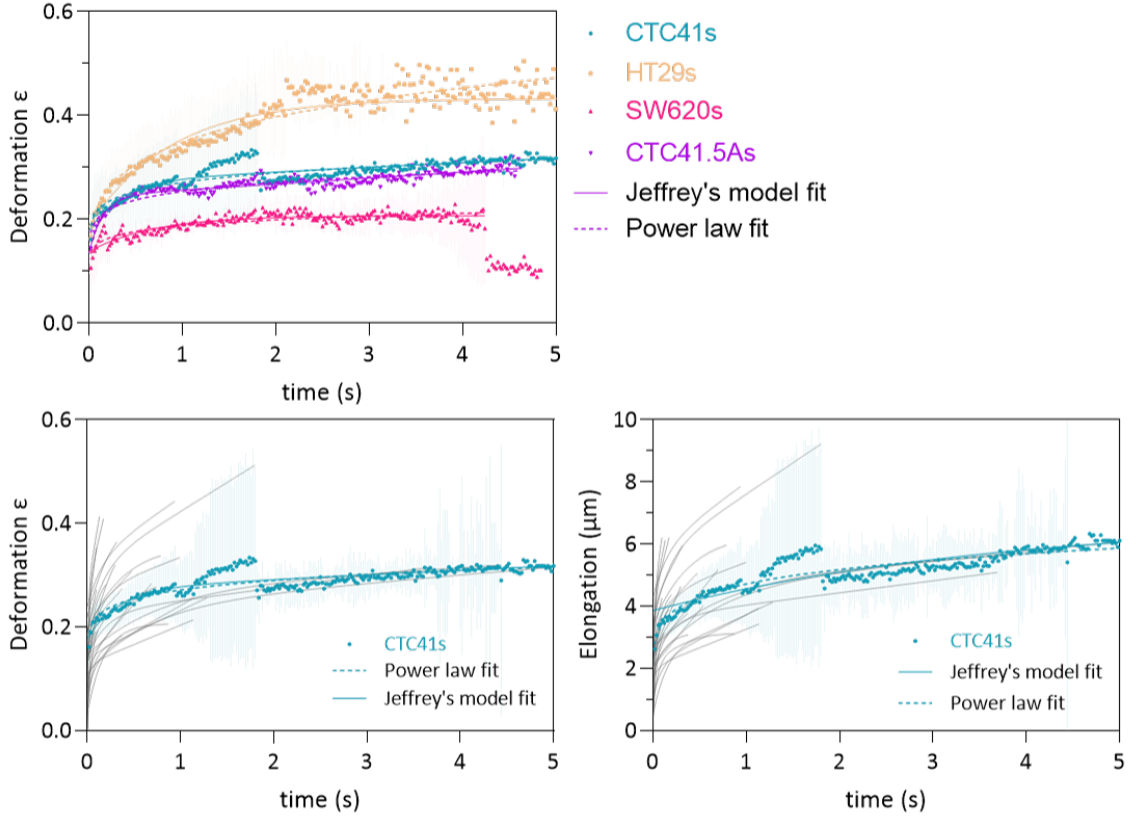


**Figure 2.5** – Deformation curves. (a) Mean curves for all four cell lines and fits with either Jeffrey’s model (continuous line) or power law model (dashed line). Though the fits were performed on the elongation, we represent here the deformation for the sake of comparison of lines with different median diameters, and coherence with the next section on recovery. (b) Mean deformation and elongation curves and their fits (in color) and each replicate fit (in grey) of the CTC41 cells.

We next aimed at extracting rheological parameters from the deformation curves of cells within the constriction. The shape of the deformation curves (first viscoelastic deformation followed by a linear viscous deformation, as can be seen in Fig.2.5) led us to use a Jeffrey’s model (serial association of a Kelvin-Voigt element with a dashpot) to fit the data. Short-time scale deformation is governed by the viscoelastic deformation of the Kelvin-Voigt element, while long-time scale deformation is governed by the linear elongation of the dashpot element. Within that framework, the balance between the force applied by the pressure difference on both sides of the object with the forces resulting from the viscoelastic contribution first, then the viscous

flow results in a two-terms equation of the form :

$$\varepsilon(t) = \frac{R_{eff}\Delta P}{a_0 E} \left[ \left( 1 - e^{-\frac{E}{3\pi\eta_1}t} \right) + \frac{E}{3\pi\eta_2}t \right]$$

In order to have a fitting expression independent of the cell diameter  $a_0$ , the actual fits in Prism are performed on the elongation  $a_0\varepsilon(t) = a(t) - a_0$  :

$$a_0\varepsilon(t) = \frac{R_{eff}\Delta P}{E} \left[ \left( 1 - e^{-\frac{E}{3\pi\eta_1}t} \right) + \frac{E}{3\pi\eta_2}t \right]$$

As variability between cells is quite important (see replicates in Fig.2.5b), the mean curve appear to be quite noisy, and thus hard to interpret. However, we can observe that each cell lines reach different plateau levels, related to different  $1/E$  values. We thus deduce that among the colon cell lines, we expect SW-620 cells to have an higher elastic modulus than CTC41 and CTC41.5A cells ; and HT-29 cells to have the lower elastic modulus as they deform more than the others.

**Fit on the mean curves.** As the majority of cells already escaped the constriction after 2s (as can be seen with each replicates of CTC41 cells in Fig.2.5b), we chose to limit our analysis to a window of 2s. Indeed, we do not trust the fit of the viscous part as it depends mainly on a very small number of cells, as evidenced from Fig.2.5.

We thus only consider the following expression of the Kelvin-Voigt model :

$$a_0\varepsilon(t) = \frac{R_{eff}\Delta P}{E} \left( 1 - e^{-\frac{E}{3\pi\eta_1}t} \right)$$

Alternatively, a power law fit was used as well :

$$a_0\varepsilon(t) = \frac{R_{eff}\Delta P}{K} \left( \frac{t}{t_0} \right)^\beta + C$$

with  $\beta$ ,  $K$  and  $C$  constants to be determined (by convention,  $t_0$  is choosen equal to 1 s) [Balland, 2006]. The exponent  $\beta$ <sup>1</sup> quantifies viscoelasticity of the material ( $\beta=0$  corresponds to a perfect elastic solid,  $\beta=1$  to the ideal viscous liquid).

The resulting parameters for both fits can be found in Tab.2.1 below.

**Fits on individual cells, and comparison with breast cancer cells.** We report in Fig.2.6 the values obtained for individuals fits ( $E$ ,  $\eta_1$ , and if the arrest time is long enough  $\eta_2$ ), when these were able to be computed, for both breast and colon cell lines.

First, it is worth noting the difference between parameters calculated from mean curves (Tab.2.1) and the median of parameters calculated from individual fits (Fig.2.6). We explain

---

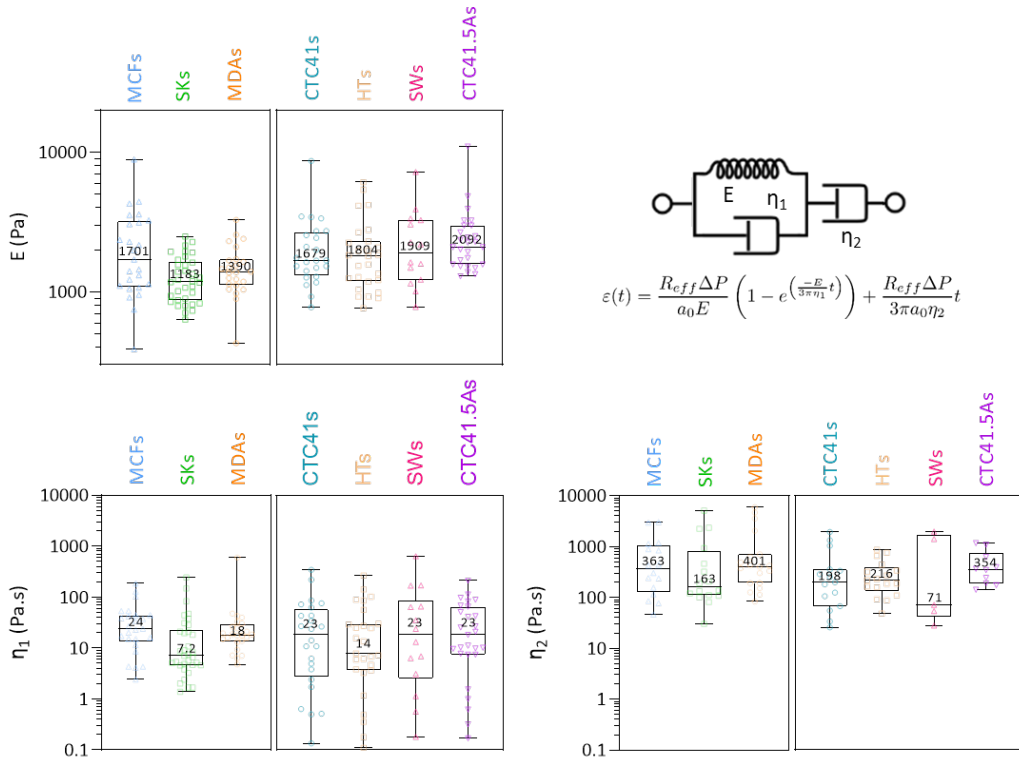
1. In the paper draft, the exponent  $\beta$  is referred to as a more generic  $n$

Kelvin-Voigt				
	CTC-41	HT-29	SW-620	CTC-41.5A
$\tau$	0.86 s [0.55-1.17]	1.37 s [1.07-1.68]	1.01 s [0.63-1.39]	0.31 s [0.27-0.35]
$E$	1.40 kPa [1.24-1.56]	0.81 kPa [0.73-0.89]	2.74 kPa [2.39-3.09]	1.81 kPa [1.68-1.94]
$\eta_1$	0.127 kPa.s [0.087-0.168]	0.118 kPa.s [0.102-0.135]	0.294 kPa.s [0.207-0.380]	0.060 kPa.s [0.049-0.070]
$R^2$	0.8151	0.9629	0.8393	0.9219

Power law				
	CTC-41	HT-29	SW-620	CTC41.5A
$\beta$	0.14 [0.127-0.229]	0.21 [0.198-0.246]	0.07 [0.063-0.101]	0.12 [0.115-0.141]
$R^2$	0.800	0.785	0.504	0.885

**Table 2.1** – Parameters [95% CI] obtained from Kelvin-Voigt model and power law fits (restricted to the first 2 s), using  $R_{eff} = 6.27 \mu\text{m}$  and  $\Delta P = 6 \text{ mbar}$ .



**Figure 2.6** – Individual cells fit parameters ( $E$ ,  $\eta_1$  and  $\eta_2$ ) using Jeffrey's model deformation. When  $\eta_2$  wasn't able to be computed, fit was changed to Kelvin-Voigt model ( $E$  and  $\eta_1$  only).

these differences with the fact that some cells were not able to be fitted (mostly due to bad quality of the data), though these cells did contribute in the mean curve.

Then, the comparison of elastic moduli  $E$  between breast cancer cell lines determines SK-BR-3 to be the softer cells. Here the CTC41 and HT-29 cells appear to be the softer among colon cancer lines.

Though order of magnitude of  $\eta_1$  is similar for breast and colon lines, we observe some colon cells to have lower extreme values. The viscous modulus  $\eta_2$  could be computed for cells for which arrest time is above  $\approx 1$  s. For each cell lines, the order of magnitude is of a few 100 Pa.s (though a bit lower for SW-620s cells for which the value has been computed for only 5 cells).

### 4.3 From deformation to recovery

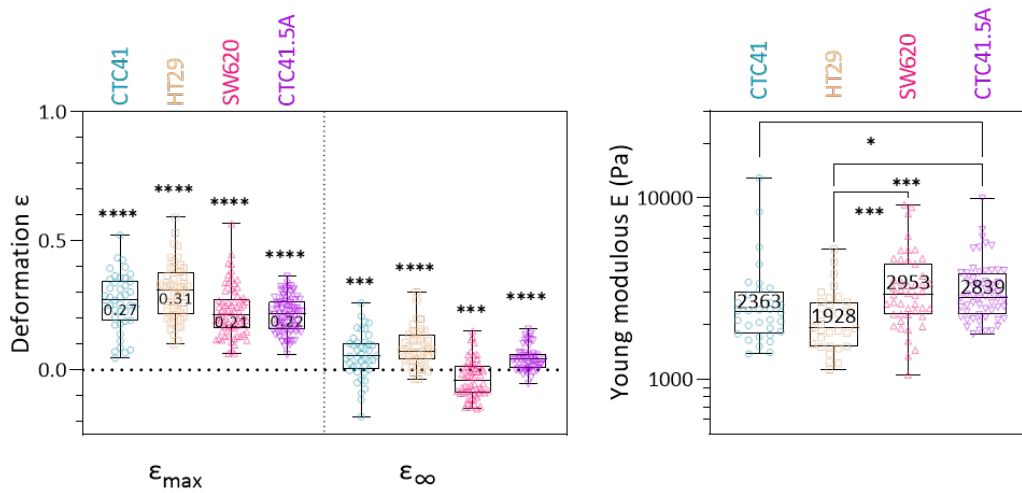


**Figure 2.7** – Deformation (b) Cell deformation measured in the constriction ( $\epsilon_{max}$ ) and after recovery ( $\epsilon_{\infty}$ ). The statistical difference to  $\epsilon_0 = 0$  is shown. (c) Distribution of  $E_{tot} = \frac{\Delta P}{\epsilon_{max}}$  for the three cell lines. The statistical comparison between each cell lines is represented.

**Cells recover almost entirely from the deformation.** As the cell escapes the constriction, the applied stress on the cell is suddenly released. We measure the remaining deformation  $\epsilon_{\infty}$  after 50 s of recovery (chosen experimentally as nothing evolves anymore after 50 s). Comparison between  $\epsilon_{max}$  and  $\epsilon_{\infty}$  is given Fig.2.7a. Max longitudinal strains range from  $\approx 20\%$  for the small metastatic SW-620 and CTC41.5A lines to  $30\%$  for the large primary CTC41 and HT-29 lines. No significant differences were found between each lines, while each dataset was individually statistically different from  $\epsilon_0 = 0$ . The final infinite deformation values  $\epsilon_{\infty}$  range from  $-4\%$  to  $7\%$  for each lines, and are each statistically different from either  $\epsilon_0 = 0$  or  $\epsilon_{max}$ . We conclude that cells do recover to a large extent from the imposed deformation, though a small residual deformation subsists at the end of the recovery. We evaluated in the paper the pressure drop across a cell to be of the order of 0.1 mbar (10 Pa). The resulting deformation would then only represent  $1\%$  for a cell of 1 kPa Young modulus. We thus conclude that the observed residual deformation to result from cell plasticity, i.e. irreversible deformation. We hypothesize that

the surprisingly low  $\varepsilon_\infty$  value for SW-620 cells might originate from the fact that their initial diameter may have been overevaluated, as small cells travel in the main channel very rapidly due to the absence of friction with the floor and ceiling and thus may appear blurry due to the cell displacement during image acquisition.

**Estimation of the cell Young modulus from its maximal deformation.** The fits above give us a first determination of an elastic modulus. We'll try here to evaluate the cell Young modulus based on the measurement of the maximal deformation. When the cell is in the constriction, the stress  $\sigma$  applied is of the magnitude of  $\Delta P$  and results in a deformation  $\varepsilon_{max}$ . Through Hooke's law, we can correlate the stress  $\sigma$  to the max longitudinal strain  $\varepsilon_{max}$  :

$$\sigma \approx \Delta P \approx E_{tot}\varepsilon_{max} \text{ thus } E_{tot} \approx \frac{\varepsilon_{max}}{\Delta P}$$

We thus deduce from each individual measurement of  $\varepsilon_{max}$  (see Fig.2.7a) a value for the Young modulus  $E_{tot}$  for each cell. The distribution is given Fig.2.7b. Median Young modulus values are  $\approx 2.4$  kPa for CTC41,  $\approx 1.9$  kPa for HT-29,  $\approx 3.0$  kPa for SW-620s and  $\approx 2.8$  kPa for CTC41.5A. We observe that these values follow the same trend as the elastic moduli resulting from the Kelvin-Voigt fits, though the values are higher here.

Interestingly, we found here the metastatic lines to have in average an higher elastic modulus as the primary lines. As we'll discuss later, these results are quite surprising as the majority of the literature suggests that the more aggressive cells are often softer than their less aggressive or non-malignant counterparts.

#### 4.4 Recovery of colon cells display two regimes

**Cell recovery displays two regimes : a fast elastic regime followed by a slower viscoelastic one.** Similarly to the recovery of breast cancer lines, the recovery of colon cancer lines also displays two regimes of different nature : a fast elastic regime, followed by a longer slower viscoelastic regime. We fitted the data points with successively increasing number of exponential decays until we obtain a fit of reasonable quality, i.e. providing a good visual adequacy between the curve and the points, to which any addition of more phase decay does not yield any improvement. Rheologically, this corresponds to an serial association of Kelvin-Voigt elements of different characteristic times. We found the best fit to be a sum of three exponential decays (as represented in Fig.2.8). All data and fits tested can be found in appendix C. The general form of the equation then becomes

$$\varepsilon(t) = (\varepsilon_{max} - \varepsilon_\infty) \left( a_{fast} \exp^{-t/\tau_{fast}} + a_{medium} \exp^{-t/\tau_{medium}} + a_{slow} \exp^{-t/\tau_{slow}} \right) + \varepsilon_\infty \quad (2.1)$$

As  $\varepsilon_{max}$  and  $\varepsilon_\infty$  varies with each cell, we defined a normalized strain  $\varepsilon_{Norm}$  as

$$\varepsilon_{Norm}(t) = \frac{\varepsilon(t) - \varepsilon_\infty}{\varepsilon_{max} - \varepsilon_\infty} = \frac{a(t) - a_\infty}{a_{max} - a_\infty}$$

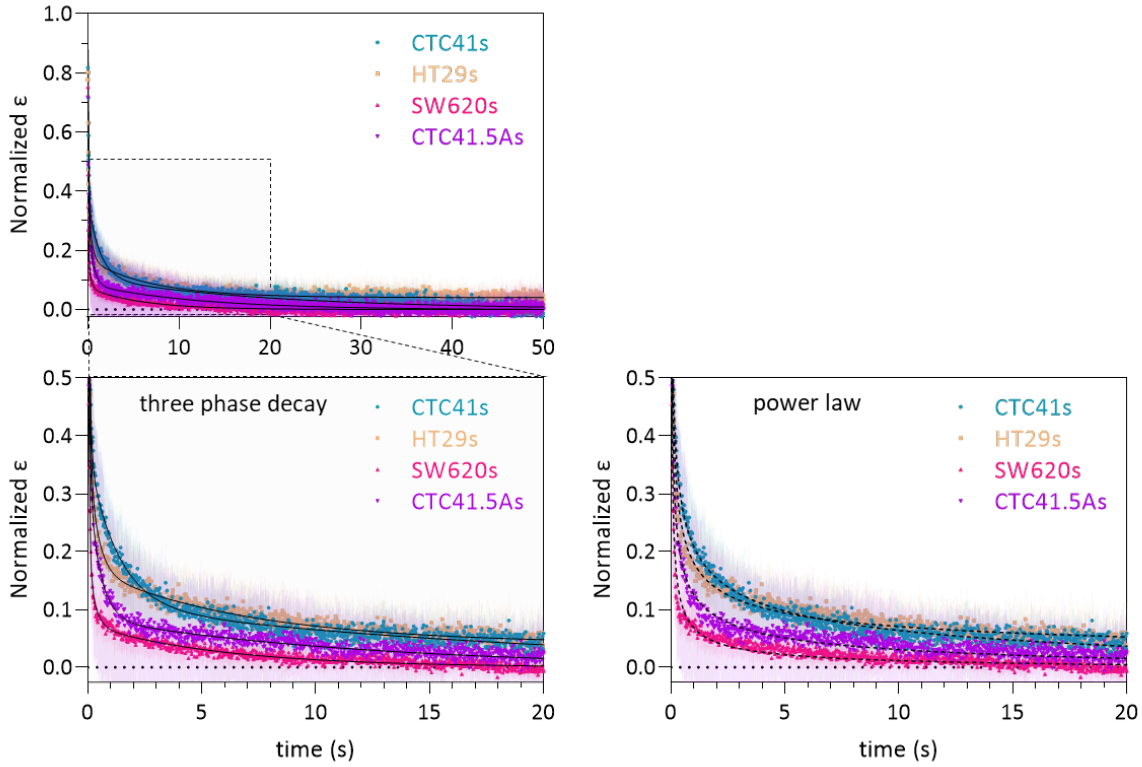


**Figure 2.8** – Cell recovery. Mean normalized  $\varepsilon(t)$  curves after exiting the constriction (taken as starting point  $t=0$ ). Bottom graph displays zoom over the first 20 seconds. Error bars represent confidence interval at 95%. Fitting curves represent three-phases decay (bottom left) or power law (bottom right) fits of the mean curves. Corresponding characteristic times (with confidence interval at 95%) are reported in Tab.2.2.

Recovery equation 2.1 then becomes :

$$\varepsilon_{Norm}(t) = a_{fast} \exp^{-t/\tau_{fast}} + a_{medium} \exp^{-t/\tau_{medium}} + a_{slow} \exp^{-t/\tau_{slow}} \quad (2.2)$$

with  $a_i$  and  $\tau_i$  ( $i = fast, medium, slow$ ) the respective amplitude and characteristic time of each exponential decay. Once again, similarly to the findings on breast cancer cells, all fast characteristic times were found to be less than 100ms (70 ms for CTC41, 61 ms for HT-29, 43 ms for SW-620s and 63 ms for CTC41.5A). We thus chose to merge the fastest exponential, defined only by a few time points for which we might lack precision<sup>2</sup>, in the elastic regime (see Fig.2.9)

We then define  $\Phi_{VE} = a_{medium} + a_{slow}$  as the fraction of the viscoelastic regime in the total recovery. The table of Fig.2.2 displays the results of these fits for each cell lines.

**Different colon cell lines have specific viscoelastic regimes.** Whereas recovery curves for breast cancer seems to overlap nicely, here we observe higher differences within the colon cancer cell lines. The recovery curve of SW620 cells drops more rapidly than the others (reaching 90% of recovery within 50ms), as it can also be appreciated in the fit parameters : it displays

2. Experimentally, these points are often associated to the journey of the cell towards its trap, eventually causing blurring

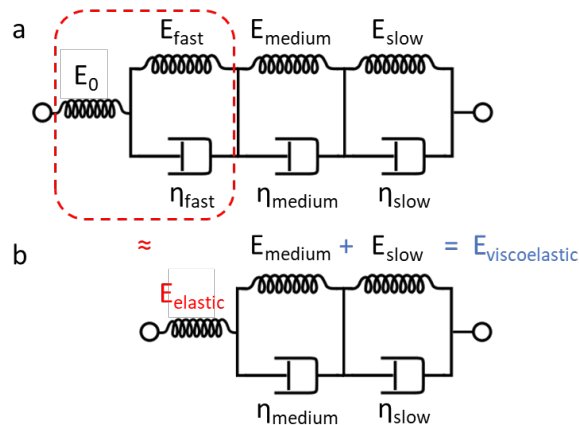


**Figure 2.9** – Rheological models for cell recovery. a) Rheological model corresponding to the three phase decay description made for the cell recovery, including the three characteristic times  $\tau_{fast}$ ,  $\tau_{medium}$  and  $\tau_{slow}$ . b) Merging of the faster characteristic time with the spring  $E_0$  into a spring of modulus  $E_{elastic}$ .

the lower fraction of viscoelastic regime  $\Phi_{VE}$  (20% compared to >34% for all other cell lines) and faster characteristic times, both slow (5.8 s) and medium (0.27 s). A similar behavior can be observed to a lesser extend for CTC41.5A cells (with a relatively small proportion of the slow regime). On the opposite, both CTC41 and HT-29 cells display a more important part of viscoelasticity in their recovery, associated with longer characteristic times (up to 19.5 s for CTC41s cells).

**Different colon cell lines present different rheological parameters.** Using the fit parameters obtain above, we deduce the elastic and viscous moduli for the different regimes. We measure the SW-620s cells to have a higher elastic regime modulus than the other cell lines (2.28 kPa), to be associated with its faster and sharper recovery.

We observe the viscoelastic regime to present an elastic modulus between 0.5 kPa and 1 kPa for all cell lines. The values obtained for viscous moduli associated with the slow and medium characteristic times range from 0.10 to 0.76 kPa.s and from 1.21 to 4.69 kPa.s respectively. The maximum is obtained for the CTC41 cell line, which on the graph is characterised by the most important viscoelastic regime, associated with higher characteristic times, while the minimum is reached with the SW-620s cells.

**Power law fits.** Alternatively, recovery curves were fitted with a power law equation of the form

$$\varepsilon_{Norm}(t) = \left(\frac{t}{t_0}\right)^{-n} + C$$

with C a constant The power law exponents obtained for each cell lines are  $n_{CTC41s} = 0.30$ ,  $n_{HTs} = 0.39$ ,  $n_{SWs} = 0.55$  and  $n_{CTC41.5As} = 0.40$ . The higher the exponent is, the more elastic the recovery. These values recapitulate well the order between curves observed on the graph.

The values we measure here are of the same order or higher that the ones observed for the

three phase decay fit				
	CTC41	HT-29	SW-620s	CTC41.5A
$a_{medium}$	26.5 % [25.5-27.5]	21.8 % [18.5-27.3]	12.8 % [9.8-15.9]	25.6 % [23.5-27.8]
$\tau_{medium}$	1.28 s [1.21-1.36]	0.38 s [0.33-0.46]	0.27 s [0.22-0.35]	0.49 s [0.45-0.54]
$a_{slow}$	10.8 % [10.5-11.1]	12.9 % [12.5-13.5]	7.4 % [7.0-7.7]	8.6 % [8.4-8.8]
$\tau_{slow}$	19.6 s [18.9-20.2]	7.00 s [6.71-7.32]	5.80 s [5.52-6.09]	12.0 s [11.4-12.7]
$R^2$	0.953	0.950	0.943	0.945
$\Phi_{VE}$	37.3 % [36.0-38.6-29.5]	34.7 % [30.9-38.6]	20.2 % [16.8-23.6]	34.2 % [23.5-27.8]
$E_{tot}$	2.22 kPa [1.80-2.56]	1.94 kPa [1.79-2.26]	2.86 kPa [2.43-3.28]	2.73 kPa [2.56-3.11]
$E_{elastic}$	1.39 kPa [1.12-1.61]	1.26 kPa [1.14-1.49]	2.28 kPa [1.93-2.63]	1.79 kPa [1.67-2.06]
$E_{viscoelastic}$	0.83 kPa [0.67-0.96]	0.67 kPa [0.58-0.81]	0.58 kPa [0.45-0.71]	0.93 kPa [0.85-1.08]
$\eta_{medium}$	0.76 kPa.s [0.60-0.88]	0.16 kPa.s [0.13-0.21]	0.10 kPa.s [0.07-0.14]	0.34 kPa.s [0.30-0.41]
$\eta_{slow}$	4.69 kPa.s [3.78-5.44]	1.75 kPa.s [1.59-2.06]	1.21 kPa.s [1.02-1.42]	2.81 kPa.s [2.57-3.25]
power law fit				
	CTC41	HT-29	SW-620s	CTC41.5A
$n$	0.30 [0.293-0.306]	0.39 [0.382-0.397]	0.55 [0.541-0.561]	0.40 [0.389-0.404]
$R^2$	0.948	0.929	0.896	0.933

**Table 2.2** – Parameters obtained from the three phase exponential decay and power law fits of the cell recovery and deduced rheological parameters. Values represent median and 95% confidence intervals.

breast cancer cell lines.

**Comments on the fitting of recovery.** The approach described in the paper submitted to Lab on Chip, in this chapter on the whole cell and in the following one dedicated to the nucleus, reflects our attempt at constructing rheological models that would allow to fit the data. Since the submission of this manuscript, the state of our comprehension has advanced, particularly

thanks to the pertinent inputs of the reviewers and of the jury. Under the assumption that the recovery could be considered independently of the deformation. By doing so, we implicitly assumed that the cell relaxed from the imposed stress in the constriction as it exits. We now think that this may be a too strong approximation considering the fact that the cell is still deforming as it escapes the constriction.

To take this into account, we'll approach the release of the stress as the cell escapes the constriction as the addition of a delayed stress of opposite amplitude, which would bring the overall stress experienced by the cell back to 0 (see [Bonakdar, 2016] for instance).

The equations describing both deformation and recovery in the framework of Burgers rheological model considering a cell of arrest time  $T$  then become :

$$\varepsilon_{Burgers}(t) = \frac{R_{eff}\Delta P}{a_0} \begin{cases} \frac{1}{E_0} + \frac{1}{E_1} \left( 1 - \exp\left(\frac{-E_1}{3\pi\eta_1}t\right) \right) + \frac{1}{3\pi\eta_2}t & \text{if } t \leq T \text{ (deformation)} \\ \frac{1}{E_1} \left( \exp\left(\frac{-E_1}{3\pi\eta_1}(t-T)\right) - \exp\left(\frac{-E_1}{3\pi\eta_1}t\right) \right) + \frac{1}{3\pi\eta_2}T & \text{if } t > T \text{ (recovery)} \end{cases} \quad (2.3)$$

The cell rheological behavior is the combination of an elastic component  $E_0$  which deforms and recovers instantly, a viscoelastic component which deforms and recovers with a characteristic time  $\tau_1 = \frac{\eta_1}{E_1}$ , and a viscous deformation  $\eta_2$  which deforms linearly but do not recovers. We'll also note the necessary contribution of the arrest time in the new set of equations, which means that the analysis has to be carried at a cell by cell basis, and can't be based on the mean curves only.

Similarly, using a power law formalism, cell behavior can be modeled using the following equations become :

$$\varepsilon_{PowerLaw}(t) = \frac{R_{eff}\Delta P}{a_0} \begin{cases} \left( \frac{1}{E_{ve}} + \frac{1}{E_{pl}} \right) \left( \frac{t}{t_0} \right)^\beta & \text{if } t \leq T \text{ (deformation)} \\ \frac{1}{E_{ve}} \left[ \left( \frac{t}{t_0} \right)^\beta - \left( \frac{t-T}{t_0} \right)^\beta \right] + \frac{1}{E_{pl}} \left( \frac{T}{t_0} \right)^\beta & \text{if } t > T \text{ (recovery)} \end{cases} \quad (2.4)$$

where the behavior is decomposed between a viscoelastic contribution  $E_{ve}$  which recovers once the cells escapes, and a plastic contribution  $E_{pl}$  expressing the presence of a residual deformation..

The previously generated data have to be reanalyzed with this new formalism. Our first results suggest that these equations allows to unify the behavior in deformation and recovery with a low number of parameters, which is expected of a strong model and was not the case in the previous analysis.

## 5 Discussion & Perspectives

In this section, we'll discuss first about the device and its design, and establish a comparison with other devices in the literature. Then we'll elaborate our results on cell rheology, in particular under the framework of cancer and the basic knowledge about cancer cell rheology.

## 5.1 About the design and experiment

**Different levels of deformations for cells of different size.** We made the choice here to compare all cells of different size with a constriction of the same width  $w = 6 \mu\text{m}$ . This results in different levels of deformations for each cell (as can be seen in the paper and in Fig.2.7a) : Bigger cells are deformed more (and often for a longer duration) than smaller cells. We chose to quantify this level of deformation by measuring the max longitudinal strain  $\varepsilon_{max}$ .

The other choice would be to adapt the size of the constriction to the diameter of the cells studied, so that the deformation level remain the same, which is the case with other experimental technics such as AFM for instance (where the indentation can be adapted to each cell). However this solution would prove hard to implement here as it would require to have a catalog of chips with different constrictions sizes, and cells still present significant variations of diameters even within a cell line.

Similarly, all cells do not spend the same duration in the constriction. With a much more complex design, the arrest time could be adjusted by tuning the pressure gradient in order to accelerate or on the contrary slow down cell deformation and transit through the constriction. This would require a feedback loop between a real-time cell tracking and the pressure controller (that in practice may not be fast enough), and to reduce the number of constriction to one only.

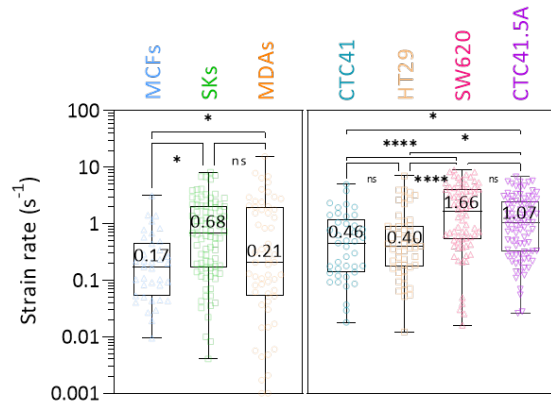


**Figure 2.10** – Strain rate applied to the cells in the constriction.

**Estimation of the strain rate.** In order to compare with other methods, we estimate the strain rate  $\dot{\varepsilon}$  of deformation in our device as  $\dot{\varepsilon} = \frac{\bar{\varepsilon}}{t_0}$  [Urbanska, 2020] where  $\bar{\varepsilon}$  is the mean absolute strain of a cell and  $t_0$  the duration of the deformation (i.e. the arrest time in our case). In a constriction of identical dimensions, [Urbanska, 2020] numerically calculated the mean absolute strain to be  $\approx 40\%$  of the max longitudinal strain  $\varepsilon_{max}$  (considering that the cell deforms from a sphere of diameter  $a_0$  into an ellipsoid of dimensions  $a_{max}$ ,  $w = 6 \mu\text{m}$  and  $h = 15 \mu\text{m}$ ). Based on this approximation (as the confining channel section dimensions are the same as our constriction section), we then evaluated the strain rate for each cell analyzed above.

We found the strain rate applied to the cell to be of the order of 0.1 to 1 s<sup>-1</sup>. The strain rate is higher for the smaller cells (SK-BR-3, SW-620, CTC41.5A) as they cross the constriction

the fastest. We acknowledge that the top part of these graphs may be truncated as some cells that went through the constriction in less than 20 ms and were excluded from our analysis. These rates are similar to other constriction-based microfluidic devices ( $0.04 \text{ s}^{-1}$  in [Urbanska, 2020]) or AFM measurements ( $0.1\text{-}1 \text{ s}^{-1}$  in [Omidvar, 2014],  $0.1 \text{ s}^{-1}$  in [Nematbakhsh, 2017]), though it is higher than other experimental designs such as micropipette aspiration ( $< 0.02 \text{ s}^{-1}$  in [Pachenari, 2014] and  $< 0.05 \text{ s}^{-1}$  in [Tabatabaei, 2019]).

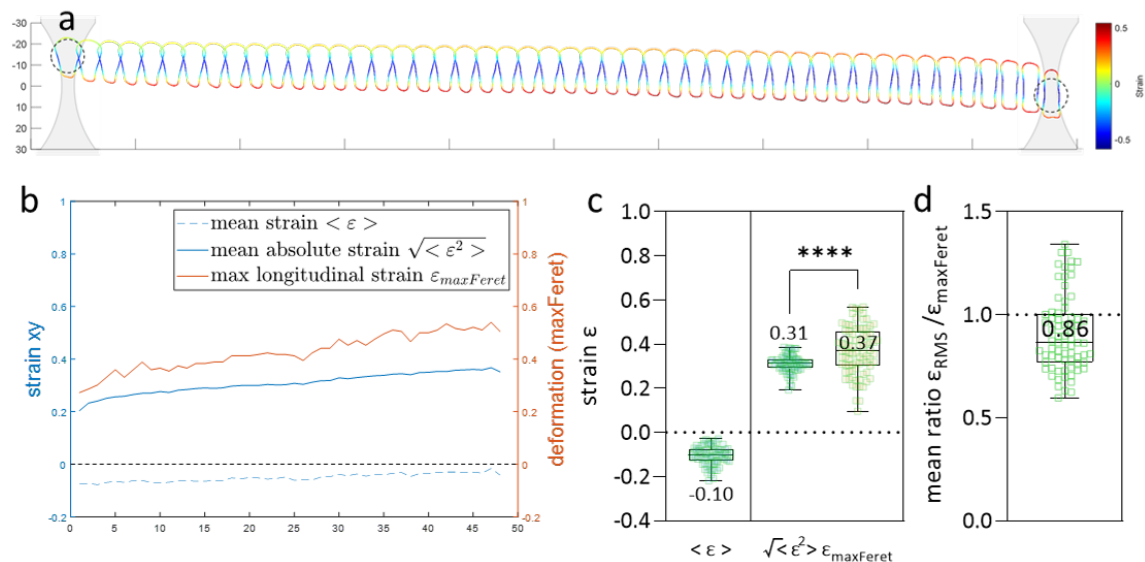


**Figure 2.11** – Strain pattern during deformation (a) Strain evaluated at each point of the cell contour in the xy plane as a SK-BR-3 cell deforms (red : elongation  $\epsilon > 0$ , blue : compression  $\epsilon < 0$ ). (b) Comparison of mean strain ( $\langle \epsilon \rangle$ , blue dotted line) and mean absolute strain (root mean square  $\sqrt{\langle \epsilon^2 \rangle}$ , blue continuous line) to the deformation calculated from the max Feret diameter (orange line). Values are computed on SK-BR-3 cells. (c) Box plot of : temporal average of mean strain  $\langle \epsilon \rangle$ , maximal values of mean absolute strain  $\sqrt{\langle \epsilon^2 \rangle}$  and maxFeret  $\epsilon_{\max}$  deformation. (d) Average of ratio of mean absolute strain over maxFeret deformation.

**Strain pattern in the cell during deformation.** Due to the shape of the constriction, the strain pattern in the cell is complex (compression in the middle of the constriction, elongation at the front and back of the cell). As an attempt to better describe the deformation, we determined the strain  $\epsilon$  at each point of the cell contour in the xy-plane (compared to the initial diameter, see Fig.2.11a). We observe that the middle part of the cell in the neck of the constriction experience compression, while the back and front extremities of the cell are in elongation. To quantify the average deformation of the cell, we define the mean strain as  $\langle \epsilon \rangle$  and the mean absolute strain as  $\sqrt{\langle \epsilon^2 \rangle}$ , both computed over the points of the contour. Evolution of these quantities are represented Fig.2.11b, and compared to the maximal longitudinal deformation (based on the max Feret diameter) that we used through this study. Interestingly, both follow similar trends.

Assuming the cell is incompressible and deforms only in the xy-plane (as we chose the channel height to confine cells in the z-dimension), we expect the mean strain to average to 0. However, we measure the average of the mean strain for all SK-BR-3 cells to be -0.10 (see Fig.2.11c). We propose three hypothesis to explain the overall compression of the cell in the xy-plane :

- First, the cell may not be incompressible, and rapidly loses volume as it enters the constriction. Though this loss of volume would have to happen in  $< 20$  ms as the strain of the first acquired point is already negative. [Venkova, 2022] observed such a fast loss of volume of  $\approx 10\%$  following deformation by confinement of HeLa Kyoto cells.
- Second, overall compression is compensated by an elongation in the z-direction, and the average strain over the volume of the cell then equals to 0.
- Third, we overestimated the diameter of the cell in the main channel. Though we were careful in excluding blurry images to measure it, as the cell moves during the exposure time the acquired area may cover a surface slightly bigger than the cell actually is.

We believe the second hypothesis to be the most plausible. We would indeed expect the mean strain to keep decreasing if the cell was able to continuously lose volume upon increasing deformation. And in case of an overestimation of the initial diameter, we would expect the mean strain to remain constant and equal to the error we made on the measure. Oppositely, the increase towards zero of the mean stress can be easily understood if we consider an increasing elongation in the xy-plane as the cell progresses through the constriction together with an elongation in the z-direction which cannot evolve due channel confinement.

We observe the mean absolute strain and max longitudinal deformation to follow the same trend, though interestingly mean absolute strain turns out smoother and less noisy. In Fig.2.11c, we compared the maximal strain measured on these curves. When SK-BR-3 displayed a 0.37 maximal strain when computed with the max Feret diameter (see also the paper), the max strain was evaluated to 0.31 with a narrower distribution using the mean absolute ratio. At each point of the deformation in the constriction, the mean absolute strain is a fraction of the max longitudinal strain. We evaluated this fraction to be about 86% for SK-BR-3 cells (see Fig.2.11d).

This similitude in trend between both measurement legitimates the use of the maximal longitudinal strain as a measure of deformation. However, we acknowledge that the values we report in this chapter that depend on the maximal deformation (elasticity and viscosity moduli) may be correct to within a factor of  $\approx 0.86$ . In further Pachinko experiments and analysis, the mean absolute ratio will be added to the measurements recorded.

A few studies addressed the issue of strain pattern determination through numerical approaches. [Abarca-Ortega, 2024] aim to describe fluid forces and cell deformation. In this study, the cells are considered to be visco-hyperelastic, homogeneous, and isotropic under quasi-static progressive loading (incremental steps of pressure until deformation equilibrium is reached). This approach revealed the heterogeneous distribution of stresses within the cell, with a maximum located close to the contact points between the cell and the wall surface.

[Chen, 2024] modeled the cell as an homogeneous droplet enclosed by a hyperelastic film (membrane), in order to determine regions of higher membrane deformation and resulting surface tension. The deformation was able to induce formation of plasma membrane pores in the region of higher surface tension, thus proving the interest of cell squeezing for absorption of foreign substances.

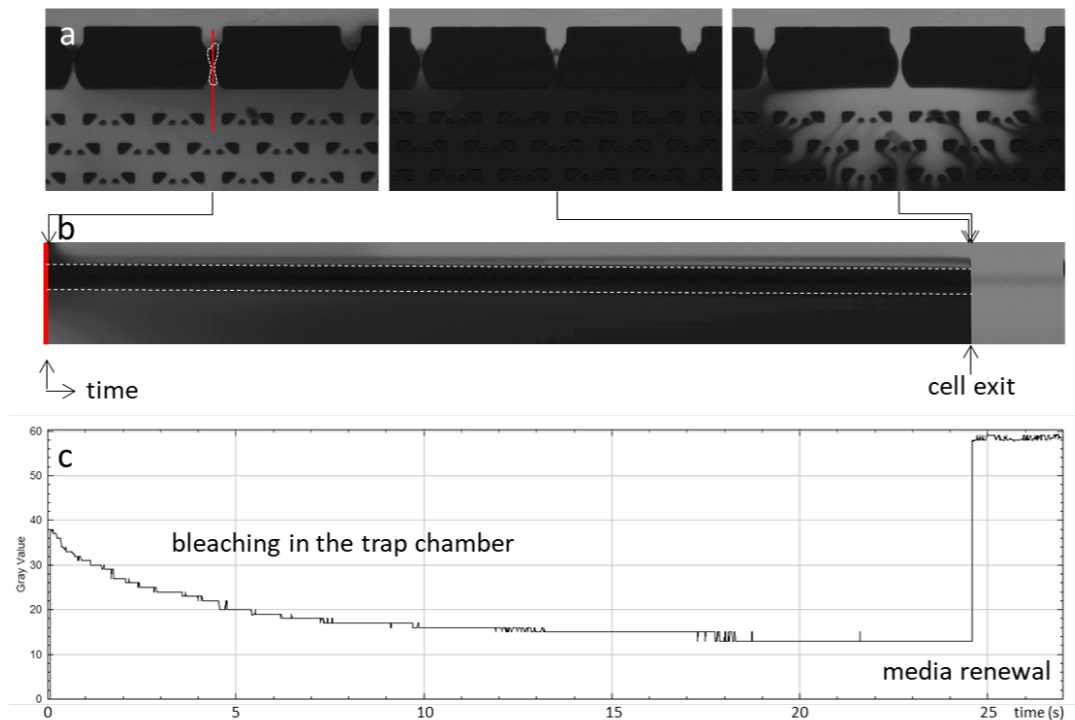


**Figure 2.12** – Closure of constriction by cells. (a) Pictures of the Pachinko chip filled with fluorescent media (10kDa Dextran-FITC) as a MDA-MB-231 cell enters the third constriction (left), then just before (center) and after (right) the cell exits the constriction. When all constrictions are occupied, the fluorescent media in the downstream recovery chamber is photo-bleached, until a constriction opens and the medium is renewed. (b) Temporal reslice kymograph of the pixel intensity along the red line represented in (a). White dotted lines represent cell boundaries. (c) Pixel intensity within the trap chamber.

**About the pressure difference  $\Delta P$  across the constriction.** In our calculations we used  $\Delta P = 6$  mbar, based on numerical simulations (see Suppl.Infos of the paper), as the pressure difference applied on cells stuck in the constriction. In fact, this value is a theoretical maximum under the assumption that the cell occupies entirely the constriction. Indeed, a flow leak around the cells in the constriction would result in a lower effective pressure difference applied on the cell. These leaks might originate from any mismatch between the originally spherical cells and the rectangular constriction if the deformation doesn't close the constriction [Preira, 2013; Moore, 2023]. Experimentally, we validated the absence of any significant leak. By injecting fluorescent-labeled media (FITC-dextran 10 kDa, 1 mg/mL) into the device, we observed photobleaching of the media in the trap chamber within a few seconds when constrictions were occupied by cells, while media in the main channel was renewed and thus did not photobleach (see Fig.2.12). If significant leaks were present around arrested cells, then some media downstream the cells would have been renewed and photobleaching would not be observed. We acknowledge that this proof only concerns cells who spend enough time in the constriction to see photobleaching happen. It is possible that cells that go very rapidly through the constriction do not deform sufficiently to block the constriction. Thus the effective pressure difference would be less than  $\Delta P = 6$  mbar, though high enough to deform and have the cell go through the constriction. For these cells,

values of elasticity and viscosity deduced would be overestimated.

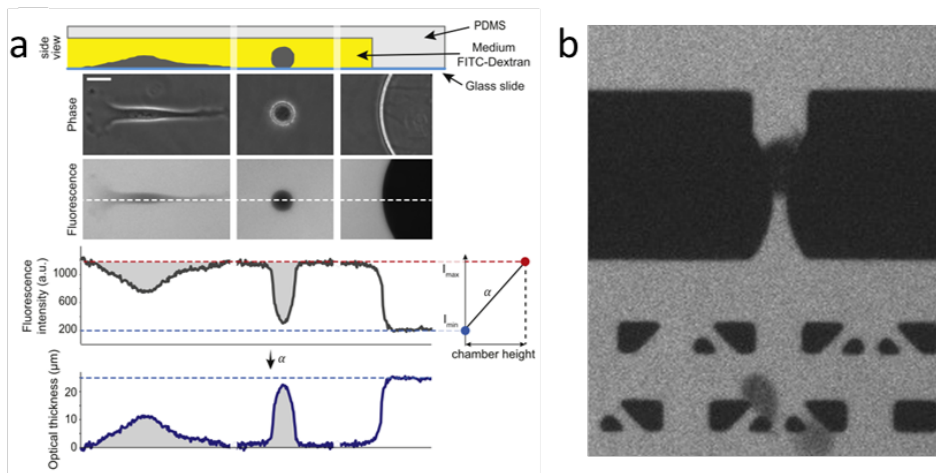


**Figure 2.13** – Volume measurement by fluorescence exclusion microscopy (FXm). (a) Principle of the FXm (adapted from [Cadart, 2017]). (b) FXm image of MDA-MB-231 cells acquired with a confocal spinning disk microscope, with one cell in the constriction and one cell in a trap.

**About the cell volume.** Cell volume can be indirectly measured through fluorescence exclusion microscopy (FXm) [Cadart, 2017; Braïni, 2018]. The media contains a cell-impermeable fluorescent dye (here FITC-dextran 10kDa). The presence of a cell will result in a decrease of fluorescent intensity due to volume exclusion of the media, proportional to the volume of the object. We evaluated the possibility to measure the volume of cells going through the Pachinko device, as recent study highlighted the potential loss of volume of HeLa Kyoto cells under confinement [Venkova, 2022]. However, experiments were rendered difficult by the need to acquire images at a high framerate (50 fps) over a prolonged period of time ( $\approx 50$  s), which with the current set-up led to inhomogeneous photobleaching of the media and prevented volume measurements (see section above). A solution was recently found imaging with a confocal spinning disk with a more sensitive camera to reduce the laser intensity and thus prevent photobleaching. Further experiments will allow us to follow the volume of cells as they are undergoing fast deformation to determine

- whether the incompressibility hypothesis we made earlier is valid.
- or if the cell lose volume in response to fast deformation, and if so to what extent and under which timescale, as the timescale may inform us on the underlying mechanism (diffusion, aquaporines, transient holes in the membrane).
- if the potential loss if volume is reversible, and if so under which timescale.

**About the constriction geometry.** Previous work in our team demonstrated the impact of several constrictions geometries on the arrest time of cells [Ahmad-Cognart, 2020]. Arrest time decreases as the constriction approach gets sharper. In the literature, constrictions designs are often sharper than in our design [Gabriele, 2009; Xia, 2018; Davidson, 2019; Jebane, 2023].

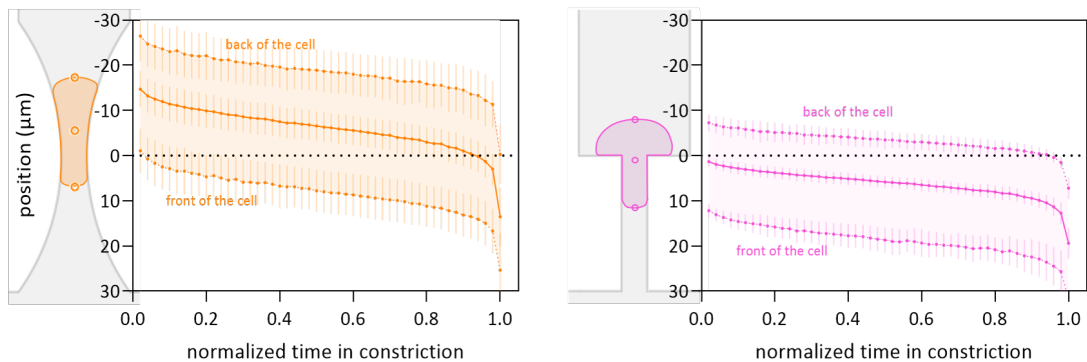


**Figure 2.14** – Spatio-temporal dynamics of MDA-MB-231 cells during their passage through two different constriction geometries.

The resulting arrest time is often decoupled into an entry time (where the cell deforms) followed by a transit time (where the cell slides through the channel). We compared the progression of MDA-MB-231 cells into 2 different constriction designs : our  $6\ \mu\text{m}$ -wide constriction design with a circle arc profile, and a sharp transition from  $26\ \mu\text{m}$  to a  $6\ \mu\text{m}$ -wide straight channel (see Fig.2.14). We found in both cases that the cell move forward into the constriction as it is being deformed. The deformation thus seems never entirely decoupled from the transit. Then, as the deformation level is high enough , the cell rapidly transits through and escape the constriction (see last points of the spatio-temporal graph) . We then conclude than the parameter we defined as arrest time is closer to the reported entry time as defined in the literature. To observe and measure a transit time, we would need to modify the constriction and add a long enough straight channel to accommodate the entire deformed cell.

We finally evaluated the influence of the constriction anisotropy. Indeed, as the constriction is a  $6 \times 15\ \mu\text{m}^2$  rectangle, the cell is more deformed in one direction. As presented in the Suppl.Materials of the paper, we followed cell recovery in a square constriction of similar area ( $9 \times 9\ \mu\text{m}^2$ ). The recovery in a square constriction displays the same two regimes as observed with the  $6 \times 15\ \mu\text{m}^2$  constriction. An advantage of square constriction is that the deformation measurement is less sensitive to cell flipping in the trap chamber, as all sides present the same deformation. However, this only applies to AR and other measurement based on the deformation in the direction of the minor axis. The elongation measurement is unchanged as the cell major axis stays within the plane of observation due to the spatial confinement in the z-direction provided by the channel ceiling.

## 5.2 About the rheology

Recovery was almost never studied in comparison with constriction-induced deformation. In a rare example, [Gabriele, 2009] compared deformation and recovery of THP-1 monocytes deformed in a  $4 \times 17\ \mu\text{m}^2$  channel. Though several drug treatments were tested (Latrunculin A, Blebbistatin, Jasplakinolide) and affected largely the dynamics of deformation, none seemed to

affect the dynamics of shape recovery. Moreover, in all conditions, the recovery of the aspect ratio was characterized by a relaxation within  $\approx 50$  s.

**Comparison with the literature.** In this work we compared cells of tumor origin only. It would be interesting to analyse non-tumoral cell lines in our device. Based on the literature, we expect non-tumoral cell lines to be stiffer (higher Young modulus and higher viscosity modulus). We presented in the introduction the MCF-10A cells as a non-tumoral cell line of breast tissue origin. Many other models of breast cancer lines exist, including commercial immortalized cell lines [Dai, 2017], or xenografts [Woo, 2021]. An interesting example of other lines that could have been tested are MCF10DCIS, a xenograft mouse model derived from the MCF10A cell line, which recapitulates the transition from *in situ* to invasive stages of breast cancer progression [Nader, 2021a].

We discussed in the paper the comparison of our rheological parameters estimation with reported comparable values in the literature. We found the MDA-MB-231 to be the softer and more fluid-like, both in deformation and recovery, in accordance with the literature [Guck, 2005 ; Tabatabaei, 2019]. Increase in softness is a recognized signature of tumorigenesis [Alibert, 2017], and a fluid-like behavior might be an asset for survival in the circulation, enhancing the probability of the occurrence of metastasis

Similarly for the colon cells, other largely used cell lines that we could have tested include human tumoral Caco-2 or SW-480 (primary tumor derived from the same patient as lymph node metastatic SW-620) or non-tumoral NCM460 [Bjerknes, 2006].

Interestingly we measure here the colon metastatic lines (SW-620 and CTC41.5A) to have an higher elastic modulus than the primary lines (CTC41 and HT29). The colon cancer lines were overall less studied than the breast cancer ones so finding values to compare with prove to be difficult. In a micropipette aspiration experiment, [Pachenari, 2014] reported HT-29 cells (grade I) to present an higher apparent elasticity and viscosity than SW480 cells (grade IV). However, instantaneous Young modulus was higher for high grade cells, relating to the existence of extensively build-up actin networks at the cell cortex, meaning that high grade cancer cells could resist more to initial deformation. Similarly, [Brás, 2022] reported SW620 metastatic cells to present the highest Young's and storage moduli compared to primary HCT15 and HCT116 cells, with a defined cortical actin ring with distributed F-actin filaments. On the contrary, when compared in a AFM experiment, SW-480 were shown to be stiffer than their metastatic SW-620 counterpart, though these differences could be related to the difference in adherent morphology of these cells (elongated vs round respectively) [Palmieri, 2015]. The sparsity and diversity of results obtained in the literature thus calls for a better characterization of these cells, which this work aims to contribute to.

Only a minority of studies show similar results in other cancers, with more metastatic cells being stiffer. For instance, using AFM [Bastatas, 2012] showed that low grade metastatic prostate cancer cells have higher elastic moduli than highly metastatic cells. When probed globally, grade IV glioblastoma cells were shown to be softer than grade III astrocytoma cells, while they appear stiffer at the intracellular level, which could be explained by changes in the composition and

spatial organization of the cytoskeleton and by changes in nuclear mechanics [Alibert, 2021].

To summarize, a change of cell rheological properties towards a softer and more fluid-like behavior is expected for cells of higher metastatic potential.

Regarding the comparison between CTC41 and CTC41.5A, both lines originating from the same patient (CTC41 was isolated before the lines of treatment, and CTC41.5A after patient relapse). Additionally to the observed decrease in cell size for CTC41.5A, which correlated with a faster transit through constrictions, we observed a surprising increase in elastic modulus and decrease in viscous modulus, both in deformation and recovery. The CTC41.5A, which present the liver marker ALDOB+ (indicating that these cells come from a secondary liver metastasis), appear in our system more rigid and more fluid-like.

**Comparison of rheological models based and power law fits** As it can be expected, increase in the number of parameters tends to result in a better fit (higher  $R^2$ ). We showed here for the cells that the three phase decay fit (7 parameters,  $R^2 \approx 0.94-0.98$ ) worked better than the two phase decay fit (5 parameters,  $R^2 \approx 0.92-0.97$ ) and way better than one phase decay fit (3 parameters,  $R^2 \approx 0.6-0.9$ ). However, models with finite number of relaxation times may be too simple to describe complex behaviors. Hence power law rheology models as gained some interest for its capacity to provide very good fits with a low number of parameters (3 parameters,  $R^2 \approx 0.9-0.97$ ).

Power laws may result from other cellular mechanisms. Poroelastic models (the cytoplasm is considered as a porous elastic meshwork within a fluid) [Moeendarbary, 2013] where deformation is limited by the friction of the fluid through the pores of the elastic meshwork, show a power-law dependency at long time scales ( $> 0.1-0.2$  s). Soft glassy materials (the cell is imagined to consist of many disordered elements held in place by attractive or repulsive bonds, traps, or energy wells formed between neighboring elements) [Kollmannsberger, 2009] considers the cells as remodelable. The binding energies are weak enough to allow the elements to occasionally hop out of their trap and change their position. Power-law rheology arises from a wide distribution of energy well depths such that the distribution of element lifetimes is scale-free.

Values for the exponent  $\beta$  derived in the power law model, referred to as the fluidity  $\beta$ , are typically between 0.1 and 0.5 for cells [Kollmannsberger, 2011], which corresponds to the range of values we obtained. In recovery, we kept an initial exponent  $-n$  that will be replaced by  $\beta$  with the reworked equations.

Overall, the modeling process was hard to implement as simple models (such as Kelvin-Voigt or Burgers) were not successful in representing the data. We thus choose to increase the number of parameters (especially additional characteristic times) to better fit the data by adding Kelvin-Voigt elements in series, at the expense of the simplicity of the model. A compromise can be found with the power law models as they allow for a good fit with less parameters, though their interpretation is also more complicated.

**About the estimation of the Young modulus from the maximal deformation** We estimated the Young modulus of deformed cells through Hooke's law as  $E \approx \frac{\Delta P}{\varepsilon_{max}}$ . However we acknowledge that this approach raises questions that we wish to discuss here. Given the fixed geometry of the constriction,  $\varepsilon_{max}$  depends only on the initial cell size. Moreover, as  $\Delta P$  should be fixed and independent of the cell, we expect  $E_{tot}$  to depend only on the cell size, and not its rheological properties... which makes little sense. We explain it by the fact that the Hooke's law is established through a balance of forces (externally applied, and resulting from the deformation of inner chemical bonds that constitutes the material). However, in the constriction the cell is deforming continuously, and is thus out of equilibrium. As we chose  $\Delta P$  high enough so that the cell goes through the constriction, the cell escapes the constriction before reaching its equilibrium strain. This may result in an underestimation of the actual strain resulting from  $\Delta P$ . Said otherwise, the measured  $\varepsilon_{max}$  could be achieved with a pressure difference  $\Delta P_{eff} < \Delta P$ . The proposed equation  $E = \frac{\Delta P}{\varepsilon_{max}}$  only holds for cells that would stop in the constriction and experience a deformation at equilibrium under the applied stress  $\Delta P$ .

The correct way to measure the Young modulus would be to increase the pressure difference stepwise starting from zero, waiting for the cell to reach an equilibrium position in the constriction between each steps, until the cell escapes the constriction. The effective pressure difference  $\Delta P_{eff}$  when this happens should be used to determine the Young modulus as  $E = \frac{\Delta P_{eff}}{\varepsilon_{max}}$ .

Complementary experiments would be required to evaluate the error we made in our analysis by computing the Young modulus as we did.

**About the approximation we made in the evaluation of the elastic component in rheological models.** Due to experimental limitations, as described earlier, we chose to merge the fastest of the exponential decay obtained by the fit to the elastic regime. Rheologically, this means neglecting the viscous component  $\eta_{fast}$  as described in Fig.2.9, which allows to define an equivalent elastic modulus  $E_{elastic} \approx E_0 + E_{fast}$ .

During the curve fitting process, we made the choice to keep a three decay fit among the one and two phase decay (see data in Annex.C) but only further analysed the medium and slow decay out of the three. However, the fit was able to compute parameters to this fast exponential decay ( $a_{fast}$  and  $\tau_{fast}$ ) which allows us to compute rheological parameters in a similar way as we did for the medium and slow decays. The values for  $\eta_{fast}$  are of the order of  $\approx 100$  Pa.s for each cell lines. This value isn't far away from the one computed for  $\eta_{medium}$ , or to the values reported in the literature for the cytoplasm [Hochmuth, 2000 ; Wang, 2019].

Thus, we acknowledge that our hypothesis of an elastic nature of this first decay may not hold against that of a viscoelastic origin linked to the rheological behavior of the cytoplasm. Further experiments with a better resolution (achieved with a better camera) should allow to better decipher the transition from elastic to viscoelastic and to evaluate precisely the relative fraction of elastic and viscoelastic regimes.

### 5.3 About the cytoskeleton

**About the drug treatments.** As a first step towards understanding the role of cell components in the overall mechanical behavior of the cell, we perturbed the cytoskeleton of MDA-MB-231 cells using Latrunculin A and Y-27632 (see the paper). The same approach could be used in the future for MCF-7 and SK-BR-3 cells, and colon cell lines by extension.

We used Latrunculin A over Latrunculin B in our experiments for its longer lasting effects [Spector, 1989]. Both bind actin monomers near the nucleotide binding cleft and prevents them from polymerizing. We selected the use of Y-27632 over blebbistatin to inhibit actomyosin contractility, as blebbistatin is reportedly phototoxic which thus complicates live imaging using this drug. Y-27632 is a ROCK inhibitor. ROCK pathway increases contractility by increasing phosphorylation of myosin II light chain. Its inhibition results in a decrease actomyosin activity. We selected the effective Y-27632 concentration based on the increased spreading of the cells, as lamellipodia formation is under control of Rac1 which activation under normal conditions is inhibited by the ROCK pathway.

In a  $6 \times 15 \mu\text{m}^2$  confinement channel, [Byun, 2013] reported that Latrunculin B treatment ( $5 \mu\text{g}/\text{mL}$ ) induced a 3.8-fold increase in the entry velocity of H1975 cells, thus revealing an increased deformability of the cells.

To complete the analysis, we may have investigated other drug treatments :

- Cytochalasin D as an alternative to Latrunculin A for actin polymerisation inhibition through different mechanism [Wakatsuki, 2001].
- Nocodazole interacts with microtubules polymerisation. Used at a low concentration, it allows for cell cycle arrest by blocking the cell into mitosis by preventing spindle formation. At a higher concentration, it results in microtubules depolymerisation [Jebane, 2023].
- Jasplakinolide, oppositely to Latrunculin, increase cell stiffness by inducing actin polymerisation through stimulation of nucleation. [Gabriele, 2009 ; Dupire, 2020].

**$6 \times 15 \mu\text{m}^2$  constrictions result in a regime of small deformations.** As we described in the introduction section 3.3.1, under strong confinement, cells can form blebs. This detachment of the plasma membrane from the underlying cortex is observed for a confinement below a threshold height ( $\approx 5\text{-}6 \mu\text{m}$ ), though this value varies for each cell type [Lomakin, 2020].

In our usual  $6 \times 15 \mu\text{m}^2$  constrictions, we do not observe any bleb formation. We thus consider the deformation regime to be small enough to not induce plasma membrane detachment. As presented in the paper, blebs were observed in  $6 \times 6 \mu\text{m}^2$  square constrictions, indicator of a change towards a strong deformation regime.

In a confined channel of reducing width, [Hu, 2017] studied deformations of breast lines MCF-7 and MDA-MB-231. Modelisation of the deformation using SLS model (standard linear solid, serial association of a spring and a Kelvin-Voigt element) allowed to access instantaneous and relaxed elasticity, as the cell first enters into the confined channel, progresses while deforming

and then reaches its equilibrium position/deformation. This illustrates the evolution of apparent elasticity as the deformation increases in the constriction.

In the same device, [Hu, 2018] reported a jump in apparent elastic moduli for deformation  $\epsilon > 0.5$ , corresponding to the sollicitation of the nucleus. The increase in modulus produced by the nucleus was smaller for MDA-MB-231 cells than for MCF-7 cells, indicating that MDA-MB-231 cells have a softer core. Following this observation, and several other studies of the mechanics of the nucleus, we will in the next chapter focus on the dynamics of deformation and recovery of the nucleus.

## 6 Short Conclusion

In this chapter, we presented the design and use of the Pachinko microfluidic chip. It allows to deform single cancer cells under flow within capillary-like constrictions, and to capture them within single cell nests traps to study their morphological recovery.

We demonstrated the study of morphological deformation and recovery at the whole cell level for three lines of breast cancer (presented in a submitted publication) and four colon cancer cell lines.

Our main findings at the whole cell level are the following :

- At the population level, cell arrest time depends on its size first. Then, for cells of similar size, the arrest time correlates with expected metastatic potential (for breast cancer lines). For colon cancer cells, the differences between primary and metastatic lines are more easily explained through their overall differences in cell size and arrest time.
- The dependence of the arrest time on the cell diameter shows less variability for cells representing an advanced stage of cancerous disease, suggesting a selection phenomenon highlighted by a mechanical signature.
- Cell deformation is characterized by a first viscoelastic increase, followed by a linear viscous increase.
- Cells recover almost entirely from the deformation, though we do observe some remaining deformation that may be attributed to cell plasticity.
- Recovery following flow-induced deformation presents two regimes : A fast elastic regime, followed by a slower viscoelastic regime.
- Viscoelastic recovery displays two characteristic times of the order of 1 s and 10 s.
- The presence on an actin cytoskeleton is required for recovery. Inhibiting actomyosin activity led to partial and slower recovery.
- We inferred rheological moduli for the different lines based on the fit of their recovery.

# CHAPTER 3

## PACHINKO : FOCUS ON THE NUCLEUS

In the previous chapter, we focused our study on the deformation and recovery mechanics at the whole cell level. However, as we explained in the introduction, this behavior stems from the combinatorial responses of inner cell components, including the cytoskeleton and the nucleus. We started to develop this point through the use of pharmacological treatments to perturb the actin cytoskeleton and the acto-myosin contractility. We will complete our approach by a study of the dynamics of the nucleus.

As the cell biggest organelle, its mechanics contributes greatly to that of the cell. Its stiffness is evaluated to be 2-10 times higher than that of the cytoplasm [Friedl, 2011b]. In the literature, the nucleus is often described as a complex viscoelastic material (chromatin) enveloped by an elastic shell (lamins) [Dahl, 2004; Stephens, 2017]. As high strain on the nucleus may results in damages, either the rupture of the nuclear envelope or double stranded DNA breaks [Nader, 2021a], it is important to understand the mechanics of the nucleus as it will influence the cells survival and behavior.

In this chapter, we'll present the dynamics of deformation and recovery of nuclei in the environment of the cell, studied in the Pachinko device. More precisely, we'll use Hoechst staining to follow nucleus morphology. We'll first show that the recovery of the nucleus is almost entirely elastic, then that a vimentin cage-like structure around the nucleus may contribute to this elastic behavior.

## 1 About the arrest time

### 1.1 Link with diameter

**Arrest time measurement is independent of staining** . As expected, staining cells with either DIL (membrane) or Hoechst (nucleus) does not impact crossing dynamics of the cell though the constriction. Indeed, no significant differences were observed between arrest distributions measured with either staining (see Fig.3.1a). We just note that minimal values are lower

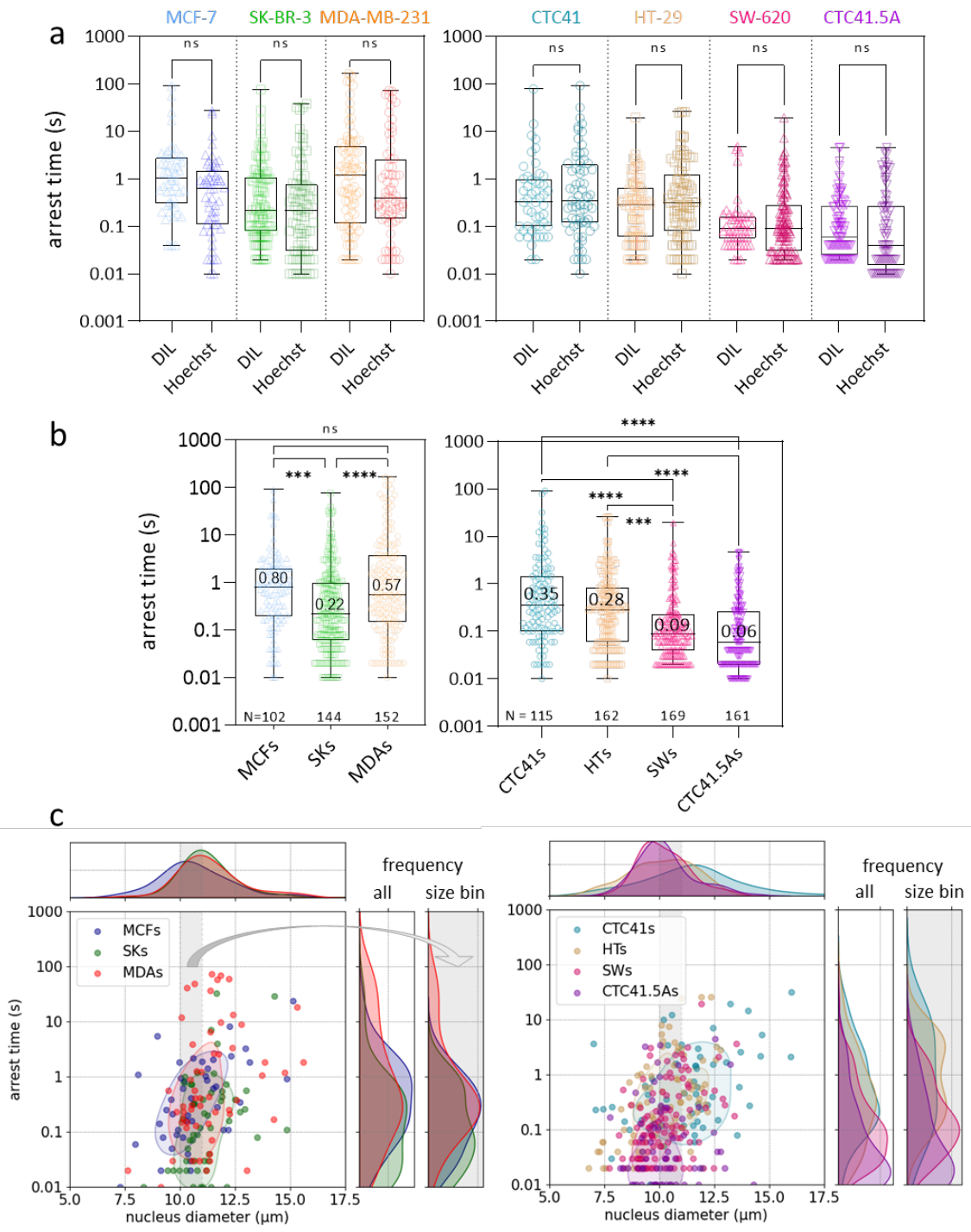


**Figure 3.1** – Arrest time of the nuclei of breast and colon cell lines. (a) Comparison of arrest times measured either with DIL or Hoechst staining (b) Pooling of arrest times distribution (both DIL and Hoechst measurements). Displayed values refer to the median. All significant differences are shown. (c) Scatter plots of the arrest time as a function of nucleus diameter. The contours of the highest points density are represented for each cell line. Top and side plots around the central scatter plot represents the density of nucleus diameters (top) or arrest times (right). Gray side plots represent the density of arrest times selected within the size bin 10-11  $\mu\text{m}$  (highlighted in gray in the central plot).

with Hoechst staining (0.01 ms) as we were able to increase the acquisition framerate from 50 to 100 fps due to the better contrast with Hoechst staining. We thus pooled all measurements together to determine the arrest time distribution (see Fig.3.1b).

**Arrest time distribution differs between cell types.** Merging the data points obtained on nuclei with the ones obtained at the level of the whole cell confirmed that the arrest times display different distributions between cell lines (see Fig.3.1b), as we already observed in the previous chapter.

We update the values that we presented in the paper for the breast cancer lines : MCF-7 cells display the highest median arrest time (800 ms), SK-BR-3 the lowest (220 ms) while MDA-MB-231 cells display an intermediate value (570 ms). Moreover, the significance of the differences between these three cell types increased with addition of more data points.

For colon cancer lines, we still observe two separate groups : CTC41 and HT-29 primary cell lines show no significant differences, as do SW-620 and CTC41.5A metastatic cell lines. As already observed for breast cancer cells, the significance of the differences between cell lines also increased, including addition of a significant difference between HT-29 and SW-620 cell lines, further separating both groups.

**Arrest time and nucleus diameter show no clear dependence.** We previously established a trend between the cell size and arrest time.

Though MCF-7 cells display slightly smaller nuclei (median 10.5  $\mu\text{m}$ ) compared to SK-BR-3 and MDA-MB-231 cells (11.4  $\mu\text{m}$  and 11.3  $\mu\text{m}$  respectively), it doesn't correlate with a significant lower arrest time (see Fig.3.1c). We even observe the opposite. Looking at nuclei of similar sizes, e.g. within the 10-11  $\mu\text{m}$  window (Fig.3.1c) does not change our conclusion.

Looking at the colon lines, we observe that the CTC41 cell lines have a higher nucleus diameter (median 11.5  $\mu\text{m}$ ) compared to HT-29, SW-620 and CTC41.5A cells (10.4  $\mu\text{m}$ , 10.1  $\mu\text{m}$  and 9.8  $\mu\text{m}$  respectively). Here too, there is no clear dependence between the size of the nucleus and the arrest time at the population level. Though we do observe a higher arrest time for CTC41 cells, the HT-29 cells of lower median nucleus size show a non-significant distribution of arrest time with the CTC41 cells (see Fig.3.1c). The differences in arrest time between the primary and metastatic lines were better explained by the differences in cell diameter, as described in the previous chapter.

## 2 Deformation of nuclei in the constriction

### 2.1 Deformation curves and fits

We then seek to follow the evolution of the deformation as the nucleus goes through the constriction. We plot in Fig.3.2 the mean deformation curves of nucleus for all cell lines.

These curves are difficult to fit, as the number of cells to contribute to the mean decreases versus time as more and more cells escape the constriction, thus resulting in a higher and higher noise as the arrest times increase. As we have done before for cells, we limit the fit to the first

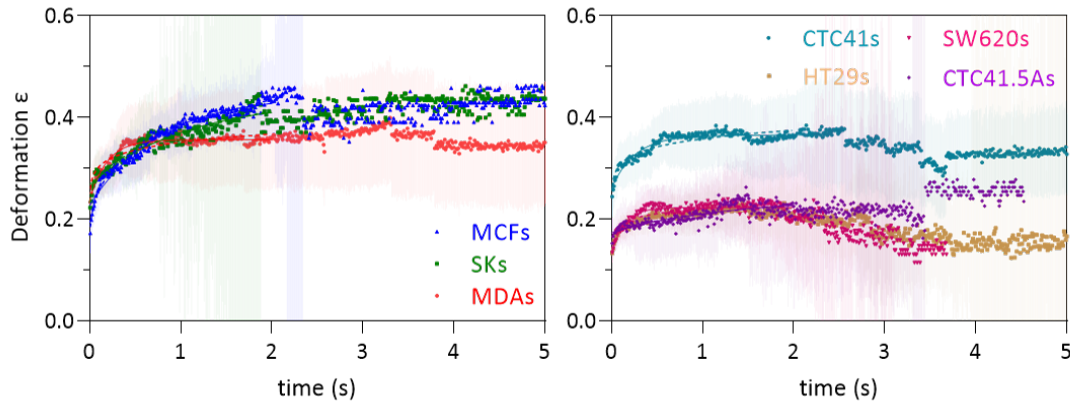


**Figure 3.2** – Deformation of the nucleus in the constriction (a) Mean deformation curves for all four cell lines and fits with either Kelvin-Voigt model (continuous line) or power law model (dashed line).

2 s. We represent on the graph the curves for the Kelvin-Voigt model and the power law fit. We report the corresponding parameters in the table 3.1.

Kelvin-Voigt

	MCFs	SKs	MDAs	CTC41	HTs	SWs	CTC41.5A
$\tau$	0.68 s [0.63-0.73]	1.65 s [1.09-2.21]	0.19 s [0.16-0.22]	0.34 s [0.32-0.37]	0.29 s [0.25-0.33]	0.14 s [0.12-0.17]	0.57 s [0.36-0.77]
$E$	1.38 kPa [1.34-1.41]	1.70 kPa [1.41-1.99]	2.31 kPa [2.11-2.52]	2.58 kPa [2.48-2.68]	4.68 kPa [4.32-5.03]	3.49 kPa [3.12-3.87]	5.26 kPa [4.58-5.94]
$\eta_1$	0.099 kPa.s [0.092-0.107]	0.298 kPa.s [0.244-0.352]	0.046 kPa.s [0.037-0.056]	0.093 kPa.s [0.083-0.102]	0.143 kPa.s [0.115-0.170]	0.054 kPa.s [0.040-0.067]	0.316 kPa.s [0.190-0.441]
$R^2$	0.970	0.883	0.813	0.946	0.832	0.447	0.547

Power law

	MCFs	SKs	MDAs	CTC41	HTs	SWs	CTC41.5A
$\beta$	0.23 [0.193-0.265]	0.54 [0.431-0.659]	0.07 [0.059-0.088]	0.09 [0.081-0.097]	0.08 [0.077-0.100]	0.07 [0.061-0.093]	0.10 [??-0.299]
$R^2$	0.972	0.889	0.566	0.777	0.785	0.548	0.534

**Table 3.1** – Fit parameters resulting from the Kelvin-Voigt and power law fits on deformation curves

Overall, the shape of the deformation curves of breast cancer nuclei is quite similar. MDA-MB-231 nuclei however reach a lower plateau than the other two types, which translates into a higher elasticity and a lower viscosity. As for the colon lines, we observe the CTC41 to deform to an higher extend than the other lines, which corresponds to a lower elastic modulus.

However, we acknowledge the quality of the fits to be quite poor (see values of  $R^2$ ). Among the possible explanations of this insufficient quality, let's mention that due to the flared geometry of the exit of the constriction, we observed that some nuclei start to recover while the whole of the cell is still being stuck in the constriction (see CTC41, HT-29 and SW-620 nuclei for

instance). Such a phenomenon, by mixing the dynamics of deformation and recovery, is expected to interfere with the analysis of the deformation regime. Following this observation, we'll propose in Appendix D an evolution of the Pachinko design to remedy it, among other modifications.

Thus, we'll remain cautious about the obtained parameters. We can still notice the magnitude of the parameters to be similar ( $E \approx 1\text{-}5$  kPa and  $\eta_1 \approx 50\text{-}300$  Pa.s), with higher elastic values for MDA-MB-231 cells among the breast cancer lines, and CTC41.5A among the colon cancer lines.

**Fit on the individual cells.** As the mean fits were not conclusive, we turned to individual fits of each cell and plot the distribution of  $E$ ,  $\eta_1$  and, if the arrest time is long enough,  $\eta_2$  obtained from these individual fits in Fig.3.3 for both breast and colon cells. Let's note that some individual curves, for which the fitting procedure failed, were discarded of this analysis.

We observe the elasticity values  $E$  obtained from individual fits to be of the same order as those from the mean curves, though viscosity values  $\eta_1$  were consistently lower for all cell lines ( $\approx 10\text{-}50$  Pa.s for individual fits, vs  $\approx 50\text{-}300$  Pa.s for the mean). Estimation for  $\eta_2$  viscosity, corresponding to the linear increase in deformation at long time scale, gives values in the range 200-1000 Pa.s, with values being higher for colon nuclei than breast nuclei. As the arrest time for CTC41.5A cells is the lowest among all colon cell lines, only a few CTC41.5A nuclei were recorded long enough to be fitted with a Jeffrey's model. The increased viscosity  $\eta_2$  compared to the other colon cell lines shown in Fig.3.3 can be thus consider as an artefact resulting from a limited and biased cell sampling.

Comparing the values obtained for the whole cell and nucleus separately, we do observe the nucleus to present higher elastic modulus in average for both breast and colon cancer lines. We also note an increase in long-term viscosity  $\eta_2$  for the nuclei of colon lines, which isn't observed for breast cancer lines.

## 2.2 Nucleus positioning through the constriction

To further decipher the respective contribution of the nucleus and cytoplasm in the arrest time, we next examined the position of the center of mass and longitudinal extent of both cells and nuclei during their journey into the constriction (Fig. 3.4a). We focused on cells and nuclei which spend long enough time in the constriction so that at least 100 points were recorded. The temporal position of these cells and nuclei was normalized by their respective arrest time so that all enter the constriction at  $t_{Norm} = 0$  and exit at  $t_{Norm} = 1$ .

First, we observed that these positions display a remarkable coincidence of the center of mass of the nuclei and of the cells for all cell lines (Fig. 3.4a). Overall, the cell and nuclei rapidly enters the constriction, then they linearly progress through the narrow 6  $\mu\text{m}$  wide opening until most of the cell (Fig. 3.4b) and nucleus (Fig. 3.4c) has crossed the neck of the constriction.

We observe SK-BR-3 cells to first stop further in the constriction compared to the others, which is linked to their relative smaller diameter. Overall, the nucleus and cell membrane deform and transit simultaneously as they are crossing the constriction. Thus, we cannot exclude either element as being a limiting factor in the process of cell crossing. Indeed, if the limiting behavior

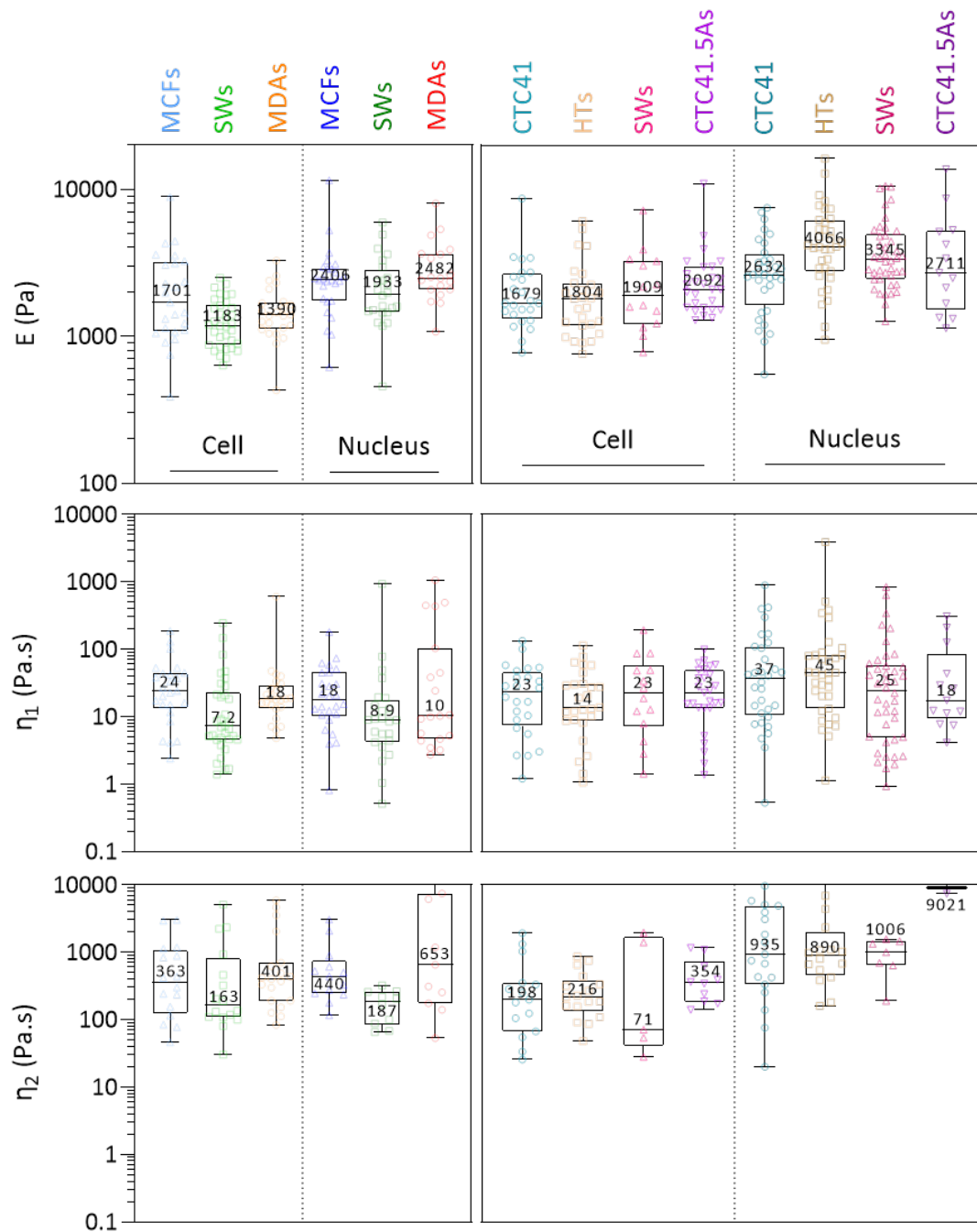


**Figure 3.3** – Individual cells fit parameters ( $E$ ,  $\eta_1$  and  $\eta_2$ ) using Jeffrey's model deformation. When  $\eta_2$  wasn't able to be computed, fit was changed to Kelvin-Voigt model ( $E$  and  $\eta_1$  only). Cells for which the fit did not converged were excluded from the plots.

of the nucleus due to its high viscosity compared to the cytoplasm seems intuitive, studies showed that disrupting the acto-myosin cortex of cells with Latrunculin B results in reduced arrest time [Urbanska, 2020; Byun, 2013], thus confirming the contribution of the cell cortex in the overall arrest time as well.

Interestingly, we did not observe any rearrangement of the nucleus within the cell as they

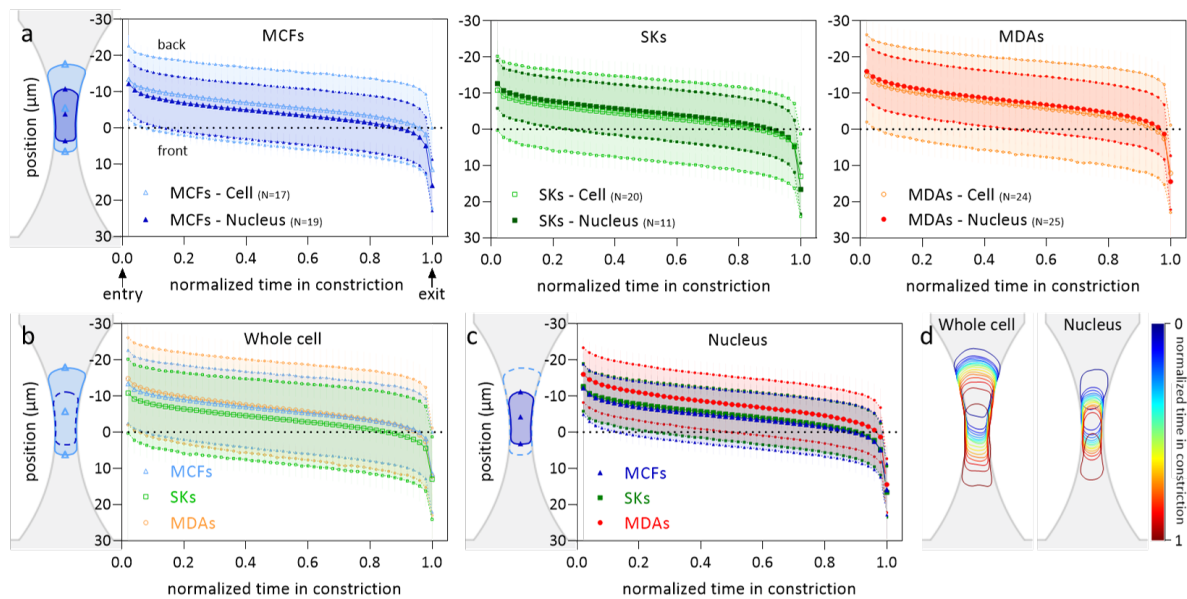


**Figure 3.4** – Spatio-temporal dynamics of cell and nucleus inside the constriction. (a) Cell and nucleus center position ( $\pm$ SD) relative to the center of the constriction as the cell crosses the constriction. Upper and lower curves represent respectively back and front position of the cell. For each cell, time has been normalized by  $1/\text{arrest time}$  to overlay curves. Only curves with at least 50 points were considered for this graph. (b&c) Superimposition of the curves shown in (a) to compare only cells (b) or (c) nucleus positions between cell lines. (d) Outline of an example of a whole cell and a nucleus at different time points as they progress through the constriction.

are being deformed. The nucleus seems to remain at the same position within the cell during the transit through the constriction. Indeed, we could have expected the stiffer nucleus to relocate at the rear of the cell, similarly to what can be observed during free migration [Gundersen, 2013].

In these cells which spend  $> 1$  s in the constriction, we do observe a linear progression regime as they cross the constriction. This regime could be associated with the viscous linear increase in deformation reported by [Davidson, 2019] for instance.

### 3 From deformation to recovery

We measured the maximal deformation of nuclei during their deformation. For breast cancer lines, max deformation ranges from 30 to 35% (with no significant differences between the three cell lines). It ranges from 20 to 40% in colon cell lines with a significant distinction between the median of CTC41 and the rest, which could be explained by the bigger size of CTC41 nuclei.

Compared to the whole cell (see previous chapter), the nuclei max strain is slightly inferior than for the whole cell, with the exception of CTC41 cells due to the size of their nuclei. We can thus deduce that the nucleus is being less deformed than the rest of the cell, as the nucleus is expected due to its higher Young modulus than the cytoplasm [Friedl, 2011b].

**With the exception of CTC41, nuclei of all cell lines recover almost entirely from the deformation.** Indeed, values for  $\varepsilon_\infty$  are close to zero, which characterizes complete recovery.

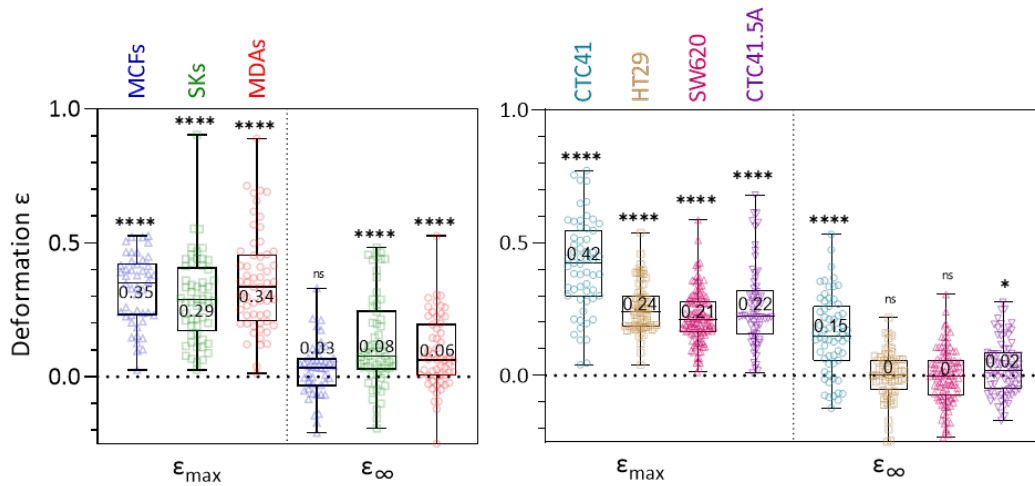


**Figure 3.5** – Nucleus deformation measured in the constriction ( $\epsilon_{max}$ ) and after recovery ( $\epsilon_{\infty}$ ). Statistical difference to  $\epsilon_0 = 0$  is shown.

At the whole cell level, we attributed small residual deformations (sometimes significant) to plasticity (as reported for SK-BR-3 and MDA-MB-231 nuclei in similar conditions [Ahmad-Cognart, 2020]).

However, the residual deformation in CTC41 nuclei approach 15% in average. We could attribute this to nuclei plasticity or remodelling as the nuclei was deformed.

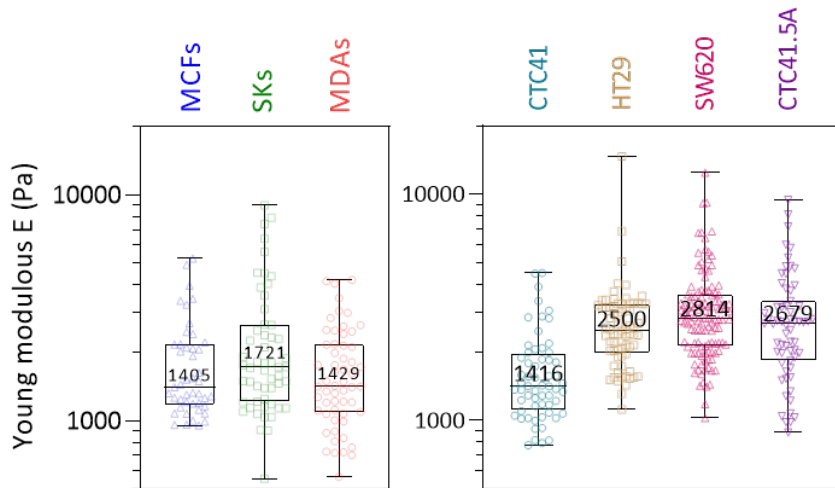


**Figure 3.6** – Distribution of  $E_{tot} = \frac{\Delta P}{\epsilon_{max}}$  for the three cell lines. Statistical comparison between each cell lines is represented.

Similarly to the approach we took at the whole cell level, we estimate a value for elasticity using Hooke's law :

$$\sigma \approx \Delta P \approx E_{tot} \epsilon_{max}$$

The resulting values for  $E_{tot}$  are given Fig.3.6. They range at  $\approx 1.4$ -1.7 kPa for breast lines ; and

between 1.4 kPa for CTC41 nuclei to  $\approx 2.5$ -2.8 kPa for HT-29, SW-620 and CTC41.5A nuclei. We'll compare these values with the behavior of nuclei in recovery.

## 4 Results : Nucleus recovery is mostly elastic

### 4.1 Recovery curves and fits

As the cell escapes, the constraint applied on the nucleus is released, leading to its morphological recovery. The deformation thus decreases rapidly, as seen on representative images in Fig.3.7. The corresponding recovery curves are shown in Fig.3.8.

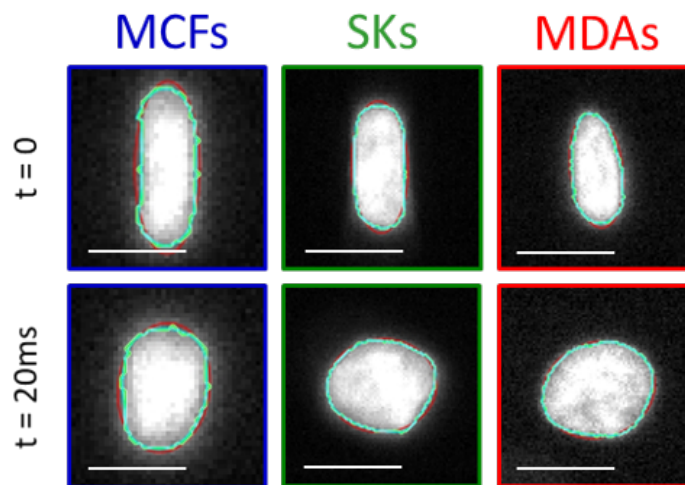


**Figure 3.7** – Representative breast nuclei recovery. Images were taken at the last image in the constriction ( $t = 0$ ) and 20 ms ( $t = 20$  ms) following escape from the constriction. Scale bar = 20  $\mu\text{m}$ .

**Recovery is composed of a fast elastic regime followed by a slower viscoelastic recovery.** Interestingly, a two phase decay (instead of three for the whole cell, see Suppl.Fig.C) provides high quality fits for the recovery curves of the nuclei of all cell lines, leading to the expression  $\varepsilon_{Norm}(t) = a_{fast} \exp^{-t/\tau_{fast}} + a_{slow} \exp^{-t/\tau_{slow}}$ . Except for MDA-MB-231 cells, we found for each cell lines that the characteristic time  $\tau_{slow}$  is of the order of the second, while  $\tau_{fast}$  is of the order of 100 ms (see Tab.3.2).

Similarly to the approach taken at the whole cell level, as the order of magnitude for  $\tau_{fast}$  is close to our acquisition framerate, we chose to merge it with the elastic regime. We define  $\Phi_{VE} = \frac{a_{slow}}{a_{fast} + a_{slow}}$  as the transition from elastic to viscoelastic regime, in the case of a two exponential decay fit. From this measure, we then find two groups : MCF-7, SK-BR-3 and CTC-41 nuclei display a  $\Phi_{VE} \approx 12\%$  on one side ; and HT-29, SW-620 and CTC41.5A display  $\Phi_{VE} \approx 6\%$  on the other. The elastic regime thus presents a higher proportion ( $\approx 94\%$ ) in the recovery for the latter group.

For the case of MDA-MB-231 nuclei, both measured characteristic times fall within the range that we defined as elastic, with  $\tau_{slow}$  being quite different than all the other cell lines. We thus

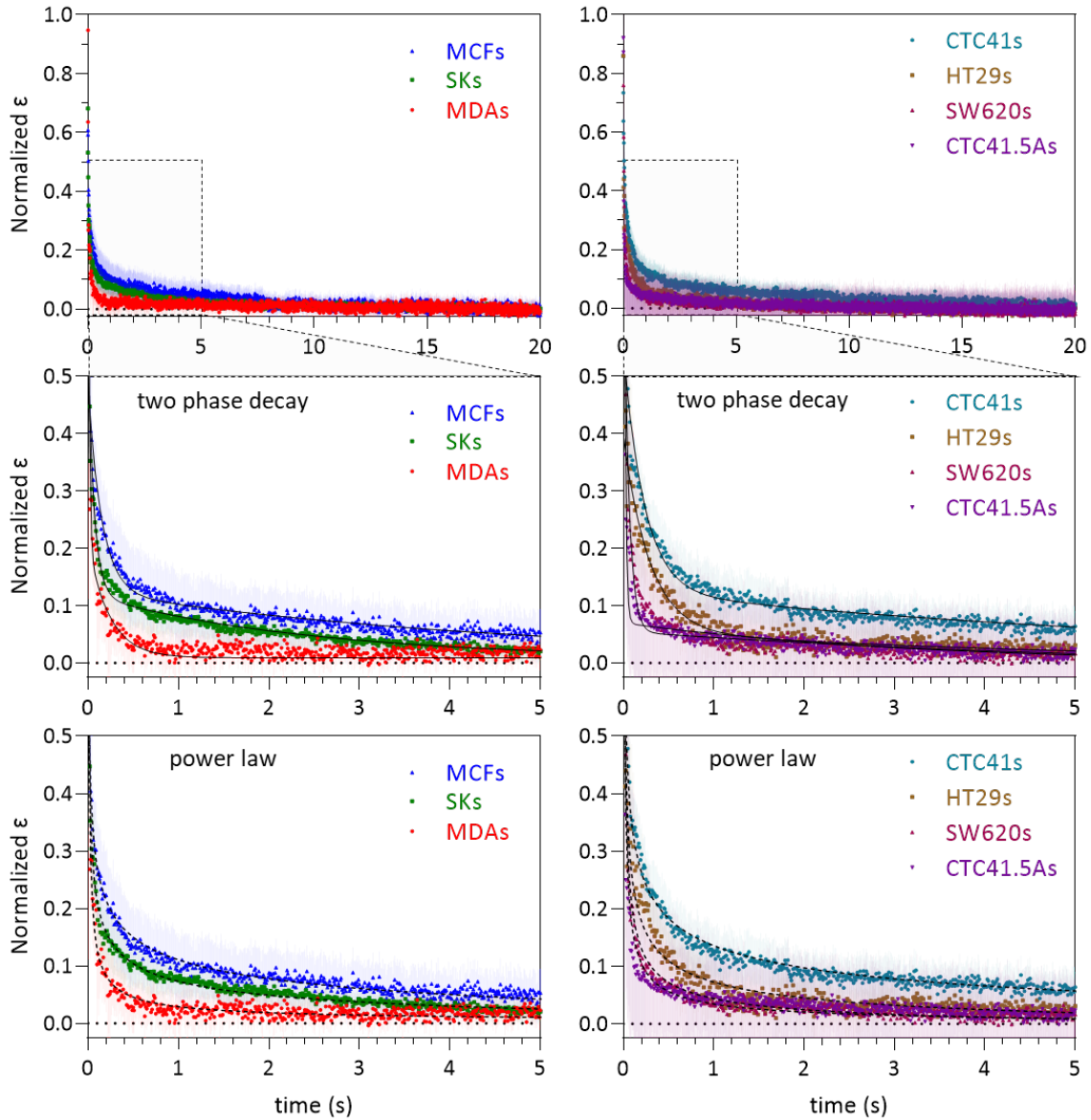


**Figure 3.8** – Nucleus recovery. Mean normalized  $\varepsilon(t)$  curves after exiting the constriction (taken as starting point  $t=0$ ). Bottom graphs display a zoom over the first 5 seconds of the recovery curves for breast (left) and colon (right) nuclei. Error bars represent confidence interval at 95%. Fitting curves represent two-phases decay (middle graphs) or power law (bottom graphs) fits of the mean curves. Corresponding characteristic times (with confidence interval at 95%) are reported in table 3.2.

chose to arbitrarily attribute to this cell line a  $\Phi_{VE} = 0$ , meaning we consider its recovery to be entirely elastic (though we could have chosen another value, making it closer to HT-29, SW-620 and CTC41.5A).

**Power law fits recapitulate elastic recovery better than a two phase decay.** Finally, we also computed power laws fits. The resulting exponents are  $n_{MDAs} = 0.66$ ,  $n_{SKs} = 0.36$  and  $n_{MCFs} = 0.26$  for breast nuclei, reflecting very well the relative arrangement of the three curves,

two phase decay fit							
	MCFs	SKs	MDAs	CTC41	HTs	SWs	CTC41.5A
$\tau_{fast}$	0.15 s [0.14-0.16]	0.069 s [0.067-0.072]	0.013 s [0.012-0.014]	0.23 s [0.22-0.24]	0.29 s [0.28-0.30]	0.055 s [0.053-0.059]	0.026 s [0.025-0.027]
$\tau_{slow}$	4.92 s [4.71-5.15]	2.45 s [2.39-2.52]	0.23 s [0.224-0.240]	6.51 s [6.17-6.89]	6.18 s [5.57-6.94]	5.74 s [5.17-6.40]	3.77 s [3.52-4.06]
$R^2$	0.945	0.968	0.759	0.963	0.93	0.915	0.868
$\Phi_{VE}$	12.2 % [11.9-12.4]	11.3 % [11.1-11.4]	0 % *	11.7 % [11.6-12.0]	6.1 % [5.8-6.3]	6.7 % [6.5-6.8]	6.7 % [6.5-7.0]
$E_{tot}$	1.71 kPa [1.47-2.24]	2.16 kPa [1.71-2.70]	1.79 kPa [1.47-2.17]	1.42 kPa [1.26-1.68]	2.50 kPa [2.20-2.85]	2.85 kPa [2.63-3.16]	2.69 kPa [2.02-2.85]
$E_{elastic}$	1.50 kPa [1.29-1.97]	1.91 kPa [1.52-2.40]	1.79 kPa [1.47-2.17]	1.25 kPa [1.12-1.49]	2.35 kPa [2.07-2.68]	2.66 kPa [2.46-2.95]	2.51 kPa [1.88-2.66]
$E_{viscoelastic}$	0.21 kPa [0.18-0.27]	0.24 kPa [0.19-0.30]		0.17 kPa [0.15-0.20]	0.15 kPa [0.13-0.17]	0.19 kPa [0.17-0.21]	0.18 kPa [0.14-0.19]
$\eta_{slow}$	1.02 kPa.s [0.87-1.35]	0.59 kPa.s [0.47-0.75]		1.09 kPa.s [0.95-1.30]	0.94 kPa.s [0.79-1.11]	1.09 kPa.s [0.95-1.26]	0.68 kPa.s [0.51-0.75]
power law fit							
	MCFs	SKs	MDAs	CTC41	HTs	SWs	CTC41.5A
$n$	0.26 [0.254-0.270]	0.36 [0.357-0.386]	0.66 [0.644-0.677]	0.30 [0.290-0.303]	0.42 [0.413-0.435]	0.55 [0.544-0.563]	0.63 [0.617-0.650]
$R^2$	0.951	0.976	0.812	0.966	0.905	0.920	0.846

**Table 3.2** – Parameters obtained from the two phase exponential decay and power law fits of the nucleus recovery and deduced rheological parameters. Values represent median and 95% confidence intervals.

with that of MDA-MB-231 being closest to the axes .

As for the colon lines, the some ordering can be observed :  $n_{CTC41} = 0.30$ ,  $n_{HTs} = 0.42$ ,  $n_{SWs} = 0.55$  and  $n_{CTC41.5A} = 0.63$ .

Similarly to the results obtained with the fits based on rheological models, we find MDA-MB-231, SW-620, CTC41.5A (and HT-29 to a lesser extent) to be the more elastic. Though, the power law fit require less parameters and gives good quality (see  $R^2$ ).

## 5 Link with cancer aggressiveness

### 5.1 EMT and vimentin

In the recovery curves we observed differences of behavior between the cell lines that we'll try now to explain by looking at the protein levels of some proteins involved in the nucleus mechanics, namely the lamins and the vimentin intermediate filaments.

To do so we quantified the relative proteins levels for vimentin and lamin A, C, B1 and B2. We present Fig.3.9a the first results of the Western Blots I performed on the breast cancer cell lines with the help of Kotryna Vaidižulytė. We also provide the quantification for colon cancer lines (Fig.3.9b) performed by Kotryna Vaidžiulytė and Nassiba Abbade (with more replicates).

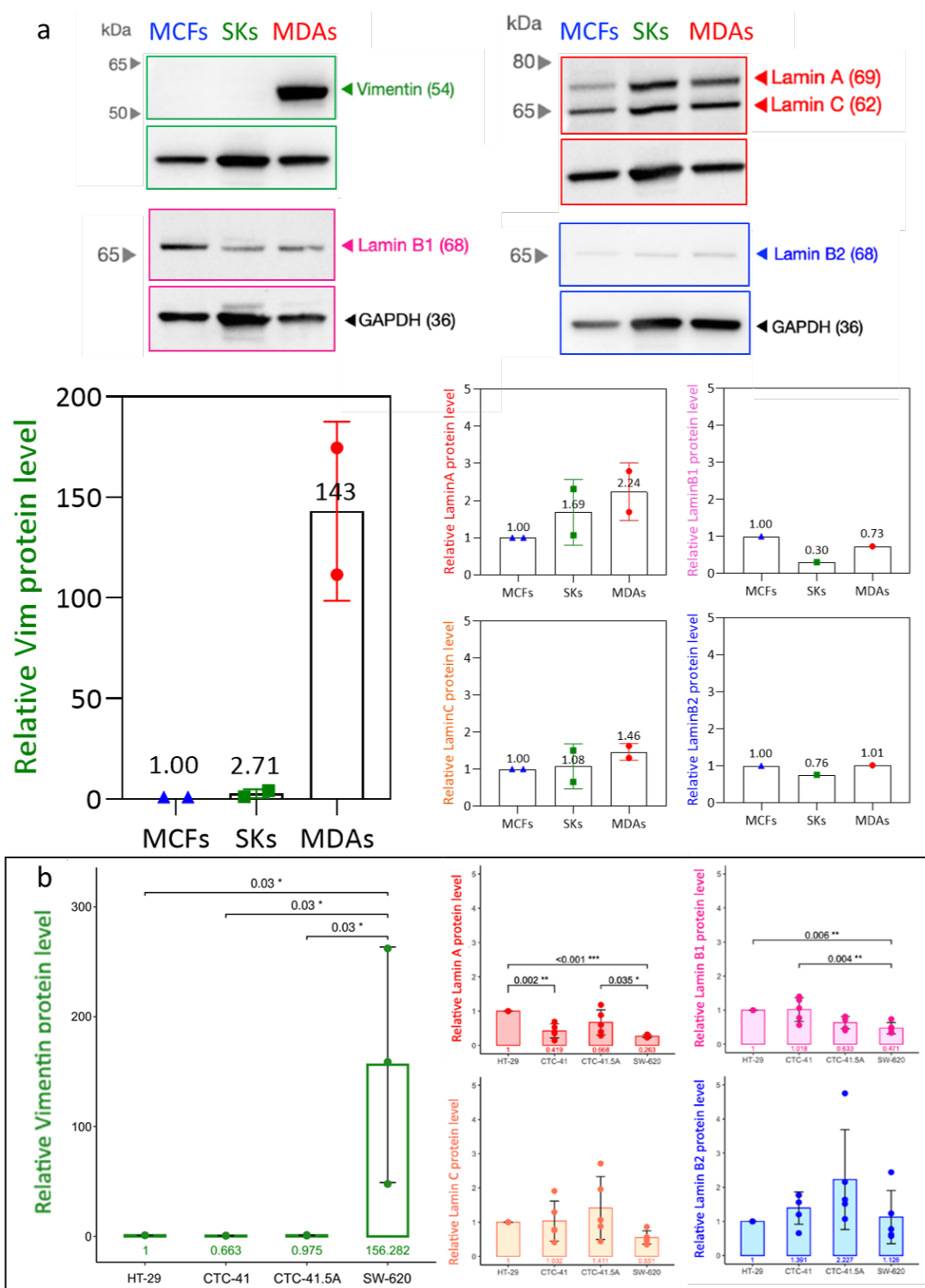


**Figure 3.9** – Quantification of vimentin, lamin A, lamin C, lamin B1 and lamin B2 levels in (a) breast and (b) colon cancer cell lines. Representative blots (top) and quantification of relatives levels (normalized to GAPDH levels). For reference, MCF-7 and SW-620 levels are set to 1. Western blots on colon cell lines were performed by Nassiba Abbade and Kotryna Vaidžiulytė (Breast : N = 2 for Vim, Lamin A and C ; N = 1 for Lamin B1 and B2).

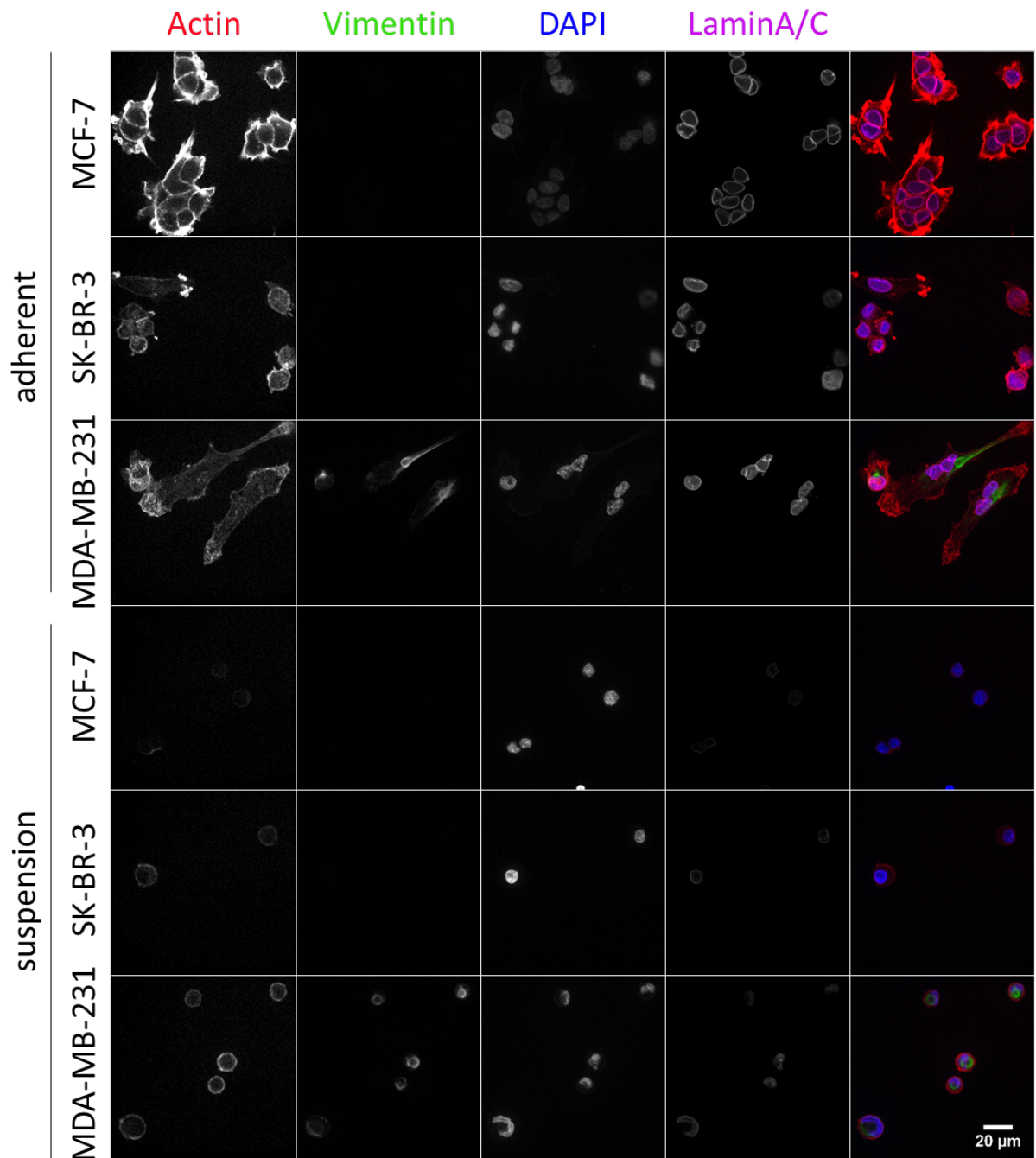


**Figure 3.10** – Immunofluorescence staining of breast cancer cells for actin (phalloidin, red), vimentin (green), nucleus (DAPI, blue) and Lamin A (magenta). Only MDA-MB-231 cells present a vimentin cage, both in adherent and suspended state.

**Vimentin is only expressed in MDA-MB-231 and SW-620 cells** . These two lines are among the ones we refer to as metastatic. As we saw in the introduction, vimentin is also a marker for the epithelial-to-mesenchymal transition (EMT). As it can be appreciated in MDA-MB-231 suspended cells (Fig.3.10), vimentin forms a cage-like structure around the nucleus. Interestingly, we observe the vimentin organisation to be different in adherent MDA-MB-231 cells.

**Relative lamins levels are close between cell lines.** The difference in lamins proteins levels are more subtle. As LaminA/C is known to contribute to the nucleus mechanics [Lammerding, 2006], and because the differences in Lamins B1&2 are relatively small, we will focus our interest on LaminA/C. Interestingly, with only 2 replicates, it would appear than MDA-MB-231 display an higher level of Lamin A (and C to a lesser extent) than MCF-7 and SK-BR-3. Similarly, CTC41 and SW-620 display a lower Lamin A level compared to the other cell lines.

Among the recovery curves, we identified a more elastic nucleus recovery for MDA-MB-231, SW-620 and CTC41.5A cells, and HT-29 to a lesser extent. The case of MDA-MB-231 could be explain by the presence of a vimentin cage around the nucleus. Though HT-29 and CTC41.5A do not express vimentin, their laminaA/C levels is higher than for SW-620s, which could contribute to the more elastic nature in their recovery. Then we are left with MCF-7, SK-BR-3 and CTC41 cells, which do not express vimentin and have lower levels of lamins A/C, and are the one to present the higher proportion of viscoelasticity in their nucleus recovery.

## 6 Role of vimentin filaments

As we identified different vimentin expression patterns in the different cell lines, we then sought to understand its effect in nucleus rheology. The literature describes vimentin to have a cage-like structure around the nucleus and act as a "shock absorber" [Block, 2017]. To do so, we chose to knock down vimentin levels in SW-620 cells, and reversely to expressed it in a cell line where it is endogenously absent, i.e. HT-29.

### 6.1 Vimentin knockdown in SW-620 cells

#### 6.1.1 Protocol optimisation

Contrary to other cytoskeletal filaments (actin, microtubules, ...), we found no drugs able to depolymerize the vimentin network. This can be attributed to the stable nature of intermediate filaments networks. We thus turned to short interfering RNA (siRNA) to knock down the expression of vimentin proteins in the cells. An optimisation of the silencing protocol was performed by an intern, Nassiba Abbade, with the help of Kotryna Vaidžiulytė. Among the different conditions tested (see Fig.3.11a), we selected the condition "2x48h", which corresponds to 2 successive transfections of siRNA for a duration of 48h (96h total). This condition was successful in reducing vimentin protein levels by  $\approx 90\%$ , and is next referred to as "siVim" cells ("siNT" is used for the control treated in a similar way with non-targeting siRNA).

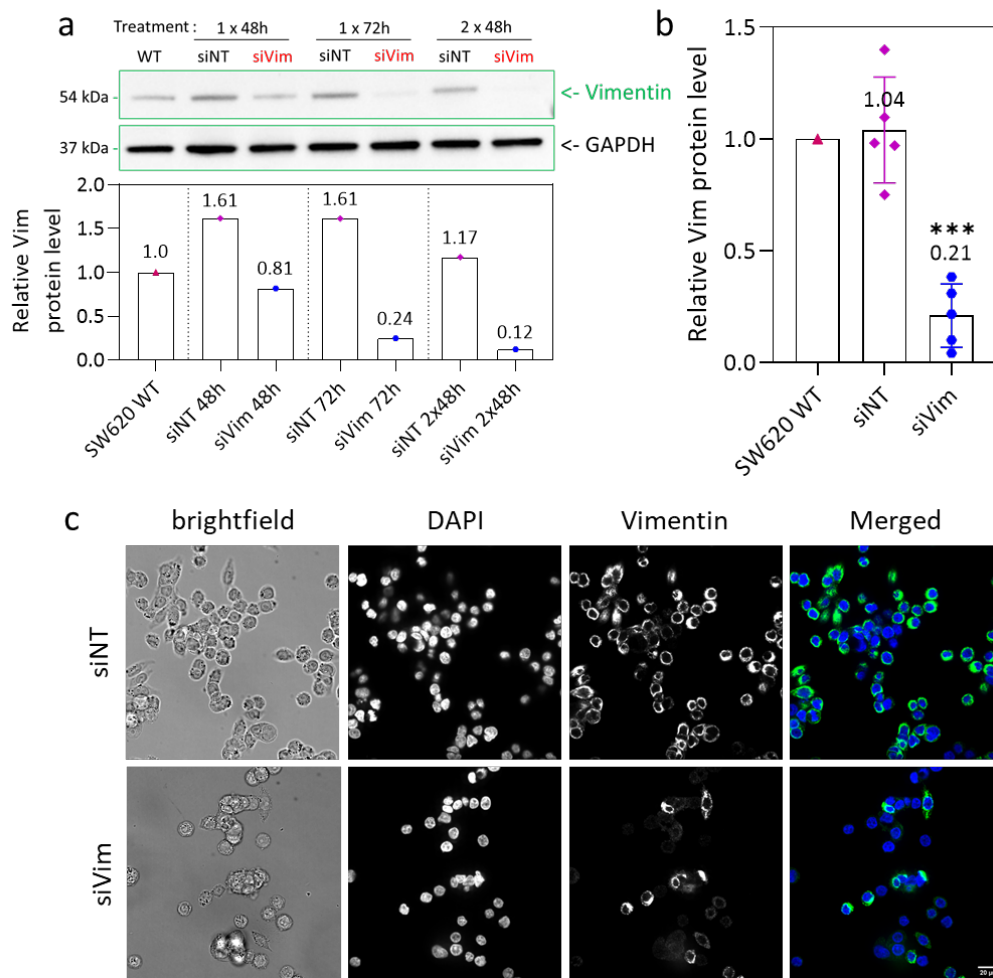


**Figure 3.11** – Optimisation of siRNA transfection protocol in SW-620 cells. (a) Different treatment duration are tested (48h, 72h, 2x48h). Vimentin protein levels (relative to GAPDH) are quantified at the end on the transfection. WT = non treated wild type SW-620 cells, siNT = non-targeting siRNA, siVim = Vimentin targeting siRNA. (b) Relative vimentin protein levels in all performed experiments. Vimentin protein levels are decreased by  $\approx 80\%$  in average. (c) Immunofluorescence of siRNA transfected SW-620 cells for 2x48h (scale bar = 20  $\mu\text{m}$ ). Images were taken at the end of the transfection.

Immunofluorescence imaging of the siRNA transfected cells confirmed the efficiency of the protocol. The overall proteins levels in siVim cells were decreased, and remaining vimentin protein show disorganisation compared to the control (see Fig.3.11b).

During experiments with these transformed cells, vimentin protein levels were assessed after each silencing protocol, and compared to siNT cells. In all experiments, the vimentin levels were reduced by  $\approx 80\%$  in average (see Fig.3.11a).

### 6.1.2 Change to $3 \times 15 \mu\text{m}^2$ constrictions

We began using these cells in Pachinko experiments and noticed that almost all of the cells were going through the  $6 \times 15 \mu\text{m}^2$  constrictions in less than one frame ( $< 10 \text{ms}$ ). Analysis of these first sequences revealed that the siRNA treated cells (both siVim and siNT) displayed

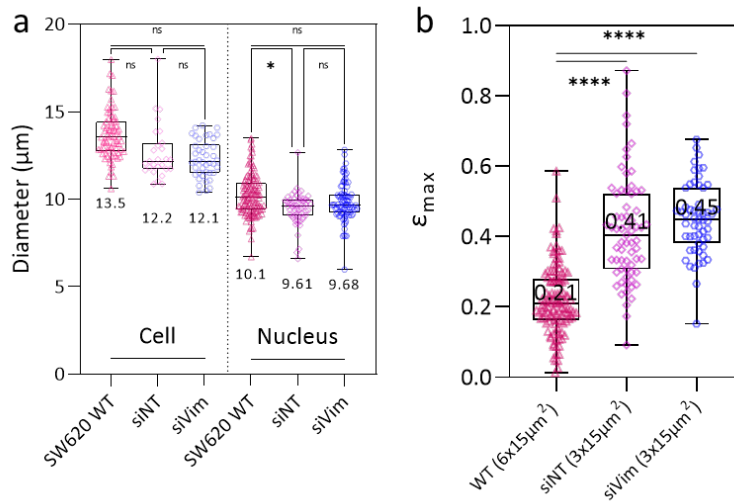


**Figure 3.12** – (a) Box plots of SW-620 cells diameters. WT = non treated wild type SW-620 cells and nucleus, siNT = non-targeting siRNA, siVim = Vimentin targeting siRNA. (b) Max deformation levels in WT SW-620 cells ( $6 \times 15 \mu\text{m}^2$  chip) and siRNA transfected SW-620 cells ( $3 \times 15 \mu\text{m}^2$  chip).

significantly reduced diameters ( $> 1 \mu\text{m}$  at the cell level, see Fig.3.12a). We attribute this decrease in size to the high confluency of cells in wells at the moment of harvesting, as cells volume start to decrease do to the compaction. Indeed, during the 2x48h treatment, SW-620 cells kept growing beyond the threshold of confluence. The starting cell seeding density was probably too high and this parameter (and the depending ones : amount of siRNA and reagents per cell) would need to be adjusted in following experiments.

Nonetheless, in order to use these cells, we chose to use chips with smaller constriction width ( $3 \times 15 \mu\text{m}^2$  constrictions) so that cells arrest time are long enough to be analyzed. However, using these smaller constrictions resulted in a higher median deformation levels of nuclei in the constriction ( $\approx 40\text{-}45\%$ , see Fig.3.12b) than the typical ones for nuclei in previous experiments ( $\approx 20\%$  for SW-620 nuclei).

### 6.1.3 Recovery of siVim SW-620 nuclei

We present Fig.3.13 the mean recovery curves for siRNA transfected SW-620 cells.

Even though deformation levels are different, we observe a nice overlap between the WT SW-620 nuclei deformed in  $6 \times 15 \mu\text{m}^2$  constrictions, and siNT SW-620 nuclei deformed in  $3 \times 15 \mu\text{m}^2$  constrictions.

**Vimentin knockdown impairs elastic recovery in SW-620 nuclei.** As it can be seen in the graphs, we observe the mean recovery of siVim SW-620 nuclei to display a stronger signature of the viscoelastic regime.

The curves were modeled with a two phase decay fit. Though both fast and slow characteristic times are similar in both fits ( $\tau_{fast} \approx 170 \text{ ms}$  for siNT and  $130 \text{ ms}$  for siVim ;  $\tau_{slow} \approx 5.65 \text{ s}$  for siNT and  $5.25$  for siVim), the difference in both fits can be appreciated through the amplitude

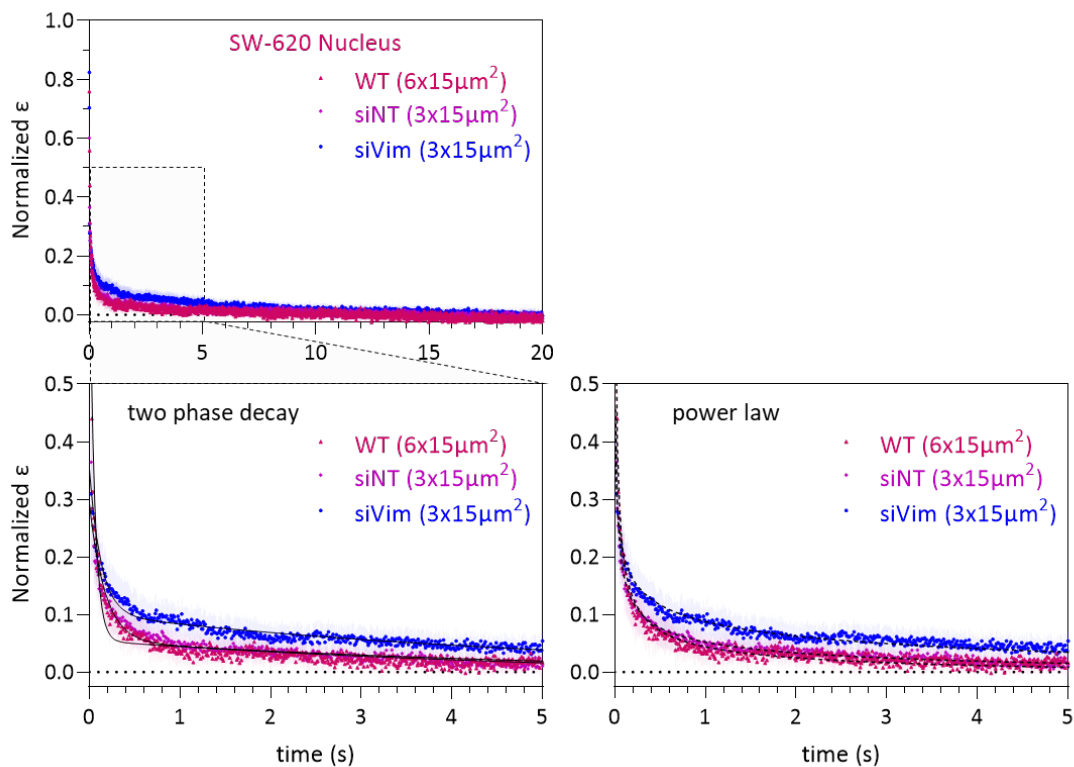


**Figure 3.13** – Impact of Vimentin knock-down in SW-620 cells on nucleus recovery. Mean normalized  $\varepsilon$  curves after exiting the constriction (taken as starting point  $t=0$ ). Bottom graph displays zoom over the first 20 seconds. Error bars represent confidence interval at 95%. Fitting curves represent two-phases decay (bottom left) or power law (bottom right) fits of the mean curves.

of the viscoelastic regime (associated to  $\tau_{slow}$ ) : It represents  $\approx 6\%$  for siNT nuclei and  $\approx 10\%$  for siVim nuclei. Even if the differences appears small, they can be appreciated on the graph and are of the same order of magnitude of the differences observed between the colon cell lines previously described. This is characterized particularly highlighted through the lower exponent in power law fits for siVim nuclei ( $n_{siVim} = 0.21$ ) than for siNT nuclei ( $n_{siNT} = 0.40$ ) and WT ( $n_{WT} = 0.55$ ).

We then deduce that the vimentin cage-like structure formed around the nucleus plays a role in the rheological properties of the nucleus, more precisely increasing its elasticity.

## 6.2 Expression in HT-29 cells

We then took the opposite approach and expressed vimentin in HT-29 cells that do not endogenously express it. We dispose of two plasmids, each containing the gene for the vimentin protein, tagged with either mEmerald (#54299, Addgene) or mCherry (#55158, Addgene). We'll refer to these plasmids respectively as "mEmerald" and "mCherry".

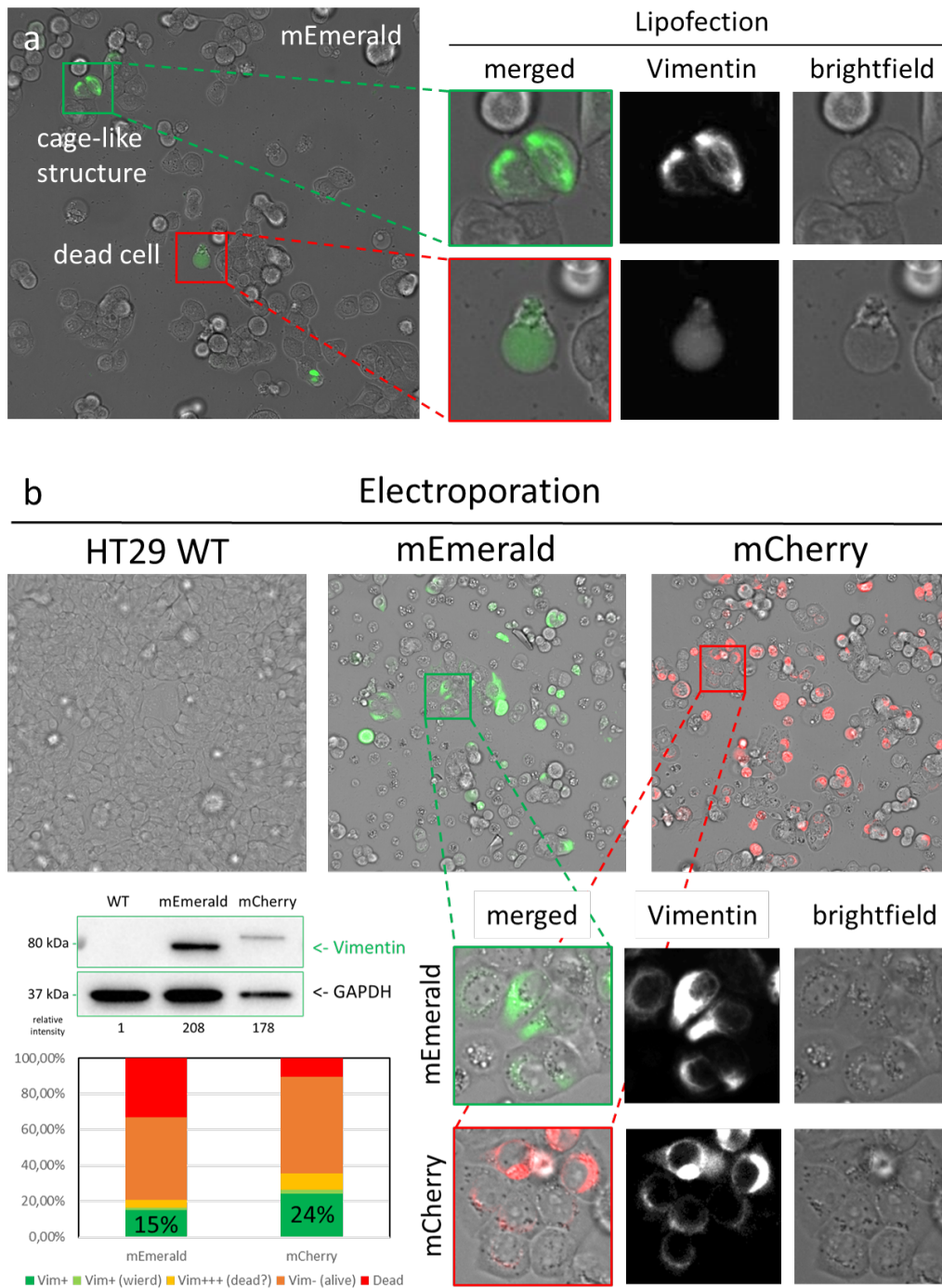


**Figure 3.14** – Optimisation of vimentin transfection protocol. Two plasmids were tested, referred as "mEmerald" and "mCherry" (see text for more details). (a) Imaging of "mEmerald" transfected cells through lipofection. (b) Imaging of "mEmerald" and "mCherry" transfected cells through electroporation. Quantification of relative vimentin protein levels. Classification of transfection efficiency (Vim+ : good transfection level and good protein organisation, Vim+++ : over-expression of vim, Vim- : absence of visible vimentin). "mCherry" plasmid was selected for further experiments.

### 6.2.1 Transfection protocol

To transfect the two plasmids into HT-29 cells, we first tried lipofection (see Fig.3.14a). This method resulted in a low transfection efficiency ( $< 10\%$ ) and a few cells which incorporated an excessive amount of plasmids. Though the organisation of vimentin in the rest of Vim+ cells was well recapitulating the expected cage-like structure around the nucleus.

We then turned to electroporation to insert the plasmids into the HT-29 cells (see Fig.3.14b), which increase overall efficiency. Transfection with "mCherry" plasmid was selected in the end as it resulted in  $\approx 24\%$  of the cells to display correct levels of vimentin with a good organisation.

### 6.2.2 Recovery of trVim HT-29 nuclei

These cells were used in Pachinko experiments with  $3 \times 15 \mu\text{m}^2$  constrictions. We'll refer to the transfected cells as "trVim". The resulting recovery curves are shown in Fig.3.15.

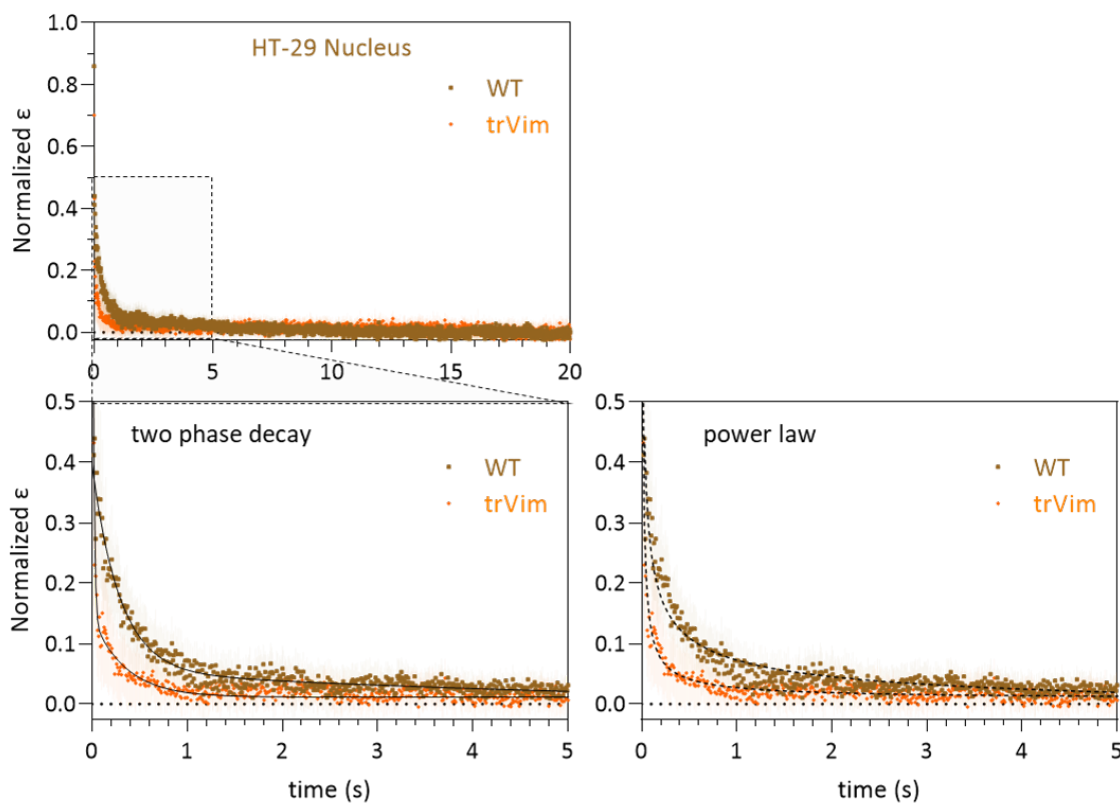


**Figure 3.15** – Impact of Vimentin expression in HT-29 cells on nucleus recovery. Mean normalized  $\varepsilon(t)$  curves after exiting the constriction (taken as starting point  $t=0$ ). Bottom graph displays zoom over the first 20 seconds. Error bars represent confidence interval at 95%. Fitting curves represent two-phases decay (bottom left) or power law (bottom right) fits of the mean curves.

**Vimentin expression enhance elastic recovery in HT-29 nuclei.** We observe that trVim nuclei recover faster from the deformation than WT HT-29 nuclei.

Compared to two characteristic times returned by the fit for HT-29 ( $\tau_{fast} = 290$  ms and

$\tau_{slow} = 6.2$  s), the same fit for the trVim nuclei returns a characteristic time  $\tau_{fast} = 350$  ms (and a second one = 14 ms that we'll disregard for it being too close to the acquisition frame rate of 10 ms). Power law fit exponent increase from  $n = 0.42$  for WT to  $n = 0.75$  for trVim HT-29 nuclei.

We acknowledge that the recovery curve for trVim HT-29 nuclei contain cells with heterogeneous levels of vimentin expression et organisation. To improve cellular homogeneity, we envision to sort the cells through FACS at the end of the transfection selecting for cells with the best organisation, and establish a stable transfected line with homogeneous characteristics.

We conclude from these first two experiments that the presence of a perinuclear cage of vimentin filaments seems to play a major role in the nucleus elasticity. We'll discuss later about the potential role this may have in the progression of cancer cells.

## 7 Discussion

In this section, we'll first discuss about the consequences of nucleus deformation. Though it induces damages in the nuclei, we'll show that it does not result in loss of viability. Then we'll elaborate our results on nuclei rheology, in particular under the framework of cancer and the basic knowledge about cancer cell rheology.

### 7.1 Nuclear damages and Viability

#### 7.1.1 DNA damages and nucleus envelope rupture ?

It has been observed in several studies that the nucleus experiences damages under confinement [Raab, 2016 ; Denais, 2016 ; Nader, 2021a]. Notably, as the confinement increases, nuclear wrinkles start to unfold, then the tension in the nuclear membrane increases until rupture [Nader, 2021b]. Nuclear membrane can detach from the lamina and form unstable blebs that end up rupturing [Raab, 2016]. At this points of rupture, cytoplasmic proteins can enter the nucleus. TREX-1, a cytoplasmic endonuclease, is able to induce damages to DNA strands [Nader, 2021b]. While these damages would results in senescence in normal cells, they are able to promote invasive behaviors in cancer cells (through induction of EMT for instance) [Nader, 2021a]. Simultaneously, both nuclear envelope (NE) and DNA damages are able to be repaired, which involves ESCRT proteins restoring NE integrity, as well as BAF1 and the DNA repair pathways [Raab, 2016 ; Lusk, 2020].

We would like to investigate next the apparition and possible reparation of deformation-induced damages to the nucleus in the  $6 \times 15 \mu\text{m}^2$  constrictions. We obtained MDA-MB-231 cell line stably expressing 53BP1 : :GFP and cGAS : :mCherry from Matthieu Piel lab [Nader, 2021a]. 53BP1 is a nuclear protein involved in the reparation of DNA damages and thus accumulates as foci to the site of double strand DNA breaks. cGAS is a cytoplasmic protein that detects and binds DNA in the cytosol (in combination with TREX-1 they allow for detection and removal of viral DNA in the cytosol) and thus allow us to detect sites of nuclear envelope rupture that

resulted in DNA leaking to the cytosol. These transformed lines will be used in the Pachinko device to evaluate the damages to the nucleus.

In a free migration experiment through constrictions, [Denais, 2016] observed NE rupture in  $\approx 2\%$  of cells going through a constriction of equivalent cross section than ours ( $90 \mu\text{m}^2$ ). When NE rupture happened, it was located at the front of the nucleus in most cases, where the curvature in the lamina was the more intense. This percentage increased above 10% when the cross section was reduced below  $30 \mu\text{m}^2$  (which in our case would correspond to a  $2 \times 15 \mu\text{m}^2$  constriction). However, the proportion could very well increase in response to forced migration through constrictions as in the Pachinko device. This is why we decided to assess the viability of our cells trapped in the recovery chamber, as presented in the next section.

### 7.1.2 Long term viability after fast deformation

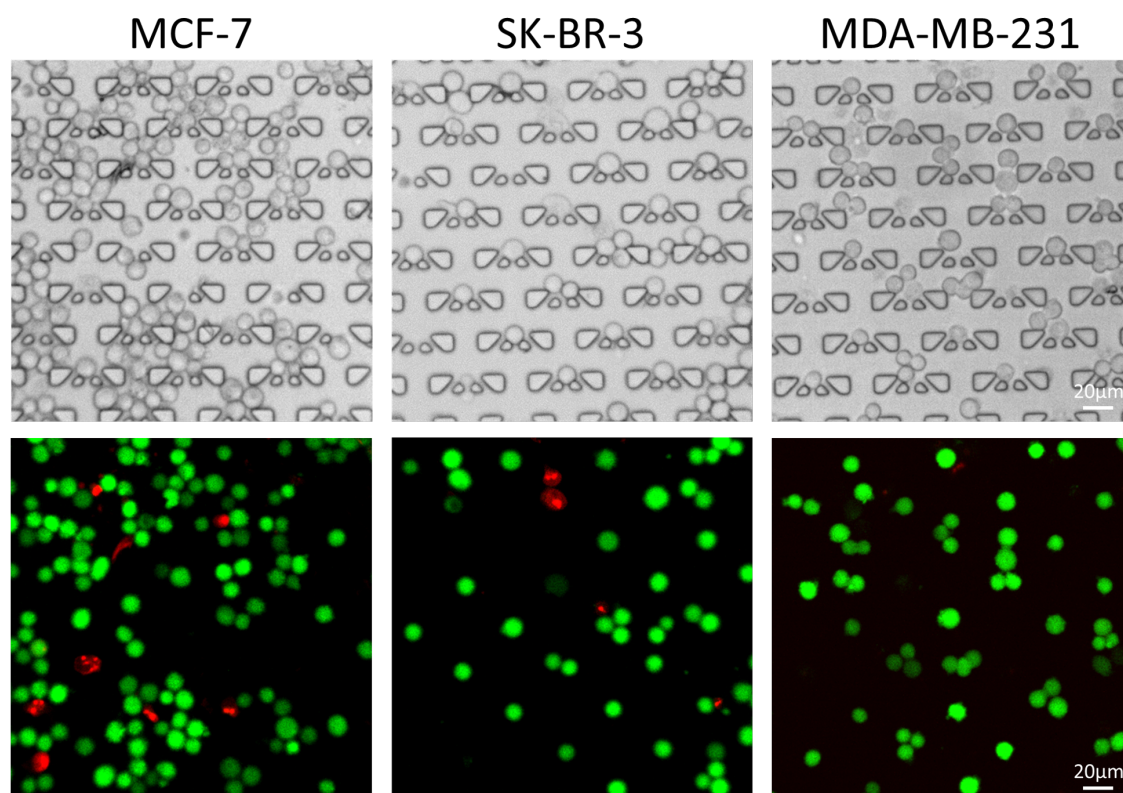


**Figure 3.16** – Viability 1h after passage through constriction was assessed in all breast lines through live (calcein AM, green)/dead (propidium iodide, red) imaging. Traps were overfilled with cells for this experiment.

Though our study only focused on the first minute following deformation, it is possible that effects of deformation manifest at a longer time-scale, possibly in response of nuclear damages. Thus, we preliminarily tested for cell viability through live/dead imaging 1h after passage through the constrictions. In all three breast cancer cell lines, cells were largely still alive 1 hour after a single deformation through  $6 \times 15 \mu\text{m}^2$  in the Pachinko device (see Fig.3.16). Though we

observed a few more dead cells in MCF-7 cells, their viability following harvesting was also typically lower, and so were the cells injected in the chip.

## 7.2 About the rheology

We summarize here some of the points we made in the previous chapters dedicated to whole cell behaviors which remain pertinent when discussing the nucleus.

- As the constriction geometry is fixed, the level of deformation and strain rate experienced by nuclei still depends on their size. Smaller nuclei are deformed less, but also cross the constriction faster in average.
- The same complex deformation pattern (compression in the middle, elongation on both ends) is observed in the nucleus, and evaluating the strain based on the measurement of the max longitudinal strain may results in rheological values true within a multiplicative factor less than 1 (that we estimate to 0.75 for SK-BR-3 nuclei, data not shown). Moreover, as the nucleus is smaller in average than the channel height, it could very well simultaneously deform in the z-direction until it reaches confinement by the channel ceiling.
- Similarly, as the analysis were similar, the discussion we made about Young modulus estimation or the elastic approximation of the faster exponential decay remains true in this chapter.

**Nuclei deformation corresponds to a regime of small deformation.** Deformation levels were estimated to be between 20% and 40% for all cell line (Fig.3.5). The width of the constriction (6  $\mu\text{m}$ ) falls within the range of confinement were we could expect to see nuclei unwrinkling [Lomakin, 2020]

**Comparison with the literature.** In deformation experiments, the nucleus is often characterized as viscoelastic [Guilak, 2000 ; Dahl, 2004 ; Davidson, 2019 ; Jebane, 2023].

Our main observation is the surprisingly fast recovery of nuclei, that we chose to attribute to elasticity. It appears from the literature that the properties of the nucleus depend on the time scale and amplitude of the applied force. The nucleus has either elastic characteristics, where it deforms instantly and reversibly like a spring as we observed in recovery, or viscous properties, resembling a liquid, resisting shear flow and strain linearly with time as we observed in deformation.

For instance, an elastic response of fibroblasts nuclei was observed in less than 1 s in [Nee-lam, 2015] following deformation. This behavior was abolished in LMNA-/- cells, underlying the role of lamins in the elastic recovery. More generally, the elastic property of the nucleus was often associated to the lamina network surrounding the nucleus [Lammerding, 2006], more precisely Lamin A/C. This statement corroborates our hypothesis that in the absence of vimentin, elasticity in recovery was associated to the respective levels of lamins.

Regarding the lamins levels of breast cancer cells, MDA-MB-231 have a higher level than MCF-7 cells [Lewinska, 2017 ; Alghanem, 2020], as we confirmed through immunoblotting. Though,

lower lamin A levels were associated with enhanced confined cell migration and metastatic capacity [Bell, 2022], which contradicts the expected order between MDA-MB-231 and MCF-7 cells.

In colorectal cancer, Lamin A was reported as a risk biomarker [Willis, 2008]. Higher levels of lamin A were associated with a worse prognosis, through increase of invasiveness. Conversely, in others studies low lamin A levels correlated with increased disease recurrence in stage II and III colon cancer [Belt, 2011]. In the immunoblotting analysis performed by Kotryna Vaidžiulytė, we observed an increase in the levels of lamin A (and C to a lower level) as the cancer progressed from CTC41 to metastatic CTC41.5A lines. However, in metastatic SW-620 cells the lamin A levels were quite low.

These seemingly opposite results justify the need to dig deeper in the comprehension of the nucleus properties and the metastatic potential of a cell. A softer nuclei may present as an advantage for metastasis as it allows for increased deformation and motility. However, it may come with the cost of a more fragile nucleus.

**The nucleus as the poroelastic material.** Some papers argue that the nature of nucleus' mechanics is better described by poroelasticity, rather than viscoelasticity. Under the hypothesis of nuclei behaving as a linear isotropic poro-elastic material, we could explain the presence of characteristic times in a supposedly entirely elastic material. Indeed, within poro-elastic materials, modification of the object shape is limited by friction of the solvent through pores of the matrix (here the chromatin). Hence characteristic times are introduced in the behavior, which depend on respective fractions of matrix and solvent, elasticity of the matrix network and the size of pores in the matrix [Wei, 2016; Rollin, 2023a].

**Isolated nuclei.** We observed in the Pachinko device the nucleus in its cellular environment. Thus, the properties of the nucleus were not independent of its surroundings, notably the cytoskeleton linked to it through the LINC complexes. Indeed, we showed that the presence of a vimentin cage-like structure influenced the elasticity of the nucleus. Some work on isolated nuclei may help to isolate the mechanical properties of the nucleus only [Dahl, 2005]. Under deformation by micromanipulation, [Stephens, 2017] concluded that the mechanics of isolated nuclei are reasonably representative of the *in vivo* force response of the nucleus, as no changes were observed in measured spring constants.

In a  $3 \times 3 \mu\text{m}^2$  constriction, [Jebane, 2023] studied the flow-induced deformation of isolated nuclei obtained from cells carrying a lamin A/C mutation or submitted to a treatment impacting the lamin A/C maturation. Interestingly, the behavior of isolated nuclei was not able to recapitulate the one observed at the whole cell level, thus suggesting that interaction with the cytoskeleton, and not only the properties of the nuclear envelope, modulates the properties of the nucleus.

Similarly, it would be interesting to analyze the behavior of enucleated cells and compare with the results obtained in the previous chapter. Surprisingly, under AFM characterisation with

small deformations (3  $\mu\text{m}$  indentation), [Efremov, 2020] did not observe a softening of cytoplasts (enucleated cells) compared to the original cells (fibroblasts), while nucleoplasts (nuclei surrounded by plasma membrane) were substantially softer.

**Vimentin filaments act as a "shock absorber" to protect the nucleus.** We hypothesized the vimentin intermediate filaments (VIFs) around the nucleus to contribute to its elasticity. Similarly, [Patteson, 2019] reported the VIFs perinuclear cage to provide a protective structure that resists extreme deformations to maintain the structural integrity of the nucleus. Its function is to maintain nuclear shape against the imposed deformations, acting like an elastic spring.

Thus, the VIFs network contribute among others to maintain nuclear mechanical homeostasis against localized forces. [Neelam, 2015] pulled on fibroblasts nuclei using a micropipette to deform them. Upon force removal, the original shape and position were restored quickly within a few seconds. This stiff, elastic response required the presence of vimentin, lamin A/C, and SUN (Sad1p, UNC-84)-domain protein linkages, but not F-actin or microtubules.

In accordance with the above, [Block, 2017] reported that the VIF cage-like structure around the nucleus seems to act as a "shock absorber" by dissipating energy upon unfolding of the filament structure. Then, at longer time scale, the VIF cage can be deformed, allowing for a "safe" regime of deformation for the nucleus.

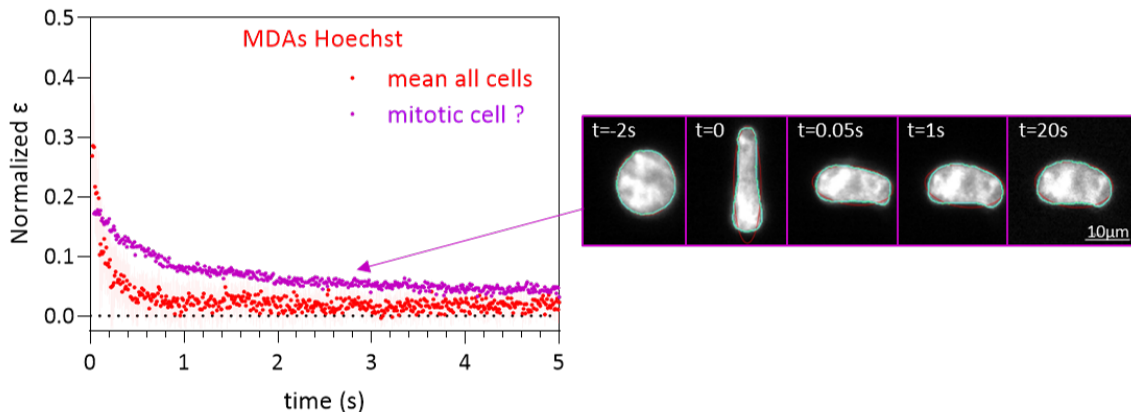


**Figure 3.17** – Example of a MDA-MB-231 nuclei that exhibit high viscosity in its recovery. Images at different time points of the MDA-MB-231 nuclei associated to the curve in purple, compared to the mean of all MDA-MB-231 recovery in red. The characteristic time  $\tau_{slow}$  for the purple nucleus has been measured at 2.37 s, compared to 0.23 s for the mean of nuclei.

**Do mitotic cells display higher and slower viscoelastic recovery?** We observed a small fraction of big nuclei that did not recover, and displayed a highly viscous behavior (see an in Fig.3.17, though remaining deformation was subtracted during  $\epsilon_{Norm}$  normalization and is thus not visible on the curve). The relatively low characteristic time the nuclei presented here is  $\tau_{slow}=2.37$  s, i.e. ten times less than the one measured for the mean of MDA-MB-231 nuclei. We attributed this behavior to cells undergoing mitosis. Indeed, it has been reported that cell properties vary during cell cycle, including an almost 2-fold decrease in elasticity and viscosity

in the G2/M state compared to G0 [Teng, 2018]. This decrease could be understood from the disassembly of nuclear lamina during mitosis.

In order to confirm our hypothesis and study the mechanics of mitotic cells, cell cycle could be arrested in mitosis by treatment with nocodazole, a microtubule-disrupting drug [Venturini, 2020].

### 7.3 Validation of rheological models

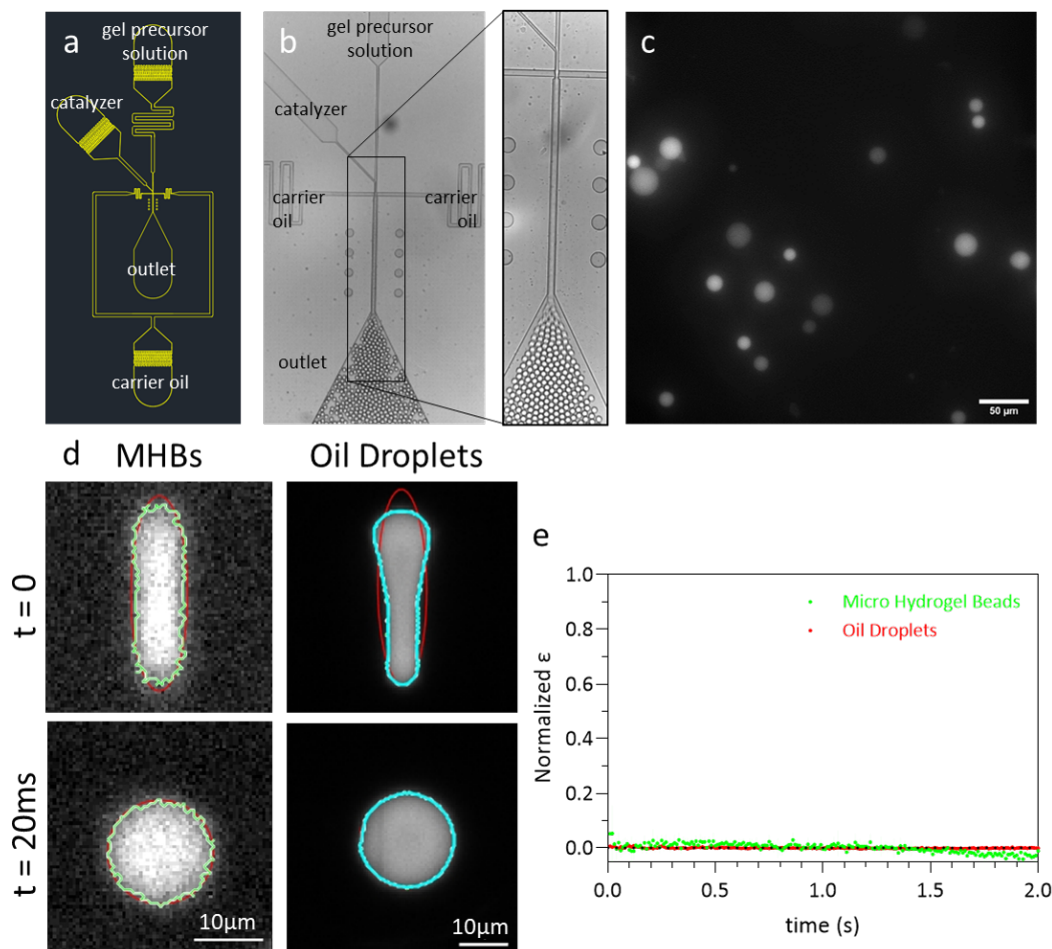


**Figure 3.18** – Physical models in the Pachinko device. (a) Design of Micro Hydrogel Beads (MHBs) production microfluidic chip. (b) Images of MHBs production. (c) Fluorescent images of MHBs displaying distribution of sizes (and intensity). Scale bar = 50 μm. (d) Representative images of MHBs (FITC) and Oil Droplets (NileRed) in the constriction ( $t=0$ ) and just after exiting the constriction ( $t=20$  ms) (e) Mean recovery curve of MHBs and Oil Droplets, displaying perfect elastic behavior.

#### 7.3.1 Micro Hydrogel Beads

In order to characterize the behavior of truly elastic objects in our Pachinko device with  $6 \times 15 \mu\text{m}^2$  constrictions, we used home made MicroHydrogel Beads (MHBs) as a model of elastic materials.

**Production of MHBs.** MHBs were produced from PolyAcrylamid (PAA) with the help of Simon Dumas with a protocol developed in the team (adapted from [Zilionis, 2017]). This protocol was adapted to introduce fluorescence in the beads by inclusion of Fluorescein O-methacrylate in the gel precursor mix. Rapidly, acrylamid solution (A4058, Sigma) was mixed with acrylamid :bis-acrylamid 19 :1 solution (A9926, Sigma) to create the gel precursor solution. APS catalyser (final concentration 0.3%) was added to the mix just before the flow-focusing junction that allows formation of a stream monodisperse droplets by emulsification between two flows of carrier oil (HFE-7500 + 1% surfactant, see Fig.3.18a&b). Relative flow of each solution allows to set the concentration of the catalyst, and the size of the droplets. Collected beads were then placed at 60-75°C overnight to polymerize the gel. Beads were then washed in a series of successive solution to transfer them in aqueous solution (TBSET buffer).

By tuning the fraction of flow between the gel precursor mix and oil carrier fluid, we were able to create droplets of varying size, hence reproducing the distribution of nuclei size (5-20  $\mu\text{m}$ , see Fig.3.18c).

**MHBs are perfectly elastic.** We observed the recovery of MHBs in the Pachinko device to be perfectly elastic (see Fig.3.18d&e). MHBs recovered their spherical size as soon as they exit the constriction. The return to the spherical shape in less than one acquisition frame and a flat recovery express the fully elastic nature of our beads, validating the ability of the Pachinko device to highlight an elastic behavior.

### 7.3.2 Oil Droplets

**Oil droplets are perfectly elastic as well.** Similarly, as an attempt to model a perfect viscous behavior, we had oil droplets go through the Pachinko device. The oil droplets provided by Jacques Fattaccioli (Dep. de Chimie, ENS PSL - IPGG) were generated from lipiodol oil through a porous membrane (monodisperse distribution,  $\approx 12 \mu\text{m}$ ) [Pinon, 2022]. The oil droplets were stained with lipophilic marker NileRed. However, we observed droplets recovery to be instantaneous (similarly to MHBs, see Fig.3.18d&e).

Indeed, the oil droplets properties evaluated using a plate-plate rheometer. [Pinon, 2022] show a constant storage modulus  $G' \approx 10^3 \text{ Pa}$  and loss modulus of  $G'' \approx 20\text{-}200 \text{ Pa}$ , meaning that the viscous contribution of the oil could be neglected and that the overall behavior of the droplet is dominated by its surface tension. Thus, oil droplets recovered from the deformation similarly as elastic objects.

The observation of perfect elastic behavior in MHBs and oil droplets highlights the difference with nuclei recovery. We thus confirm our analysis that nuclei display a small viscoelastic component, although their recovery is largely dominated ( $> 90\%$ ) by an elastic behavior.

## 8 Perspectives

**Simultaneous imaging of cell and nucleus dynamics.** We observed a distribution of properties, both at the level of the cell and nucleus. It would be interesting to record the

dynamics of a single cell and its nuclei at the same time. To do so, we would need to perform a double staining and a dual acquisition. In the first few attempts we made, we were limited by the rate of opening/closure of the different shutters of the microscope used.

**About the role of vimentin in the recovery.** In order to fully describe the role of vimentin in the recovery of nuclei, we would like to replicate the results obtained in the breast cancer cell lines : express vimentin in MCF-7 cells, and decrease its expression in MDA-MB-231. A first attempt using the 2x48h siRNA protocol on MDA-MB-231 cells led to a  $\approx 50\%$  decrease of vimentin expression (quantified by immunoblotting).

Regarding the experiments on colon cancer cell lines, we would like to replicate the silencing experiment on SW-620s cells while adjusting the initial seeding concentration. This way, we would be able to compare the cells in the same  $6 \times 15 \mu\text{m}^2$  constriction as performed in all other experiments. As for the expression of vimentin in HT-29 cells, as we explained earlier, we would like to sort the cells through FACS in order to homogenize the vimentin expression levels among the cells.

**About the role of lamins and chromatin.** Even if we observed that the absence of a vimentin decreased the elastic proportion of the recovery, the recovery remains largely elastic in all cases. According to the literature, this elastic behavior could be associated to the lamin network underlying the inner nuclear membrane [Swift, 2013]. In the same way as for vimentin filaments, a silencing protocol could be performed to decrease the levels of the different lamins, notably Lamin A/C. We would expect to observe a decrease of the elastic component of the recovery following silencing or its increase following overexpression of lamins genes.

Similarly, to evaluate the contribution of the chromatin bulk to the mechanics of the nucleus, one could modulate its compaction level in order to change its mechanical properties [Pajerowski, 2007; Stephens, 2017]. The chromatin can either be softened by digestion with micrococcal nuclease (MNase), or accumulation of decondensed euchromatin with trichostatin (TSA). Conversely, heterochromatin compaction can be induced by addition of  $\text{MgCl}_2$  to stiffen the chromatin network.

**Complete the study on damages.** Finally, as a complement to the analysis of cells survival following repetitive deformations that we'll present in the next chapter, we would like to measure the occurrence (and possible reparation) of nuclear damages induced by the fast deformation of the nuclei. As described earlier, the analysis would focus on nuclear envelope rupture (cGAS) and double strand DNA breaks (53BP1,  $\gamma\text{H2AX}$ ).

## 9 Short Conclusion

In this chapter, we focused our interest on the morphological deformation and recovery of nuclei inside cells. We recapitulate here our main findings :

- The arrest time was better correlated with the cell size rather than the nucleus size. Both the cytoskeleton and the nucleus contributes to resistance to deformation. As a consequence, we found the same differences in arrest time between cell lines as described in the previous chapter.
- Though the analysis of nuclei deformation was complicated, we observed on individual fits values of elastic  $E$  and viscous moduli  $\eta_2$  to be higher than the ones measured at the whole cell level.
- We found the recovery of nuclei to be mostly elastic ( $> 90\%$  recovery in less than 1 s). The recovery happens much faster than at the whole cell level observed in the previous chapter.
- Among the breast cancer cell lines, we observed the MDA-MB-231 cells to recover faster. The same can be said for SW-620 and CTC41.5A, and HT-29 to a lesser extent, for colon cells lines. These cells are the ones we referred to as being more metastatic.
- Though the rheological models based modelization lacked robustness, we were able to extract rheological parameters. These parameters recapitulated the Young modulus estimations based on the max deformation. The order in elasticity proportion observed was better correlated to the exponent in power law rheology fits.
- We correlated part of the elastic behavior to the presence of a vimentin perinuclear cage around the nucleus. Removal of this structure in SW-620 cells impaired elastic behavior in recovery, while addition of this cage in HT-29 cells enhanced it.

In previous chapters, we focused on a single-cell, flow-induced deformation in a capillary-like constriction. We investigated the morphological recovery occurring within a few seconds following the deformation.

However, in the body, CTCs experience multiple repeated deformation over the course of their short lives in the circulation, which could last up to a few hours [Meng, 2004 ; Stott, 2010]. Several studies explored the role of fluid shear stress on cancer cells behavior, including survival or gene expression, by either modulating the flow speed [Barnes, 2012 ; Ma, 2017 ; Regmi, 2017] or by introducing changes in tubing diameters [Alvarado-Estrada, 2021]. From the literature, we retain that fluid shear stress has a deleterious effect on cells, as observed both *in vivo* [Fidler, 1970 ; Weiss, 1990] and *in vitro* [Regmi, 2017], though malignant cells fare better than non-tumoral cells [Barnes, 2012]. However, the question of repeated deformations was more rarely studied. [Ahmad-Cognart, 2020] showed changes in gene expression following a single passage through five consecutive constrictions, while [Jiang, 2023] demonstrated increase resilience of cancer cells as an adaptation to repetitive deformation.

We present here the development of a recirculation microfluidic chip with capillary-like constrictions and of the experimental setup to establish recirculation within the chip. We used this recirculation setup to compare the properties of MCF-7 and MDA-MB-231 cells. We demonstrate the first results on cell survival, vesicles production and nucleus damages accumulation.

## 1 Experiment design

We aimed at constructing a microfluidic chip, through which cells would be submitted to repeated deformations over a long period of time.

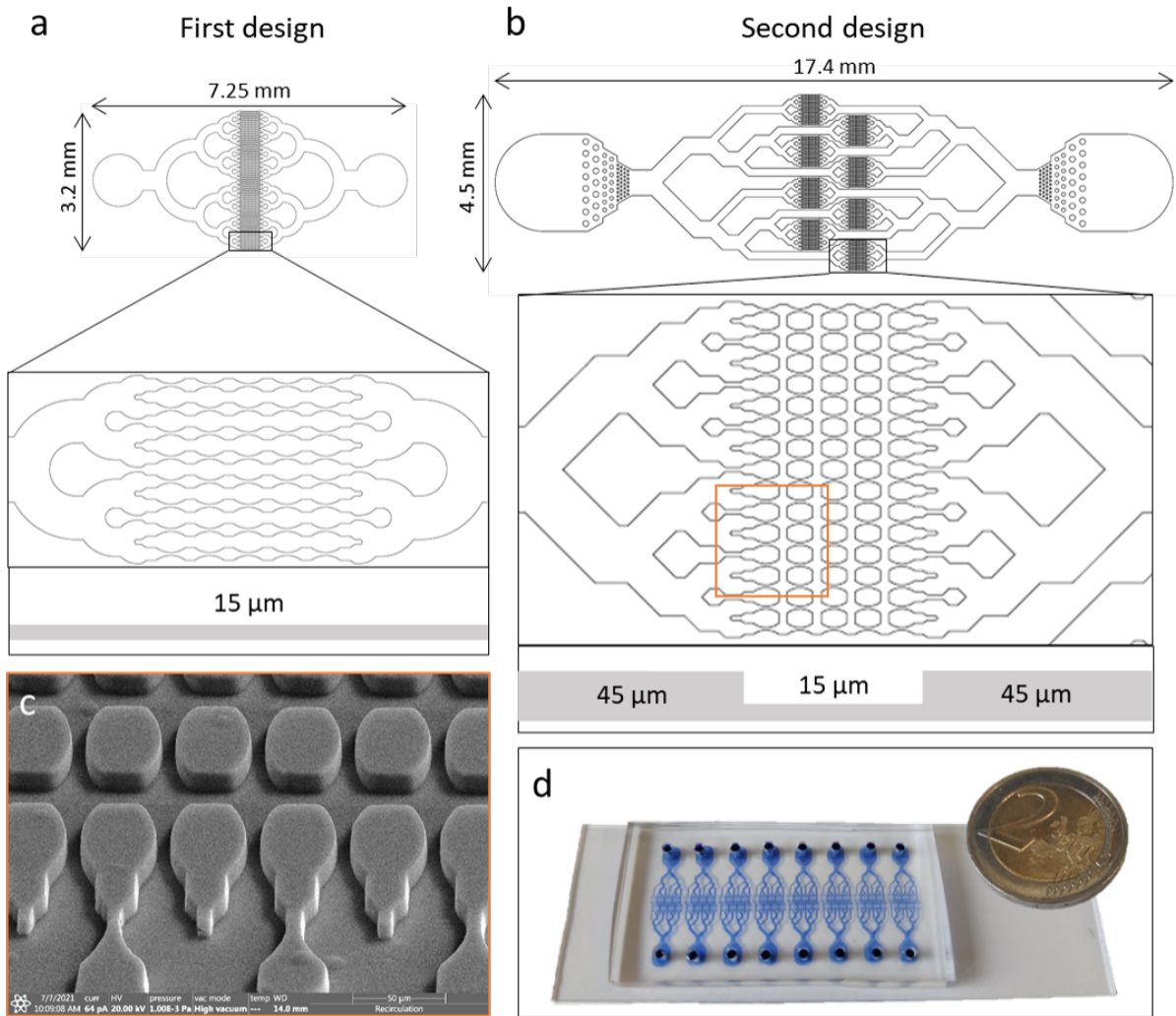


**Figure 4.1** – Designs of the recirculation microfluidic chips. First (a) and second (b) iteration of the design, presenting series of five successive  $6 \times 15 \mu\text{m}^2$  constrictions. (c) Scanning Electron Microscopy image of the constrictions array, zoom on the orange region in (b). (d) Photo of the assembled microfluidic chip.

## 1.1 Microfluidic chip

### 1.1.1 First design

To construct a recirculation chip, we parallelized lines of five consecutive  $6 \times 15 \mu\text{m}^2$  constrictions, as this series of constriction was already studied in the team [Ahmad-Cognart, 2020]. To increase the cell throughput of the device, we increased the number of channels up to 68 channels in parallel (see Fig.4.1a).

As a nod to biomimetism, we referred to *in vivo* data to dimension the channel widths hierarchy from the inlet/outlet in the overall design of the chip. Similarly to vessel organisation in the lung, the ratio of the widths between two successive connecting channels upward and downward the constricted area is set to 0.75. This ratio is conserved through several species [Lapi, 2007; Kassab, 1994; Ellsworth, 1987], including humans [Huang, 1996]. It explains why

the section of the aorta is a tiny fraction of the total surface of capillaries, as the total area increases at each vessel branching.

One consideration in the construction was to limit the hydraulic resistance of the chip so that flow could be sustained by the available pressure controllers limited to 1 bar, which limits the number of parallel constrictions that can be used (see later simulations).

The determination of recirculation parameters is made of several compromises dictated by experimental limitations. We aimed at achieving cycles of  $\approx 4$  min, slightly higher than the  $\approx 1$  min reported in [Blom, 2003]. We set a flow of  $1 \mu\text{L}/\text{min}$  in each channel, i.e. a total flow of  $64 \mu\text{L}/\text{min}$  in a chip with 64 parallel channels, which amounts to recirculated volume of  $\approx 250 \mu\text{L}$  (minimum volume required to fill reservoirs and tubings with liquids). We acknowledge this flow to be higher than the ones reported *in vivo* for capillaries [Kornfield, 2015; Follain, 2020]. Though, reducing it would result in either much longer cycles, or amount of liquids too small to work with.

### 1.1.2 Second design

A few experiments with the first design led us to conceive a second generation of recirculation microfluidic chips (see Fig.4.1b, c and d). Improvements in the new iteration of devices include :

- Increase in the number of channels up to 128 in parallel (divided in 8 sections of 16 parallel channels).
- Addition of filters near to the inlet/outlet to catch the bigger debris that might clog the microchannels.
- Implementation of more sharp angles to prevent regions of cell arrest between branching of the channels.
- Connection of the different channels between each of the constrictions, allowing for cells to change directions if one of the constriction happened to be already occupied or clogged. This also has the benefit of reducing the effective pressure difference on the cells by a factor 5 as compared with a series of five consecutive constrictions in the first design.
- More importantly, increase in the height of the delivery channels to decrease the fluidic resistance outside of the zone of nominal height filled with constrictions. The height of the connecting channels was increased to  $45 \mu\text{m}$ , in order to reduce the resistance of these connecting elements. This results in a reduction of the total pressure required to establish a flow through the device (see Fig.4.2 and Tab.4.1).

This second design with 128 channels allows to work with a more comfortable volume of  $500 \mu\text{L}$ , at a flow of  $1 \mu\text{L}/\text{min}$  per channel with cycles of  $\approx 4$  min.

### 1.1.3 Numerical simulations

Using Comsol Multiphysics, we computed numerically the pressure drop in a 128-channels chip of the second design, with different height for the main channels ( $15$ ,  $30$  or  $45 \mu\text{m}$ ). For calculations, the flow was set to  $1 \mu\text{L}/\text{min}$  per channel.

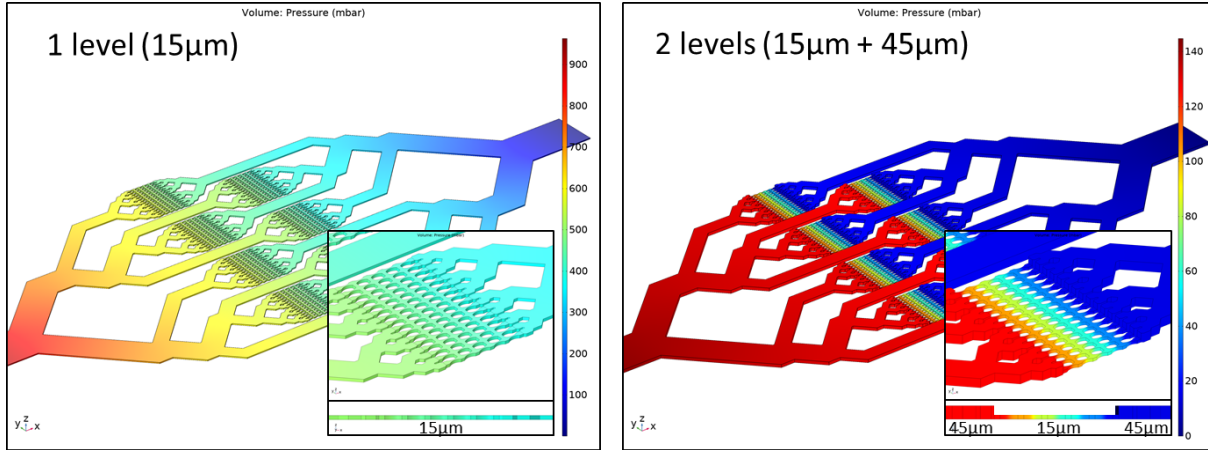


**Figure 4.2** – Numerical simulations of flow within the recirculation chip in a second design chip with either 1 (a) or 2 (b) levels (Comsol MultiPhysics). Simulations were conducted in a 3D geometry using laminar flow physics.

	Old design		New design	
	1 level	1 level	2 levels	2 levels
First level	15 $\mu\text{m}$	15 $\mu\text{m}$	15 $\mu\text{m}$	15 $\mu\text{m}$
Second level	/	/	30 $\mu\text{m}$	45 $\mu\text{m}$
Total drop	550 mbar	960 mbar	220 mbar	160 mbar
Constriction drop	108 mbar (20%)	120 mbar (12.5%)	115 mbar (52%)	112 mbar (70%)
Drop per constriction	21.6 mbar	24 mbar	23 mbar	22.4 mbar

**Table 4.1** – Pressure levels obtained numerically for the different chips designs

We observe that the pressure drop necessary to establish a flow through the constrictions section is  $\approx 110\text{-}120$  mbar. It corresponds to a pressure drop of  $\approx 22\text{-}24$  mbar in each of the five constrictions.

In a design with only one level (15  $\mu\text{m}$ ), more than 80% of the pressure applied is used to establish a flow through the main channels. This proportion decreases  $\approx 50\%$  when the main channel height is increased to 30  $\mu\text{m}$ , and down to 30% for 45  $\mu\text{m}$ . Thus increasing the height in the main channel allows to work with a lower total pressure, from  $\approx 1$  bar with one level (15  $\mu\text{m}$ ) down to  $\approx 160$  mbar with two levels (15 and 45  $\mu\text{m}$ ).

#### 1.1.4 Experimental considerations

We observed experimentally that chips tend to clog rapidly if cells are injected in the device without any preparation. Indeed, as some cells die within the device, they release their DNA into the media which aggregate with cells and debris to clog the chip (see Fig.4.3).

To increase the possible duration of the experiments, we propose the following modifications :

- The cell viability in the injected suspension was improved using magnetic sorting of dead and apoptotic cells (Dead Cell Removal kit, Miltenyi).

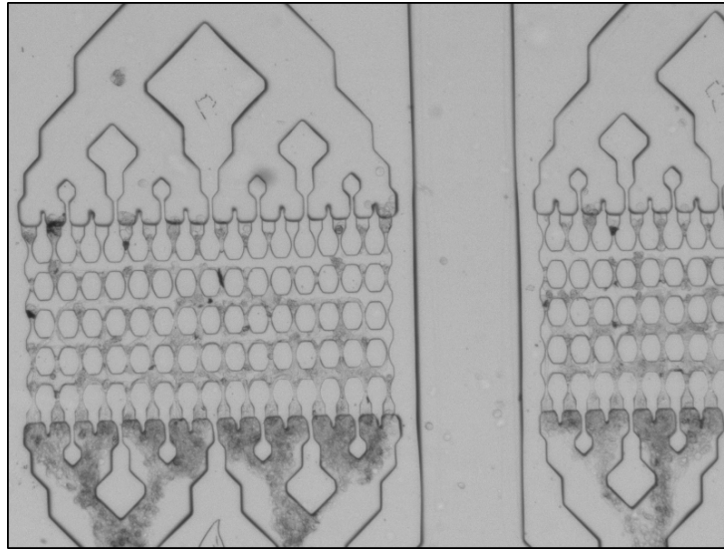


**Figure 4.3** – Image of a chip clugged with DNA.

- 
- Addition of DNase (2000 U/mL) in the recirculation media to digest any DNA that may be released.

With these modifications, the recirculation was able to be maintained for more than 4 hours.

## 1.2 Implementation of the recirculation fluidic system

To produce a sustained flow within the chip, we compared several setups. We first evaluated methods using pressure controllers to create the flow. Indeed, as compared to peristaltic pumps (see further down in the manuscript, such instruments do not introduce additional mechanical stress on the cells.

### 1.2.1 Back and forth using pressure controllers

This first method of establishing flow was developed with the help of Cyril Bonhomme, a M2 intern for a duration of 3 months.

As pressure controllers were already used for the Pachinko experiment, we investigated their use to create a "back and forth" flow within the microfluidic chip, thus achieving an alternated flow between the two reservoirs. To do so, a pair of coupled pressure controllers is connected to each end of the chip. Each controller successively pushes a determined volume at a set flow rate (128  $\mu\text{L}/\text{min}$ ) for a certain pre-determined number of cycles (see Fig.4.4 for the setup).

Though this setup was successful in establishing a alternated flow within the chip, we observed that the number of cells actually recirculating at each cycle decreased exponentially (see Fig.4.5 for an example). Within a few cycle, only a small fraction (20% of cells within 10 cycles) of injected cells were actually going through the constrictions and experimenting deformations. Our hypothesis is that the cell number initially present in the recirculated volume gradually

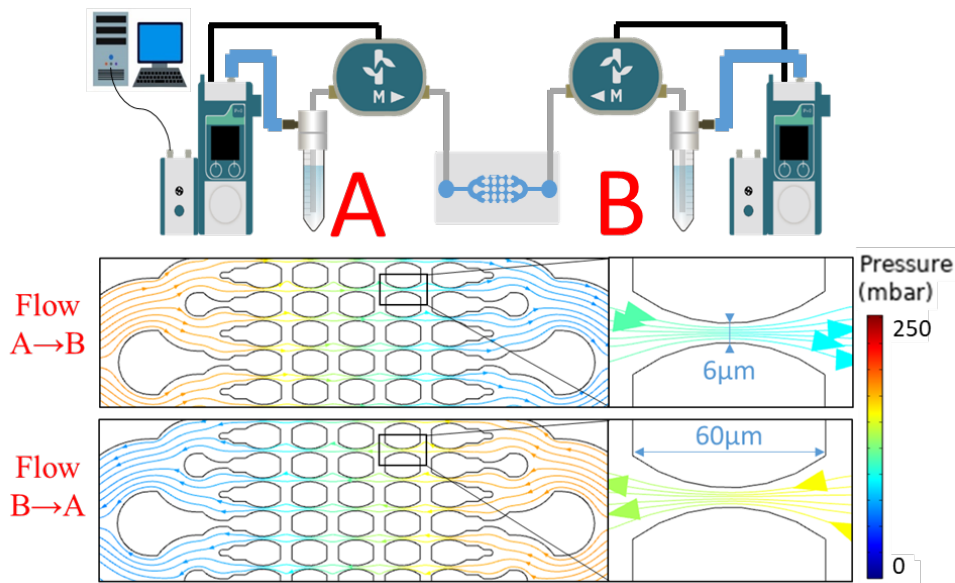


**Figure 4.4** – Use of couple pressure controller to create a back and forth flow within the chip. Streamlines through the microfluidic chip in both steps of recirculation (flow A→ B and flow B→ A).

diffuse to a bigger volume, due to the mismatch between cells and flow speed. Thus the concentration of cells within the recirculated volume decreases at each cycle.

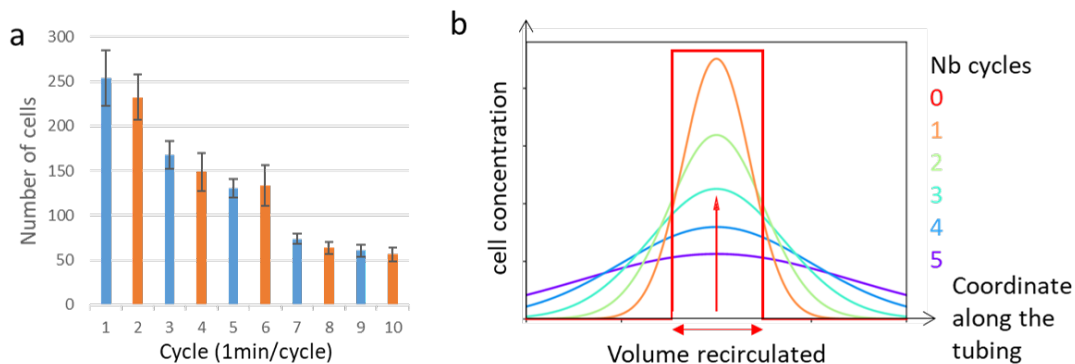


**Figure 4.5** – Evolution of cell concentration in the design. (a) Number of cells that transited through the device during each cycle. (b) Explanation of cell number diminution with each cycle.

To remedy this, we changed towards methods allowing for recirculation in an uni-directional manner. If the flow is always going in the same direction through the chip, no cells can be lost and all cells will experience the same number of deformations.

### 1.2.2 Omi recirculation instrument by Fluigent

In our search for alternatives to the previous setup, we contacted the company Fluigent which was developing a recirculation instrument named Omi. The device (now commercially available) was designed to establish media recirculation through organs-on-chips. As a beta tester for

Fluigent, I realized several experiments with the device to evaluate if it was also suitable for the recirculation of a suspension of cells in a culture medium.

The device allows for recirculation from the inlet reservoir (RI) through the microfluidic chip into the outlet reservoir (RO). When either RI is empty or RO is full, the content of the outlet reservoir RO is transferred back into the inlet reservoir RI through a side channel, thus completing the recirculation cycle. Side reservoirs (I and O) allow for injection or sampling of liquid during the experiment. Flow is achieved through the pressurisation of the reservoirs with a pump located within the device, and is able to deliver  $\approx 600$  mbar max at  $37^\circ\text{C}$ , which is sufficient to establish a flow in the latest version of the recirculation chips with two levels.

The device can function in a incubator environment ( $37^\circ\text{C}$ , 5%  $\text{CO}_2$ ) thus providing perfect conditions for the cells.



**Figure 4.6** – Recirculation using Omi device (Fluigent). (a) Device and reservoirs layout. (b) Viability of MDA-MB-231 cells recirculated with Omi through a control chip (BE-Flow Standard from BEOnChip, straight channel of  $375\ \mu\text{m}$  height) for 5 days.

The viability of recirculating MDA-MB-231 cells in suspension was assessed. Good viability (above 50%) was observed for up to five days. However, as we'll explain below, we cannot guaranty the conditions of the experiment.

Indeed, the device presented several limitations in its use for our application. Recirculation steps is achieved using optical detection of fluid levels in each reservoir. Thus, a minimal volume is required in each reservoir, effectively creating "dead volume". We estimate this dead volume to amount to  $\approx 2$  mL (reservoirs and internal channels). During a cycle, only  $128\ \mu\text{L}$  is recirculated, which represents 6.4% of the total volume. Assuming homogeneity of cells in suspension, only  $\approx 6\%$  of the cells is actually submitted to deformation at each cycle. Conversely, if the totality of the volume is injected through the chip, it takes 15 min for the volume to be circulated at  $128\ \mu\text{L}/\text{min}$ . Moreover, increasing the number of channels adequately (x15) would result in a minimum pressure of 1.8 bar to cross the constrictions, way above the range of pressure delivered by the internal pump. Increasing the flow within the chip will take us away even further from *in vivo* values, and would similarly be limited by the available pressure. As we were not satisfied with Omi performance for our cell recirculation application or any of the options to improve

these performances at our level, we looked for a third option.

### 1.2.3 Use of a peristaltic pump

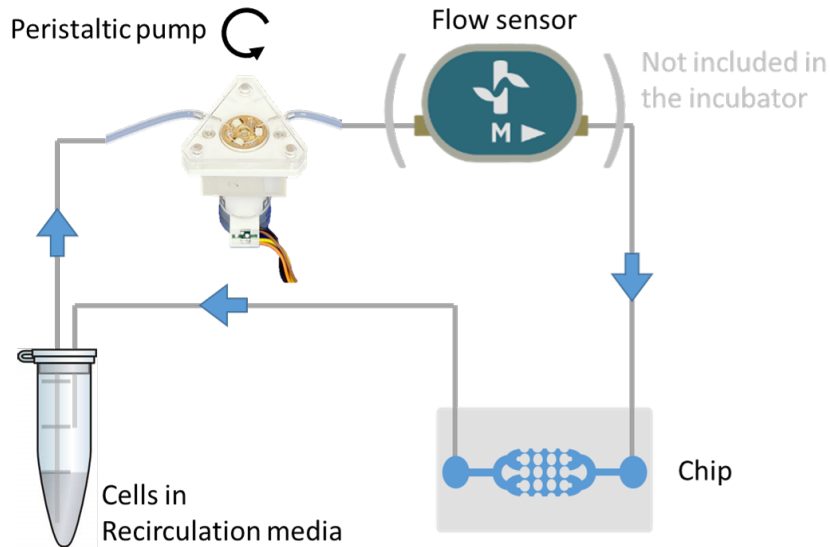


**Figure 4.7** – Recirculation setup using a peristaltic pump as a motor.

We ended up using a peristaltic pump to circulate cells within our microfluidic device. Though these pumps are known to induce mechanical deformation of the tubes, and thus on the suspended cells, this would introduce a similar bias through all conditions, allowing us to conduct comparative studies.

The peristaltic pump creates a flow by compressing the flexible tubing under a "roller" and pushing it forward. Using a flow sensor, we calibrated the pump rotation speed required to produce a  $128 \mu\text{L}/\text{min}$  flow through the chip. The setup described in Fig.4.7 can be placed inside an incubator for optimal cell conditions ( $37^\circ\text{C}$ , 5%  $\text{CO}_2$ ).

In all the experiments that will be presented now, the live cells fraction isolated through magnetic sorting is resuspended in a recirculation media, composed of :

- serum-free culture media (DMEM GlutaMax, 1% Pen/Strep).
- HEPES 25 mM, to keep the pH constant through the experiment.
- DNase 2000 U/mL, to digest DNA released by dead cells.
- OptiPrep 15%, to increase media density and limit sedimentation in the reservoir.

## 2 Study of circulated breast cancer cells

The peristaltic pump device presented above has been used to submit MCF-7 and MDA-MB-231 cells to repeated deformations over a prolonged period. We'll present here the first results

obtained regarding cell viability, vesicles production, damages accumulation. We will finally give some of the perspectives opened by these results.

## 2.1 Viability of recirculated cells

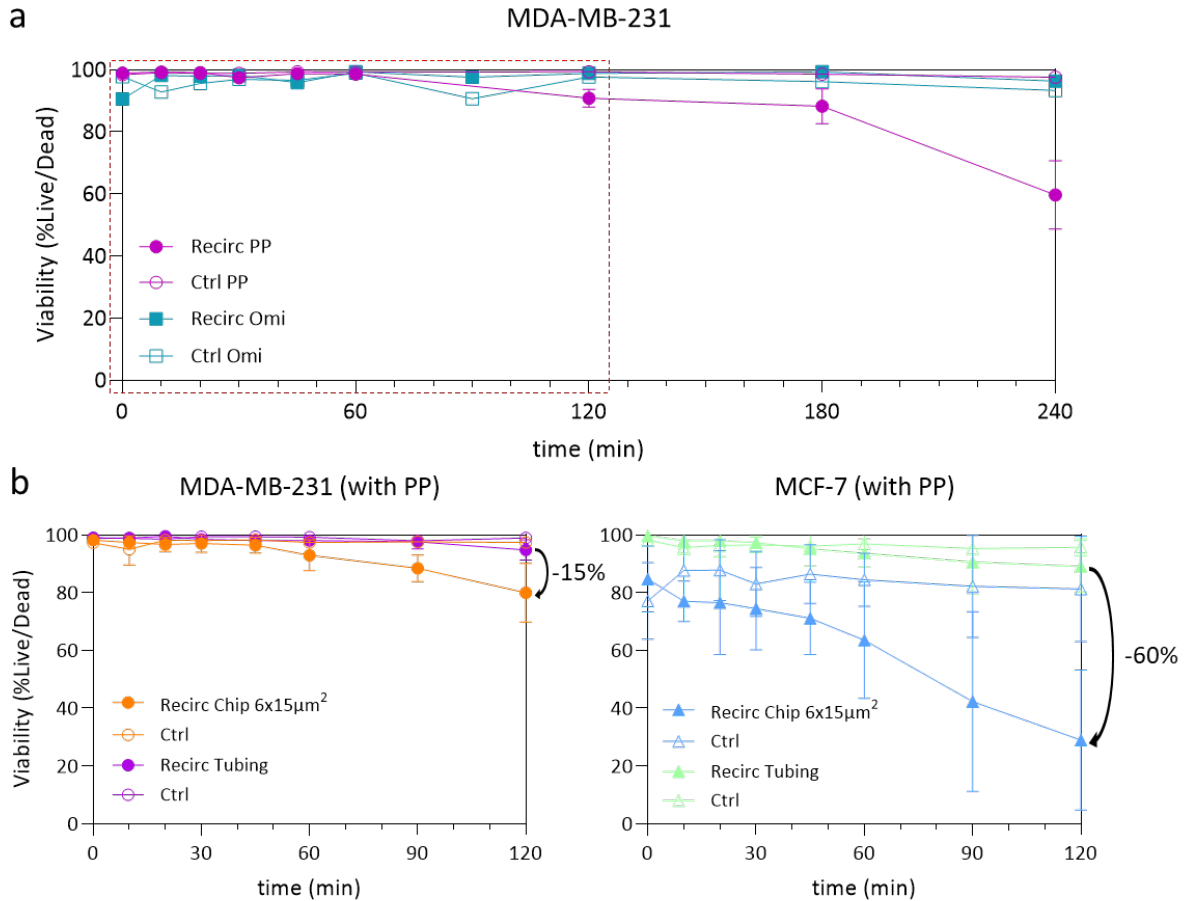


**Figure 4.8** – Viability of recirculated cells. (a) Recirculation within tubing was accomplished either with Omi device (Recirc Omi) or a peristaltic pump (Recirc PP). Ctrl refers to the non-recirculated cells. (b) Viability of MCF-7 and MDA-MB-231 cells recirculated with a peristaltic pump through either the chip (Recirc Chip 6x15  $\mu\text{m}^2$ ), through tubing only (Recirc Tubing), or not recirculated (Ctrl).

**Use of peristaltic pump offer a good cell viability for 2 hours.** We first assessed the use of peristaltic pump for our application. In that aim, MDA-MB-231 cells were recirculated for a period of 4 hours within tubing (0.5 mm inner diameter) only, with either the peristaltic pump or Omi (see Fig.4.8a). We observed no decrease in viability (assessed through live/dead staining at the end of the experiment) with Omi over the duration of the experiment, though the cells may have been stressed to a lower level according to the limitations we presented above. Regarding the peristaltic pump, we observed a slight decrease in viability, with an onset at the time point of 2h of recirculation (-10%) up to -40% after 4 hours. This decrease may be a consequence of either the fluid shear stress encountered by cells through the tubing, or of the

cell damages induced by the pump. In either case, we chose to limit the duration of further experiments to 2 hours when evaluating the influence of repeated deformations on the cells.

**Addition of repeated deformations though constrictions induce a decrease in cell viability, more important for MCF-7 cells.** We then compared the viability of MDA-MB-231 and MCF-7 cells after their recirculation in tubing only or through the recirculation chip including a series of five  $6 \times 15 \mu\text{m}^2$  constrictions (see Fig.4.8b). We observed a decrease in viability to different extent according to the experimental conditions after 2 hours. First, this decrease was limited for MDA-MB-231 cells : the loss of viability after 2 hours increased from 5% when recirculated through tubing only, to 20% with the addition of the chip with constrictions. This effect was more pronounced for MCF-7 cells, which displayed an additional 60% loss of viability induced by the multiple cell passages through the chip : the loss of viability increased from 10% with tubing only, to 70% with the addition of constrictions. The different observed between the two non-recirculated controls for MCF-7 cells is surprising and will be investigated with the addition of more replicates.

We thus conclude that MCF-7s are much more sensitive to repeated deformations than MDA-MB-231 cells.

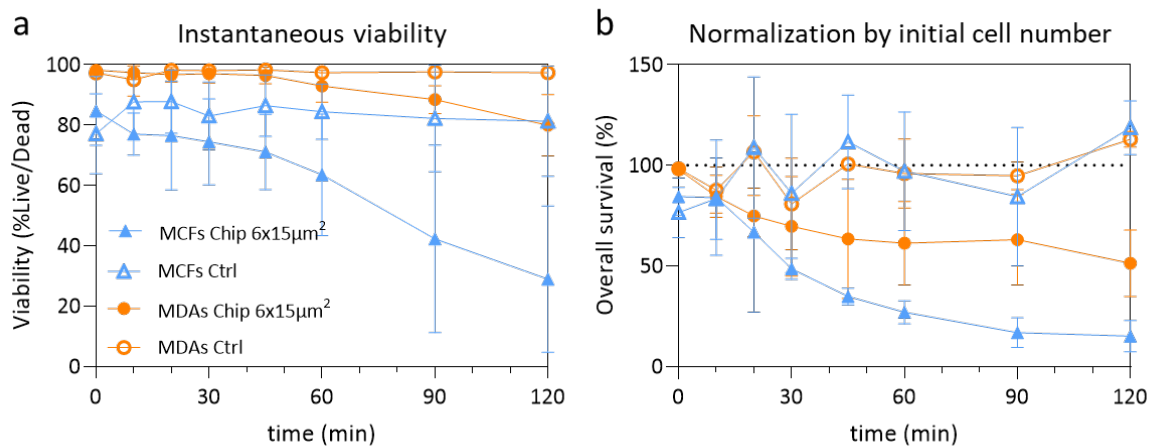


**Figure 4.9** – Viability of recirculated MCF-7 and MDA-MB-231 cells. Instantaneous viability (a) and overall survival (b) at different time points through the chip with  $6 \times 15 \mu\text{m}^2$  constrictions. Ctrl refers to the non-recirculated cells. (N=3 for all conditions)

**Overall cell survival confirms the higher loss in viability of MCF-7 cells upon circulation.** Additionally to the loss of viability (Fig.4.9a), we observed that the number of cells actually in recirculation circuit also decreases with time. The diminution may be explained by the disappearance of dead cells through lysis. We thus defined an overall survival, as the proportion of live cell present at a time point, compared to the initial number of live cells at the

beginning of the experiment :

$$\text{Overall Survival (t)} = \text{Viability (t)} \times \frac{\text{Number of cells (t)}}{\text{Initial number of cells}}$$

The evolution of the overall survival can be appreciated in Fig.4.9b. We observe a decrease in overall survival after 2 hours of  $\approx 50\%$  for MDA-MB-231 cells, and  $\approx 80\%$  for MCF-7 cells, thus confirming a higher deleterious effect of repeated deformation on MCF-7 cells than on MDA-MB-231 cells.

We acknowledge high variability on the count of cells. Indeed, the number of cells is currently evaluated by counting the number of cells in a  $5 \mu\text{L}$  sampling placed in a well of a 96 well plate. The variability may arise from an incorrect sampling (due to non-uniform cell allocation at different points of the fluidic circuit), or from a spatial inhomogeneity in cell seeding at the bottom of the well during image acquisition. This variability is particularly evident in the control condition which we would have expected to be less variable with a survival close to 100%.

## 2.2 Vesicles production under stress and deformation

Under stress, cells are able to produce extracellular vesicles (EVs) [Thompson, 2023]. These objects, whose size ranges from tens to hundreds of nanometers, exert many functions including cellular communication and signaling. These particles can be classified in several categories : microvesicles, exosomes, and apoptotic bodies, based upon their biogenesis, release pathways, size, content, and function [Doyle, 2019]. The EVs produced by CTCs may prove useful as biomarkers for early cancer detection [Tatischeff, 2023], and are thought to be able to spread cancer genes [Rak, 2012] or even promote metastasis [Wan, 2022].

Our objective here is to explore the mechanisms of the production of EVs in experimental conditions set to reproduce the mechanical stresses (either fluid shear stress and/or deformations) CTCs experience in the circulation. We present here the concentration and size distribution of vesicles as a first step in the understanding of the specificity of vesicles production in CTCs produced after 2h of circulation in our device.

**Vesicles enumeration and size distribution depend on the equipment used.** Due to their size in the hundreds of nm, it is impossible to observe vesicles with a microscope. To quantify vesicles production, we used and compared two optic-based detection technics :

- NanoSight (NS300, Malvern Panalytical). Detection is based on the light scattering of particles, and allows to detect particle  $> 40 \text{ nm}$ . Sample concentration has to be within the range  $[10^7\text{-}2.10^8]$  particle/mL, so samples may have to be diluted first.
- Videodrop (Myriad). Detection is based on interferometry, and allows to detect particle  $> 80 \text{ nm}$ .

The size measurement of these nanoparticles is based on the detection of the brownian movement, which magnitude depends on the hydrostatic radius of the particle.

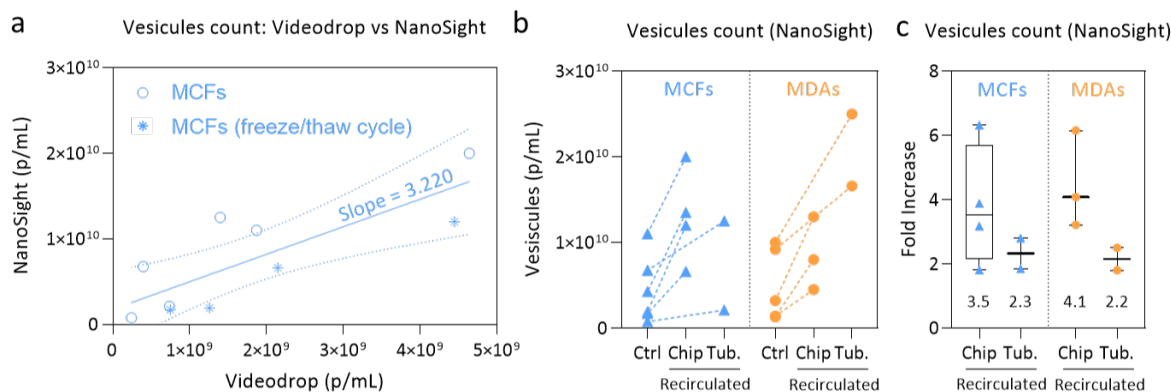


**Figure 4.10** – Vesicles production from circulating MDA-MB-231 and MCF-7 cells. (a) Comparison between two detection equipment (NanoSight and VideoDrop). (b) Production of vesicles in either the chip or the tubing only, compared to the non-circulated control. (c) Fold Increase of vesicles production by recirculated cells compared to the non-circulated control. Values represent the median.

Both equipment are sensitive to different range of nanoparticles sizes, with NanoSight being able to detect smaller particles. We follow reports of other users of these equipment that concentrations obtained with both apparatus are proportional. We show that the values obtained with the NanoSight are systematically higher than those from the VideoDrop, with a factor  $\approx 3.2$  for MCF-7 cells (slope  $3.22 \pm \text{SE } 0.83$   $p=0.0048$ , see Fig.4.10a).

Due to the unavailability of both equipment at the time of the experiments, some samples have been frozen at  $-80^\circ\text{C}$  before measurements (represented by snowflakes on the graph). The influence of freeze/thaw cycle of vesicles sample quality is unclear, however we acknowledge it may have an effect on the vesicles number and/or the size distribution.

### Both fluid shear stress and repeated deformations increase vesicles production.

We measured the production of vesicles at the end of each recirculation experiment (Fig.4.10b). Over the course of 2 hours, the production from cells recirculating through tubing, and thus submitted to shear stress and stress from the peristaltic pump, was increased by a factor  $\approx 2.2$ -2.3 for both cell lines (though replicates need to be completed). Addition of the chip with  $6 \times 15 \mu\text{m}^2$  constrictions increased this factor to 3.5 for MCF-7 cells, and up to 4.1 for MDA-MB-231 cells (see Fig.4.10c).

During the experiment, the cells are kept in a serum-free medium, as serum contains a lot of vesicles and sample production would be lost within the noise. We acknowledge that the baseline value for vesicles production (above  $10^3$  particles/cell) is quite high, even for the control, and present some unexpected variability. A baseline reference from a high number of experiments in controlled conditions will be established for each cell lines to define the expected vesicles production, and thus identify experiments that may derive due to others factors. Simultaneously, as washing steps do not remove all the vesicles, the measurement of vesicles number at time point  $t = 0$  will be added to future experiments, and will be subtracted from all measurements at  $t = 2\text{h}$ . This should result in an increase of the fold increases values presented in Fig.4.10c.

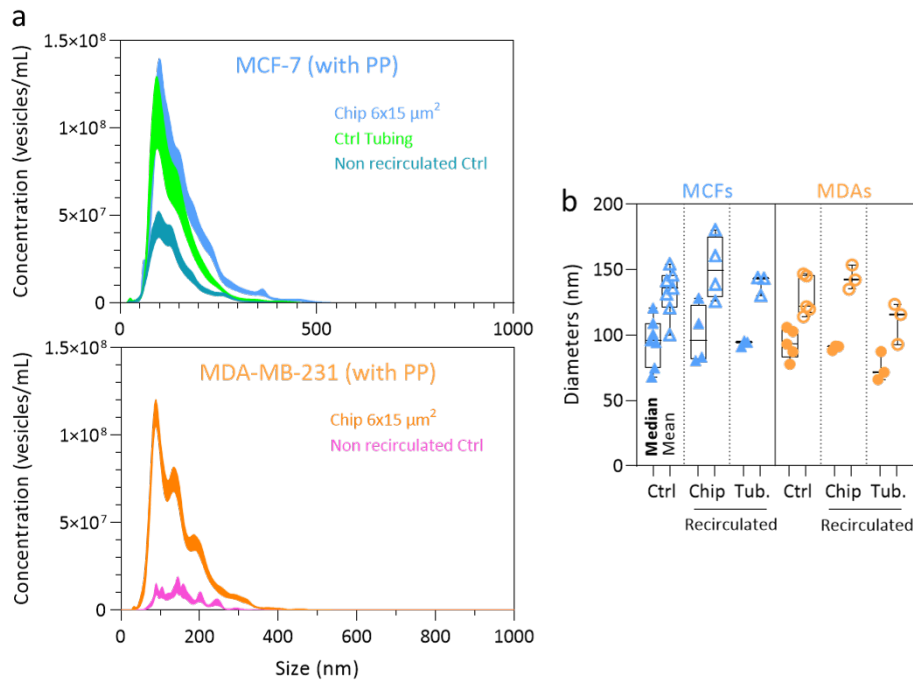


**Figure 4.11** – Size distribution of vesicles (count by NanoSight) (a) Average size distribution in  $6 \times 15 \mu\text{m}^2$  chip, tubing, and non-recirculated conditions for MCF-7 and MDA-MB-231 cells. (b) Comparison of median (plain points) and mean (hollow points) diameters for the replicates of the distribution presented in (a).

**Vesicles size distribution remains mainly unchanged between conditions.** We averaged the size distribution obtained with the NanoSight measurement (see Fig.4.11a, MDA-MB-231 tubing condition wasn't included due to a high different in baseline levels including in the respective controls). These curves allow to appreciate the increase in vesicles production between the non-recirculated control and the recirculated conditions. We observe the distributions to be similar, as exemplified by the similarity between median and mean diameters in each conditions (Fig.4.11b).

We observe the initial peak around 100 nm to be conserved. We also note a slight increase in the levels of the bigger objects produced. However, our analysis does not allow to distinguish between bigger vesicles and apoptotic bodies, which would display diameters with this range ( $> 500$  nm).

### 2.3 Nuclear damages accumulation

As we've seen in the Pachinko device that a single deformation can induce damages in the nucleus, we evaluated nucleus damages at different times points through the experiment. We first focused on the morphological deformation of the nuclei, as quantified by their aspect ratio, at different time points (see Fig.4.12)

**Nucleus deformation increases with the recirculation time.** Overall, we observed an increase in the nuclei AR during the first hour, then a stagnation or slight decrease at the 2

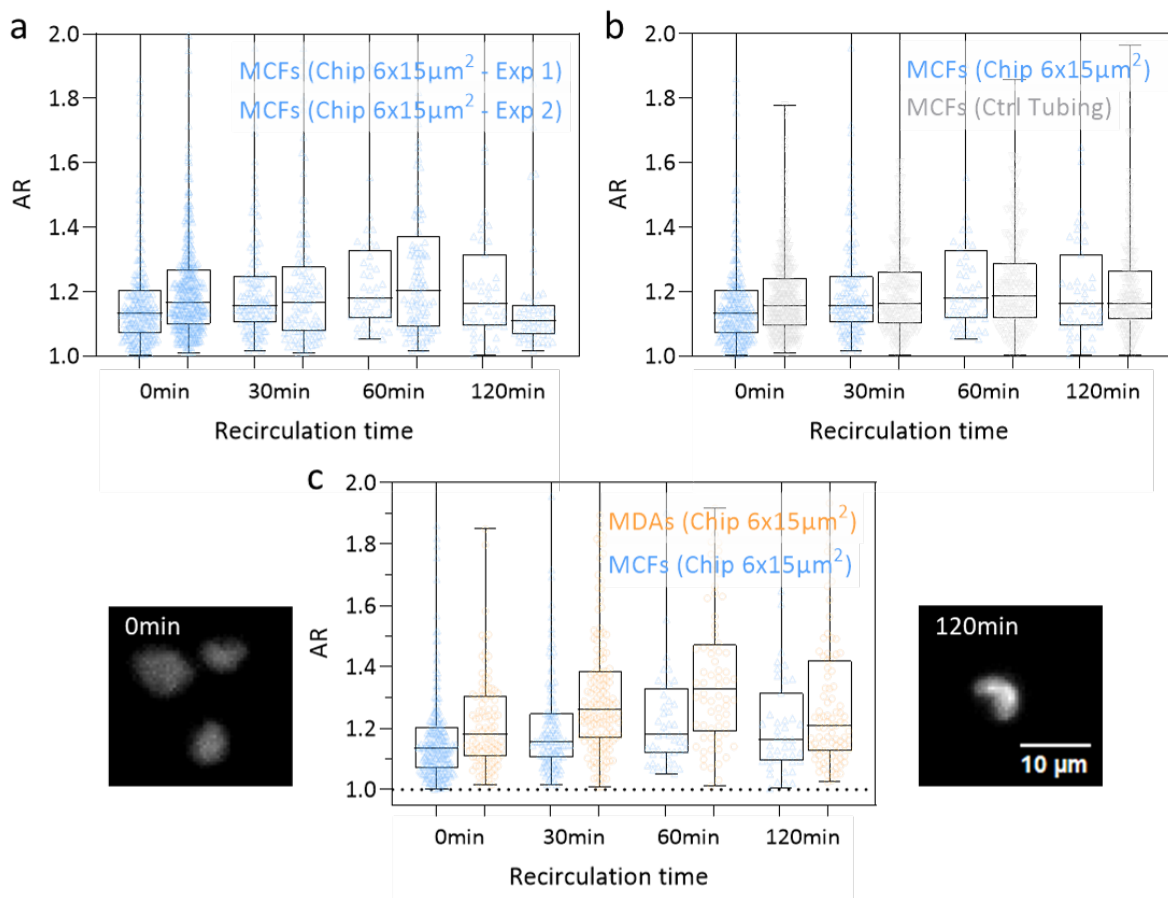


**Figure 4.12** – Aspect ratio of recirculated nuclei. (a) Inter-experiments reproducibility. (b) Nucleus morphological changes of MCF-7 cells recirculated in  $6 \times 15 \mu\text{m}^2$  constrictions chip or tubing only. (c) Nucleus morphological changes of MCF-7 and MDA-MB-231 cells recirculated in  $6 \times 15 \mu\text{m}^2$  constrictions chip. Images display examples of MDA-MB-231 nuclei for 0 and 120 min time points.

hour time point. Though the dispersion in AR is high, we observed this trend to be reproducible between experiments (Fig.4.12a). Interestingly, we did not observe additional damages in MCF-7 nuclei with the introduction of the  $6 \times 15 \mu\text{m}^2$  chip compared to the recirculation through tubing (Fig.4.12b). We hypothesize that cells damaged within the constrictions may be removed from the system through lysis and are thus not collected in the analysis, which is coherent with the cell number decrease observed in the viability study.

**Increase in nuclei deformation is more pronounced in MDA-MB-231 cells.** Finally, though their nuclei are slightly more deformed to begin with, we observe the increase in AR to be bigger in MDA-MB-231 nuclei (from 1.18 to 1.33 during the first hour) than in MCF-7 nuclei (from 1.13 to 1.18).

Interestingly, we observed this increase to stop or reverse after two hours. We propose the following hypothesis to account for this observation :

- The nucleus adapt and recover from the deformation. This recovery would be more present in MDA-MB-231 cells, which may be linked to the presence of the vimentin cage-like

structure around the nucleus as evoked before. It has been reported that MDA-MB-231 cells are able to efficiently repair their nucleus damages, including membrane envelope rupture [Raab, 2016].

- The cells with more deformed nuclei die and are removed from the system through lysis. This would imply that the capacity to restrict nucleus deformation to a limited range is an advantage for cell survival through the circulation.

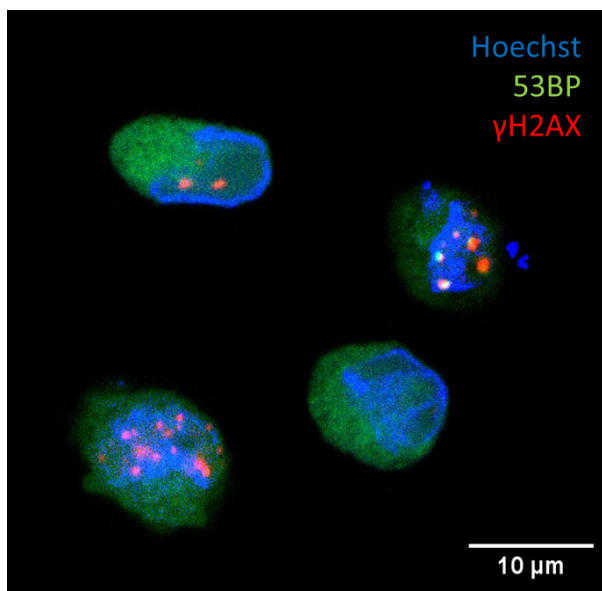


**Figure 4.13** – Immunostaining of MDA-MB-231 cells after 2 hours of recirculation with the  $6 \times 15 \mu\text{m}^2$  constrictions chip. Blue = Hoechst, Green = 53BP, Red =  $\gamma$ H2AX.

We tested for accumulation of damages within the nucleus in the form of double-strand DNA breaks. We used a 53BP::GFP stable MDA-MB-231 cell line established in the lab of Matthieu Piel to visualize sites of double-strand breaks in the form of 53BP foci. Indeed, 53BP is recruited at the site of breaks to achieve DNA repair. In addition, we performed an immunostaining for  $\gamma$ H2AX, a marker of the phosphorylation of H2AX histone which is required for the assembly of DNA repair proteins at the sites containing damaged chromatin. First experiments revealed the presence of sites of double-strand DNA breaks (see an example with MDA-MB-231 cells in Fig.4.13). This staining will need to be repeated at different time points and to be quantified.

## 3 Discussion

### 3.1 About the microfluidic chip and recirculation setup

**Alternatives to PDMS.** The microfluidic chips that we used is made of PDMS, whose Young modulus is about 2 MPa. The cells are deformed against constrictions which are more stiffer than *in vivo* capillaries constrictions (tissue stiffness about 10 kPa). The difference with the modulus of the cell (about 1 kPa) is much smaller and may allow for the vessel to deform as well, making for a more gentle deformation than against a PDMS wall. To improve on the difference of modulus

between the cell and the constrictions, we explored possibilities of using other materials. We constructed chips using Ecoflex, an other silicon-based elastomer of Young modulus around 100 kPa [Vaicekauskaite, 2020]. Additionally to the gain in physiological relevance, we observed these softer chips to be "self-clearing" : the constrictions expands with the upstream build-up of pressure following clogging with debris, which in turns allows the debris to go through and clear the constriction.

To mimic the *in vitro* conditions even more, we would ideally used components of the ECM such as collagen. Channels can be formed within a polymerised collagen gel using laser ablation, thus allowing the construction of any channels shape, including constrictions, with a good resolution (around 2  $\mu\text{m}$ ) [Pinon, 2024]. Other devices have also been able to reproduce a microvasculature network lined with endothelial cells within a collagen gel to study the transit of cancer cells under flow [Chen, 2017].

Similarly, the constrictions section is a  $6 \times 15 \mu\text{m}^2$  rectangle. Designing a circular constrictions to better reproduce capillaries would require more complex technics. Some papers achieved circular complex channels, using diffraction during resin exposure [Fenech, 2019] or through laser ablation technique described above [Pinon, 2024].

**Alternatives to the peristaltic pump.** As we were not satisfied with using a peristaltic pump, we propose other set-up to initiate recirculation within the chip. One way to approach it is to start from the "back and forth" setup presented first, and adapt it using switches and valves so that each cycle goes in the same direction (similarly to the Omi device construction).

### 3.2 About vesicles

We presented here and compared two detection methods of vesicles production in our designed recirculation system. Other methods exist and may complement our analysis, such as exoid TRPS [Shao, 2018] or nanoFCM [Loconte, 2023]. Moving forward, we'll prioritize the use of the Videodrop for vesicles quantification, for its ease and fastness of use (1 single 8  $\mu\text{L}$  deposit,  $\approx 30$  s per sample) compared to the NanoSight ( $> 500 \mu\text{L}$  required, including a dilution, and  $> 5$  min per sample).

**Vesicles production kinetics.** This will allow us to determine the kinetics of vesicles production by measuring rapidly the number of vesicles at each time point. Indeed, as we observed a decreased viability during recirculation, the overall number of cells that contribute to vesicles production decreases as the recirculation goes on. We thus may expect that the increase in vesicles number starts rapidly, and then slows down as more and more cells die. We may conversely hypothesize that cells vesicles production increase upon repeated deformations, and may even compensate for loss of viability. Following the kinetics of vesicles production will help us answering these questions.

As we observed DNA to act as a biological glue, we may also hypothesize that released DNA upon cell death may capture a fraction of vesicles leading to an underestimation of the vesicles production in some conditions.

**Vesicles content and surface markers analysis.** Going further into the analysis, we would like in the future to extract more information than vesicles size and number, especially regarding their content. Surface markers or proteins content can be analyzed through cytometry or immunoblotting [Théry, 2018]. These analysis could reveal markers or proteins specific to circulating cancer cells.

Vesicles could be sorted through different technics (Size exclusion chromatography, differential ultracentrifugation, immuno-precipitation) to access the different types and/or populations of vesicles [Cocozza, 2020]. Additionally, the use of fluorescently labeled CD9 (marker of EVs) stable cell lines would allow to decipher between objects produced through exocytosis or membrane budding, who present CD9, and those produced through other pathways who don't (apoptotic bodies for instance, produced during apoptosis).

Finally we could test on the biological efficiency of the produced vesicles using functional studies, to test for pro- or anti-inflammatory properties for instance [Olejarz, 2020].

**About vesicles and metastasis.** In cancer, EVs have been shown to transfer tumor-specific molecules among cancer cells, healthy cells, and tumor microenvironment [Abhange, 2021], as well as promoting proliferation, migration, invasion, and metastatic spreading in target cells [Green, 2015 ; Goh, 2020].

Interestingly, a recent study showed that MDA-MB-231-derived small EVs were able to promote the formation and elongation of cellular protrusions, soften the cell body, and induce chromatin decondensation in recipient cells such as MCF-7 cells [Senigagliaesi, 2022a]. All these characteristics may contribute to the survival of cells through circulation and the subsequent formation of metastasis. The elastic modulus of both MDA-MB-231 cells and MCF7 cells treated with EVs produced by MDA-MB-231 cells were significantly lower if compared to the untreated MCF7 cells, simultaneously to an increased level of filamentous f-actin [Senigagliaesi, 2022b].

### 3.3 About what happens in the cell

The survival of cancer cells under flow conditions was already reported in the literature [Barnes, 2012 ; Ma, 2017 ; Regmi, 2017 ; Alvarado-Estrada, 2021]. However, only a few studies include cell deformation induced by constrictions.

A previous work performed in our team has focused on the single passage of SK-BR-3 and MDA-MB-231 cells through a series of five  $6 \times 15 \mu\text{m}^2$  [Ahmad-Cognart, 2020]. We reported SK-BR-3 nuclei area to increase in response to shear stress, and less to the additional strain provided by constrictions. This behavior is also confirmed by the variations of circularity and aspect ratio. Conversely, MDA-MB-231 cells appeared quite insensitive to the transition from a suspended to a circulated state, but display significant changes in nucleus size and morphology when constricted. Marking for DNA damages with  $\gamma\text{H2AX}$  revealed DNA damage and repair activity is significantly activated in circulated SK-BR-3 cells, but not in MDA-MB-231 cells (which displayed higher basal repair activity). We also reported changes in EMT-related genes expression towards a mesenchymal phenotype in both cell types.

By forcing cancer cells to flow through  $5 \mu\text{m}$ -wide constrictions, [Jiang, 2023] demonstrated

that mechanical deformation can select a tumor cell subpopulation that exhibits resilience to mechanical squeezing-induced cell death, as revealed by up-regulation of proliferation and DNA damage response pathways. The selection of resilience to deformation trait was shown on several cancer lines, including MCF-7 and MDA-MB-231 cells.

**Cell death through mechanical lysis.** [Weiss, 1985] proposed a theoretical framework of hemodynamic destruction of intravascular cancer cells. They evaluated that the blood pressure-induced membrane tension increase  $\Delta\sigma$  is given by

$$\Delta\sigma = \frac{\Delta p R_{cell}}{2}$$

where  $\Delta p$  is the pressure drop across a cancer cell, and  $R_{cell}$  is the cell radius, which closely approximates to capillary radius  $R$

In our system, we estimate this increase  $\Delta\sigma$  to be  $\approx 22.5 \text{ mbar} \times 15 \text{ }\mu\text{m} / 2 \approx 17 \text{ mN/m}$ , or  $17 \text{ dyn/cm}$ . [Weiss, 1985] reported  $\Delta\sigma$  to be of the order of  $7.3 \text{ dyn/cm}$  in myocardial capillary, and  $1.6 \text{ dyn/cm}$  in pulmonary capillaries.

The usual values found in the literature for membrane tension are in the range of  $10^{-3} \text{ N/m}$ , i.e.  $1 \text{ dyn/cm}$ . The increase of membrane tension to the blood pressure would bring the membrane tension close to, or above, the tension we reported in the introduction for cell lysis ( $10^{-2} \text{ N/m}$ ) [Gauthier, 2012]. We then make the conclusion that the decrease in cell number measured during recirculation may be attributed to cell destruction through lysis. This observation is consistent with reports of cancer cell death under flow conditions, both *in vivo* [Fidler, 1970; Weiss, 1990] and *in vitro* [Regmi, 2017].

We acknowledge that the membrane tension increase produced in our device is an order higher than *in vivo* expectations. We could reduce the pressure drop within the constriction by lowering the flow we impose during recirculation. Though to keep short recirculation cycles, we would need to reduce the recirculated volume and change the setup to reduce the minimal volume required (cell reservoirs, tubings, ...) in further experiments.

### 3.4 About metastasis

We show here that the combination of shear stress and deformations result in an increased cell death for both MCF-7 and MDA-MB-231 cells. However, it may be more relevant to focus on the cells that do survive as they may have been selected for their better phenotypes and/or induction of relevant genes for survival and metastasis formation.

As we described in the introduction, exposition to fluid shear stress is able to induce EMT and promote stemness in cancer cells [Fuh, 2021].

**Shear stress and drugs resistance.** Other studies report that fluid shear stress exposition is able to induce resistance to typical anti-cancerous treatments. For instance, [Triantafillu, 2019] reported synergistic increase of drug resistance-related gene expression in MCF7 cells co-treated

with FSS and drugs (paclitaxel, doxorubicin), as well as increase in stem cell properties. The latter increase from FSS may contribute to drug resistance via the STAT3/NANOG pathway.

Conversely, [Regmi, 2018] reported an inverse, i.e. deleterious consequence of circulation in lung, breast, and cervical cancer cells. FSS significantly increased the potency of the ROS-generating drugs (doxorubicin and cisplatin), but had little effect regarding non-ROS-generating drugs (taxol and etoposide). Though the shear stress level was 4 times higher in [Triantafillu, 2019] (60 dyn/cm<sup>2</sup>) compared to [Regmi, 2018] (15 dyn/cm<sup>2</sup>) and may contributed to these discrepancies, the search for a unified mechanism behind these seemingly contradictory results must be carried out.

## 4 Perspectives

We presented in this section some first results on the recirculation experiments conducted on MCF-7 and MDA-MB-231 cells. We focused here on the influence of repeated constrictions-induced deformations on cell survival, vesicles production and nuclear damages accumulations (though the latter need to be completed and quantified). More analysis are currently in progress to complete this study thanks to Arthur Salles, who has joined the team as a PhD student in partnership with Fluigent.

**About viability measurements.** We evaluated the viability of recirculated cells by acquiring several images of these cells after seeding them in 96 well-plate. This measure is however marred by the variability inherent to seeding inhomogeneity in the well. To improve on that aspect, we would need a more precise measure of cell number and fluorescence, that could be provided with a plate reader for instance to capture the entirety of the well. Other fluorescence-based viability markers could have been explored as well such as Alamar Blue (measure of reducing power cells, as a marker of viability) or ToxiLight (titration in the media of the enzyme adenylate kinase (AK), released from damaged cells).

**Complementary analysis.** In the future, we would like to assess if any changes occurred in the proliferation rate of cells post-circulation. In that aim, we plan to study their growth rate by sampling cells from the recirculation system at different time points. After an initial recoil at the population level due to an overall loss of viability, we expect the surviving cells to long recirculation times through the chip to have been selected for and display increase proliferation capacity.

At the end of the experiment, the media is collected and cells are separated from the media through centrifugation. We already analyzed the vesicles present in the supernatant. The cell pellet collected was lyzed and stored at -80°C in prevision of future transcriptomics analysis (RT-qPCR, RNA-seq). We expect to see changes in the expression of EMT-related genes, but we'll consider as well genes related in the nucleus dynamics, proliferation and stemness.

To take this idea one step further, we could collect at the end of the recirculation experiment, the cells that survive and put them back into culture to establish a new cell population. We

expect this population to have different characteristics than the original lines it originates from, such as increase proliferation, DNA repair capacity, change in rheological properties.

This selected population could be investigated in the recirculation system to evaluate changes in survival, vesicles production, damages accumulation, etc... Similarly, these cells could be analysed in the Pachinko device to investigate changes in their rheological properties.

Using the Pachinko device, we identified vimentin as an important protein in the context of fast deformation dynamics. We plan to study in the recirculation system the effect of vimentin silencing in MDA-MB-231 cells and vimentin expression in MCF-7 cells. Under the hypothesis that the vimentin cage-like structure protect the nucleus from fast deformation, we expect the survival of siVim MDA-MB-231 to decrease compare to WT MDAs, and inversely the survival of Vim+ MCF-7 cells to increase.

**More relevant cell models.** Finally, we aimed at circulate in our system more pertinent cells, i.e. closer to the *in vivo* material. Indeed, as easy to use as commercial cell lines are, they present several limitations including numerous accumulated mutations [Dai, 2017]. Cancer cells isolated from patient derived xenografts would for instance offer a cancer cells model closer to the patient and conserve the original human tumor characteristics [Woo, 2021].

During this project, we initiated a work to isolate cancer from cells from ascite fluid. Ascite fluid is an abnormal build-up of fluid in the body of cancer patient, that is punctured to relieve the patient and is thus considered as medical waste. In this fluid can be found some cancer cells that "leaked" from the tumor, among other cell types like red blood cells, fibroblasts and leukocytes. We can consider these primary cells as naive from the circulation, which is a strong asset in the framework of our experiments about the role of circulation on cancer cells. To isolate the cancer cells from among other the cells types contained with the ascite fluid, we implemented a several step protocol :

- The red blood cells were lysed using an hypotonic media.
- The fibroblasts were removed based on the difference of adhesion with cancer cells.
- Either the leukocytes were removed through magnetic sorting using anti-CD45 labelled magnetic beads, or the cancer cells were similarly selected as EpCAM+ (CD326) cells.

Though we still need to characterize the cells fraction issued from the separation to make sure it is composed of cancer cells only, it would be interesting to characterize these cells within our device. The results, notably cell survival, could be analysed in regard with the clinical data from the patient from whom these cells originate.

## 5 Short Conclusion

In this chapter we introduced a microfluidic chip designed to submit cells to repeated deformations in capillary-like constrictions. We presented a setup to establish a recirculation flow within the chip using a peristaltic pump.

We conducted experiment for a duration of two hours. Cells were recirculated at a flow of 1  $\mu\text{L}/\text{min}$  per channel ( $\approx 22.4$  mbar drop per constriction) within cycles of  $\approx 4$  minutes each. During a full experiment, cells were deformed in 5 successive  $6 \times 15 \mu\text{m}^2$  for 30 times in average.

In accordance to the literature, we showed decrease survival of MCF-7 and MDA-MB-231 cells submitted to repeated deformations. Survival was impacted to a higher extend in MCF-7 cells (80% loss of viability after 2 hours), compared to MDA-MB-231 cells (50% loss of viability). This denotes that MDA-MB-231 present better characteristics regarding survival to fluid shear stress and fast deformations. This observation can be associated to the higher metastatic potential of MDA-MB-231 cells as representative of triple negative breast cancer.

The stress produced by the flow resulted in an increase production of vesicles by the cells. This production was additionally increased when cells are submitted to repetitive deformations.

We observed increased nucleus morphological deformation associated with fluid shear stress.

A similar work with the chips designed was conducted by partners in the lab of Catherine Alix-Panabieres in Montpellier. They were able to show different behaviors between the circulating tumor cell lines established in their lab, that will hopefully result in a publication soon.

## 1 Microfabrication

Microfabrication was performed in the clean room of the Institut Pierre Gilles de Gennes.

### 1.1 Chrome mask fabrication

Channels designs were drawn on AutoCAD. Wafer layout was assembled on CleWin5. Chrome masks were fabricated using the litholaser ( $\mu$ PG101, Heidelberg Instruments) The microfluidic device layout was etched on a photosensitive resin-coated chrome-glass substrate (Nanofilm) following standard technics to obtain the adequate mask of the device. Rapidly, the positive photoresist layer on top of the chrome mask was illuminated with a laser according to the imported design (resolution  $< 1 \mu\text{m}$ ). The mask was developed in a AZ3115B :Water 1 :3 bath to remove exposed resin, then rinsed with water and dried. The chrome layer that appeared in the exposed regions was etched away using chrome etchant for 1 min on a shaker at 60 rpm, letting the transparent quartz underneath appear. Structures were checked under a microscope. Then remaining photoresin was removed using acetone. An example of chrome mask can be seen in Fig.5.1b.

### 1.2 Photolithography

Wafer were fabricated using MJB4 then MA/BA6 aligners (Süss MicroTec). We describe rapidly here the process to create a  $15 \mu\text{m}$  resin layer, as used in the Pachinko device. To achieve other targets heights, parameters need to be adjusted according to the table Tab.5.1. A thin  $15\mu\text{m}$  layer of negative photoresist SU-8 (SU-8 2015, Kayaku Advanced Materials) was spin-coated on a silicium wafer (3000 g, 30 s), baked rapidly (3min,  $90^\circ\text{C}$ ), then exposed through the chrome mask ( $140 \text{ mJ}/\text{cm}^2$ ). The wafer was baked (4min,  $90^\circ\text{C}$ ), developed in PGMEA to dissolve unexposed resin, then baked once more at  $200^\circ\text{C}$ .

If the design include a second layer (for second generation of recirculation chips, or square constriction Pachinko designs for instance), the processed was repeated a second time to create

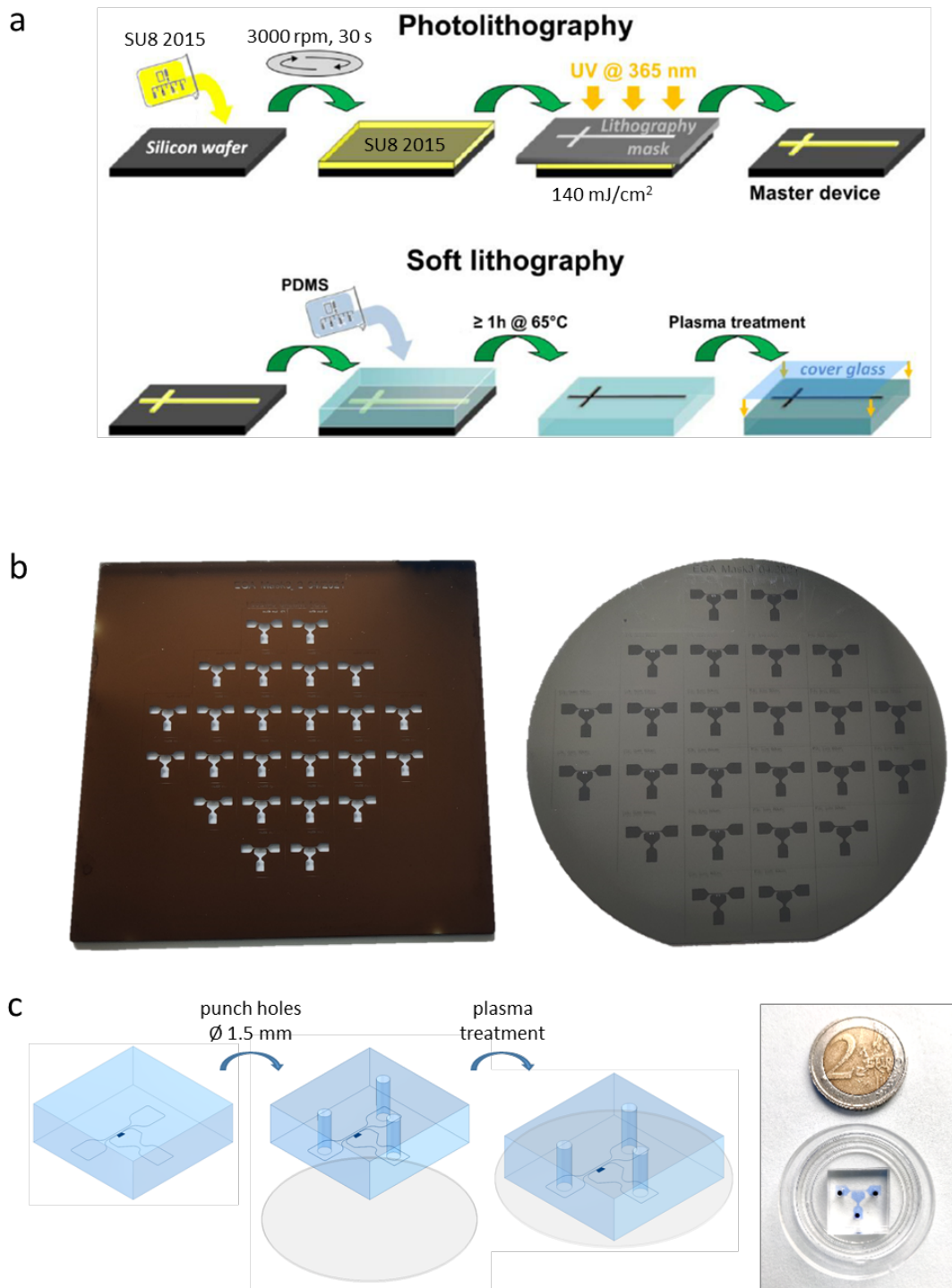


**Figure 5.1** – Vesicles production of recirculated. (a) Photolithography and soft-lithography principle (adapted from [Ma, 2014]). (b) Chrome mask and wafer master mold. (c) PDMS microfluidic chip assembly.

Target height	Resin	Spincoating	Pre-bake	Exposure	Post-bake	Development
6 $\mu\text{m}$	SU8-2007	3500rpm, 30s	2min 95°C	115 mJ/cm <sup>2</sup>	3min 95°C	2min
9 $\mu\text{m}$	SU8-2010	3500rpm, 30s	2min20s 95°C	120 mJ/cm <sup>2</sup>	3min20s 95°C	2min20s
10 $\mu\text{m}$	SU8-2010	3000rpm, 30s	2min30s 95°C	125 mJ/cm <sup>2</sup>	3min30s 95°C	2min30s
15 $\mu\text{m}$	SU8-2015	3000rpm, 30s	3min 95°C	140 mJ/cm <sup>2</sup>	4min 95°C	3min
45 $\mu\text{m}$	SU8-2050	3500rpm, 30s	1min 65°C then 5min 95°C	150 mJ/cm <sup>2</sup>	1min 65°C then 6min 95°C	5min

**Table 5.1** – Photolithography parameters. Prior to resin deposition, wafers were dehydrated at 200°C for 10 min. At the end, wafers were hard-baked at 200°C for > 10 min.

the top resin layer. Alignment was performed before second exposure.

Exact height of the device was measured with a mechanical profilometer (Dektam 6M profilometer, Veeco). As resin properties depend on the external conditions (room temperature, air humidity), the resin layer height was systematically checked after each wafer production.

Wafer surface was rendered hydrophobic by silanization under vacuum with (tridecafluoro-1,1,2,2-tetrahydrooctyl)trichlorosilane (AB111444, abcr) after activation via plasma cleaning.

### 1.3 Soft lithography

PDMS mix (10 :1 base :curing agent, Sylgard 184) was prepared, degassed, and poured over the resin structures of the silanized silicium wafer (height  $\approx$  5 mm). PDMS was left to degassed under vacuum for 15 min so that it perfectly matches the resin structures, then cured at 70°C for 3 h. PDMS was removed from the wafer mold, and individual chips were cut apart. Inlets and outlets were punched out at a 1.5mm diameter. PDMS was cleaned using 70% Ethanol and Isopropanol, then dried with a azote air gun. PDMS chips and fluorodishes were plasma cleaned then immediately bonded together to seal the microfluidic chip. On the day of the experiment, microfluidic chips were washed with 70% Ethanol then PBS, then passivated by injecting 100  $\mu\text{L}$  of 1 mg/mL solution of pLL-PEG (pLL(20)-g[3.5]-PEG(5), Susos) for 30 min, then rinsed with PBS.

## 2 Cell Biology

### 2.1 Cell culture

Seven adherent or non-adherent cancer cell lines, originating from breast or the colon cancer were used in this study. Breast MCF-7, SK-BR-3 and MDA-MB-231 cell lines were available in the team. Colon HT-29, SW-620 and both established CTC permanent cell lines (CTC-41 and CTC-41.5A) were provided by our collaborators in the laboratory of Catherine Alix-Panabières in Montpellier [Cayrefourcq, 2015; Soler, 2018]. Short description of these cell lines is provided in Tab.5.2.

The used CTCs cell lines are the first permanent cell line derived from CTCs taken from a colorectal cancer patient at different time points in the course of the disease [Cayrefourcq, 2015].

Cell line	Culture	Cell origin	Age	Sex
MCF-7	adherent	Breast adenocarcinoma (primary tumor)	69	F
SK-BR-3	adherent	Breast adenocarcinoma (metastasis pleural effusion)	43	F
MDA-MB-231	adherent	Breast adenocarcinoma (metastasis)	51	F
HT-29*	adherent	Colorectal adenocarcinoma (primary tumor)	44	F
SW-620*	adherent	Colorectal adenocarcinoma (lymph node metastasis)	51	M
CTC-MCC-41*	suspension	Metastatic cancer cells (released from the primary tumor)	57	M
CTC-MCC-41.5A*	suspension	Metastatic cancer cells (released from a secondary tumor)	57	M

**Table 5.2** – Description of the human cancer-derived cell lines used in this study. \* : Provided by Catherine Alix-Panabières’s team (LCCRH, CHU Montpellier).

All adherent cell lines except for SW-620 were maintained in Dulbecco’s Modified Eagle’s Medium (DMEM GlutaMax, ThermoFisher 10566016) supplemented with 10% Fetal Bovine Serum (FBS, Gibco 10270-106) and 1% of Penicillin-Streptomycin (100x, 10’000 U/ml penicillin, 10’000 µg/mL streptomycin, Gibco 151140-122).

The SW-620 cell line requires Roswell Park Memorial Institute medium (RPMI 1640, with L-Glutamine 2 mM and sodium bicarbonate, Sigma 8758), completed with 10% of FBS (FBS, Gibco 10270-106) and 1% of Penicillin-Streptomycin (100x, 10’000 U/ml penicillin, 10’000 µg/mL streptomycin, Gibco 151140-122).

The colon CTC lines (CTC-MCC-41 and CTC-MCC-41.5A) were maintained in non-adherent culture conditions, in RPMI 1640 with L-glutamine supplemented with 10% FBS, 1% Insulin-transferrin-sodium selenite (ITS, Sigma I3146), 50 ng/mL of human Epidermal Growth factor (hEGF, Miltenyi) and 10 ng/mL of human Fibroblastic Growth factor (hFGF, Miltenyi). All cell cultures were maintained at 37°C and 5% CO<sub>2</sub>.

All cell lines were tested negative for mycoplasma contamination with either Mycoplasma-Check (Eurofins) service (colon lines), or through the biochemistry platform of UMR168 (breast lines).

### 2.1.1 Cell staining

To enable live imaging, two fluorescent markers are used to selectively label specific targets.

**Cell membrane :** To capture the dynamic behavior of the entire cell, we employ DIL (1,1’-Diocadecyl-3,3,3’,3’-Tetramethylindocarbocyanine Perchlorate), a lipophilic membrane stain exhibiting an orange-red fluorescence (excitation wavelength  $\lambda_{exc} = 552$  nm, emission wavelength  $\lambda_{em} = 566$  nm). DIL is diluted in culture medium at 20 µg/mL. Cells are exposed to the DIL solution and incubated for a minimum of 1 h at 37°C.

**Nucleus :** For visualizing the deformation and subsequent recovery of the nucleus, we employ Hoechst, a blue fluorescent dye (Hoechst 33342) that specifically binds to DNA ( $\lambda_{exc} = 350$  nm and  $\lambda_{em} = 452$  nm). Hoechst is diluted in PBS at 25 µg/mL. Cells are incubated in the Hoechst solution for a duration of 10 min at 37°C.

## 2.2 Treatments

Following harvesting of the cells, either 30  $\mu\text{M}$  Y-27632 (Tocris 1254) or 0.5  $\mu\text{M}$  Latrunculin A (Sigma L5163) was added to the preparation. Dilutions were prepared in the experimental media: serum-free DMEM, supplemented with 1% Pen/Strep, 25 mM HEPES and 2'000 U/mL DNase. Cells were left to incubate for 30 min at 37°C before being injected into the microfluidic Pachinko device.

### 2.2.1 Vimentin silencing

For transient vimentin knockdown, a reverse transfection protocol was performed, entailing the addition of the treatment complex to freshly passaged cells. SW-620 were seeded in a 6-well plate with an initial cell number ranging from 500'000 to 1'000'000. The transfection complex consisting of siRNA (targeting vimentin expression or non-targeting, all from Dharmacon), Lipofectamine RNAi-MAX reagent (Invitrogen 13778075), and Opti-MEM (Gibco 31985070) was meticulously prepared in accordance with the manufacturer's guidelines. In the case of wild-type controls, an equivalent volume of Opti-MEM was applied. References for the used products are listed in Table 5.3. Subsequent to the addition of treatments, the medium was renewed 24 hours post-transfection. It is noteworthy that, for the double transfection condition, the second transfection was administered to cultured cells rather than freshly passaged cells. Evaluation of knockdown efficiency was conducted 48 or 72 hours post-transfection via Western Blot analysis employing standardized techniques.

Following the optimization process, double-transfected cells (2x48h) were selected as the experimental model for conducting Pachinko experiments. Consequently, 48 h after the second transfection, cells were harvested and divided into two equal portions: one for subsequent lysis (to allow future immunoblotting analyses) and the other for labeling purposes (to enable Pachinko experiments).

siRNA	Description	Format	Target	Reference
siVim	ON-TARGETplus Human Vim siRNA	SMARTpool	VIM gene transcripts	Dharmacon (Horizon Discovery) D-001810-10-05#
siNT	ON-TARGETplus Non-targeting Control Pool	SMARTpool	none	Dharmacon (Horizon Discovery) L-003551-00-0005

**Table 5.3** – List of siRNA transcripts references.

### 2.2.2 Vimentin transfection

For the transient overexpression of vimentin through lipofection, a reverse transfection protocol was performed, entailing the addition of the treatment complex to freshly passaged cells. Cells were cultured on a 6-well glass-bottom cell culture plate to enable subsequent live imaging. The initial cell number was set at 500'000. Transfection was carried out with a fluorescently-tagged DNA plasmid (2.5  $\mu\text{g}$ , Addgene, see Tab.5.4) complexed with Lipofectamine 3000 (Invi-

trogen) mixed in Opti-MEM (GIBCO). For wild-type controls, an equivalent volume of Opti-MEM (GIBCO) was applied. References for the used plasmids are listed in Table 5.4. The efficiency of overexpression was evaluated via live imaging 24 or 48 hours after transfection and was completed with immunoblotting analysis.

For transfection through electroporation experiments, cells were harvested and 3'000'000 cells were added to the prepared plasmid (3  $\mu\text{g}$ ) and Nucleofector 100  $\mu\text{L}$  solution mix (Lonza). The mix was transferred in a amaxa certified cuvette and placed in the Nucleofector 2b Device (Lonza). Program T-020 was used, then cells were immediatly removed from the cuvette with 500  $\mu\text{L}$  of media and transferred into a culture dish. The efficiency of overexpression was evaluated via live imaging 24 or 48 hours after transfection and was completed with immunoblotting analysis.

Plasmid	Gene insert	Tag (C-terminal on backbone)	$\lambda_{exc}$ (nm)	$\lambda_{em}$ (nm)	Reference
mCherry-Vimentin-N-18	Human VIM NM_003380.9	mCherry	587	610	Addgene #55158
mEmerald-Vimentin-7	Human VIM NM_003380.9	mEmerald	487	509	Addgene #54299

**Table 5.4** – List of plasmids references.

### 2.3 Cell preparation

**Pachinko experiments :** Following staining, and optionally treatment, cells were trypsinized for 5 min and harvested. Cells were counted and resuspended at  $\approx 400'000$  cells/mL in serum-free media, supplemented with 1% Pen/Strep, 25 mM HEPES and 2'000 U/mL DNase, and optionally the drug treatment.

**Recirculation experiments :** Cells were trypsinized for 5 min and harvested, before being filtered through a 40  $\mu\text{m}$  pore cell strainer. Cells were pelleted at 500 g for 5 min, then resuspended in 100  $\mu\text{L}$  Dead Cell Removal Microbeads solution (Dead Cell Removal Kit, Miltenyi) and incubated for 15 min at room temperature. Dead and dying cells fraction was separation on a LS column (Miltenyi) placed in a magnetic MidiMACS Separator (Miltenyi). Live cells fraction was eluated through the column using 4x3 mL of binding buffer 1x, then pelleted at 500 g for 5 min and resuspended at 1 million cells/mL in 1 mL recirculation media. Recirculation media is composed of serum-free DMEM, supplemented with 1% Pen/Strep, 25 mM HEPES, 2'000 U/mL DNase and 15% OptiPrep. 500  $\mu\text{L}$  were injected into the recirculation device, and the other 500  $\mu\text{L}$  were kept on the side as a control.

## 2.4 Biochemistry

### 2.4.1 Live/Dead imaging

To quantify viability of cells (sampled during recirculation for instance), an equal volume of Live/Dead 2x mix (LIVE/DEAD™ Cell Imaging Kit (488/570), ThermoFisher) was added to the cells. Cells were incubated for 15 min at room temperature then imaged under a videomicroscope. Live cells are stained with green Calcein AM, and dead nuclei with red Propidium Iodide (PI).

In recirculation experiments, viability was counted as the ratio of live cells over total number of cells. Regarding nucleus counting, a threshold of 50 pix<sup>2</sup> (i.e. > 20 μm<sup>2</sup>) was used to differentiate between dead cells and debris (stained with PI as well).

### 2.4.2 Immunofluorescence

For imaging of adherent conditions, two hundred thousand cells were cultured for 24-48 hours on coverslips covered with Poly-L-Lysine (PLL) 0.1% (Sigma), then fixed with 4% Paraformaldehyde (PFA) in Dulbecco's phosphate-buffered saline (DPBS) (Gibco - ThermoFisher Scientific) for 15 minutes at room temperature (RT). Conversely, for imaging of cells in suspension, 5 μL of cells in suspension were placed on a PLL-coated glass slide and immediately fixed with 4% PFA. Afterwards, cells were rehydrated with DPBS twice and then permeabilized with 0.1% Triton X-100 (Sigma) in DPBS for 15 min at RT. After two instant washes in DPBS, blocking was performed in 4% Bovine Serum Albumine (BSA, Sigma) in DPBS (PBS-BSA) for 5 min at RT. Cells were stained for one hour with primary antibodies (ABs) diluted accordingly to Tab.5.5 in PBST 2% BSA and then washed twice with DPBS. Coverslips were incubated with fluorescently labeled secondary ABs, diluted accordingly to Tab.5.5 in PBST 2% BSA, for at least one hour at RT. After two more instant washes in DPBS, coverslips/glass slides were drained on a Kimwipe (Kimtech), mounted using EverBrite Hardset Mounting Medium with DAPI (Biotium), and left at +4°C overnight before being sealed with nail polish and imaged.

### 2.4.3 Immunoblotting

Cells were lysed in Radioimmunoprecipitation assay (RIPA) buffer (25 mM Tris-HCl, pH 7.6, 150 mM NaCl, 1% NP-40, 1% sodium deoxycholate, 0.1% SDS) (ThermoFisher Scientific) containing freshly added 1x EDTA (Thermo Fisher Scientific) and 1x Protease and phosphatase inhibitors (Halt Protease & Phosphatase Inhibitor Cocktail, Thermo Fisher Scientific). Lysates were passed through a 25G needle ten times and incubated for 5 min on ice, then cleared by centrifugation at 16'000 g for 5 min at 4°C. Protein lysates were mixed with 1x Laemmli buffer and heated for 10 min at 95°C. Proteins were separated using a 4-12% polyacrylamide gel (NuPAGE 4-12% Bis-Tris Gel 1mm x 10-well mini, ThermoFisher Scientific) with a standard sodium dodecyl sulfate polyacrylamide gel electrophoresis (SDS-PAGE) protocol in 500 mL of 20x NuPAGE MOPS SDS Running Buffer (ThermoFisher Scientific). Separated proteins were transferred to a nitrocellulose membrane at a voltage of 23 V for 6 min in a dry transfer iBlot device (ThermoFisher Scientific), according to the manufacturer's protocol. Membranes were blocked for 2 hours at room temperature (RT) and on a shaking platform, using 3% Bovine Serum Albumin

Target	Host	Clonality	Labelled	Reference	Final concentration
<i>Primary Antibodies</i>					
Lamin A/C	mouse	monoclonal		Sigma SAB4500236	1 :1000 (WB) 1 :200 (IF)
Lamin B1	rabbit	polyclonal		Abcam ab16048	1 :1000 (WB)
Lamin B2	rabbit	monoclonal		Abcam ab151735	1 :1000 (WB)
Vimentin (SP20)	rabbit	monoclonal		Abcam ab16700	1 :1000 (WB) 1 :200 (IF)
MLC II	rabbit	polyclonal		Cell Signaling 36725	1 :500 (WB)
p-MLC II (T18/S19)	rabbit	polyclonal		Cell Signaling 36745	1 :500 (WB)
GAPDH	rabbit	monoclonal		Cell Signaling 21185, clone 14C10	1 :2000 (WB)
$\gamma$ H2AX (Ser139)	mouse	monoclonal		Millipore 05-636-25ug, clone JBW301	1 :500 (IF)
<i>Secondary Antibodies</i>					
Rabbit IgG(H+L)	goat	polyclonal	HRP conjugate	Invitrogen #65-6120	1 :5000 (WB)
	goat	polyclonal	AlexaFluor 546	LifeTechnologies A11071	1 :1000 (IF)
Mouse IgG(H+L)	goat	polyclonal	HRP conjugate	Invitrogen #65-6520	1 :5000 (WB)
	goat	polyclonal	Cy5	ThermoFisher A10524	1 :500 (IF)
	goat	polyclonal	AlexaFluor 488	LifeTechnologies A11017	1 :1000 (IF)

**Table 5.5** – List of antibodies (ABs) used in immunoblotting (WB) and immunofluorescence (IF) experiments.

(BSA) (Sigma) in Phosphate-Buffered Saline (PBS) containing 0.1% Tween 20. The antibodies (ABs) used and their corresponding concentration are shown in Tab.5.5. Separate blots were probed with different primary ABs and all blots were probed with ABs against GAPDH, as a loading control. Primary ABs were diluted in the blocking solution and incubated with agitation overnight at 4°C. After three 10-minutes washes in PBST (PBS with 0.1% Tween 20), the blots were probed with Horseradish Peroxidase (HRP) conjugated secondary ABs diluted in the blocking solution (1 :5'000), and incubated for 3 h and on a shaking platform and at RT. After a single 1-hour wash followed by two 5-minutes washes in PBST, imaging was performed with ChemiDoc Touch Biorad 2 Imager using SuperSignal West Pico Chemiluminescent Substrate (ThermoFisher Scientific). Analysis was performed using ImageLab.

### 2.4.4 Vesicles collection

At the end of recirculation, the tubing circuit was emptied and collected in a eppendorfs. Cells were removed by centrifugation at 500 g for 5 min. The supernatant was collected and centrifuged at 2000 g for 10 min at 4°C. The supernatant was collected carefully and transferred to another eppendorf for analysis. The sample containing vesicles was stored overnight at 4°C for analysis on the next day, or frozen at -80°C for a longer conservation.

## 3 Experiments

**Preparation of the chip :** Prior to usage, the solutions undergo filtration (220nm PTFE filters) and are then injected into inlet 1 using a syringe, needle, and tubing. The microfluidic chip undergoes a series of washing steps, starting with 100  $\mu$ L of 70% ethanol, followed by 100  $\mu$ L of PBS. To ensure optimal performance and prevent cell adhesion, the channel is passivated with 1 mg/mL pLL-g-PEG (poly(L-lysine)-g-poly(ethylene glycol), SuSoS) as described below for a duration of 30 minutes to one hour. Any excess pLL-g-PEG is subsequently washed away using PBS.

Microfluidic chips are prepare the same for both Pachinko and Recirculation experiments. The following section below refer to the Pachinko experiment. The experimental setup consists mainly of a fluidic system (microfluidic chip and pressure controllers) and an acquisition system (see Fig. 5.2).

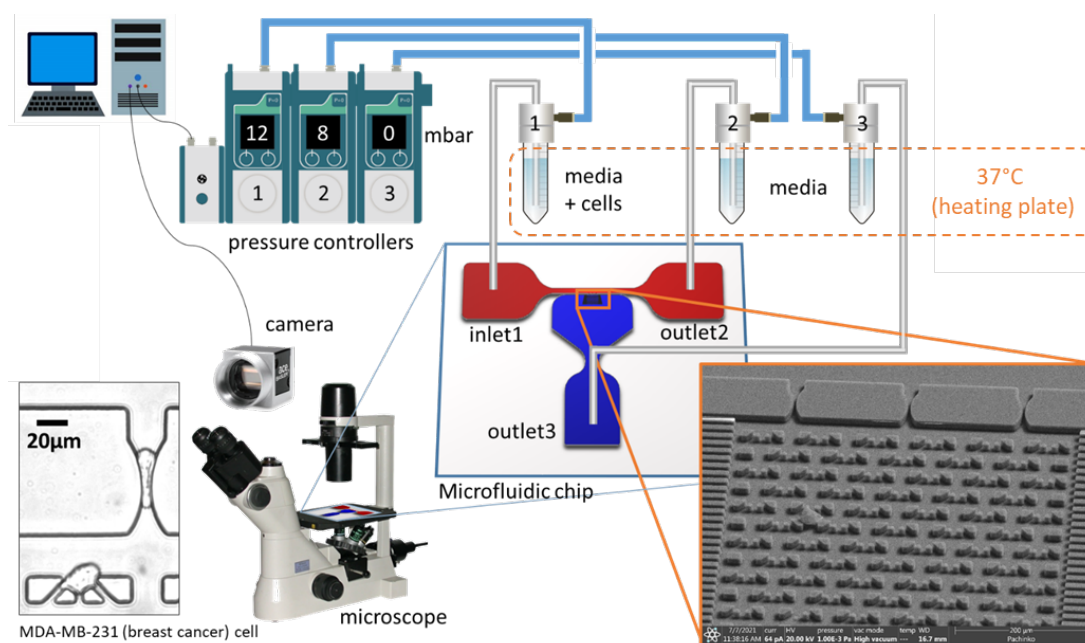


**Figure 5.2** – Experimental setup for Pachinko.

**Fluidic system :** The cell suspension ( $\approx 400'000$  cells/mL) was placed in an Eppendorf tube mounted with a p-cap (Fluigent) connected to the inlet 1 of the microfluidic chip through a fluidic

tubing (ID .02in, OD .06in, Tygon ND-100-80, Cole-Parmer). Outlets 2 & 3 were connected to Eppendorf tubes containing the same media without cells. The cell suspension and media were kept at 37°C on a hot plate for the whole duration of the experiment. Three Flow-EZ pressure controllers (Fluigent), monitored by All-in-One software (A-i-O 2019, Fluigent), are employed to regulate the pressure drop across the constrictions.

**Acquisition system :** For recording the experiment, the chip was securely mounted on an inverted microscope (Nikon Eclipse TS100) with a 10X objective (N10XW-PF - 10X Nikon CFI Plan Fluorite Objective, 0.30 NA, 3.5 mmWD). A fluorescence microscope cube filter (TLV-TE2000 - Thorlabs Microscopy Filter Cubes), specific to the fluorophores used, is adapted, along with a high-speed acquisition camera (acA1920-150um Basler AG, pixel size 4.8µm\*4.8µm). Pylon Viewer software (pylon 6.3.0 Camera Software Suite for Windows, Basler AG) is employed to control the camera settings.

The exposure time is set to a minimum ( $\approx 2$  ms), and the acquisition rate is fixed either at 50 fps for whole-cell analysis or at 100 fps for nucleus analysis. Recording was conducted in a light-controlled environment where minimal or no ambient light was present.

**Operation on the Microfluidic Chip :** Inlet 1 and outlet 2 pressure were set to 12 and 8 mbar respectively to initiate a flux of cells in the device main channel. The pressure in outlet 3 was initially kept at 10 mbar to prevent cells from entering constrictions then decreased to 0mbar to allow cells to enter.

Simultaneously, fluorescence and acquisition were started to capture cells entering the constrictions. The recording is stopped when the majority of the traps are filled. The experiment can be repeated multiple times using the same chip by flushing the cells out of the trap chamber with higher pressure at outlet 3.

## 4 Data Analysis

### 4.1 ImageJ

#### Cell trajectory reconstruction

Sequences of fluorescent cell or nucleus moving through the device were binned on ImageJ. Cell tracks were reconstructed using the TrackMate plugin on ImageJ[Tinevez, 2017] Briefly, fluorescent objects were detected with a threshold based method, then detected spots were linked on each successive images (linear motion LAP tracker) to reconstruct tracks. Parameters of the detection and tracking algorithms were adjusted to each sequence. Tracks were manually reviewed and corrected for punctual errors in track reconstruction. Track coordinates were exported to Matlab (R2020a, MathWorks) for downstream analysis.

## 4.2 Matlab

**Cell arrest time determination :** Only complete tracks (i.e. with images before and after deformation in the constriction) were selected for the analysis. Entry and exit time points were defined as the index of the first image where the cell y-position exceeds respectively the constriction entry and exit y-coordinate. The arrest time of a cell was determined as elapsed time between entry and exit time points. For the fastest cells which can cross the constriction in less than 1 frame, we attribute to these cells an arrest time corresponding to the inverse of the acquisition frame rate, i.e. 20 ms.

**Image analysis and segmentation :** For each cell track, for each time point in the cell track, a region of interest around the cell position was drawn in the original images. The selected section of the image was binarized : Hoechst-stained nuclei images were binarized with a threshold determined with Otsu's method [Otsu, 1979]. DIL-stained membrane images were segmented with 2 thresholds calculated using Otsu's method, to account for fluorescent intensity heterogeneity in the cell. Non-background layers were merged together to recreate cell binarized region. Images were filtered to keep the biggest structure in the image. Major and minor axes of the ellipse that have the same normalized second central moments as the binarized region were measured.

**Cell parameters extraction :** The diameter of the cell can be estimated by measuring the average area of the shape in the main channel assuming that the 2D projection of the cell is a circle through the relation  $a_0 = \sqrt{\frac{4A}{\pi}}$  between the cell diameter  $a_0$  and the binarized region area  $A$ . Elongation  $\varepsilon$  and aspect ratio  $AR$  of the cell or nucleus were defined with major axis  $a$  and the minor axis length  $b$  as  $\varepsilon(t) = \frac{a(t)-a_0}{a_0}$  and  $AR(t) = \frac{a(t)}{b(t)}$  where  $a_0$  is the average value of the diameter measured in the main channel. Maximal  $\varepsilon_{max}$  and end value  $\varepsilon_{\infty}$  were determined for each cell using Matlab Cftool application interface, and used to compute the normalized deformation  $\varepsilon_{Norm}(t) = \frac{\varepsilon(t)-\varepsilon_{\infty}}{\varepsilon_{max}-\varepsilon_{\infty}}$ . Incomplete and blurry images were manually excluded from the analysis based on visual examination of corresponding images.

## 4.3 Python

**Contour plots :** Contour and density plots were generated for each cell lines data sets using Python gaussian kernel density estimation. For better visualization, one density level was overlaid on scatter plots to indicate region of highest points density. Kernel density plots for each parameter was added right and on top of the graph to represent this parameter distribution.

## 4.4 GraphPad Prism

**Mean recovery curves and fits :** For each cell (resp. nucleus), normalized elongation values of the cell during recovery were imported on Graphpad Prism9 software (GraphPad Software Inc., USA) (with time  $t=0$  s taken as the last image of the cell in the constriction). For each cell

lines, mean curves and corresponding 95% confidence interval were plotted. These mean curves were used to fit according to the developed models described in the text.

**Statistical analysis :** All statistical evaluations were conducted using the Graphpad Prism9 software (GraphPad Software Inc., USA). Independent groups were compared using the non-parametric Mann-Whitney test (arrest times, diameters, Young modulus), or Wilcoxon matched-pairs rank test in the case of paired data ( $\varepsilon_{max}$  vs  $\varepsilon_{\infty}$ ). Significance is reported as the following : \* :  $p \leq 0.05$ , \*\* :  $p \leq 0.005$ , \*\*\* :  $p \leq 0.005$ , \*\*\*\* :  $p \leq 0.001$ .

In this study, we designed two complementary microfluidic devices to study the short- and long-term response of cancer cells to fast flow-induced capillary-like constriction-based deformations. These devices aim to reproduce the stresses and deformation that cancer cells may encounter as they navigate in the blood circulation and in particular through the microcapillary bed. The main focus of this work was thus the still under-studied dissemination step in the bloodstream as part of the metastatic cascade. We investigated the behavior of seven cancer cells lines; three from breast cancer and four from colon cancer, as representative of different clinical phenotypes.

**In the first Pachinko device,** we focused on the morphological deformation and recovery of cancer cells under flow. We correlated the time it takes for a cell to cross the constriction to its size first, and notably to its metastatic potential at the clinical level for breast cancer. Indeed, as the literature points towards [Alibert, 2017], we found metastatic breast cancer cells to be softer. Interestingly, as other studies did [Pachenari, 2014; Brás, 2022], we found the opposite for colon cells, which remains to be investigated.

By trapping the cells after their deformation to study their recovery, we were able to report that the morphological recovery of cells present two regimes : a first almost instantaneous elastic regime, followed by a slower viscoelastic regime which present characteristic times of the order of 1 s and 10 s. By modeling this behavior with rheological models or power-law theory, we estimated rheological parameters for each of the cell lines. Though, we acknowledge this approach was complicated by the sometimes poor quality of the fits.

We report that both the nucleus and the cytoskeleton instead contribute to the resistance to deformation. Inhibiting the actin cytoskeleton contractility resulted in a partial slower recovery, while its disassembly prevented cell recovery overall.

We then studied the dynamics of nucleus deformation and recovery. Though the nucleus is described as a complex viscoelastic material [Dahl, 2004], we showed that nuclei recover surprisingly in an almost entirely elastic way, exhibiting more than 90% recovery in less than 1 second for all cell lines, and even faster for the more metastatic lines. Relating to the first immunoblotting results, we associated the elastic recovery to depend of the presence of a vimentin perinuclear cage, then on the protein levels of Lamin A/C if the former is absent. Thus we observed MDA-MB-231 and SW-620 nuclei, which are surrounded by a vimentin cage, to display

---

higher elasticity in recovery than the other studied lines. Then CTC41.5A and HT-29 nuclei presented higher elasticity than CTC41 nuclei which could be correlated to higher lamin A/C levels.

As others did, we hypothesize the role of vimentin intermediate filaments forming a perinuclear cage as a protective structure for the nucleus. Its relative rigidity upon fast deformation acts as a "shock absorber" and protects the nucleus from sudden deformation which may result in nuclear damages [Block, 2017]. Then, at a slower rate, the cage can be deformed, allowing the nuclei to deform within a "safe" regime. Similarly, we may advance the same hypothesis regarding the higher instantaneous elasticity measured in more metastatic colon cell lines at the cell level. A denser actin cortex may provide similar protection against fast deformation.

**In the second recirculation device,** we explored this notion of cancer cell survival following forced deformations. We implemented a recirculation device that allowed to submit cancer cells to repetitive deformations, similarly to what they may encounter circulating the blood. We showed that loss of survival was more limited in the more metastatic MDA-MB-231 cells compared to MCF-7 cells. This results calls to the more aggressive nature of metastatic triple negative breast cancer for which MDA-MB-231 cells are representative, compared to the luminal breast cancer represented by MCF-7 cells [Kast, 2015]. Similarly to the previous paragraph we may call the mechanical properties of cells and/or nuclei, including the presence of a protective vimentin perinuclear cage, as well as possibly different damages repair pathways, to explain the survival differences. The ability to transit and survive through constrictions may prove to be essential to promote metastasis.

Alternatively, we could hypothesize that as cells are getting stuck within small capillaries, it encourages interaction with the endothelium and facilitates extravasation. Thus, it has been observed that colorectal cancer forms preferentially metastasis to the liver ( $\approx 50\%$  of CRC patients [Vatandoust, 2015]) that drains the region via the portal vein and acts as a filter capturing CTCs.

We also showed proof of increased vesicles production in response to fluid shear stress, and additionally to deformation. We may postulate the messenger role of these vesicles, as a way to collectively adapt to the stresses and deformation encountered in the circulation [Senigagliaesi, 2022b].

**About the relevancy of CTCs.** While ctDNA has been included in the diagnostic determination for some cancer (detection of epidermal growth factor receptor mutations in non-small-cell lung cancer for instance [Normanno, 2017]), the clinical use of CTCs still remains currently limited. The main limitation resides in their rarity and subsequent complicated detectability. As the detection threshold was set as low as 5 CTCs per 7.5 mL blood sample [Cristofanilli, 2004], the absence of detected CTCs does not necessarily relate to their absence from the blood. Moreover, available capture devices rely on either the presence of surface markers, or specific size and rheological properties [Kumar, 2022], both of which may potentially not recapitulate the heterogeneity of CTCs.

Though they remain excellent study models to understand the progression of metastasis [Pantel, 2016]. CTCs lines isolated from patients [Cayrefourcq, 2015 ; Koch, 2020] offer a more pertinent model than immortalized cell lines, while retaining the same ease of use compared to other alternatives (PDX, ascites, ...). On our devices, we were for instance able to show the evolution of mechanical properties (towards smaller and more rigid phenotype) of cells isolated from the same patient before treatment and after relapse.

**Cancer, EMT and stemness.** We explained that cells undergoing the EMT transition may be better suited to survive in the blood circulation [Thiery, 2009]. Indeed, the mesenchymal phenotype is the one of leukocytes, which have to be able to deform as they migrate through the blood or within tissues. However, leukocytes are unable to proliferate. If a cancer cell was to remain stuck in the mesenchymal state after its escape from the circulation, it would not be able to proliferate and start a new metastasis. What makes a cancer cell dangerous may not be the capacity to undergo EMT to migrate and survive the blood circulation, but to be able to switch between both phenotypes accordingly. This behavior is an example of cell plasticity [Friedl, 2011a]. When the cells needs to migrate and withstand stresses and deformation, it adopts a mesenchymal phenotype. Conversely, when it needs to be able to proliferate again, it undergoes MET (reverse EMT) and adapts a epithelial phenotype [Roy, 2021]. More recently, cancer cells were found to exist at an intermediate state between epithelial and complete mesenchymal states, known as partial/hybrid EMT. These cells are able to acquire stem-like characteristics, which serve as critical drivers of tumor progression [Nassar, 2016].

It would appear that a rare population of undifferentiated cells is responsible for tumour formation and maintenance. This sub-population is referred to as tumor-initiating cells, or as "cancer stem cells" for their capacity for both tumor initiation and sustaining tumor growth. In colon cancer, these cells were identified as part the high-density CD133+ population, which accounts for about 2.5% of the tumor cells [Ricci-Vitiani, 2007]. Subcutaneous injection of colon cancer CD133+ cells readily reproduced the original tumour in immunodeficient mice, whereas CD133- cells did not form tumors. In breast cancer, this sub-population was shown to be ALDH1+ which correlated to successful engraftment in immunodeficient mice and predicted poor prognosis in the patient [Ginestier, 2007 ; Charafe-Jauffret, 2013]. In a mammary tumor progression model, these "cancer stem cells" could be derived from human mammary epithelial cells following the activation of the Ras-MAPK pathway and can be accelerated by EMT induction [Morel, 2008].

In that regard, understanding the mechanisms that induce EMT and/or stemness is essential to the comprehension of metastasis. If the shear stress has been identified as one of them [Fuh, 2021], we think the addition of constriction-based deformations may enhance it [Ahmad-Cognart, 2020]. Though we did not have time to perform the experiments here, we should be able in the future to evaluate the expression of related genes in cancer cells that were repeatedly deformed under flow.

---

**About treatments.** The discovery that cancer cells were able to escape the immune response by expression of the PD1 ligand (which results in death of the immune cell [Iwai, 2002]) allowed for the development of new immunotherapies. Target PD1-PDL1 interaction or the many similar other, they aim at restoring the capacity of immune cells to target the tumor [Alsaab, 2017].

Recently, the development of antibody-drug conjugates (ADCs) brought real improvement by allowing to deliver drugs to specific cells based on the expression of target antigen. As an example, ado-trastuzumab emtansine (T-DM1) was the first ADC to be approved by the FDA in 2013 for the treatment of metastatic breast cancer (targeting the HER2 marker) [Amiri-Kordestani, 2014]. By increasing the drug-to-antibody-ratio, a new generation of ADCs is able to target cells with very low or none antigen expression by diffusion of the payload to neighbour cells, referred to as the bystander effect [Giugliano, 2022], thus bringing a possible answer to cancer heterogeneity.

If targeting the cell mechanical properties prove to be a successful strategy to prevent metastasis in the future, we could imagine using ADCs to deliver drugs to either impact the cytoskeleton, nuclear proteins, EMT and more.

Le projet s'intéresse à l'étape clé, et pourtant peu étudiée, qu'est le passage des cellules cancéreuses dans la circulation sanguine dans le processus métastatique. La cascade métastatique est un processus complexe, trop souvent létal d'un point de vue clinique, impliquant une phase intermédiaire dans la circulation sanguine. Les cellules issues de la tumeur primaire acquièrent alors le statut de cellules tumorales circulantes (CTCs). Les capillaires sanguins présentant un diamètre typique bien inférieur à celui de la cellule cancéreuse, et même de son noyau [Follain, 2020], les CTCs se retrouvent soumises à de forts stress et fortes déformations [Perea Paizal, 2021]. L'étape "circulante" des cellules cancéreuses reste mal comprise et peu étudiée, mais il est probable qu'il ne s'agisse pas d'une simple étape de dissémination passive. Le rôle des forces mécaniques est bien documenté dans le cancer, y compris l'influence du flux sur l'augmentation des capacités de migration [Dash, 2022], la surexpression des gènes liés à la transition épithélio-mésenchymateuse [Ahmad-Cognart, 2020], ou au caractère souche des cellules [Dash, 2022]. Par ailleurs, l'application de stress sur plusieurs heures favorise la survie des cellules les plus molles montrant un potentiel métastatique plus élevé que leurs homologues plus rigides [Lv, 2021], ainsi que l'enrichissement de cette sous-population aux caractéristiques mécaniques plus molles [Alvarado-Estrada, 2021]. Dans ce cadre, la question de ma thèse porte sur les processus de sélection et de transformation des CTCs du fait des stress mécaniques qu'elles subissent dans la microvasculature :

### **Quelles sont les réponses et adaptations des Cellules Tumorales Circulantes aux stress et déformations rencontrées dans la microvasculature ?**

Au niveau méthodologique, j'adresse cette question à l'aide de modèles microfluidiques de la microvascularisation sanguine. Mes travaux visent plus précisément à induire et comprendre les réponses cellulaires et subcellulaires à des déformations fortes et rapides en condition de stress hydrodynamique mais aussi, de façon plus originale, à étudier les processus de récupération après ces déformations. La compréhension de la réponse globale des CTCs dans la circulation peut se révéler essentielle dans l'identification de nouvelles cibles thérapeutiques visant à prévenir la formation de métastases.

Deux dispositifs microfluidiques ont été développés pour étudier la mécanobiologie des CTCs. Ces dispositifs constituent des modèles *in vitro* des constriction présentes dans les capillaires

---

sanguins. Le premier dispositif vise à l'étude de la déformation et de la récupération à court terme (ms-s) à l'échelle de la cellule unique dans une constriction. Le second dispositif vise à l'étude de la survie et des modifications d'expression génique, à une échelle de temps typique dans la circulation (min-h), d'une population de CTCs soumises de façon répétée à des déformations dans des constriction.

## Chapitre 1 - Introduction.

Dans cette étude, on s'intéresse à la cellule cancéreuse comme objet rhéologique, dont les propriétés sont viscoélastique. Ces propriétés mécaniques à l'échelle globale émergent de son organisation intracellulaire. Parmi les éléments qui constituent la cellule, nous porterons un intérêt plus particulier au noyau, au cytosquelette et à la membrane plasmique. Le noyau a été décrit comme un objet viscoélastique complexe [Stephens, 2017], entouré par une enveloppe aux propriétés élastiques formées de lamines [Dahl, 2004 ; Lammerding, 2006]. Le cytosquelette est composé de plusieurs filaments (actine, microtubules, filaments intermédiaires : Fig.R.1a) aux propriétés principalement élastiques [Blanchoin, 2014]. La vimentine, un filament intermédiaire présent uniquement dans les cellules de type mésenchymale, s'organise sous la forme d'une cage entourant le noyau (voir insert Fig.R.1a) et semble agir comme un "absorbeur de chocs" [Block, 2017]

Pour accéder à ces propriétés mécaniques, on étudie la relation entre le stress appliqué sur un objet et la déformation qui en résulte. De nombreuses techniques expérimentales ont été mises au point [Alibert, 2017] pour obtenir cette relation. En ce qui concerne le cancer, la littérature semble converger vers l'idée que les cellules cancéreuses sont plus "molles" que leurs homologues non cancéreux (voir [Guck, 2005 ; Omidvar, 2014 ; Mandal, 2016 ; Hu, 2017 ; Nematbakhsh, 2017 ; Tabatabaei, 2019] pour le cancer du sein).

Parmi ces techniques, les dispositifs microfluidiques permettent d'étudier les cellules en suspension, reproduisant ainsi les conditions physiologiques du passage des cellules dans le sang [Byun, 2013 ; Hu, 2017 ; Urbanska, 2020 ; Ahmad-Cognart, 2020]. Lors de leur passage dans la circulation sanguine, les cellules cancéreuses acquièrent le statut de Cellules Tumorales Circulantes (CTCs), et sont soumises à des fortes contraintes hydrodynamiques [Follain, 2020] : contraintes de cisaillement et déformations. En effet, les capillaires sanguins - les plus petits vaisseaux de notre organisme - ont un diamètre pouvant descendre jusqu'à quelques microns (3-4  $\mu\text{m}$ , Fig.R.1b) [MacDonald, 1995 ; Müller, 2008]. Dans ces endroits que nous dénommerons constriction, les CTCs - de diamètre 15-20  $\mu\text{m}$  en moyenne - doivent se déformer pour les traverser. Ces conditions peuvent occasionner des dommages aux cellules et induire la mort cellulaire (Fig.R.1c). La majorité des CTCs en circulation vont y mourir [Zeidman, 1950 ; Weiss, 1990], le problème réside alors dans la fraction qui parvient à survivre et coloniser d'autres organes distants pour y former des métastases.

Ainsi, plusieurs dispositifs microfluidiques ont été mis au point pour étudier l'impact des forces hydrodynamiques sur les CTCs. Par exemple, il a été montré *in vitro* que l'application de

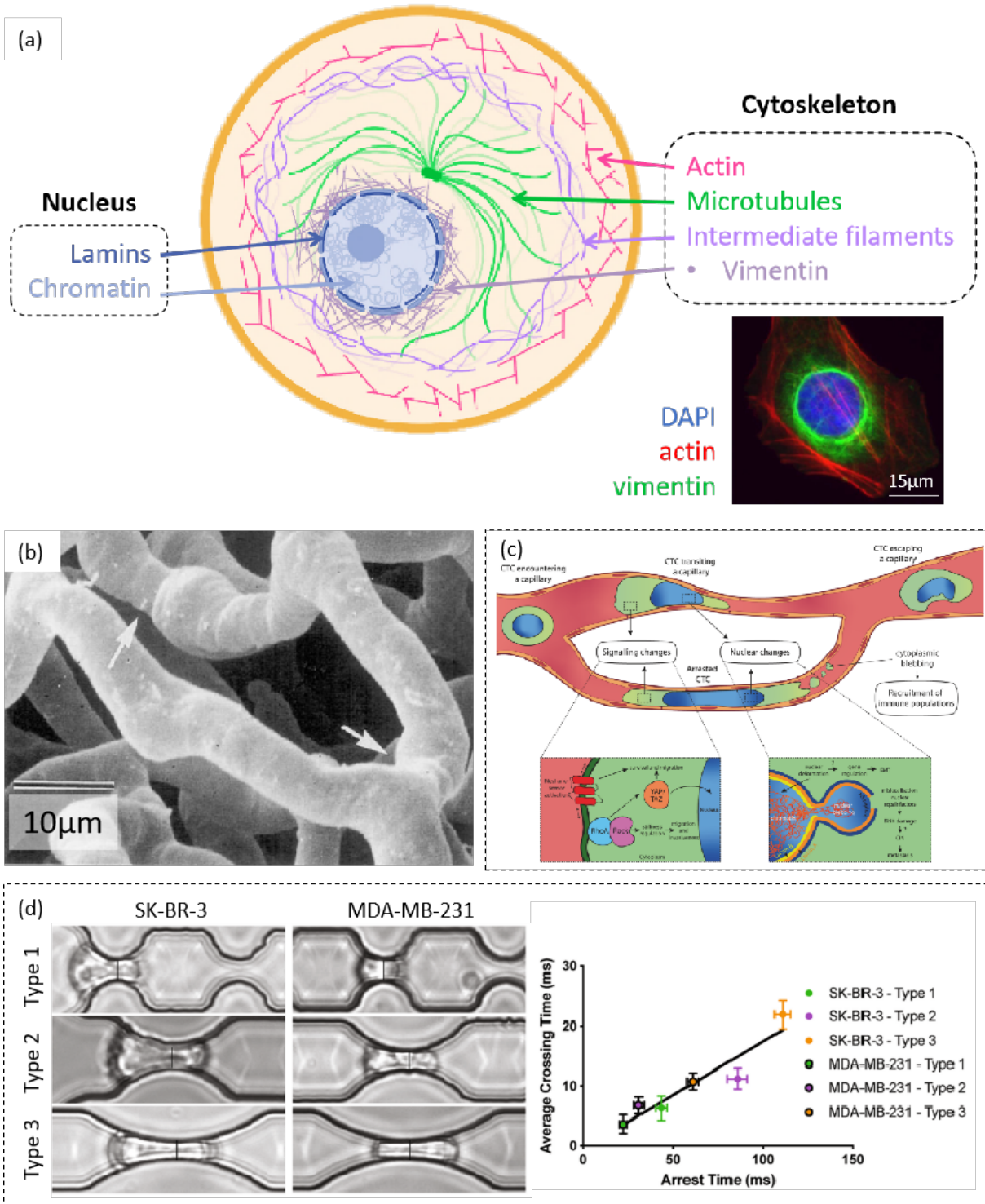


**Figure R.1** – Représentation schématique d’une cellule et des composants principaux intervenant dans les propriétés mécaniques (pour des raisons de clarté, le noyau est représenté bien plus petit qu’en réalité). L’insert détaille l’organisation en cage périnucléaire de la vimentine [Patteson, 2020]. (b) Les CTCs doivent se déformer pour traverser les constriction (adapté de [Perea Paizal, 2021]). (c) Imagerie électronique des constriction dans les capillaires (pancreas murin, [MacDonald, 1995]). (d) Puce microfluidique reproduisant une série de constriction pour l’étude de 2 lignées cellulaires de cancer du sein [Ahmad-Cognart, 2020].

---

contraintes de cisaillement réduisent la viabilité de cellules cancéreuses en circulation [Barnes, 2012 ; Regmi, 2017], même s’il est intéressant de noter qu’elles s’en sortent mieux que les cellules non-malignes.

L’effet de la déformation des cellules cancéreuses a lui été étudié en situation de confinement statique [Liu, 2015 ; Lomakin, 2020], de migration spontanée au travers de constrictions [Raab, 2016 ; Davidson, 2020], et de migration forcée au travers de constrictions [Hou, 2009 ; Byun, 2013 ; Ahmad-Cognart, 2020] (voir un exemple Fig.R.1d). Ces dispositifs ont notamment pu mettre en évidence le rôle du noyau comme facteur limitant en déformation, ou encore l’acquisition de propriétés favorable à la formation de métastases (caractère souche, transition épithélio-mésenchymateuse).

En revanche, ces dispositifs s’intéressent uniquement à la déformation des CTCs, et ignorent quasi systématiquement leur récupération. Dans cette étude, nous porterons un intérêt particulier à l’étude de la récupération à l’échelle de la cellule entière (Chapitre 2) et de son noyau (Chapitre 3), ainsi qu’à l’effet à plus long terme de déformations répétées (Chapitre 4).

## Chapitre 2 - Dispositif Pachinko, étude à l’échelle de la cellule.

Le premier dispositif développé, nommé Pachinko, utilise une différence de pression appliquée par des contrôleurs externes pour contraindre une cellule à se déformer dans une constriction reproduisant les capillaires sanguins, de section  $6 \times 15 \mu\text{m}^2$ . Une fois la cellule suffisamment déformée, elle traverse la constriction et est ensuite capturée dans des pièges microfluidiques pour permettre l’observation de sa récupération. L’analyse a été semi-automatisée pour permettre le suivi chaque cellule dans la puce microfluidique, segmenter les images pour obtenir la forme de la cellule ou de son noyau, et ainsi quantifier sa déformation puis récupération au cours du temps (voir Fig.R.2a pour le design et principe).

Plusieurs lignées cellulaires ont été analysées dans ce dispositif. Le premier modèle cellulaire de CTC utilisé, consiste en trois lignées de cancer du sein ; MDA-MB-231, SK-BR-3 et MCF-7, chacune représentative des grands sous-types de cancer du sein. Les résultats obtenus sur ces lignées sont présenté dans un article preuve de concept accepté pour publication dans Lab-On-Chip. Nous avons pu établir que :

- A l’échelle de la population, le temps d’arrêt d’une cellule dans une constriction est lié à sa taille (Fig.R.2b). Ainsi, la lignée SK-BR-3 ayant en moyenne un diamètre inférieur aux 2 autres lignées, traverse plus rapidement la constriction que les 2 autres.
- A diamètre égal, le temps d’arrêt d’une cellule devient inversement lié à l’agressivité du sous-type de cancer dont est extrait la cellule. Ainsi, les MDA-MB-231 (sous-type le plus agressif de cancer du sein triple négatifs) traversent plus rapidement la constriction que les SK-BR-3 (HER2+) et que les MCF-7 (exprimant les récepteurs hormonaux). Ces résultats sont en accord avec la littérature, qui associe l’agressivité des cellules cancéreuses avec leur déformabilité dans d’autres dispositifs [Byun, 2013 ; Alibert, 2017 ; Urbanska, 2020]
- A l’échelle intra-cellulaire, le temps d’arrêt semble être principalement sous le contrôle de la déformation du noyau dans la constriction. En effet, le suivi de la position du noyau lors

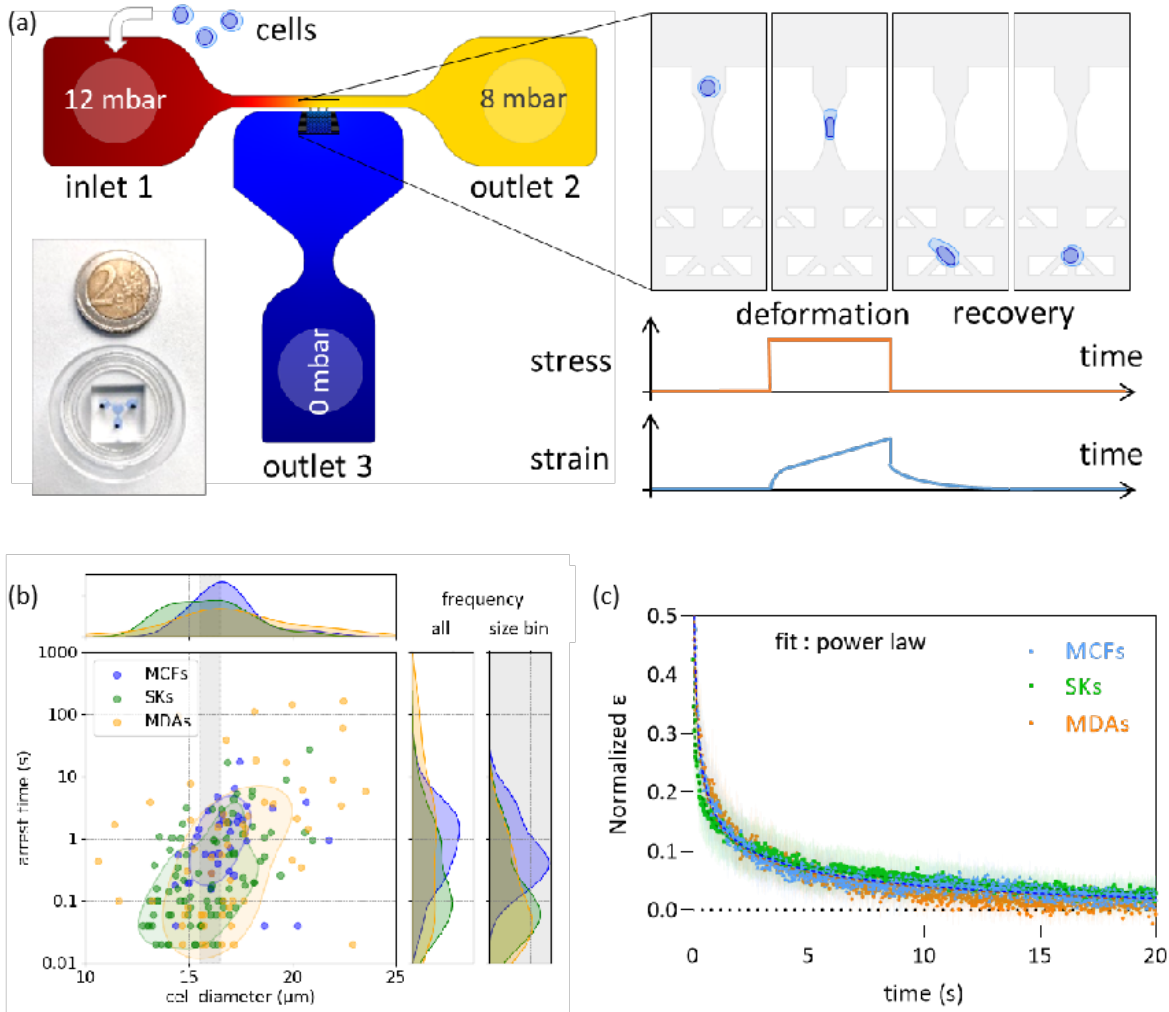


**Figure R.2** – Principe du dispositif Pachinko. (a) Design du dispositif et principe théorique de l’application de déformation des cellules cancéreuses dans une constriction  $6 \times 15 \mu\text{m}^2$ . L’observation de la récupération se fait dans des pièges microfluidiques dédiés. (b) Relation entre taille de la cellule et temps d’arrêt dans la constriction. A taille égales, les MDA-MB-231 passent plus rapidement que les autres lignées moins agressives. (c) Les courbes moyennes de récupération se composent d’un premier régime élastique, suivi d’un régime viscoélastique.

de sa déformation dans la constriction montre que la cellule s’échappe à partir du moment où son noyau passe le centre de la constriction. Le noyau est le facteur limitant dans la déformation de la cellule.

- La déformation des cellules est caractérisée par une première partie viscoélastique, suivie par une augmentation linéaire de type visqueuse : cela correspond à un modèle rhéologique de Jeffrey. Alternativement, la déformation peut aussi être modélisée grâce à un formalisme de type loi de puissance.
- Les cellules récupèrent de leur déformation de façon presque complète, et cette récupération se compose d’un régime élastique quasi instantané, suivi d’un régime viscoélastique à plus long-terme (voir Fig.R.2c pour les courbes normalisées). Les temps caractéristiques mis

---

en jeu dans la récupération viscoélastique sont de l'ordre de la dizaine de secondes. Une faible déformation plastique (de l'ordre de 5%) subsiste lorsque la forme de la cellule arrête d'évoluer. Afin de modéliser le comportement obtenu, nous avons mis au point un modèle rhéologique faisant intervenir 3 éléments de Kelvin-Voigt, et donc 3 temps caractéristiques. Cependant, formalisme en loi de puissance semble expliquer de façon plus simple ce comportement (2 paramètres nécessaires pour la loi de puissance, contre 7 pour le fit sur modèle rhéologique généralisé).

- La présence d'un cytosquelette d'actine intact est requise pour observer une récupération. Cette dernière est absente lorsque le cytosquelette est dépolymérisé (Latrunculin A, 0.5  $\mu\text{M}$ ), et incomplète lorsque l'activité de la myosine est inhibée (Y27, 30  $\mu\text{M}$ )
- Un décollement de la membrane plasmique du cortex d'actine se produit, aussi appelé bleb, lorsque le taux de déformation dépasse un certain seuil (observé dans des constriction de  $6 \times 6 \mu\text{m}^2$ ). La récupération de la cellule est alors plus lente (de l'ordre de 100s).

Nous avons complété l'étude obtenue sur les cellules de cancer du sein par un autre type de cancer. Grâce à des partenaires (laboratoire de C. Alix-Panabières, LCCRH, CHU Montpellier), nous avons pu obtenir plusieurs lignées uniques de CTCs, isolées à partir d'un même patient atteint d'un cancer du côlon à différents instants de progression de la maladie [Cayrefourcq, 2015]. Deux de ces lignées (CTC41 obtenue avant traitement, et CTC41.5A obtenue après rechute), ainsi que des lignées commerciales de cancer du côlon (HT-29 cancer du côlon primaire, et SW-620 cancer du côlon métastatique) ont été analysées dans le dispositif Pachinko.

Nous avons pu observer des résultats similaires à ceux des lignées de cancer du sein. En déformation, les lignées considérées les plus agressives (SW-620 et CTC41.5A) se déforment plus rapidement que leurs homologues moins agressifs. En récupération, la lignée CTC41 du patient obtenue avant traitement se rapproche des HT-29 (cancer primaire), alors que la lignée CTC41.5A du patient obtenue après rechute se rapproche des SW-620 (cancer métastatique). On observe par ailleurs que les propriétés mécaniques de la lignée métastatique CTC41.5A semblent plus homogènes que pour la lignée originale CTC41, ce qui est à mettre en regard avec la sélection par la circulation sanguine de ce clone métastatique. Cette évolution des propriétés mécaniques de cellules issues d'un même cancer à différents stades de l'évolution de la maladie témoigne de l'importance des stress mécaniques dans la progression du cancer et de l'adaptation des cellules en réponse. Nous faisons ainsi l'hypothèse que les propriétés mécaniques des cellules cancéreuses sont reliées à l'agressivité du cancer.

### Chapitre 3 - Étude à l'échelle du noyau.

En raison de son important rôle dans les propriétés mécaniques à l'échelle globale, nous avons porté un intérêt plus particulier au noyau. Les noyaux des 7 lignées décrites précédemment ont été analysées dans le dispositif Pachinko, via un marquage nucléaire Hoechst. Nous avons pu observer que :

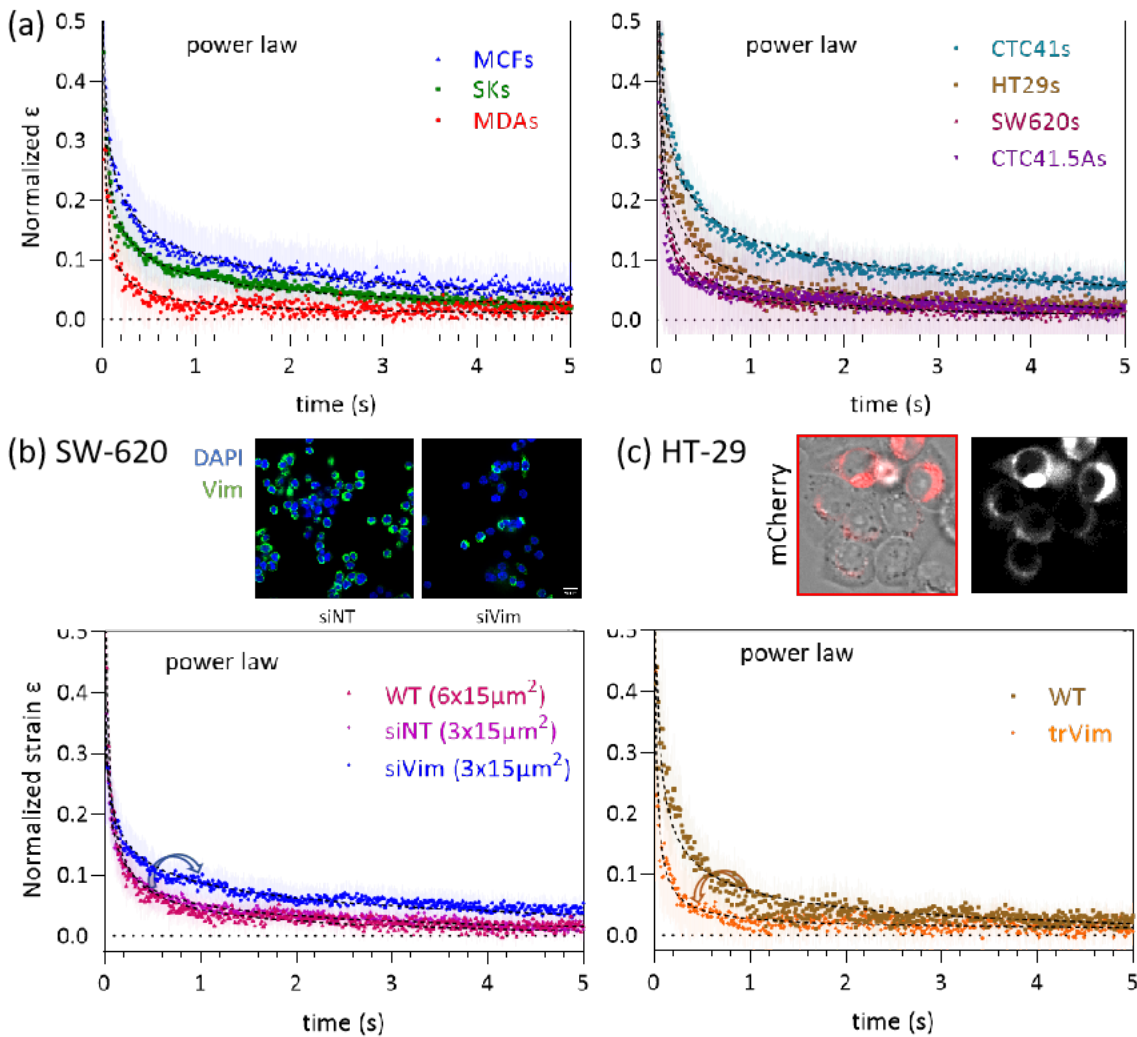


**Figure R.3** – Récupération à l'échelle des noyaux. (a) Courbes moyennes de récupération pour les 3 lignées de cancer du sein et 4 lignées de cancer du colon. (b) La diminution par siRNA des niveaux de vimentine au sein des SW-620 réduit son comportement élastique. (c) L'ajout de vimentine par transfection dans les HT-29 augmente son comportement élastique.

- La récupération à l'échelle du noyau est quasiment complète, présentant une déformation plastique résiduelle de l'ordre de 5%. Cette récupération se compose d'un régime élastique quasi instantané, suivi d'un faible régime viscoélastique à plus long-terme, avec des temps caractéristiques environ 10 fois plus rapides qu'à l'échelle de la cellule ( $< 1$  s, voir Fig.R.3a).
- La proportion du régime élastique est d'autant plus importante parmi les lignées les plus agressives (MDA-MB-231, SW-620 et CTC41.5A). La récupération de ces lignées se rapprochent du comportement de l'élastique parfait, comme observé pour des microbilles d'hydrogel.
- Les lignées les plus agressives (MDA-MB-231 et SW-620) présentent une cage de vimentine périnucléaire, confirmée par quantification des niveaux de protéines (immunoblotting) et imagerie. Le rôle de cet structure dans les propriétés du noyau est investiguée par la suite.

- 
- Les niveaux de vimentine dans la lignée SW-620 sont diminués d'environ 80% par transfection siRNA. Cette diminution affecte le comportement élastique en récupération de ces noyaux (Fig.R.3b).
  - De façon inverse, la vimentine a été exprimée dans la lignée HT-29 qui ne l'exprime pas de façon endogène. L'ajout de cette cage de vimentine augmente le comportement élastique de ces noyaux (Fig.R.3c).
  - Les modulations d'élasticité liées à la présence ou absence de vimentine ne permettent pas d'expliquer l'entièreté du comportement élastique observé. Sur la base des quantifications de niveaux de protéines, nous postulons un rôle important de la protéine Lamine A dans ce comportement.

La vimentine a été décrite dans la littérature comme ayant un rôle protecteur, agissant comme un "absorbeur de chocs" [Block, 2017] pour protéger le noyau de déformations trop rapides. Cette protéine est par ailleurs exprimée au cours de la transition épithelio-mésenchymateuse, un des marqueurs des changements intervenant lors de la cascade métastatique. Nous allons par la suite nous intéresser à son rôle dans la survie des CTCs soumises à des déformations répétées en circulation.

## Chapitre 4 - Réponse aux déformations répétées en circulation.

Afin de nous rapprocher des conditions physiologiques observées lors du passage dans le sang des CTCs, à savoir son caractère cyclique et répété sur des longs temps de circulation, nous avons développé un dispositif permettant la recirculation de cellules au travers de séries de constriction afin d'étudier l'effet à plus long terme des déformations répétées sur une population de CTCs (voir Fig.R.4a pour le design de la puce). Nous avons porté cette étude sur 2 lignées de cancer du sein : MCF-7 (dépourvue de vimentine) et MDA-MB-231 (présentant une cage de vimentine périnucléaire). Nous avons pu montrer :

- La recirculation des cellules au sein de la puce microfluidique a pu être atteinte à l'aide d'une pompe péristaltique sur une durée de 2h, avec des cycles de l'ordre de 4min.
- La viabilité des cellules a été impactée par la recirculation : Les cellules MCF-7 ont perdu  $\approx 80\%$  de viabilité au bout de 2h, cette perte de viabilité se limite à 50% pour les MDA-MB-231 (voir Fig.R.4b). Cette différence suggère que les MDA-MB-231 sont mieux adaptées pour survivre aux stress et déformations rencontrés dans la circulation sanguine. Cette observation est en concordance avec les données cliniques montrant que les cancers triple négatifs (dont sont issus les MDA-MB-231) forment plus de métastases que les cancers luminaux (MCF-7) [Kast, 2015].
- La production de vésicules extracellulaires augmente en réponse aux contraintes de cisaillement, d'un facteur  $\approx 2.2-2.3$ . L'addition de déformations répétées dans la puce microfluidique augmente ce facteur à 3.5 pour les cellules MCF-7 et 4.1 pour les MDA-MB-231. Ces vésicules présentent un intérêt à la fois comme biomarqueur pouvant être retrouver

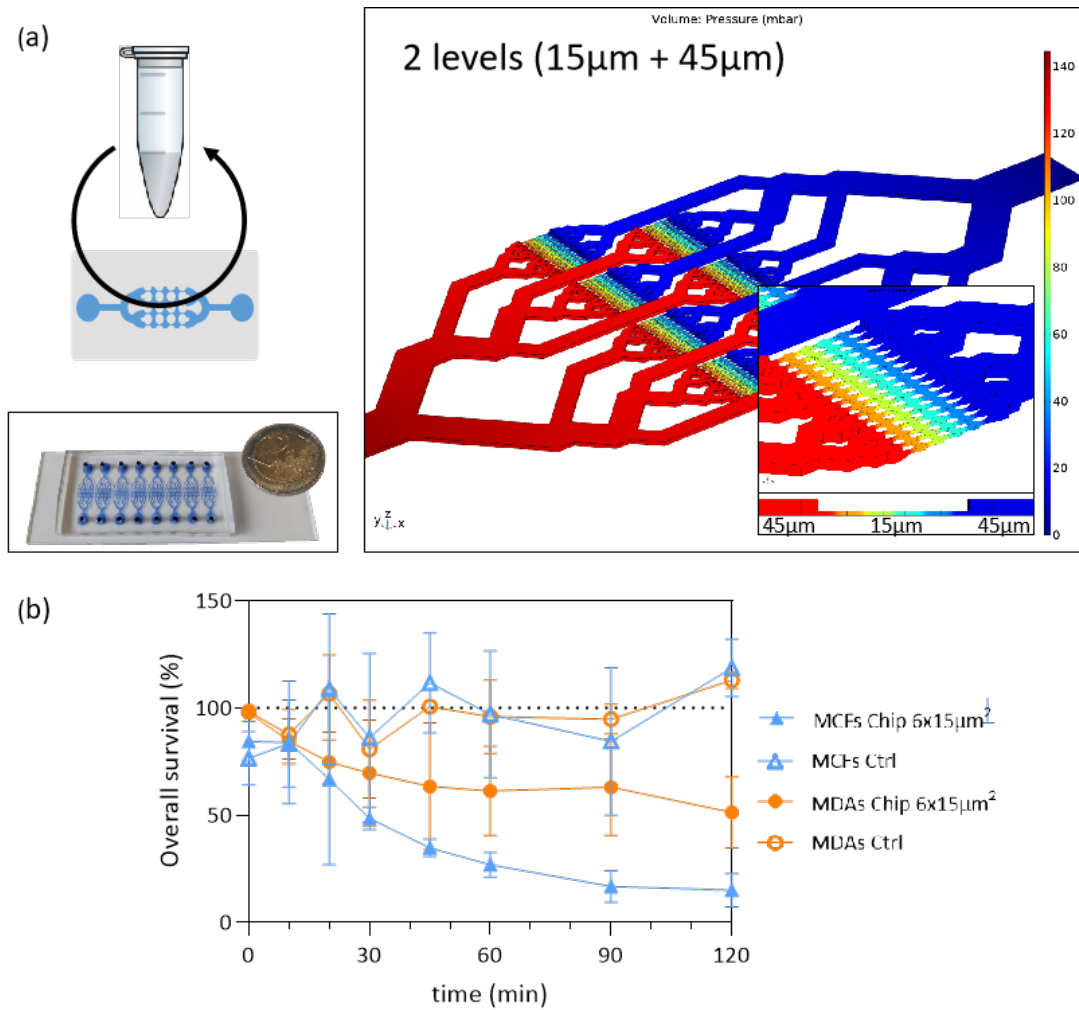


**Figure R.4** – Étude des déformations répétées sous circulation. (a) Dispositif microfluidique permettant la recirculation aux travers de constrictions  $6 \times 15 \mu\text{m}^2$ . (b) Évolution de la survie des lignées MCF-7 et MDA-MB-231 au cours de la recirculation dans la puce microfluidique (contrôle = cellules non recirculées).

dans le sang, ainsi que comme messager pouvant promouvoir le potentiel métastatique au sein d'autres cellules cancéreuses [Green, 2015 ; Goh, 2020].

- Nous avons observé l'accumulation de dommages au sein des noyaux via l'augmentation de leur rapport d'aspect. Cette accumulation est plus prononcée pour les noyaux des MDA-MB-231.
- Des premiers tests réalisés depuis le rendu de ce manuscrit semblent montrer que l'addition ou le retrait de la cage de vimentine au sein des cellules semblent moduler la viabilité à l'échelle de la population.

Enfin, des analyses de transcriptomiques seront prévues sur la sous-population ayant survécu pour identifier quels mécanismes, voies de signalisation et gènes ont été impliqués dans la réponse et survie aux déformations répétées.

---

L'implication de Jean-Yves Pierga (co-encadrant de la thèse, directeur de recherche et clinicien à l'hôpital de l'Institut Curie) dans le projet permettra d'avoir accès à des prélèvements de liquide d'ascites, qui sont des échantillons cliniques issus de patients et également un déchet médical contenant des cellules cancéreuses. Ce modèle intéressant de cellules cancéreuses métastatiques mais naïves de la circulation, viendra compléter l'étude faite sur les lignées commerciales du sein.

## Conclusion

Ainsi, au cours de cette étude, nous avons développé deux dispositifs microfluidiques permettant d'étudier le comportement de cellules tumorales circulantes en réponse à l'application de déformations rapides sous flux. Ces dispositifs complémentaires s'intéressent à la fois à la déformation et récupération morphologique à court terme de la cellule et de son noyau, et de l'effet à plus long terme de la viabilité et des caractéristiques d'une population soumises à des déformations répétées.

Nous espérons, par la compréhension des mécanismes gouvernant la réponse des CTCs à une ou plusieurs déformations, pouvoir identifier des cibles thérapeutiques afin de perturber ces mécanismes et empêcher les CTCs de survivre à leur passage dans la circulation sanguine, et ainsi prévenir la formation de métastases.

## A Notions of rheology

Rheology, a branch of physics and material science, investigates the mechanical behavior of materials under the influence of applied forces or stresses. It seeks to elucidate the complex interplay between stress, strain and strain rate, shedding light on the response of materials to various mechanical conditions. This field plays a pivotal role in diverse applications, spanning from the design of industrial processes to the understanding, in our case, of biological systems.

### Stress and strain

Stress ( $\sigma$ , expressed in Pa), a measure of the internal forces within a material, is defined as the force per unit area acting on a given plane. It represents the intensity of the load imposed on a material and can lead to deformation. Deformation is the change in shape or size experienced by a material in response to applied stresses. Strain ( $\varepsilon$ , dimensionless), in turn, quantifies this deformation and is expressed as the ratio of the change in size or shape to the original size or shape. Strain rate ( $\dot{\varepsilon}$ , in  $\text{s}^{-1}$ ) is the time derivative of the strain in the material and quantify the speed of change in shape or size (see Fig.A.1a).

### Ideal models

Idealized models allows to link these parameters through simple laws and equations (see Fig.A.1b). The Hookean spring exemplifies the linear elastic behavior of materials, adhering strictly to Hooke's law. This law states that the stress applied is proportional to the resulting strain, thereby characterizing the stiffness or elasticity of a material. Mathematically, stress ( $\sigma$ ) is directly proportional to strain ( $\varepsilon$ ), as expressed by the equation  $\sigma = E\varepsilon$ , where E signifies the material's Young's modulus (in Pa).

Conversely, the viscous dashpot embodies the behavior of materials exhibiting viscous flow, as opposed to elastic deformation. This behavior is characterized by a constant rate of strain in response to an applied stress, which corresponds to a linear increase in deformation over time. In this scenario, the stress-strain relationship is characterized by Newton's law of viscosity, where stress ( $\sigma$ ) is directly proportional to the rate of strain ( $\dot{\varepsilon}$ ), leading to the equation  $\sigma = \eta\dot{\varepsilon}$  (where  $\dot{\varepsilon}$  represents the time derivate). Here,  $\eta$  symbolizes the dynamic viscosity of the material (in Pa.s).

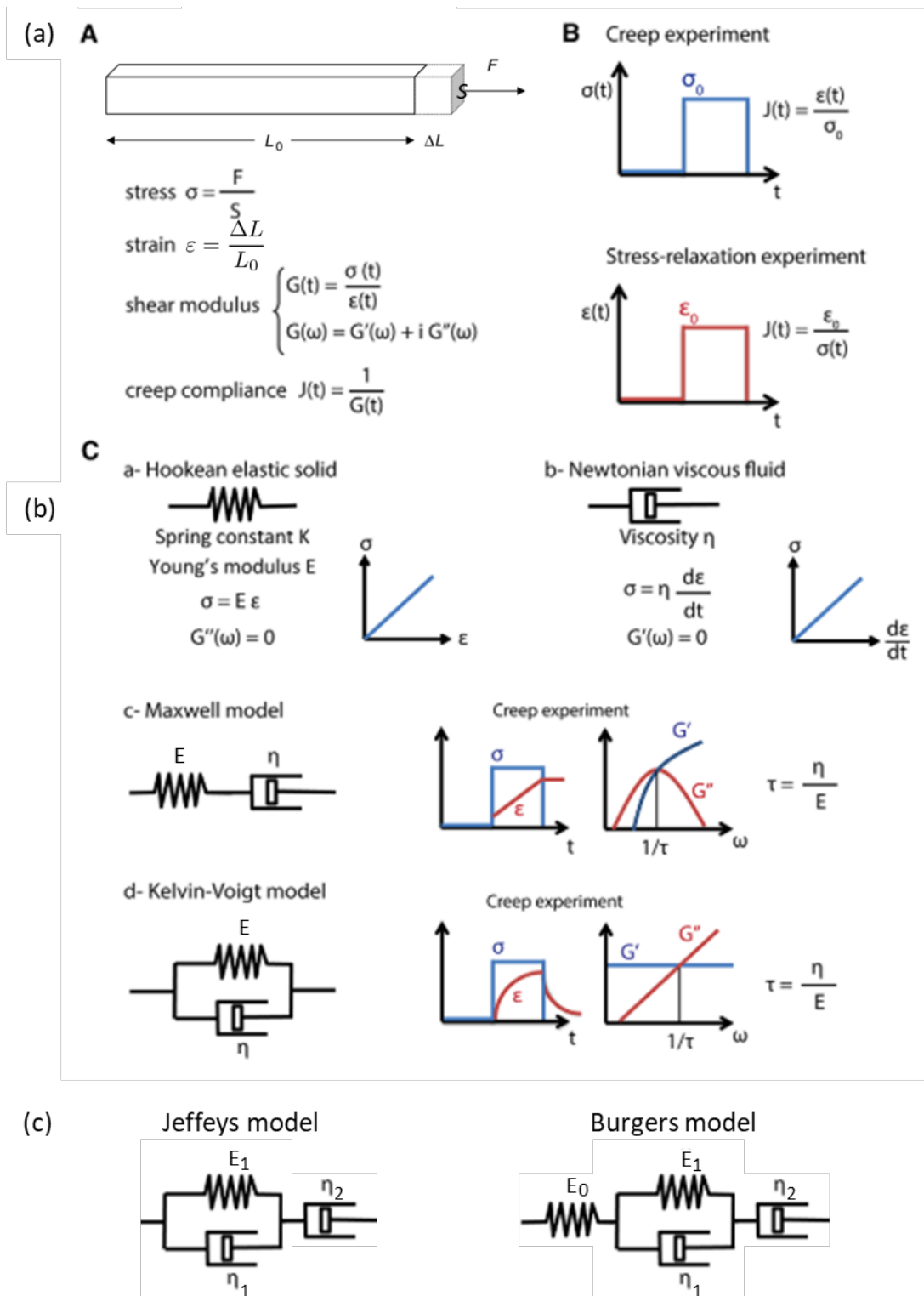


**Figure A.1** – Ideal rheological models. (a) Definition of stress  $\sigma$  and strain  $\epsilon$ , of the shear modulus  $G$  and typical experiments. (b) Schematic representations of Hookean elastic, Newtonian fluid, Maxwell and Kelvin-Voigt models, and their characteristic response to creep experiments (adapted from [Janmey, 2007] and [Alibert, 2017]). (c) Jeffreys and Burgers models representation.

These ideal models can be combined to describe more intricate material responses. By combining a Hookean spring and a viscous dashpot in series, we get the Maxwell model often used to describe viscoelastic liquids. This model predicts a time-dependent response characterized by initial elastic behavior followed by viscous flow. The association in parallel of a Hookean spring and a viscous dashpot gives the Kelvin-Voigt model, which can be used to describe viscoelastic solids. This model depicts a material that exhibits simultaneous elastic and viscous responses under applied stress.

In this last solid model, the stress is shared between the two components  $\sigma = \sigma_{spring} + \sigma_{dashpot}$ . As they are associated in series, their strain is the same  $\varepsilon = \varepsilon_{spring} = \varepsilon_{dashpot}$ . We then deduce that  $\sigma = E\varepsilon + \eta\dot{\varepsilon}$ . Similarly for the Maxwell model, assuming shared strain but same stress, we get  $\frac{\dot{\sigma}}{E} + \frac{\sigma}{\eta} = \dot{\varepsilon}$ . Thus, these models exhibit a characteristic time  $\tau = \frac{\eta}{E}$ .

More generally, we can define the shear modulus  $G$  as the ratio of the stress over the strain  $G(t) = \frac{\sigma(t)}{\varepsilon(t)}$ . This function allows to describe all behavior knowing their stress-strain response, even if they differ from ideal models. Using a complex notation, it can be rewritten as  $G(\omega) = G'(\omega) + iG''(\omega)$ . This form defines a storage ( $G'$ ) and loss modulus ( $G''$ ), which respectively quantify the elastic component of the material (stored energy, that can be restituted) and viscous component (lost energy).

## Loading and creep experiments

The response of a material that follows one of the previously described model can be assessed through simple experiments.

Loading experiments involve subjecting a material to controlled external forces or stresses while measuring the resulting deformation and strain. In tension and compression tests, for instance, a material is subjected to axial loads, allowing the determination of its Young's modulus  $E$  and yield strength. Shear tests, on the other hand, probe the shear modulus  $G$  of materials by applying tangential forces that induce shear deformation.

Depending on the experiment, the measured modulus varies. Young modulus  $E$  relates to an uniaxial deformation in the same direction as the applied force (see Fig.A.1a). If the force is applied in parallel to the surface of the material, the resulting deformation is characterized by the shear modulus  $G$ . Upon loading in one direction, the material will expand in the perpendicular direction, in order to keep a constant volume. This ratio of transverse strain to axial strain is called the Poisson coefficient  $\nu$ . In a linear homogeneous and isotropic material, all the different rheological moduli are related to each other, for instance  $E = 2G(1 + \nu)$ . If we assume that the material is incompressible, then  $\nu = 1/2$  and  $E = 3G$ .

Creep analysis, on the other hand, explores a material's behavior over extended periods under constant stress. This method involves applying a sustained stress to a material and monitoring its time-dependent deformation response. Through creep tests, material parameters such as viscosity  $\eta$  and relaxation time  $\tau$  can be inferred, shedding light on the material's viscous behavior and its ability to recover from deformation over time.

The experiments that we'll conduct in this study fall within this last category. As the cell is being deformed in the device, it will experience a constant stress which will results in its elongation. Once the stress is released, the shape of the object will evolve with time, and tend towards its original shape.

We'll model the passage of the cell through a constriction by the application of a constant stress  $\sigma_0$ , of typical amplitude  $\sigma_0 = \Delta P \times S$  where  $\Delta P$  is the applied pressure difference, and  $S$  the surface of the constriction, for a duration  $t_0$ . In this framework, the deformation and relaxation of an object that falls within the Maxwell and Kelvin-Voigt models are :

$$\varepsilon_{Maxwell}(t) = \begin{cases} \frac{\sigma_0}{E} + \frac{\sigma_0}{\eta}t & \text{if } t \leq t_0 \text{ (deformation for a duration } t_0) \\ \varepsilon_{Maxwell}(t_0) & \text{if } t > t_0 \text{ (recovery after } t_0) \end{cases} \quad (5.1)$$

$$\varepsilon_{Kelvin-Voigt}(t) = \begin{cases} \frac{\sigma_0}{E}(1 - \exp(-t/\tau)) \text{ where } \tau = \frac{\eta}{E} & \text{if } t \leq t_0 \text{ (deformation)} \\ \varepsilon_{Kelvin-Voigt}(t_0) \exp^{-t/\tau} & \text{if } t > t_0 \text{ (recovery)} \end{cases} \quad (5.2)$$

### Towards more complex models

However these simple models cannot recapitulate the whole complexity of observed behaviors, notably when they exhibit several characteristic times. Hence more complex models have been developed by associating several hookean springs and newtonian dashpots. Among all the possible combinaisons, we'll describe two that we'll use later to model our data (see Fig.A.1c).

Jeffrey's model, also known as standard linear liquid represents a linear viscoelastic material with a finite relaxation time, providing a versatile tool to analyze the transient deformation of materials.

For instance the equations of a material following Jeffrey's model submitted to a creep experiments is of the form :

$$\varepsilon_{Jeffrey}(t) = \begin{cases} \frac{\sigma_0}{E_1}(1 - \exp(-t/\tau_1)) + \frac{\sigma_0}{\eta_2}t \text{ where } \tau_1 = \frac{\eta_1}{E_1} & \text{if } t \leq t_0 \text{ (deformation)} \\ \varepsilon_{Jeffrey}(t_0) \exp^{-t/\tau_1} + \frac{\sigma_0}{\eta_2}t_0 & \text{if } t > t_0 \text{ (recovery)} \end{cases} \quad (5.3)$$

We can note that the deformation is composed of the superposition of the exponential component from the Kelvin-Voigt model and the linear increase from the dashpot. As the object recovers, the deformation of the dashpot is conserved.

In contrast, Burger's model, an extension of Jeffrey's model by adding an hookean spring in series, introduces a second relaxation time, making it suitable for describing materials with more intricate viscoelastic behavior.

These models are regularly used to model cells mechanical properties in various experiments as we've seen previously.

## Power law rheology

If the adequate model is unknown and can't be inferred from experimental data, or if a finite number of relaxation times is too simple to correctly describe the object behavior, power law rheology can be used. It allows for a continuous distribution of characteristic times, which is reflected in equations of the form  $\sigma = K(\frac{\partial \varepsilon}{\partial t})^n$  where  $K$  characterizes the cell stiffness and  $n$  the cell viscoelasticity [Kollmannsberger, 2011]. This coefficient  $n$  is often referred to as the fluidity. In creep experiments under a stress  $\sigma_0$ , the strain can be expressed as  $\varepsilon(t) = \frac{\sigma_0}{K}(\frac{t}{t_0})^n$  [Fabry, 2001; Balland, 2006].

When  $n = 0$ , we obtain Hooke's law for elastic fluid (with  $K = E$ ) described above. When  $n = 1$ , we obtain Newton's law for viscous liquids (with  $K = \eta$ ). Any viscoelastic material may be characterized by its flow behavior index  $0 < n < 1$ .

Power law models have been used in many studies to describe the behaviors of cells [Lange, 2015; Gerum, 2022] and/or the nucleus [Dahl, 2005].

## B Matlab App code

Here we provide the code used in the Matlab App created to analyse the images. The code takes information generated by TrackMate (stored in a table `tracks_complete`) to select and analyse each cells individually. For each cell, at each frame, a region around the cell is segmented to obtain the shape of the cell. The shape descriptors generated by `regionprops` are stored in a table `Results` for further analysis.

Please, don't hesitate to contact me to access the app. As it is still in development, I can't publish it online but I am willing to share it when needed.

```

1 %% Functions
2
3 function image = loadImage(app, imageIndex, trackIndex)
4 % Helper function to load the desired image
5     s = trackIndex; % current track
6     t = app.tracks_complete{s}(imageIndex, 1); % time point
7     % Selects image to open
8     img_to_open_name = fullfile( app.img_dir, app.original_img(t+1).name ); % directory
9         indexing starts at 0
10    % Opens selected image
11    image = imread(img_to_open_name);
12 end
13
14 function croppedImage = cropImage(app, image, imageIndex, trackIndex)
15 % Helper function to crop the image to desired ROI
16     s = trackIndex; % current track
17     % Position of cell in track in the track referentiel...
18     x = app.tracks_complete{s}(imageIndex, 2);
19     y = app.tracks_complete{s}(imageIndex, 3);
20     % ... and in original images
21     x_cell = floor(app.binning*x);
22     y_cell = floor(app.binning*y);
23     [h_I, l_I] = size(image);
24     % Selects ROI and crop the image
25     pos_ROI = [max(1,min(x_cell-app.SOI/2,l_I-app.SOI)) max(1,min(y_cell-app.SOI/2,h_I-
26         app.SOI)) app.SOI app.SOI]; % position of the ROI, case of a cell on the edge is
27         taken into account
28     croppedImage = imcrop(image, pos_ROI);
29 end
30
31 function BW = segmentImage(app, croppedImage, otsu)
32 % Helper function to segment the cropped image (using Otsu's method and a nb of levels =
33     otsu)
34     % Segmentation
35     thresh = multithresh(croppedImage, otsu); % define threshold
36     segmentedImage = imquantize(croppedImage, thresh); % segment image
37     BW = (segmentedImage > 1); % merge non background levels
38     % Extract maximum Area
39     BW = imfill(BW,'holes'); % fill holes
40     BW = bwareafilt(BW,1); % keep the biggest object only
41 end
42
43 %% Tracks analysis (segmentation, parameters extraction)
44
45 % Create the progress dialog

```

```
42 progressDialog = uiprogressdlg(app.UIFigure, 'Title', 'Processing', 'Cancelable', 'on');
43 totalIterations = 0;
44 for l = 1 : app.n_selected_tracks
45     s = app.list_selected_tracks(l);
46     totalIterations = totalIterations + app.constriction_index{s}(3);
47 end
48 iteration = 1;
49 % Preallocating memory
50 app.cell_shapes = cell(size(app.tracks_complete)); % cell array to store cells shapes
    properties
51
52 % Run
53 for l = 1 : app.n_selected_tracks
54     s = app.list_selected_tracks(l);
55     i_stop = app.constriction_index{s}(3);
56
57     % prepare plot
58     fig = figure(1);
59     set(fig, 'Color', 'black');
60
61     % allocating memory
62     clear videoFrames
63     videoFrames = struct('cdata', cell(1, i_stop), 'colormap', cell(1, i_stop));
64     cell_shapes_temp = struct('Centroid', cell(1, i_stop), ...
65         'Orientation', cell(1, i_stop), ...
66         'MajorAxisLength', cell(1, i_stop), ...
67         'MinorAxisLength', cell(1, i_stop), ...
68         'Eccentricity', cell(1, i_stop), ...
69         'Circularity', cell(1, i_stop), ...
70         'Area', cell(1, i_stop), ...
71         'Solidity', cell(1, i_stop), ...
72         'MaxFeretDiameter', cell(1, i_stop), ...
73         'MaxFeretAngle', cell(1, i_stop), ...
74         'MaxFeretCoordinates', cell(1, i_stop), ...
75         'MinFeretDiameter', cell(1, i_stop), ...
76         'MinFeretAngle', cell(1, i_stop), ...
77         'MinFeretCoordinates', cell(1, i_stop), ...
78         'PixelList', cell(1, i_stop), ...
79         'PixelValues', cell(1, i_stop));
80
81     for i = 1:i_stop
82
83         % frame number in trackmate file
84         t = app.tracks_complete{s}(i, 1); % first frame in directory t=0
85
86         % position of cell in track in binned images...
87         x = app.tracks_complete{s}(i, 2);
88         y = app.tracks_complete{s}(i, 3);
89         % ... and in original images
90         x_cell = floor(app.binning*x);
91         y_cell = floor(app.binning*y);
92
93         % Display the image in a separate figure
94         fig = figure(1);
95
96         % Opens selected image
97         I = loadImage(app, i, s);
98         [h_I, l_I] = size(I);
99         % Crop image
```

```

100     I_cropped = cropImage(app, I, i, s);
101
102     % Segmentation
103     BW = segmentImage(app, I_cropped, app.otsu_level);
104
105     % Smooth boundary
106     boundaries = bwboundaries(BW);
107     firstBoundary = boundaries{1};
108     % Get the x and y coordinates.
109     x = firstBoundary(:, 2);
110     y = firstBoundary(:, 1);
111     % Now smooth with a Savitzky-Golay sliding polynomial filter
112     windowWidth = 15;
113     polynomialOrder = 2;
114     x = [ x(end-windowWidth:end); x; x(1:windowWidth-1) ]; % elongate to prevent edge
115         effects
116     y = [ y(end-windowWidth:end); y; y(1:windowWidth-1) ];
117     smoothX = sgolayfilt(x, polynomialOrder, windowWidth); % filter
118     smoothY = sgolayfilt(y, polynomialOrder, windowWidth);
119     smoothX = smoothX(windowWidth:end-windowWidth); % shorten to initial size
120     smoothY = smoothY(windowWidth:end-windowWidth);
121
122     % calculate centroid, orientation and major/minor axis length of the ellipse
123     shape_stats = regionprops(BW, I_cropped, {'Centroid','Orientation', ...
124         'MajorAxisLength', 'MinorAxisLength', 'Eccentricity', 'Circularity', 'Area',
125         ...
126         'Solidity', 'MaxFerretProperties', 'MinFerretProperties', 'PixelList', '
127         PixelValues'});
128
129     if isempty(shape_stats) == false
130         % if fit succeeded
131
132         % store data
133         cell_shapes_temp(i) = shape_stats;
134
135         % calculate the ellipse line
136         theta = linspace(0,2*pi);
137         col = (shape_stats.MajorAxisLength/2)*cos(theta);
138         row = (shape_stats.MinorAxisLength/2)*sin(theta);
139         M = makehgtform('translate',[shape_stats.Centroid, 0], 'zrotate',deg2rad(-1*
140             shape_stats.Orientation));
141         D = M*[col;row;zeros(1,numel(row));ones(1,numel(row))];
142
143         % main axes
144         clf
145         ax1 = axes('Position', [0 0 1 1]);
146
147         imshow(imadjust(I_cropped), 'Parent', ax1)
148         hold(gca, 'on')
149         % ellipse in red
150         plot(gca, D(1,:),D(2,:), 'r', 'LineWidth',1)
151         hold(gca, 'on')
152         % major and minor axis in red
153         xC = shape_stats.Centroid(1);
154         yC = shape_stats.Centroid(2);
155         theta = -1*deg2rad(shape_stats.Orientation);
156         M = shape_stats.MajorAxisLength;
157         m = shape_stats.MinorAxisLength;
158         plot(gca, [xC-M*cos(theta)/2 xC+M*cos(theta)/2], [yC-M*sin(theta)/2 yC+M*sin(

```

```

155         theta)/2], 'r','LineWidth',1)
156     hold(gca, 'on')
157     plot(gca, [xC-m*sin(theta)/2 xC+m*sin(theta)/2], [yC+m*cos(theta)/2 yC-m*cos(
158         theta)/2], 'r','LineWidth',1)
159     hold(gca, 'on')
160
161     % smooth boundary in blue
162     plot(gca, smoothX, smoothY, 'c-', 'LineWidth',1); %smooth line in blue
163     hold(gca, 'off')
164
165 else
166     % if ellipse fit failed
167
168     % store null data
169     cell_shapes_temp(i).Centroid = [0,0];
170     cell_shapes_temp(i).Orientation = 0;
171     cell_shapes_temp(i).MajorAxisLength = 1;
172     cell_shapes_temp(i).MinorAxisLength = 1;
173     cell_shapes_temp(i).Eccentricity = 0;
174     cell_shapes_temp(i).Circularity = 1;
175     cell_shapes_temp(i).Area = 0;
176     cell_shapes_temp(i).Solidity = 1;
177     cell_shapes_temp(i).MaxFerretDiameter = 1;
178     cell_shapes_temp(i).MaxFerretAngle = 0;
179     cell_shapes_temp(i).MaxFerretCoordinates = [0,0];
180     cell_shapes_temp(i).MinFerretDiameter = 1;
181     cell_shapes_temp(i).MinFerretAngle = 0;
182     cell_shapes_temp(i).MinFerretCoordinates = [0,0];
183     cell_shapes_temp(i).PixelList = 0;
184     cell_shapes_temp(i).PixelValues = 0;
185
186     % Display the image only
187     ax1 = axes('Position', [0 0 1 1]);
188     imshow(imadjust(I_cropped), 'Parent', ax1)
189     hold(gca, 'off')
190
191 end
192
193 % figure labels
194 text(5, 5, [app.date_exp ' ' app.type_cells ' ' app.size_cstr ' ' app.dye ' seq'
195     app.seq_exp ' track' num2str(s)], 'Color', 'white', 'FontSize', 7.5);
196 hold(gca, 'on')
197 text(gca, 5, 10, "frame "+string(app.tracks_complete{s}(i, 1)), 'Color', 'white',
198     'FontSize', 7.5);
199 hold(gca, 'on')
200 text(gca, 5, 15, "time = "+string((i-1)/app.fps)+" s", 'Color', 'white', '
201     FontSize', 7.5);
202 hold(gca, 'on')
203 plot(gca, [5 5+10/app.pixel_size],[app.SOI-5 app.SOI-5], 'LineWidth', 2, 'Color',
204     'white'),
205 hold(gca, 'on')
206 text(gca, 10, app.SOI-10, '10um', 'Color', 'white', 'FontSize', 7.5);
207 hold(gca, 'off')
208
209 % Add whole image for cell position
210 ax2 = axes('Position', [1-(0.15+1_I/10000) 0.05 1_I/10000 h_I/10000]);
211 imshow(I)
212 hold(gca, 'on')
213 plot(gca, x_cell+D(1,:),y_cell+D(2,:), 'r', 'LineWidth', 2)
214 hold(gca, 'on')

```

```
208     rectangle('Position', [1 1 l_I-1 h_I-1], 'EdgeColor', 'white', 'LineWidth', 1)
209     hold(gca, 'off')
210
211     % Record
212     if app.recording == true
213         videoFrames(i) = getframe(gcf);
214     end
215
216     % Update the progress dialog
217     if progressDialog.CancelRequested
218         delete(progressDialog);
219         disp('Function canceled by user. ');
220         return;
221     end
222     progressPercentage = (iteration / totalIterations) * 100;
223     iteration = iteration+1;
224     progressDialog.Value = progressPercentage/100;
225     progressDialog.Message = sprintf('Processing: %d%%', round(progressPercentage));
226 end
227
228 % Store data
229 app.cell_shapes{s} = cell_shapes_temp;
230
231 % Save video
232 if app.recording == true
233     movie_filename = [app.date_exp '_' app.type_cells '_' app.size_cstr '_' app.dye '
234         _seq' app.seq_exp '_track' num2str(s) '_movie.avi'];
235     v = VideoWriter( fullfile( app.res_dir, movie_filename ) );
236     v.FrameRate = 50;
237     v.Quality = 100;
238
239     open(v);
240     writeVideo(v, videoFrames);
241     close(v);
242     clear videoFrames
243 end
```

## C Data and fits

In this section, we'll produce the data obtained for each cell lines during the study of recovery, for both whole cells and nuclei. For a better comparison, the normalized deformation  $\varepsilon_{Norm}(t) = \frac{\varepsilon(t) - \varepsilon_{\infty}}{\varepsilon_{max} - \varepsilon_{\infty}}$  is presented.

Each cell replicate is presented in light gray. Mean curves is overlaid in colored points (with its 95% confidence interval). Curves obtained from the fit with GraphPad Prism are overlaid as well. The corresponding parameters are reported in the tables following.

The mean curves were fitted with the following equations, where X is the time and Y represents  $\varepsilon_{Norm}$  :

— One Phase Decay :

$$Y = (Y_0 - \text{Plateau}) * \exp(-X/\text{Tau}) + \text{Plateau}$$

— Two Phase Decay :

$$\text{SpanFast} = (Y_0 - \text{Plateau}) * \text{PercentFast} * .01$$

$$\text{SpanSlow} = (Y_0 - \text{Plateau}) * (100 - \text{PercentFast}) * .01$$

$$Y = \text{Plateau} + \text{SpanFast} * \exp(-X/\text{TauFast}) + \text{SpanSlow} * \exp(-X/\text{TauSlow})$$

— Three Phase Decay :

$$Y_{\text{Fast}} = (Y_0 - \text{Plateau}) * \text{PercentFast} * .01 * \exp(-X/\text{TauFast})$$

$$Y_{\text{Slow}} = (Y_0 - \text{Plateau}) * \text{PercentSlow} * .01 * \exp(-X/\text{TauSlow})$$

$$Y_{\text{Medium}} = (Y_0 - \text{Plateau}) * (100 - \text{PercentFast} - \text{PercentSlow}) * .01 * \exp(-X/\text{TauMedium})$$

$$Y = \text{Plateau} + Y_{\text{Fast}} + Y_{\text{Medium}} + Y_{\text{Slow}}$$

— Power Law :

$$Y = (X/X_0)^{-n} + C$$

In the case of a three case decay, we separated the separated the recovery into two regimes, one elastic followed by one viscoelastic, notably merging the fastest exponential into the elastic regime for reasons we presented earlier. From the parameters computed here ( $Y_0$ , Plateau, PercentFast, TauFast, PercentSlow, TauSlow, PercentMedium, TauMedium), we then define as presented in the main text the following :

—  $a_{slow} = (\text{PercentSlow}) * (Y_0 - \text{Plateau})$

—  $a_{medium} = (100 - \text{PercentFast} - \text{PercentSlow}) * (Y_0 - \text{Plateau})$

—  $\Phi_{VE} = (a_{slow} + a_{medium})$

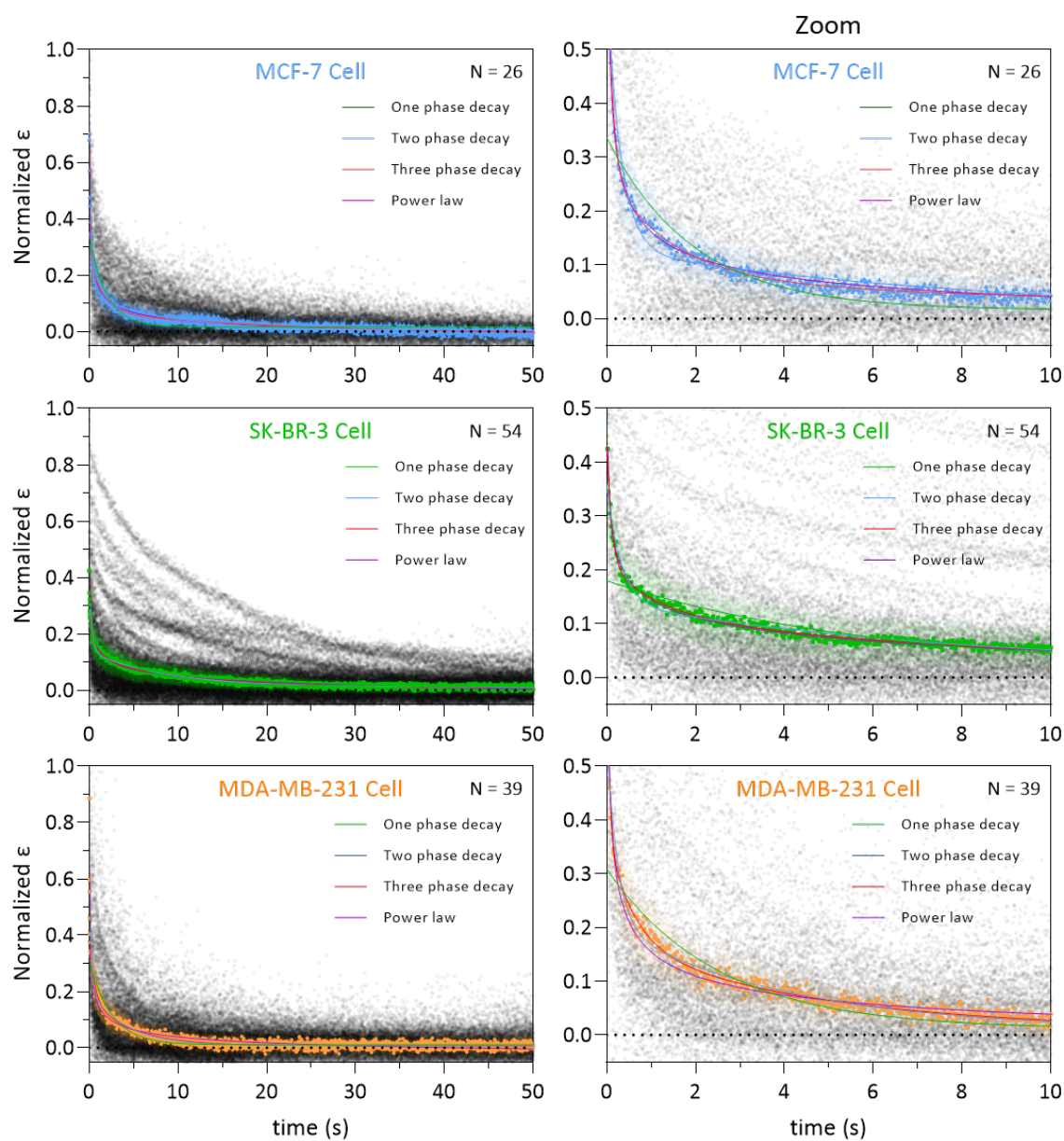


**Figure C.1** – Breast Whole Cell Fits. For each cell lines, mean recovery curves and the curves for one, two and three phase decays fits, as well as the one for the power law fit were overlaid to each cell replicates (represented as gray points).

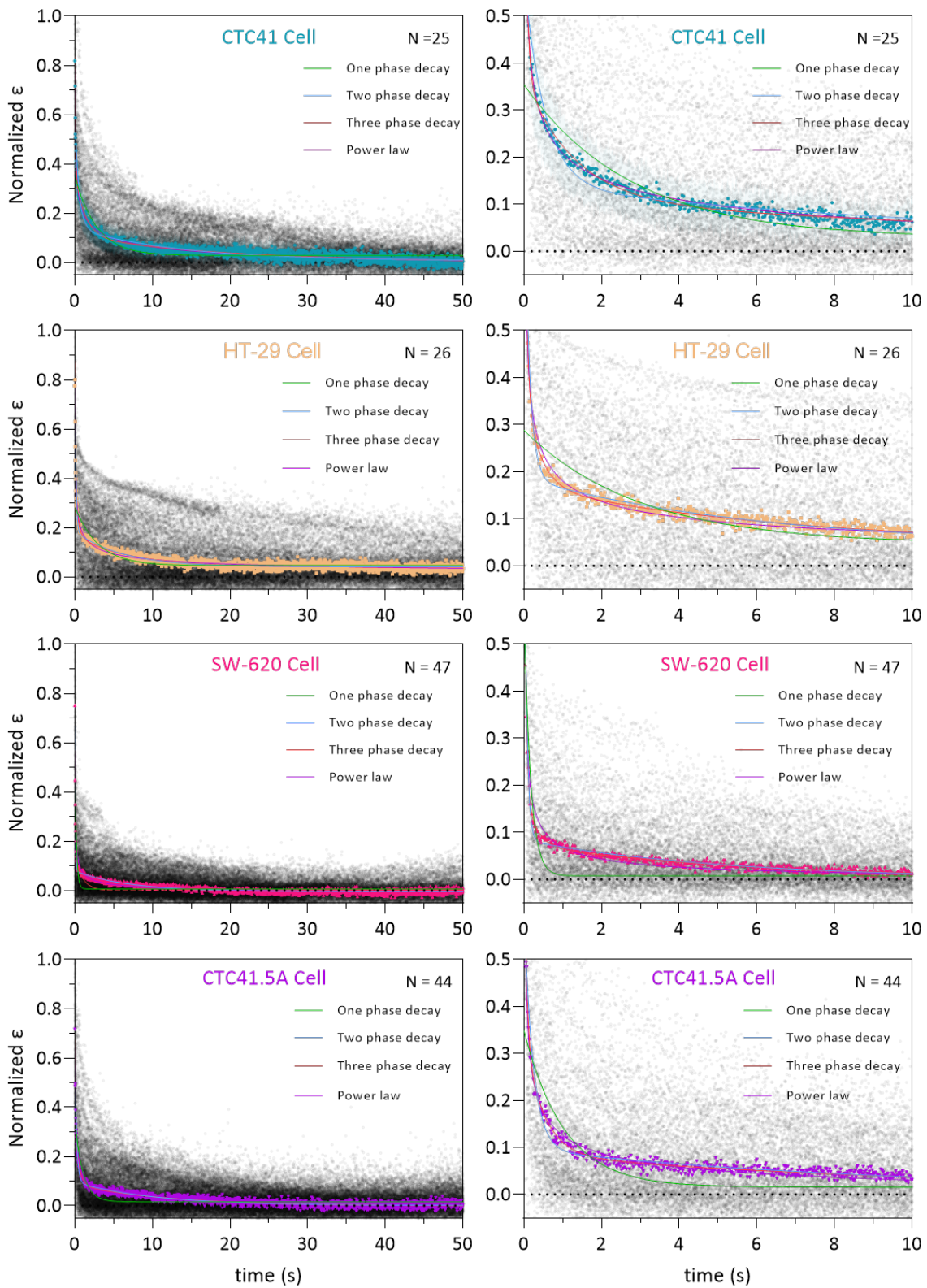


**Figure C.2** – Colon Whole Cell Fits. For each cell lines, mean recovery curves and the curves for one, two and three phase decays fits, as well as the one for the power law fit were overlaid to each cell replicates (represented as gray points).

	MCF-7	SK-BR-3	MDA-MB-231	CTC41	HT-29	SW-620	CTC41.5A
<b>One phase decay</b>							
<i>Best-fit values</i>							
Y0	0.3367	0.18	0.3083	0.3546	0.2883	0.5817	0.3489
Plateau	0.01616	0.0144	0.01099	0.02800	0.04628	0.007465	0.01546
Tau	1.963	5.918	2.5	2.782	2.980	0.1681	1.048
<i>95% CI (profile likelihood)</i>							
Y0	0.3245 to 0.3490	0.1769 to 0.1832	0.3021 to 0.3146	0.3427 to 0.3667	0.2781 to 0.2991	0.5340 to 0.6292	0.3259 to 0.3713
Plateau	0.01516 to 0.01715	0.01371 to 0.01508	0.01030 to 0.01168	0.02673 to 0.02926	0.04510 to 0.04744	0.00676 to 0.00816	0.01447 to 0.01642
Tau	1.834 to 2.103	5.716 to 6.127	2.414 to 2.589	2.604 to 2.975	2.750 to 3.222	0.1476 to 0.1944	0.9285 to 1.198
<i>Goodness of Fit</i>							
R squared	0.7983	0.8996	0.8955	0.7985	0.7363	0.6137	0.7046
<b>Two phase decay</b>							
<i>Best-fit values</i>							
Y0	0.6221	0.3584	0.5462	0.5872	0.8687	0.8992	0.6015
Plateau	0.003867	0.01054	0.00835	0.006745	0.04119	-0.0004277	0.0007461
PercentFast	79.93	63.51	63.38	77.14	82.49	90.71	84.12
Tau (slow)	8.843	8.731	4.032	13.41	6.133	5.287	10.22
Tau (fast)	0.3107	0.3173	0.2452	0.5325	0.1365	0.06431	0.2377
<i>95% CI (profile likelihood)</i>							
Y0	0.6039 to 0.6408	0.3497 to 0.3674	0.5314 to 0.5617	0.5689 to 0.6062	0.8481 to 0.8892	0.8740 to 0.9243	0.5865 to 0.6170
Plateau	0.002766 to 0.004903	0.01006 to 0.01102	0.00882	0.009149	0.04055 to 0.04183	9.799e-006	0.001583
PercentFast	79.31 to 80.53	62.67 to 64.33	62.33 to 64.40	76.40 to 77.85	81.97 to 83.02	90.38 to 91.04	83.65 to 84.58
Tau (slow)	8.293 to 9.450	8.511 to 8.961	3.903 to 4.167	12.21 to 14.83	5.933 to 6.347	5.081 to 5.510	9.740 to 10.73
Tau (fast)	0.2886 to 0.3348	0.2945 to 0.3418	0.2247 to 0.2674	0.4869 to 0.5818	0.1309 to 0.1426	0.0619 to 0.0669	0.2261 to 0.2498
<i>Goodness of Fit</i>							
R squared	0.94	0.9703	0.9568	0.9231	0.9356	0.9183	0.9313
<b>Three phase decay</b>							
<i>Best-fit values</i>							
Y0	0.8034	0.4323	0.7154	= 1.000	1.088	= 1.000	0.8146
Plateau	-0.01292	0.008402	0.007731	= 0.000	0.04026	= 0.000	-0.0008599
PercentFast	64.87	52.54	48.01	62.67	66.81	79.80	58.08
PercentSlow	10.09	25.08	23.37	10.79	12.33	7.361	10.52
Tau (Slow)	23.99	10.84	4.675	19.57	7.000	5.798	12.01
Tau (Fast)	0.1105	0.113	0.05563	0.06996	0.06080	0.04317	0.06273
Tau (Medium)	1.462	1.23	0.5831	1.281	0.3861	0.2731	0.4903
<i>95% CI (profile likelihood)</i>							
Y0	0.7849 to 0.8224	0.4201 to 0.4454	0.6796 to 0.7559		1.069 to 1.108		0.7818 to 0.8474
Plateau	-0.01660 to -0.009954	0.007839 to 0.008943	0.007254 to 0.008204		0.03958 to 0.04095		-0.001799 to 7.906e-005
PercentFast	63.81 to 65.89	50.82 to 54.15	45.10 to 50.67	61.63 to 63.72	63.52 to 70.11	76.62 to 82.97	55.58 to 60.58
PercentSlow	9.779 to 10.42	24.16 to 26.01	21.93 to 24.86	10.48 to 11.10	11.89 to 12.76	7.048 to 7.674	10.04 to 11.00
Tau (Slow)	21.51 to 27.12	10.47 to 11.24	4.490 to 4.877	18.95 to 20.24	6.711 to 7.315	5.529 to 6.094	11.40 to 12.70
Tau (Fast)	0.1038 to 0.1175	0.1013 to 0.1254	0.04595 to 0.06740	0.06613 to 0.07427	0.05587 to 0.06667	0.04065 to 0.04601	0.05564 to 0.07188
Tau (Medium)	1.376 to 1.553	1.110 to 1.362	0.5140 to 0.6643	1.212 to 1.359	0.3348 to 0.4560	0.2224 to 0.3539	0.4518 to 0.5359
<i>Goodness of Fit</i>							
R squared	0.968	0.9771	0.962	0.9529	0.9497	0.9434	0.9447
<b>Power Law</b>							
<i>Best-fit values</i>							
X0	0.01292	0.0008052	0.01035	0.01624	0.01341	0.009950	0.009678
n	0.3501	0.18	0.3342	0.2992	0.3898	0.5508	0.3961
C	-0.05632	-0.1331	-0.06206	-0.08255	-0.005393	-0.01062	-0.03329
<i>95% CI (profile likelihood)</i>							
X0	0.01241 to 0.01343	0.0007279 to 0.0008884	0.009735 to 0.01097	0.01546 to 0.01702	0.01275 to 0.01408	0.009492 to 0.01041	0.009170 to 0.01019
n	0.3446 to 0.3555	0.1744 to 0.1856	0.3269 to 0.3416	0.2924 to 0.3060	0.3822 to 0.3974	0.5411 to 0.5605	0.3887 to 0.4035
C	-0.05866 to -0.05405	-0.13990 to -0.1268	-0.06540 to -0.05886	-0.08722 to -0.07810	-0.007856 to -0.003024	-0.01157 to -0.009702	-0.03532 to -0.03135
<i>Goodness of Fit</i>							
R squared	0.962	0.9713	0.9253	0.9482	0.9289	0.8964	0.9328

Table C.1 – Parameters for the different fits tested on recovery curves at the whole cell level

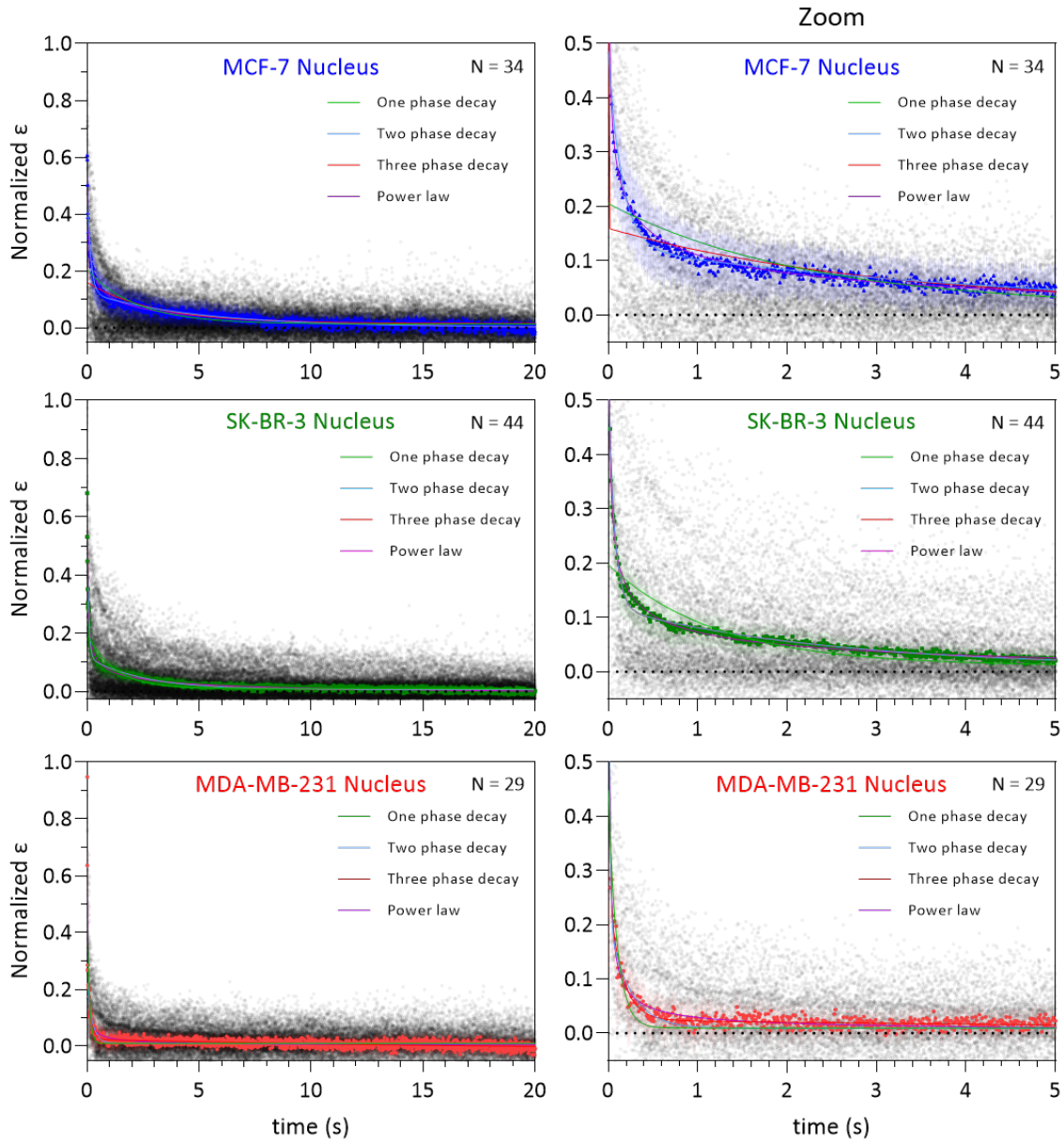


**Figure C.3** – Breast Nucleus Fits. For each cell lines, mean recovery curves and the curves for one, two and three phase decays fits, as well as the one for the power law fit were overlaid to each nucleus replicates (represented as gray points).

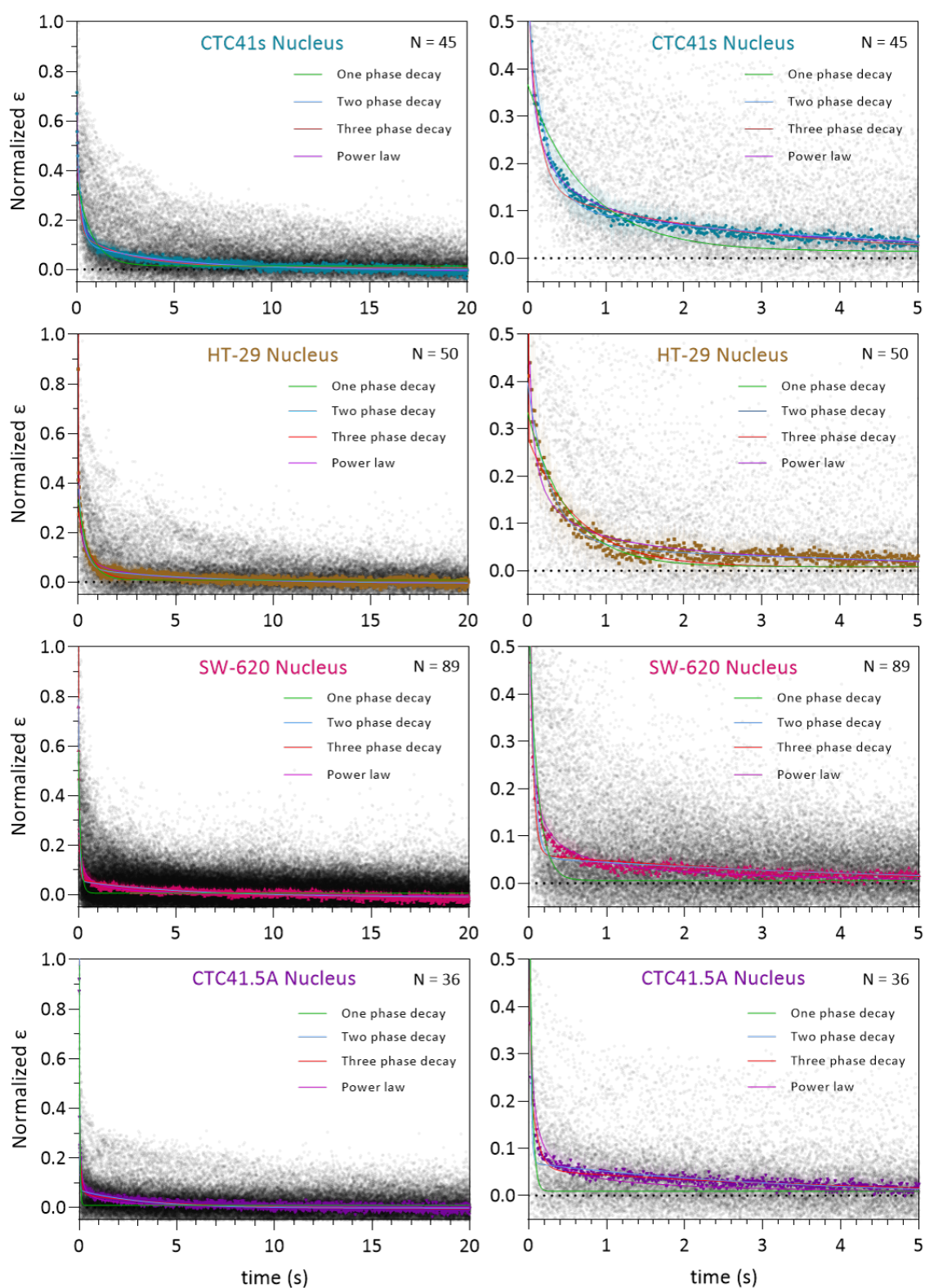


**Figure C.4** – Colon Nucleus Fits. For each cell lines, mean recovery curves and the curves for one, two and three phase decays fits, as well as the one for the power law fit were overlaid to each nucleus replicates (represented as gray points).

	MCF-7	SK-BR-3	MDA-MB-231	CTC41	HT-29	SW-620	CTC41.5A
<b>One phase decay</b>							
<i>Best-fit values</i>							
YO	0,2057	0,1976	0,4474	0,3481	0,3346	0,5867	0,9752
Plateau	0,01347	0,0105	0,009554	0,03384	0,008401	0,00562	0,009165
Tau	2,202	1,202	0,09809	1,007	0,5209	0,1116	0,03329
<i>95% CI (profile likelihood)</i>							
YO	0,1985 to 0,2131	0,1907 to 0,2047	0,4239 to 0,4720	0,3342 to 0,3624	0,3240 to 0,3453	0,5512 to 0,6236	0,8846 to 1,076
Plateau	0,01203 to 0,01488	0,009693 to 0,01131	0,008944 to 0,01016	0,03254 to 0,03511	0,007672 to 0,009129	0,004780 to 0,006458	0,008307 to 0,01002
Tau	2,043 to 2,371	1,124 to 1,285	0,09013 to 0,1068	0,9268 to 1,096	0,4947 to 0,5487	0,1008 to 0,1238	0,02902 to 0,03828
<i>Goodness of Fit</i>							
R squared	0,7933	0,8103	0,6909	0,8089	0,84	0,7094	0,6006
<b>Two phase decay</b>							
<i>Best-fit values</i>							
YO	0,4852	0,5343	= 1,000	0,5516	0,398	0,7917	= 1,000
Plateau	0,002525	0,006612	0,008878	0,008287	-0,006074	-0,01165	-0,003125
PercentFast	74,78	78,69	79,67	78,35	84,98	91,71	93,28
Tau (slow)	4,921	2,45	0,2378	6,51	6,182	5,736	3,77
Tau (fast)	0,1521	0,06955	0,01369	0,2315	0,2914	0,05583	0,02627
<i>95% CI (profile likelihood)</i>							
YO	0,4718 to 0,4990	0,5221 to 0,5468		0,5428 to 0,5604	0,3895 to 0,4065	0,7712 to 0,8122	
Plateau	0,001229 to 0,003751	0,006211 to 0,007007	0,008334 to 0,009423	0,006537 to 0,01004	-0,007752 to -0,004396	-0,01301 to -0,01029	-0,004035 to -0,002214
PercentFast	74,04 to 75,49	78,15 to 79,21	78,16 to 81,19	77,88 to 78,82	84,37 to 85,59	91,42 to 92,00	93,04 to 93,51
Tau (slow)	4,686 to 5,177	2,375 to 2,529	0,2190 to 0,2602	6,173 to 6,886	5,571 to 6,944	5,324 to 6,217	3,519 to 4,060
Tau (fast)	0,1423 to 0,1624	0,06630 to 0,07298	0,01468	0,2239 to 0,2396	0,2798 to 0,3039	0,05382 to 0,05800	0,02551 to 0,02708
<i>Goodness of Fit</i>							
R squared	0,945	0,9678	0,759	0,9632	0,9303	0,9147	0,8684
<b>Power Law</b>							
<i>Best-fit values</i>							
X0	0,002087	0,002196	0,004566	0,005014	0,005262	0,006313	0,006115
n	0,2619	0,3625	0,6606	0,297	0,4239	0,5537	0,6334
C	-0,08792	-0,03557	0,0007251	-0,07133	-0,03525	-0,01644	-0,00486
<i>95% CI (profile likelihood)</i>							
X0	0,001911 to 0,002271	0,002094 to 0,002299	0,004299 to 0,004834	0,004771 to 0,005262	0,004863 to 0,005670	0,006057 to 0,006569	0,005780 to 0,006448
n	0,2538 to 0,2700	0,3574 to 0,3676	0,6441 to 0,6772	0,2907 to 0,3032	0,4127 to 0,4351	0,5440 to 0,5634	0,6167 to 0,6503
C	-0,09353 to -0,08267	-0,03699 to -0,03419	-0,0001826 to 0,001602	-0,07532 to 0,06752	-0,03781 to 0,03282	-0,01760 to 0,01531	-0,006095 to 0,003675
<i>Goodness of Fit</i>							
R squared	0,9512	0,9756	0,8116	0,966	0,905	0,9202	0,8458

Table C.2 – Parameters for the different fits tested on recovery curves at the nucleus level

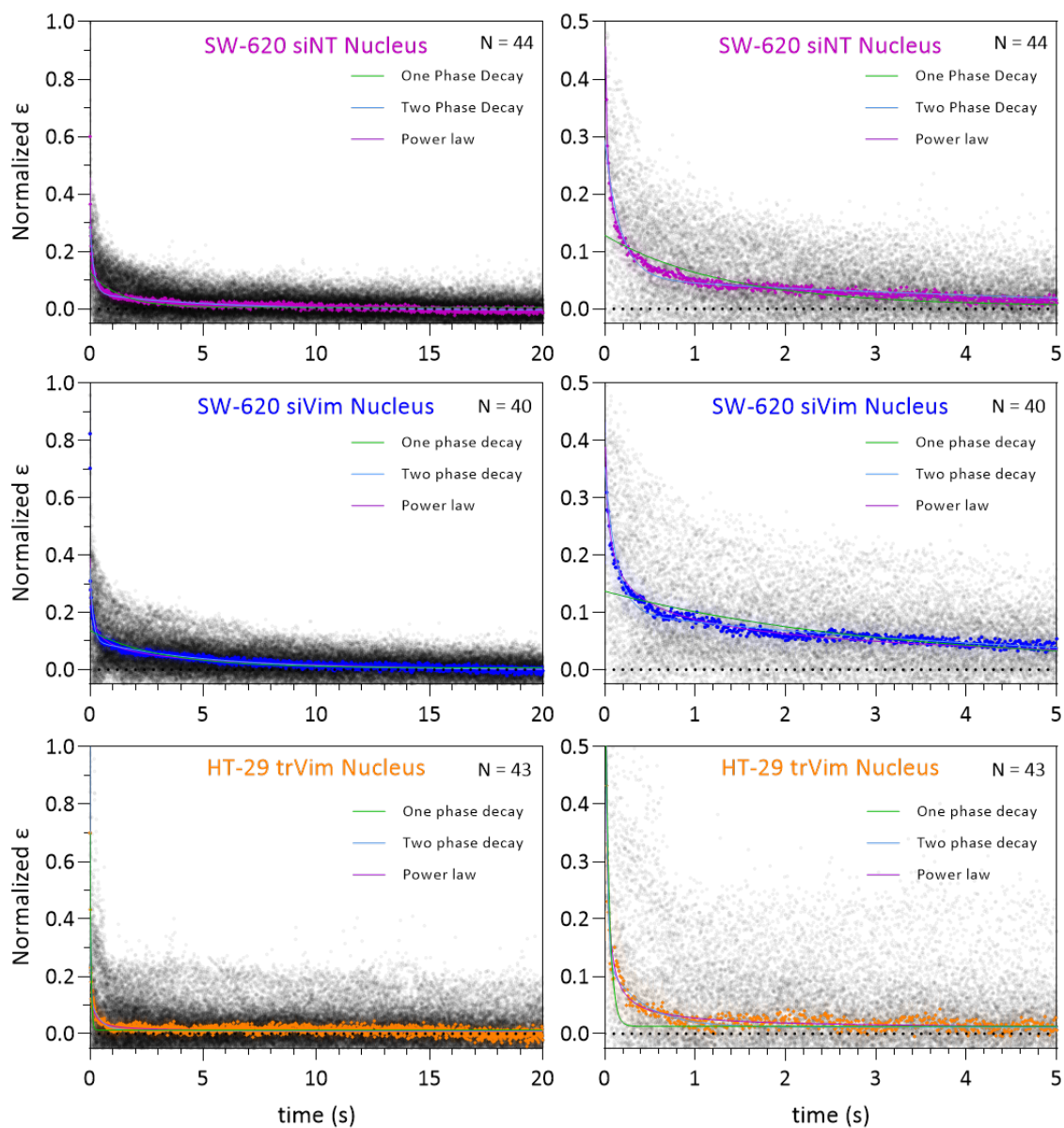


**Figure C.5** – Transformed Colon Nucleus Fits. For each cell lines, mean recovery curves and the curves for one, two and three phase decays fits, as well as the one for the power law fit were overlaid to each nucleus replicates (represented as gray points).

	HT-29 trVim	SW-620 siNT	SW-620 siVim
<b>One phase decay</b>			
<i>Best-fit values</i>			
Y0	0,6984	0,1285	0,137
Plateau	0,01286	0,004687	0,00676
Tau	0,04378	1,349	3,109
<i>95% CI (profile likelihood)</i>			
Y0	0,6621 to 0,7347	0,1259 to 0,1310	0,1348 to 0,1393
Plateau	0,01220 to 0,01353	0,004301 to 0,005074	0,006006 to 0,007513
Tau	0,04105 to 0,04691	1,309 to 1,391	3,013 to 3,213
<i>Goodness of Fit</i>			
R squared	0,6386	0,1957	0,2691
<b>Two phase decay</b>			
<i>Best-fit values</i>			
Y0	= 1,000	0,2941	0,3538
Plateau	0,01125	-0,005255	-0,0006028
PercentFast	88,01	80,12	71,35
Tau (slow)	0,3974	5,656	5,257
Tau (fast)	0,01858	0,1726	0,131
<i>95% CI (profile likelihood)</i>			
Y0		0,2846 to 0,3036	0,3399 to 0,3676
Plateau	0,01069 to 0,01180	-0,006268 to -0,004242	-0,001879 to 0,0006737
PercentFast	86,93 to 89,09	79,42 to 80,83	70,20 to 72,50
Tau (slow)	0,3582 to 0,4463	5,297 to 6,067	4,999 to 5,543
Tau (fast)	0,01770 to 0,01955	0,1641 to 0,1821	0,1223 to 0,1411
<i>Goodness of Fit</i>			
R squared	0,7685	0,2339	0,3028
<b>Power Law</b>			
<i>Best-fit values</i>			
X0	0,005782	0,001578	0,0003182
n	0,7531	0,3938	0,2079
C	0,006599	-0,02651	-0,09965
<i>95% CI (profile likelihood)</i>			
X0	0,005504 to 0,006060	0,001398 to 0,001758	0,0002435 to 0,0003928
n	0,7341 to 0,7720	0,3828 to 0,4047	0,1954 to 0,2204
C	0,005829 to 0,007368	-0,02835 to -0,02466	-0,1095 to -0,08984
<i>Goodness of Fit</i>			
R squared	0,7904	0,2413	0,3053

**Table C.3** – Parameters for the different fits tested on recovery curves at the nucleus level

## D Improvement on the Pachinko device

Having practiced the Pachinko device for quite some time now, I present Fig.D.1 some improvements to be made on the device for future users :

1. *Addition of support pillars in the chamber below the traps.* First, after plasma treatment during chip assembly, there exist a risk of collapsing the ceiling (only 15  $\mu\text{m}$ -high, but spanning over more than 3 mm) if one isn't careful enough. Second, the addition of pressure to empty the trap chamber between acquisitions tends to lift up the ceiling, which exert forces on the small pillars composing the traps and may cause them to unbound from the glass slide. The addition of pillars supporting the ceiling will prevent its collapsing during assembly, and its deformation under high pressure.
2. *Change in the constriction profile.* The circle arc profile that we use for the constrictions present the advantage of being more representative of *in vitro* capillaries constrictions. Though, deformation pattern it induces in the cell is complex and can be difficult to analyse. For instance, big cells can take the shape of an "8", where the front of the cell start to recover while the back hasn't come through the constriction. To remedy this issue, a straight channel from the middle of the constriction can be added so that the integrity of the cell experiences the same level of deformation before its escape.
3. *Change in the trap design.* Here several changes could be made. The size of the pillars composing the trap could be increased. The two small pillars in the previous design tend to break over time, thus rendering the wafer and/or epoxy replicas molds unusable. The depth of the cell housing could be increased and narrowed, to prevent cell from escaping the design, and from having several cells occupying the same trap at the same time. During emptying of the trap chambers between acquisitions, some cells tend to remain stuck below the traps. We propose to round the bottom of the traps to prevent it.

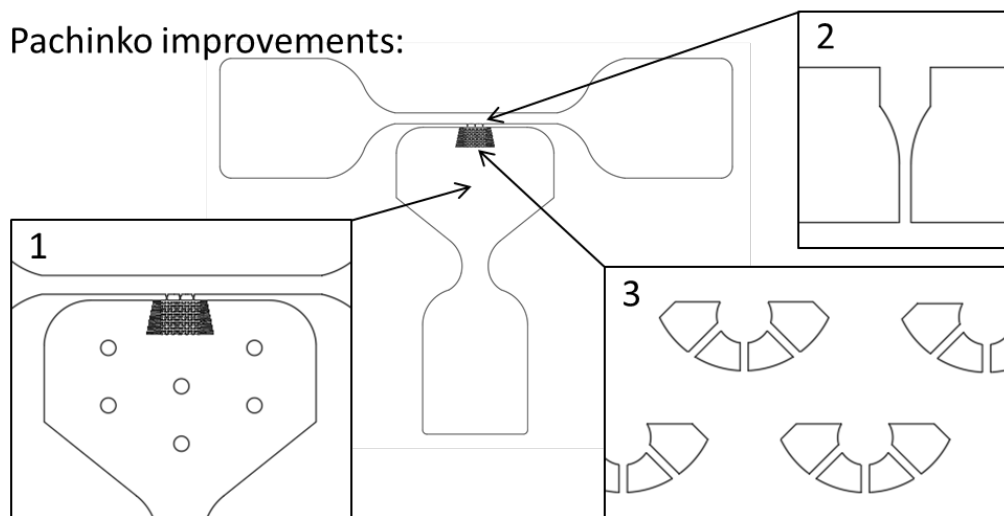


Figure D.1 – Proposed improvements of the Pachinko device.

- [Abarca-Ortega, 2024] Aldo ABARCA-ORTEGA, Blanca GONZÁLEZ-BERMÚDEZ, Cristina CASTRO-DOMÍNGUEZ, Aroa ÁLVAREZ-LÓPEZ, Cristina DÍAZ-ALCARAZ, María GARVÍA-RODRÍGUEZ, Gustavo V. GUINEA et Gustavo R. PLAZA. « Single-cell mechanical characterization in constriction-based cytometry ». *International Journal of Mechanical Sciences* (2024), p. 108979 (cf. p. 84).
- [Abercrombie, 1980] M. ABERCROMBIE. « The Croonian Lecture, 1978 - The crawling movement of metazoan cells ». *Proceedings of the Royal Society of London. Series B. Biological Sciences* 207.1167 (1980), p. 129-147 (cf. p. 19, 33).
- [Abhange, 2021] Komal ABHANGE, Amy MAKLER, Yi WEN, Natasha RAMNAUTH, Wenjun MAO, Waseem ASGHAR et Yuan WAN. « Small extracellular vesicles in cancer ». *Bioactive Materials* 6.11 (2021), p. 3705-3743 (cf. p. 137).
- [Aceto, 2014] Nicola ACETO, Aditya BARDIA, David T. MIYAMOTO, Maria C. DONALDSON, Ben S. WITTNER, Joel A. SPENCER, Min YU, Adam PELY, Amanda ENGSTROM, Huili ZHU, Brian W. BRANNIGAN, Ravi KAPUR, Shannon L. STOTT, Toshi SHIODA, Sridhar RAMASWAMY, David T. TING, Charles P. LIN, Mehmet TONER, Daniel A. HABER et Shyamala MAHESWARAN. « Circulating Tumor Cell Clusters Are Oligoclonal Precursors of Breast Cancer Metastasis ». *Cell* 158.5 (2014), p. 1110-1122 (cf. p. 20, 21).
- [Ahmad-Cognart, 2020] Hamizah AHMAD-COGNART, Jean-Louis VIOVY et Catherine VILLARD. « Fluid shear stress coupled with narrow constrictions induce cell type-dependent morphological and molecular changes in SK-BR-3 and MDA-MB-231 cells ». *Scientific Reports* 10.1 (2020), p. 1-14 (cf. p. 22, 37, 38, 41, 86, 100, 121, 122, 137, 156, 158-161).
- [Ahmed, 2013] D. AHMED, P. W. EIDE, I. A. EILERTSEN, S. A. DANIELSEN, M. EKNÆS, M. HEKTOEN, G. E. LIND et R. A. LOTHE. « Epigenetic and genetic features of 24 colon cancer cell lines ». *Oncogenesis* 2.9 (2013), e71-e71 (cf. p. 18).
- [Alberts, 2022] Bruce ALBERTS, Rebecca HEALD, Alexander JONHSON, Martin RAFF, Keith ROBERTS et Peter WALTER. *Molecular Biology of the Cell : Seventh Edition*. 2022 (cf. p. 5).
- [Alberts, 2019] Bruce ALBERTS, Karen HOPKIN, Alexander JONHSON, David MORGAN, Martin RAFF, Keith ROBERTS et Peter WALTER. *Essential Cell Biology : Fifth Edition*. 2019 (cf. p. 3).
- [Alghanem, 2020] Bandar ALGHANEM, Rizwan ALI, Atef NEHDI, Hajar AL ZAHRANI, Abdulelah ALTOLAYYAN, Hayat SHAIBAH, Omar BAZ, Alshaimaa ALHALLAJ, James J. MORESCO, Jolene K. DIEDRICH, John R. YATES et Mohamed BOUDJELAL. « Proteomics Profiling of KAIMRC1 in Comparison to MDA-MB231 and MCF-7 ». *International Journal of Molecular Sciences* 21.12 (2020), p. 4328 (cf. p. 114).
- [Alibert, 2017] Charlotte ALIBERT, Bruno GOUD et Jean-Baptiste MANNEVILLE. « Are cancer cells really softer than normal cells ? » *Biology of the Cell* 109.5 (2017), p. 167-189 (cf. p. iii, 9, 41, 88, 154, 159, 161, 169).
- [Alibert, 2021] Charlotte ALIBERT, David PEREIRA, Nathan LARDIER, Sandrine ETIENNE-MANNEVILLE, Bruno GOUD, Atef ASNACIOS et Jean-Baptiste MANNEVILLE. « Multiscale rheology of glioma cells ». *Biomaterials* 275.April (2021), p. 120903 (cf. p. 89).
- [Alix-Panabières, 2017] Catherine ALIX-PANABIÈRES, Laure CAYREFOURCQ, Thibault MAZARD, Thierry MAUDELONDE, Eric ASSENAT et Said ASSOULI. « Molecular portrait of metastasis-competent circulating tumor cells in colon cancer reveals the crucial role of genes regulating energy metabolism and DNA repair ». *Clinical Chemistry* 63.3 (2017), p. 700-713 (cf. p. 71).

- [Alsaab, 2017] Hashem O. ALSAAB, Samarsh SAU, Rami ALZHRANI, Katyayani TATIPARTI, Ketki BHISE, Sushil K. KASHAW et Arun K. IYER. « PD-1 and PD-L1 Checkpoint Signaling Inhibition for Cancer Immunotherapy : Mechanism, Combinations, and Clinical Outcome ». *Frontiers in Pharmacology* 8.AUG (2017), p. 1-15 (cf. p. 157).
- [Alvarado-Estrada, 2021] Keila ALVARADO-ESTRADA, Lina MARENCO-HILLENBRAND, Sushila MAHARJAN, Valerio Luca MAINARDI, Yu Shrike ZHANG, Natanael ZARCO, Paula SCHIAPPARELLI, Hugo GUERRERO-CAZARES, Rachel SARABIA-ESTRADA, Alfredo QUINONES-HINOJOSA et Kaisorn L. CHAICHANA. « Circulatory shear stress induces molecular changes and side population enrichment in primary tumor-derived lung cancer cells with higher metastatic potential ». *Scientific Reports* 11.1 (2021), p. 2800 (cf. p. 121, 137, 158).
- [Amiri-Kordestani, 2014] Laleh AMIRI-KORDESTANI, Gideon M. BLUMENTHAL, Qiang Casey XU, Lijun ZHANG, Shenghui W. TANG, Linan HA, Wendy C. WEINBERG, Bo CHI, Reyes CANDAU-CHACON, Patricia HUGHES, Anne M. RUSSELL, Sarah Pope MIKSINSKI, Xiao Hong CHEN, W. David MCGUINN, Todd PALMBY, Sarah J. SCHRIEBER, Qi LIU, Jian WANG, Pengfei SONG, Nitin MEHROTRA, Lisa SKARUPA, Kathleen CLOUSE, Ali AL-HAKIM, Rajeshwari SRIDHARA, Amna IBRAHIM, Robert JUSTICE, Richard PAZDUR et Patricia CORTAZAR. « FDA Approval : Ado-Trastuzumab Emtansine for the Treatment of Patients with HER2-Positive Metastatic Breast Cancer ». *Clinical Cancer Research* 20.17 (2014), p. 4436-4441 (cf. p. 157).
- [Andree, 2016] Kiki C. ANDREE, Guus van DALUM et Leon W.M.M. TERSTAPPEN. « Challenges in circulating tumor cell detection by the CellSearch system ». *Molecular Oncology* 10.3 (2016), p. 395-407 (cf. p. 27).
- [Ashworth, 1869] Thomas Ramsen. ASHWORTH. « A case of cancer in which cells similar to those in the tumours were seen in the blood after death ». *The Australian Medical Journal* 14 (1869) (cf. p. 25).
- [Au, 2016] Sam H. AU, Brian D. STOREY, John C. MOORE, Qin TANG, Yeng Long CHEN, Sarah JAVAID, A. Fatih SARIOGLU, Ryan SULLIVAN, Marissa W. MADDEN, Ryan O'KEEFE, Daniel A. HABER, Shyamala MAHESWARAN, David M. LANGENAU, Shannon L. STOTT et Mehmet TONER. « Clusters of circulating tumor cells traverse capillary-sized vessels ». *Proceedings of the National Academy of Sciences of the United States of America* 113.18 (2016), p. 4947-4952 (cf. p. 38).
- [Azadi, 2021] Shohreh AZADI, Mohammad TFAZZOLI SHADPOUR et Majid E. WARKIANI. « Characterizing the effect of substrate stiffness on the extravasation potential of breast cancer cells using a 3D microfluidic model ». *Biotechnology and Bioengineering* 118.2 (2021), p. 823-835 (cf. p. 30, 31).
- [Balland, 2006] Martial BALLAND, Nicolas DESPRAT, Delphine ICARD, Sophie FÉRÉOL, Atef ASNACIOS, Julien BROWAEYS, Sylvie HÉNON et François GALLET. « Power laws in microrheology experiments on living cells : Comparative analysis and modeling ». *Physical Review E* 74 (2 2006), p. 021911 (cf. p. 74, 172).
- [Barnes, 1989] H. A. BARNES, J. F. HUTTON et K. WALTERS. *An introduction to rheology (Vol. 1)*. Elsevier, 1989 (cf. p. 1).
- [Barnes, 2012] J. Matthew BARNES, Jones T. NAUSEEF et Michael D. HENRY. « Resistance to Fluid Shear Stress Is a Conserved Biophysical Property of Malignant Cells ». *PLoS ONE* 7.12 (2012) (cf. p. 24, 121, 137, 161).
- [Bastatas, 2012] Lyndon BASTATAS, Dalia MARTINEZ-MARIN, James MATTHEWS, Jood HASHEM, Yong J. LEE, Souad SENNOUNE, Stephanie FILLEUR, Raul MARTINEZ-ZAGUILAN et Soyeun PARK. « AFM nano-mechanics and calcium dynamics of prostate cancer cells with distinct metastatic potential ». *Biochimica et Biophysica Acta (BBA) - General Subjects* 1820.7 (2012), p. 1111-1120 (cf. p. 88).
- [Bell, 2022] Emily S. BELL, Pragya SHAH, Noam ZUELA-SOPILNIAK, Dongsung KIM, Alice-Anais VARLET, Julien L. P. MORIVAL, Alexandra L. MCGREGOR, Philipp ISERMANN, Patricia M. DAVIDSON, Joshua J. ELACQUA, Jonathan N. LAKINS, Linda VAHDAT, Valerie M. WEAVER, Marcus B. SMOLKA, Paul N. SPAN et Jan LAMMERDING. « Low lamin A levels enhance confined cell migration and metastatic capacity in breast cancer ». *Oncogene* 41.36 (2022), p. 4211-4230 (cf. p. 115).
- [Belt, 2011] E.J.Th. BELT, R.J.A. FIJNEMAN, E.G. van den BERG, H. BRIL, P.M. DELIS-VAN DIEMEN, M. TIJSSEN, H.F. van ESSEN, E.S.M. DE LANGE-DE KLERK, J.A.M. BELIËN, H.B.A.C. STOCKMANN, S. MEIJER et G.A. MEIJER. « Loss of lamin A/C expression in stage II and III colon cancer is associated with disease recurrence ». *European Journal of Cancer* 47.12 (2011), p. 1837-1845 (cf. p. 115).
- [Bersini, 2014] Simone BERSINI, Jessie S. JEON, Gabriele DUBINI, Chiara ARRIGONI, Seok CHUNG, Joseph L. CHAREST, Matteo MORETTI et Roger D. KAMM. « A microfluidic 3D invitro model for specificity of breast cancer metastasis to bone ». *Biomaterials* 35.8 (2014), p. 2454-2461 (cf. p. 31).
- [Bidard, 2016] Francois-Clement BIDARD, Charlotte PROUDHONA et Jean-Yves PIERGA. « Circulating tumor cells in breast cancer ». *Molecular Oncology* 10.1 (2016), p. 418-430 (cf. p. 25).

- [Bidard, 2021] François-Clément BIDARD, William JACOT, Nicolas KIAVUE, Sylvain DUREAU, Amir KADI, Etienne BRAIN, Thomas BACHELOT, Hugues BOURGEOIS, Anthony GONÇALVES, Sylvain LADOIRE, Hervé NAMAN, Florence DALENC, Joseph GLIGOROV, Marc ESPIÉ, George EMILE, Jean-Marc FERRERO, Delphine LOIRAT, Sophie FRANK, Luc CABEL, Véronique DIÉRAS, Laure CAYREFOURCQ, Cécile SIMONDI, Frédérique BERGER, Catherine ALIX-PANABIÈRES et Jean-Yves PIERGA. « Efficacy of Circulating Tumor Cell Count-Driven vs Clinician-Driven First-line Therapy Choice in Hormone Receptor-Positive, ERBB2-Negative Metastatic Breast Cancer : The STIC CTC Randomized Clinical Trial. » *JAMA oncology* (2021) (cf. p. 27).
- [Bjerknes, 2006] Matthew BJERKNES et Hazel CHENG. « Intestinal Epithelial Stem Cells and Progenitors ». *Methods in Enzymology*. T. 419. 2000. 2006, p. 337-383 (cf. p. 88).
- [Blanchoin, 2014] Laurent BLANCHOIN, Rajaa BOUJEMAA-PATERSKI, Cécile SYKES et Julie PLASTINO. « Actin Dynamics, Architecture, and Mechanics in Cell Motility ». *Physiological Reviews* 94.1 (2014), p. 235-263 (cf. p. 4, 7, 8, 159).
- [Block, 2017] Johanna BLOCK, Hannes WITT, Andrea CANDELLI, Erwin J.G. PETERMAN, Gijs J.L. WUITE, Andreas JANSHOFF et Sarah KÖSTER. « Nonlinear Loading-Rate-Dependent Force Response of Individual Vimentin Intermediate Filaments to Applied Strain ». *Physical Review Letters* 118.4 (2017), p. 048101 (cf. p. 6, 106, 116, 155, 159, 165).
- [Blom, 2003] J A BLOM. *Monitoring of respiration and circulation*. CRC Press LLC, 2003 (cf. p. 35, 123).
- [Bodegraven, 2021] Emma J. van BODEGRAVEN et Sandrine ETIENNE-MANNEVILLE. « Intermediate Filaments from Tissue Integrity to Single Molecule Mechanics ». *Cells* 10.8 (2021), p. 1905 (cf. p. 6).
- [Bonakdar, 2016] Navid BONAKDAR, Richard GERUM, Michael KUHN, Marina SPÖRRER, Anna LIPPERT, Werner SCHNEIDER, Katerina E. AIFANTIS et Ben FABRY. « Mechanical plasticity of cells ». *Nature Materials* 15 (10 2016), p. 1090-1094 (cf. p. 81).
- [Booth, 2015] Elizabeth A. BOOTH, Stephen T. SPAGNOL, Turi A. ALCOSER et Kris Noel DAHL. « Nuclear stiffening and chromatin softening with progerin expression leads to an attenuated nuclear response to force ». *Soft Matter* 11.32 (2015), p. 6412-6418 (cf. p. 8).
- [Bouquerel, 2022] Charlotte BOUQUEREL, William CÉSAR, Lara BARTHOD, Sarah ARRAK, Aude BATTISTELLA, Giacomo GROPLERO, Fatima MECHTA-GRIGORIOU, Gérard ZALCMAN, Maria Carla PARRINI, Marine VERHULSEL et Stéphanie DESCROIX. « Precise and fast control of the dissolved oxygen level for tumor-on-chip ». *Lab on a Chip* 22.22 (2022), p. 4443-4455 (cf. p. 31).
- [Bouquerel, 2023] Charlotte BOUQUEREL, Anastasiia DUBROVA, Isabella HOFER, Duc T. T. PHAN, Moencopi BERNHEIM, Ségolène LADAIGUE, Charles CAVANIOL, Danilo MADDALO, Luc CABEL, Fatima MECHTA-GRIGORIOU, Claire WILHELM, Gérard ZALCMAN, Maria Carla PARRINI et Stéphanie DESCROIX. « Bridging the gap between tumor-on-chip and clinics : a systematic review of 15 years of studies ». *Lab on a Chip* 23.18 (2023), p. 3906-3935 (cf. p. 31).
- [Brábek, 2010] Jan BRÁBEK, Claudia T. MIERKE, Daniel RÖSEL, Pavel VESELÝ et Ben FABRY. « The role of the tissue microenvironment in the regulation of cancer cell motility and invasion ». *Cell Communication and Signaling* 8.1 (2010), p. 22 (cf. p. 33).
- [Braïni, 2018] Céline BRAÏNI, Angelo MOTTOLESE, Ivan FERRANTE, Sylvain MONNIER et Catherine VILLARD. « High-resolution volume imaging of neurons by the use of fluorescence exclusion method and dedicated microfluidic devices ». *Journal of Visualized Experiments* 2018.133 (2018), p. 1-10 (cf. p. 86).
- [Brás, 2022] M. Manuela BRÁS, Tânia B. CRUZ, André F. MAIA, Maria José OLIVEIRA, Susana R. SOUSA, Pedro L. GRANJA et Manfred RADMACHER. « Mechanical Properties of Colorectal Cancer Cells Determined by Dynamic Atomic Force Microscopy : A Novel Biomarker ». *Cancers* 14.20 (2022), p. 5053 (cf. p. 88, 154).
- [Brau, 2011] Fabian BRAU, Hugues VANDEPARRE, Abbas SABBAAH, Christophe POULARD, Arezki BOUDAOUZ et Pascal DAMMAN. « Multiple-length-scale elastic instability mimics parametric resonance of nonlinear oscillators ». *Nature Physics* 7.1 (2011), p. 56-60. arXiv : 1006.2404 (cf. p. 4).
- [Byun, 2013] Sangwon BYUN, Sungmin SON, Dario AMODEI, Nathan CERMAK, Josephine SHAW, Joon Ho KANG, Vivian C. HECHT, Monte M. WINSLOW, Tyler JACKS, Parag MALLICK et Scott R. MANALIS. « Characterizing deformability and surface friction of cancer cells ». *Proceedings of the National Academy of Sciences of the United States of America* 110.19 (2013), p. 7580-7585 (cf. p. 37, 38, 91, 98, 159, 161).
- [Cadart, 2017] Clotilde CADART, E. ZLOTEK-ZLOTKIEWICZ, L. VENKOVA, O. THOUVENIN, V. RACINE, M. LE BERRE, Sylvain MONNIER et Matthieu PIEL. *Fluorescence eXclusion Measurement of volume in live cells*. T. 139. Elsevier Ltd, 2017, p. 103-120 (cf. p. 86).

- [Cameron, 2000] M. Dianne CAMERON, Eric E. SCHMIDT, Nancy KERKVLIT, Kishore V. NADKARNI, Vincent L. MORRIS, Alan C. GROOM, Ann F. CHAMBERS et Ian C. MACDONALD. « Temporal progression of metastasis in lung : cell survival, dormancy, and location dependence of metastatic inefficiency. » *Cancer research* 60.9 (2000), p. 2541-6 (cf. p. 21).
- [Cayrefourcq, 2015] Laure CAYREFOURCQ, Thibault MAZARD, Simon JOOSSE, Jérôme SOLASSOL, Jeanne RAMOS, Eric ASSENAT, Udo SCHUMACHER, Valérie COSTES, Thierry MAUDELONDE, Klaus PANTEL et Catherine ALIX-PANABIÈRES. « Establishment and characterization of a cell line from human Circulating colon cancer cells ». *Cancer Research* 75.5 (2015), p. 892-901 (cf. p. 28, 71, 144, 156, 163).
- [Chaffer, 2011] Christine L. CHAFFER et Robert A. WEINBERG. « A Perspective on Cancer Cell Metastasis ». *Science* 331.6024 (2011), p. 1559-1564 (cf. p. 18).
- [Charafe-Jauffret, 2013] Emmanuelle CHARAFE-JAUFFRET, Christophe GINESTIER, François BERTUCCI, Olivier CABAUD, Julien WICINSKI, Pascal FINETTI, Emmanuelle JOSSELIN, José ADELAIDE, Tien-Tuan NGUYEN, Florence MONVILLE, Jocelyne JACQUEMIER, Jeanne THOMASSIN-PIANA, Guillaume PINNA, Aurélie JALAGUIER, Eric LAMBAUDIE, Gilles HOUVENAEGHEL, Luc XERRI, Annick HAREL-BELLAN, Max CHAFFANET, Patrice VIENS et Daniel BIRNBAUM. « ALDH1-Positive Cancer Stem Cells Predict Engraftment of Primary Breast Tumors and Are Governed by a Common Stem Cell Program ». *Cancer Research* 73.24 (2013), p. 7290-7300 (cf. p. 156).
- [Chen, 2024] Jianfeng CHEN, Han LIU, Chuan LI, Xiaoxiao CHEN et Yichuan DAI. « Simulation of microfluidic intracellular delivery based on the synergy of cell squeezing and electrical field ». *Microfluidics and Nanofluidics* 28.1 (2024), p. 4 (cf. p. 84).
- [Chen, 2017] Michelle B. CHEN, Jordan A. WHISLER, Julia FRÖSE, Cathy YU, Yoojin SHIN et Roger D. KAMM. « On-chip human microvasculature assay for visualization and quantification of tumor cell extravasation dynamics ». *Nature Protocols* 12.5 (2017), p. 865-880 (cf. p. 136).
- [Chien, 1987] Shu CHIEN, Shubham MANIK, Lalit Mohan SAINI, Nikhil VADERA, V UPADHYAY, A K AGRAWAL et P N PANDEY. « A Mathematical Model on the Two Phase Renal Systolic Blood Flow in Arterioles with Special Reference to Diabetes ». *Ann. Rev. Physiol.* 6.1 (1987), p. 177-192 (cf. p. 24).
- [Choi, 2014] Sungyoung CHOI, Oren LEVY, Mónica B. COELHO, Joaquim M. S. CABRAL, Jeffrey M. KARP et Rohit KARNIK. « A cell rolling cytometer reveals the correlation between mesenchymal stem cell dynamic adhesion and differentiation state ». *Lab Chip* 14.1 (2014), p. 161-166 (cf. p. 27).
- [Cocoza, 2020] Federico COCOZZA, Eleonora GRISARD, Lorena MARTIN-JAULAR, Mathilde MATHIEU et Clotilde THÉRY. « SnapShot : Extracellular Vesicles ». *Cell* 182.1 (2020), 262-262.e1 (cf. p. 137).
- [Cox, 2019] Charles D. COX, Navid BAVI et Boris MARTINAC. « Biophysical Principles of Ion-Channel-Mediated Mechanosensory Transduction ». *Cell Reports* 29.1 (2019), p. 1-12 (cf. p. 7).
- [Cristofanilli, 2004] Massimo CRISTOFANILLI, G. Thomas BUDD, Matthew J. ELLIS, Alison STOPECK, Jeri MATEIRA, M. Craig MILLER, James M. REUBEN, Gerald V. DOYLE, W. Jeffrey ALLARD, Leon W.M.M. TERSTAPPEN et Daniel F. HAYES. « Circulating Tumor Cells, Disease Progression, and Survival in Metastatic Breast Cancer ». *New England Journal of Medicine* 351.8 (2004), p. 781-791 (cf. p. 27, 155).
- [Dahl, 2005] Kris Noel DAHL, Adam J. ENGLER, J. David PAJEROWSKI et Dennis E. DISCHER. « Power-Law Rheology of Isolated Nuclei with Deformation Mapping of Nuclear Substructures ». *Biophysical Journal* 89.4 (2005), p. 2855-2864 (cf. p. 115, 172).
- [Dahl, 2004] Kris Noel DAHL, Samuel M. KAHN, Katherine L. WILSON et Dennis E. DISCHER. « The nuclear envelope lamina network has elasticity and a compressibility limit suggestive of a molecular shock absorber ». *Journal of Cell Science* 117.20 (2004), p. 4779-4786 (cf. p. 3, 8, 93, 114, 154, 159).
- [Dai, 2017] Xiaofeng DAI, Hongye CHENG, Zhonghu BAI et Jia LI. « Breast Cancer Cell Line Classification and Its Relevance with Breast Tumor Subtyping ». *Journal of Cancer* 8.16 (2017), p. 3131-3141 (cf. p. 17, 88, 140).
- [Dash, 2022] Sanat Kumar DASH, Bamadeb PATRA, Vineeta SHARMA, Sarit K. DAS et Rama Shanker VERMA. « Fluid shear stress in a logarithmic microfluidic device enhances cancer cell stemness marker expression ». *Lab on a Chip* 22.11 (2022), p. 2200-2211 (cf. p. 25, 158).
- [Davidson, 2020] Patricia M DAVIDSON, Aude BATTISTELLA, Théophile DÉJARDIN, Timo BETZ, Julie PLASTINO, Nicolas BORGHI, Bruno CADOT et Cécile SYKES. « Nesprin-2 accumulates at the front of the nucleus during confined cell migration ». *EMBO reports* 21.7 (2020), p. 1-14 (cf. p. 34, 35, 161).
- [Davidson, 2019] Patricia M. DAVIDSON, Gregory R. FEDORCHAK, Solenne MONDÉSERT-DEVERAUX, Emily S. BELL, Philipp ISERMANN, Denis AUBRY, Rachele ALLENA et Jan LAMMERDING. « High-throughput microfluidic micropipette aspiration device to probe time-scale dependent nuclear mechanics in intact cells ». *Lab on a Chip* 19.21 (2019), p. 3652-3663 (cf. p. 11, 86, 99, 114).

- [Denais, 2016] Celine M DENAIS, Rachel M GILBERT, Philipp ISERMANN, Alexandra L. MCGREGOR, Mariska te LINDERT, Bettina WEIGELIN, Patricia M DAVIDSON, Peter FRIEDL, Katarina WOLF et Jan LAMMERDING. « Nuclear envelope rupture and repair during cancer cell migration ». *Science* 352.6283 (2016), p. 353-358 (cf. p. 112, 113).
- [Dogterom, 2019] Marileen DOGTEROM et Gijsje H. KOENDERINK. « Actin–microtubule crosstalk in cell biology ». *Nature Reviews Molecular Cell Biology* 20.1 (2019), p. 38-54 (cf. p. 6).
- [Doyle, 2019] Laura DOYLE et Michael WANG. « Overview of Extracellular Vesicles, Their Origin, Composition, Purpose, and Methods for Exosome Isolation and Analysis ». *Cells* 8.7 (2019), p. 727 (cf. p. 131).
- [Dujon, 2021] Antoine M. DUJON, Jean-Pascal CAPP, Joel S. BROWN, Pascal PUJOL, Robert A. GATENBY, Beata UJVARI, Catherine ALIX-PANABIÈRES et Frédéric THOMAS. « Is There One Key Step in the Metastatic Cascade? » *Cancers* 13.15 (2021), p. 3693 (cf. p. iv).
- [Dupire, 2020] Jules DUPIRE, Pierre Henri PUECH, Emmanuèle HELFER et Annie VIALLAT. « Mechanical adaptation of monocytes in model lung capillary networks ». *Proceedings of the National Academy of Sciences of the United States of America* 117.26 (2020), p. 14798-14804 (cf. p. 36, 91).
- [Dupont, 2011] Sirio DUPONT, Leonardo MORSUT, Mariaceleste ARAGONA, Elena ENZO, Stefano GIULITTI, Michelangelo CORDENONSI, Francesca ZANCONATO, Jimmy LE DIGABEL, Mattia FORCATO, Silvio BICCIATO, Nicola ELVASSORE et Stefano PICCOLO. « Role of YAP/TAZ in mechanotransduction ». *Nature* 474.7350 (2011), p. 179-183 (cf. p. 13).
- [Efremov, 2020] Yuri M. EFREMOV, Svetlana L. KOTOVA, Anastasia A. AKOVANTSEVA et Peter S. TIMASHEV. « Nanomechanical properties of enucleated cells : Contribution of the nucleus to the passive cell mechanics ». *Journal of Nanobiotechnology* 18.1 (2020), p. 1-11 (cf. p. 116).
- [Ellsworth, 1987] M. L. ELLSWORTH, A. LIU, B. DAWANT, A. S. POPEL et R. N. PITTMAN. « Analysis of vascular pattern and dimensions in arteriolar networks of the retractor muscle in young hamsters ». *Microvascular Research* 34.2 (1987), p. 168-183 (cf. p. 122).
- [Engler, 2006] Adam J. ENGLER, Shamik SEN, H. Lee SWEENEY et Dennis E. DISCHER. « Matrix Elasticity Directs Stem Cell Lineage Specification ». *Cell* 126.4 (2006), p. 677-689 (cf. p. 13).
- [Fabry, 2001] Ben FABRY, Geoffrey N. MAKSYM, James P. BUTLER, Michael GLOGAUER, Daniel NAVAJAS et Jeffrey J. FREDBERG. « Scaling the Microrheology of Living Cells ». *Physical Review Letters* 87 (14 2001), p. 148102 (cf. p. 172).
- [Fenech, 2019] Marianne FENECH, Vincent GIROD, Viviana CLAVERIA, Sebastien MEANCE, Manouk ABKARIAN et Benoit CHARLOT. « Microfluidic blood vasculature replicas using backside lithography ». *Lab on a Chip* 19.12 (2019), p. 2096-2106 (cf. p. 136).
- [Fidler, 1970] Isaiah J. FIDLER. « Metastasis : Quantitative Analysis of Distribution and Fate of Tumor Emboli Labeled ». *J Nat Cancer Inst* October (1970) (cf. p. 20, 121, 138).
- [Fidler, 2003] Isaiah J. FIDLER. « The pathogenesis of cancer metastasis : the 'seed and soil' hypothesis revisited ». *Nature Reviews Cancer* 3.6 (2003), p. 453-458 (cf. p. 18).
- [Fischer-Friedrich, 2014] Elisabeth FISCHER-FRIEDRICH, Anthony A. HYMAN, Frank JÜLICHER, Daniel J. MÜLLER et Jonne HELENIUS. « Quantification of surface tension and internal pressure generated by single mitotic cells ». *Scientific Reports* 4.1 (2014), p. 6213 (cf. p. 6).
- [Follain, 2020] Gautier FOLLAIN, David HERRMANN, Sébastien HARLEPP, Vincent HYENNE, Naël OSMANI, Sean C. WARREN, Paul TIMPSON et Jacky G. GOETZ. « Fluids and their mechanics in tumour transit : shaping metastasis ». *Nature Reviews Cancer* 20.2 (2020), p. 107-124 (cf. p. 15, 18, 20, 23, 123, 158, 159).
- [Follain, 2018] Gautier FOLLAIN, Naël OSMANI, Ana Sofia AZEVEDO, Guillaume ALLIO, Luc MERCIER, Mathia A. KARREMAN, Gergely SOLECKI, Maria Jesús GARCIA LEÓN, Olivier LEFEBVRE, Nina FEKONJA, Claudia HILLE, Vincent CHABANNES, Guillaume DOLLÉ, Thibaut METIVET, François Der HOVSEPIAN, Christophe PRUDHOMME, Angélique PICHOT, Nicodème PAUL, Raphaël CARAPITO, Siamak BAHRAM, Bernhard RUTHENSTEINER, André KEMMLING, Susanne SIEMONSEN, Tanja SCHNEIDER, Jens FIEHLER, Markus GLATZEL, Frank WINKLER, Yannick SCHWAB, Klaus PANTEL, Sébastien HARLEPP et Jacky G. GOETZ. « Hemodynamic Forces Tune the Arrest, Adhesion, and Extravasation of Circulating Tumor Cells ». *Developmental Cell* 45.1 (2018), 33-52.e12 (cf. p. 21).
- [Forsting, 2019] Johanna FORSTING, Julia KRAXNER, Hannes WITT, Andreas JANSHOFF et Sarah KÖSTER. « Vimentin Intermediate Filaments Undergo Irreversible Conformational Changes during Cyclic Loading ». *Nano Letters* 19.10 (2019), p. 7349-7356 (cf. p. 6).

- [Fregin, 2022] Bob FREGIN, Doreen BIEDENWEG et Oliver OTTO. « Interpretation of cell mechanical experiments in microfluidic systems depend on the choice of cellular shape descriptors ». *Biomicrofluidics* 16.2 (2022) (cf. p. 69).
- [Friedl, 2011a] Peter FRIEDL et Stephanie ALEXANDER. « Cancer Invasion and the Microenvironment : Plasticity and Reciprocity ». *Cell* 147.5 (2011), p. 992-1009 (cf. p. 156).
- [Friedl, 2011b] Peter FRIEDL, Katarina WOLF et Jan LAMMERDING. « Nuclear mechanics during cell migration ». *Current Opinion in Cell Biology* 23.1 (2011), p. 55-64 (cf. p. 33, 93, 99).
- [Fuh, 2021] Kenneth F. FUH, Robert D. SHEPHERD, Jessica S. WITHELL, Brayden K. KOOISTRA et Kristina D. RINKER. « Fluid flow exposure promotes epithelial-to-mesenchymal transition and adhesion of breast cancer cells to endothelial cells ». *Breast Cancer Research* 23.1 (2021), p. 97 (cf. p. 25, 138, 156).
- [Fuhs, 2022] Thomas FUHS, Franziska WETZEL, Anatol W. FRITSCH, Xinzhi LI, Roland STANGE, Steve PAWLIZAK, Tobias R. KIESSLING, Erik MORAWETZ, Steffen GROSSER, Frank SAUER, Jürgen LIPPOLDT, Frederic RENNER, Sabrina FRIEBE, Mareike ZINK, Klaus BENDRAT, Jürgen BRAUN, Maja H. OKTAY, John CONDEELIS, Susanne BRIEST, Benjamin WOLF, Lars-Christian HORN, Michael HÖCKEL, Bahriye AKTAS, M. Cristina MARCHETTI, M. Lisa MANNING, Axel NIENDORF, Dapeng BI et Josef A. KÄS. « Rigid tumours contain soft cancer cells ». *Nature Physics* 18 (12 2022), p. 1510-1519 (cf. p. iii, 12).
- [Gabriele, 2009] Sylvain GABRIELE, Anne-Marie BENOLIEL, Pierre BONGRAND et Olivier THÉODOLY. « Microfluidic Investigation Reveals Distinct Roles for Actin Cytoskeleton and Myosin II Activity in Capillary Leukocyte Trafficking ». *Biophysical Journal* 96.10 (2009), p. 4308-4318 (cf. p. 36, 86, 87, 91).
- [Ganesh, 2021] Karuna GANESH et Joan MASSAGUÉ. « Targeting metastatic cancer ». *Nature Medicine* 27.1 (2021), p. 34-44 (cf. p. 18).
- [García-Arcos, 2022] Juan Manuel GARCÍA-ARCOS, Johannes ZIEGLER, Silvia GRIGOLON, Loïc REYMOND, Gaurav SHAJEPAL, Cédric J. CATTIN, Alexis LOMAKIN, Daniel MULLER, Verena RUPRECHT, Stefan WIESER, Raphaël VOITURIEZ et Matthieu PIEL. « Advection percolation in the actomyosin cortex drives amoeboid cell motility ». *bioRxiv* (2022) (cf. p. 32).
- [Gauthier, 2012] Nils C. GAUTHIER, Thomas A. MASTERS et Michael P. SHEETZ. « Mechanical feedback between membrane tension and dynamics ». *Trends in Cell Biology* 22.10 (2012), p. 527-535 (cf. p. 7, 138).
- [Gerum, 2022] Richard GERUM, Elham MIRZAHOSSEIN, Mar EROLES, Jennifer ELSTERER, Astrid MAINKA, Andreas BAUER, Selina SONNTAG, Alexander WINTERL, Johannes BARTL, Lena FISCHER, Shada ABUHATTUM, Ruchi GOSWAMI, Salvatore GIRARDO, Jochen GUCK, Stefan SCHRÜFER, Nadine STRÖHLEIN, Mojtaba NOSRATLO, Harald HERRMANN, Dorothea SCHULTHEIS, Felix RICO, Sebastian Johannes MÜLLER, Stephan GEKLE et Ben FABRY. « Viscoelastic properties of suspended cells measured with shear flow deformation cytometry ». *eLife* 11 (2022), p. 1-26 (cf. p. 10, 172).
- [Ginestier, 2007] Christophe GINESTIER, Min Hee HUR, Emmanuelle CHARAFE-JAUFFRET, Florence MONVILLE, Julie DUTCHER, Marty BROWN, Jocelyne JACQUEMIER, Patrice VIENS, Celina G. KLEER, Suling LIU, Anne SCHOTT, Dan HAYES, Daniel BIRNBAUM, Max S. WICHA et Gabriela DONTU. « ALDH1 Is a Marker of Normal and Malignant Human Mammary Stem Cells and a Predictor of Poor Clinical Outcome ». *Cell Stem Cell* 1.5 (2007), p. 555-567 (cf. p. 156).
- [Gittes, 1993] F. GITTES, B. MICKEY, J. NETTLETON et J. HOWARD. « Flexural rigidity of microtubules and actin filaments measured from thermal fluctuations in shape. » *The Journal of cell biology* 120.4 (1993), p. 923-934 (cf. p. 8).
- [Giugliano, 2022] Federica GIUGLIANO, Chiara CORTI, Paolo TARANTINO, Flavia MICHELINI et Giuseppe CURIGLIANO. « Bystander effect of antibody–drug conjugates : fact or fiction ? » *Current Oncology Reports* 24.7 (2022), p. 809-817 (cf. p. 157).
- [Gkretsi, 2018] Vasiliki GKRETSI et Triantafyllos STYLIANOPOULOS. « Cell adhesion and matrix stiffness : Coordinating cancer cell invasion and metastasis ». *Frontiers in Oncology* 8.MAY (2018) (cf. p. iii, 14).
- [Goh, 2020] Chia Yin GOH, Cathy WYSE, Matthew HO, Ellen O'BEIRNE, Jane HOWARD, Sinéad LINDSAY, Pamela KELLY, Michaela HIGGINS et Amanda MCCANN. « Exosomes in triple negative breast cancer : Garbage disposals or Trojan horses ? » *Cancer Letters* 473.November 2019 (2020), p. 90-97 (cf. p. 137, 166).
- [Gold, 1990] R. H. GOLD, L. W. BASSETT et B. E. WIDOFF. « Highlights from the history of mammography. » *RadioGraphics* 10.6 (1990), p. 1111-1131 (cf. p. iii).
- [Green, 2015] Toni M. GREEN, Mary L. ALPAUGH, Sanford H. BARSKY, Germana RAPPA et Aurelio LORICO. « Breast Cancer-Derived Extracellular Vesicles : Characterization and Contribution to the Metastatic Phenotype ». *BioMed Research International* 2015 (2015), p. 1-13 (cf. p. 137, 166).

- [Guck, 2005] Jochen GUCK, Stefan SCHINKINGER, Bryan LINCOLN, Falk WOTTAWAH, Susanne EBERT, Maren ROMEYKE, Dominik LENZ, Harold M. ERICKSON, Revathi ANANTHAKRISHNAN, Daniel MITCHELL, Josef KAS, Sydney ULVICK et Curt BILBY. « Optical deformability as an inherent cell marker for testing malignant transformation and metastatic competence ». *Biophysical Journal* 88.5 (2005), p. 3689-3698 (cf. p. 9, 11, 12, 41, 88, 159).
- [Guilak, 2000] Farshid GUILAK, John R. TEDROW et Rainer BURBKART. « Viscoelastic properties of the cell nucleus ». *Biochemical and Biophysical Research Communications* 269.3 (2000), p. 781-786 (cf. p. 12, 114).
- [Guillou, 2016a] Lionel GUILLOU, Avin BABATAHERI, Michael SAITAKIS, Armelle BOHINEUST, Stéphanie DOGNI-AUX, Claire HIVROZ, Abdul I. BARAKAT et Julien HUSSON. « T-lymphocyte passive deformation is controlled by unfolding of membrane surface reservoirs ». *Molecular Biology of the Cell* 27.22 (2016). Sous la dir. de Patricia BASSEREAU, p. 3574-3582 (cf. p. 7).
- [Guillou, 2016b] Lionel GUILLOU, Joanna B. DAHL, Jung-Ming G. LIN, Abdul I. BARAKAT, Julien HUSSON, Susan J. MULLER et Sanjay KUMAR. « Measuring Cell Viscoelastic Properties Using a Microfluidic Extensional Flow Device ». *Biophysical Journal* 111.9 (2016), p. 2039-2050 (cf. p. 10).
- [Guimarães, 2020] Carlos F. GUIMARÃES, Luca GASPERINI, Alexandra P. MARQUES et Rui L. REIS. « The stiffness of living tissues and its implications for tissue engineering ». *Nature Reviews Materials* 5.5 (2020), p. 351-370 (cf. p. 13).
- [Gundersen, 2013] Gregg G. GUNDERSEN et Howard J. WORMAN. « Nuclear Positioning ». *Cell* 152.6 (2013), p. 1376-1389 (cf. p. 99).
- [Hanahan, 2022] Douglas HANAHAN. « Hallmarks of Cancer : New Dimensions ». *Cancer Discovery* 12.1 (2022), p. 31-46 (cf. p. 15).
- [Hanahan, 2011] Douglas HANAHAN et Robert A. WEINBERG. « Hallmarks of Cancer : The Next Generation ». *Cell* 144.5 (2011), p. 646-674 (cf. p. 15).
- [Hapach, 2021] Lauren A. HAPACH, Shawn P. CAREY, Samantha C. SCHWAGER, Paul V. TAUFALLELE, Wenjun WANG, Jenna A. MOSIER, Nerymar ORTIZ-OTERO, Tanner J. MCARDLE, Zachary E. GOLDBLATT, Marsha C. LAMPI, Francois BORDELEAU, Jocelyn R. MARSHALL, Isaac M. RICHARDSON, Jiahe LI, Michael R. KING et Cynthia A. REINHART-KING. « Phenotypic Heterogeneity and Metastasis of Breast Cancer Cells ». *Cancer Research* 81.13 (2021), p. 3649-3663 (cf. p. 34, 35).
- [Harbeck, 2019] Nadia HARBECK, Frédérique PENAULT-LLORCA, Javier CORTES, Michael GNANT, Nehmat HOUS-SAMI, Philip POORTMANS, Kathryn RUDDY, Janice TSANG et Fatima CARDOSO. « Breast cancer ». *Nature Reviews Disease Primers* 5.1 (2019), p. 66 (cf. p. 18).
- [Hassell, 2017] Bryan A. HASSELL, Girija GOYAL, Esak LEE, Alexandra SONTHEIMER-PHELPS, Oren LEVY, Christopher S. CHEN et Donald E. INGBER. « Human Organ Chip Models Recapitulate Orthotopic Lung Cancer Growth, Therapeutic Responses, and Tumor Dormancy In Vitro ». *Cell Reports* 21.2 (2017), p. 508-516 (cf. p. 30, 31).
- [Helvert, 2018] Sjoerd van HELVERT, Cornelis STORM et Peter FRIEDL. « Mechanoreciprocity in cell migration ». *Nature Cell Biology* 20.1 (2018), p. 8-20 (cf. p. 13).
- [Hochmuth, 2000] Robert M. HOCHMUTH. « Micropipette aspiration of living cells ». *Journal of Biomechanics* 33.1 (2000), p. 15-22 (cf. p. 6, 8, 90).
- [Hogan, 2015] Brenna HOGAN, Avin BABATAHERI, Yongyun HWANG, Abdul I. BARAKAT et Julien HUSSON. « Characterizing Cell Adhesion by Using Micropipette Aspiration ». *Biophysical Journal* 109.2 (2015), p. 209-219 (cf. p. 8).
- [Hosseini, 2022] Kamran HOSSEINI, Palina TRUS, Annika FRENZEL, Carsten WERNER et Elisabeth FISCHER-FRIEDRICH. « Skin epithelial cells change their mechanics and proliferation upon snail-mediated EMT signaling ». *Soft Matter* 18.13 (2022), p. 2585-2596 (cf. p. 10).
- [Hou, 2009] H. W. HOU, Q. S. LI, G. Y. H. LEE, A. P. KUMAR, C. N. ONG et C. T. LIM. « Deformability study of breast cancer cells using microfluidics ». *Biomedical Microdevices* 11.3 (2009), p. 557-564 (cf. p. 37, 41, 161).
- [Hu, 2017] Shuhuan HU et Raymond H. W. LAM. « Characterization of viscoelastic properties of normal and cancerous human breast cells using a confining microchannel ». *Microfluidics and Nanofluidics* 21.4 (2017), p. 68 (cf. p. 11, 41, 91, 159).
- [Hu, 2018] Shuhuan HU, Ran WANG, Chi Man TSANG, Sai Wah TSAO, Dong SUN et Raymond H.W. LAM. « Revealing elasticity of largely deformed cells flowing along confining microchannels ». *RSC Advances* 8.2 (2018), p. 1030-1038 (cf. p. 92).

- [Huang, 1996] W. HUANG, R. T. YEN, M. MCLAURINE et G. BLEDSOE. « Morphometry of the human pulmonary vasculature ». *Journal of Applied Physiology* 81.5 (1996), p. 2123-2133 (cf. p. 122).
- [Huang, 2015] Xuanzhang HUANG, Peng GAO, Yongxi SONG, Jingxu SUN, Xiaowan CHEN, Junhua ZHAO, Hui-mian XU et Zhenning WANG. « Meta-analysis of the prognostic value of circulating tumor cells detected with the CellSearch System in colorectal cancer ». *BMC Cancer* 15.1 (2015) (cf. p. 27).
- [Huh, 2010] Dongeun HUH, Benjamin D. MATTHEWS, Akiko MAMMOTO, Martin MONTOYA-ZAVALA, Hong YUAN HSIN et Donald E. INGBER. « Reconstituting organ-level lung functions on a chip ». *Science* 328.5986 (2010), p. 1662-1668 (cf. p. 31).
- [Husson, 2023] Julien HUSSON. « Measuring Cell Mechanical Properties Using Microindentation ». 2023, p. 3-23 (cf. p. 8).
- [Iwai, 2002] Yoshiko IWAI, Masayoshi ISHIDA, Yoshimasa TANAKA, Taku OKAZAKI, Tasuku HONJO et Nagahiro MINATO. « Involvement of PD-L1 on tumor cells in the escape from host immune system and tumor immunotherapy by PD-L1 blockade ». *Proceedings of the National Academy of Sciences* 99.19 (2002), p. 12293-12297 (cf. p. 157).
- [Janmey, 2007] Paul A. JANMEY, Penelope C. GEORGES et Søren HVIDT. « Basic Rheology for Biologists ». *Methods in Cell Biology* 83 (2007) (cf. p. 2, 169).
- [Jebane, 2023] Cécile JEBANE, Alice Anaïs VARLET, Marc KARNAT, Lucero M. HERNANDEZ- CEDILLO, Amélie LECCHI, Frédéric BEDU, Camille DESGROUAS, Corinne VIGOUROUX, Marie Christine VANTYGHM, Annie VIALLAT, Jean François RUPPRECHT, Emmanuèle HELFER et Catherine BADENS. « Enhanced cell viscosity : A new phenotype associated with lamin A/C alterations ». *iScience* 26.10 (2023) (cf. p. 35, 36, 86, 91, 114, 115).
- [Jiang, 2023] Kuan JIANG, Su Bin LIM, Jingwei XIAO, Doorgesh Sharma JOKHUN, Menglin SHANG, Xiao SONG, Pan ZHANG, Lanfeng LIANG, Boon Chuan LOW, G.V. SHIVASHANKAR et Chwee Teck LIM. « Deleterious Mechanical Deformation Selects Mechanoresilient Cancer Cells with Enhanced Proliferation and Chemoresistance ». *Advanced Science* 10.22 (2023), p. 1-15 (cf. p. 30, 121, 137).
- [Kassab, 1994] G. S. KASSAB, D. H. LIN et Y. C.B. FUNG. « Morphometry of pig coronary venous system ». *American Journal of Physiology - Heart and Circulatory Physiology* 267.6 36-6 (1994) (cf. p. 122).
- [Kast, 2015] Karin KAST, Theresa LINK, Katrin FRIEDRICH, Andrea PETZOLD, Antje NIEDOSTATEK, Olaf SCHOFFER, Carmen WERNER, Stefanie J. KLUG, Andreas WERNER, Axel GATZWEILER, Barbara RICHTER, Gustavo BARETTON et Pauline WIMBERGER. « Impact of breast cancer subtypes and patterns of metastasis on outcome ». *Breast Cancer Research and Treatment* 150.3 (2015), p. 621-629 (cf. p. 16, 155, 165).
- [Katara, 2018] Gajendra K. KATARA, Arpita KULSHRESTHA, Liqun MAO, Xin WANG, Manoranjan SAHOO, Safaa IBRAHIM, Sahithi PAMARTHY, Kimiko SUZUE, Gajendra S. SHEKHAWAT, Alice GILMAN-SACHS et Kenneth D. BEAMAN. « Mammary epithelium-specific inactivation of V-ATPase reduces stiffness of extracellular matrix and enhances metastasis of breast cancer ». *Molecular Oncology* 12.2 (2018), p. 208-223 (cf. p. 14).
- [Keizer, 2022] Veer I. P. KEIZER, Simon GROSSE-HOLZ, Maxime WORINGER, Laura ZAMBON, Koceila AIZEL, Maud BONGAERTS, Fanny DELILLE, Lorena KOLAR-ZNIKA, Vittore F. SCOLARI, Sebastian HOFFMANN, Edward J. BANIGAN, Leonid A. MIRNY, Maxime DAHAN, Daniele FACHINETTI et Antoine COULON. « Live-cell micro-manipulation of a genomic locus reveals interphase chromatin mechanics ». *Science* 377.6605 (2022), p. 489-495 (cf. p. 3).
- [Keller, 2019] Laura KELLER et Klaus PANTEL. « Unravelling tumour heterogeneity by single-cell profiling of circulating tumour cells ». *Nature Reviews Cancer* 19.10 (2019), p. 553-567 (cf. p. 25).
- [Khan, 2013] Z. S. KHAN et S. A. VANAPALLI. « Probing the mechanical properties of brain cancer cells using a microfluidic cell squeezer device ». *Biomicrofluidics* 7.1 (2013), p. 1-15 (cf. p. 37).
- [Koch, 2020] Claudia KOCH, Andra KUSKE, Simon A JOOSSE, Gökhan YIGIT, George SFLOMOS, Sonja THALER, Daniel J SMIT, Stefan WERNER, Kerstin BORGMANN, Sebastian GÄRTNER, Parinaz MOSSAHEBI MOHAMMADI, Laura BATTISTA, Laure CAYREFOURCQ, Janine ALTMÜLLER, Gabriela SALINAS-RIESTER, Kaamini RAITHATHA, Arne ZIBAT, Yvonne GOY, Leonie OTT, Kai BARTKOWIAK, Tuan Zea TAN, Qing ZHOU, Michael R SPEICHER, Volkmar MÜLLER, Tobias M GORGES, Manfred JÜCKER, Jean-Paul THIERY, Cathrin BRISKEN, Sabine RIETHDORF, Catherine ALIX-PANABIÈRES et Klaus PANTEL. « Characterization of circulating breast cancer cells with tumorigenic and metastatic capacity ». *EMBO Molecular Medicine* 12.9 (2020), p. 1-22 (cf. p. 28, 156).
- [Kollmannsberger, 2009] Philip KOLLMANNSBERGER et Ben FABRY. « Active soft glassy rheology of adherent cells ». *Soft Matter* 5.9 (2009), p. 1771 (cf. p. 89).
- [Kollmannsberger, 2011] Philip KOLLMANNSBERGER et Ben FABRY. « Linear and Nonlinear Rheology of Living Cells ». *Annual Review of Materials Research* 41.1 (2011), p. 75-97 (cf. p. 89, 172).

- [Kornfield, 2015] Tess E. KORNFIELD et Eric A. NEWMAN. « Measurement of retinal blood flow using fluorescently labeled red blood cells ». *eNeuro* 2.2 (2015), p. 1-13 (cf. p. 123).
- [Krebs, 2015] Matthew G. KREBS, Andrew G. RENEHAN, Alison BACKEN, Simon GOLLINS, Ian CHAU, Jurjees HASAN, Juan W. VALLE, Karen MORRIS, Janette BEECH, Linda ASHCROFT, Mark P. SAUNDERS et Caroline DIVE. « Circulating tumor cell enumeration in a phase II trial of a four-drug regimen in advanced colorectal cancer ». *Clinical Colorectal Cancer* 14.2 (2015), 115-122.e2 (cf. p. 28).
- [Krog, 2018] Benjamin L. KROG et Michael D. HENRY. « Biomechanics of the Circulating Tumor Cell Microenvironment ». *Adv Exp Med Biol.* T. 1092. 2018, p. 209-233 (cf. p. 21, 23).
- [Kumar, 2014] Amit KUMAR, Michele MAZZANTI, Martin MISTRİK, Martin KOSAR, Galina V. BEZNOUSSENKO, Alexandre A. MIRONOV, Massimiliano GARRÈ, Dario PARAZZOLI, G.V. SHIVASHANKAR, Giorgio SCITA, Jiri BARTEK et Marco FOIANI. « ATR Mediates a Checkpoint at the Nuclear Envelope in Response to Mechanical Stress ». *Cell* 158.3 (2014), p. 633-646 (cf. p. 33).
- [Kumar, 2022] Jyotish KUMAR, Soumyadeep BASAK, Ashish KALKAL et Gopinath PACKIRISAMY. « Recent advances in nanotechnology and microfluidic-based approaches for isolation and detection of circulating tumor cells (CTCs) ». *Nano-Structures & Nano-Objects* 31 (2022), p. 100886 (cf. p. 25, 26, 155).
- [Kurma, 2023] Keerthi KURMA et Catherine ALIX-PANABIÈRES. « Mechanobiology and survival strategies of circulating tumor cells : a process towards the invasive and metastatic phenotype ». *Frontiers in Cell and Developmental Biology* 11.May (2023), p. 1-15 (cf. p. 19).
- [Kusters, 2019] Remy KUSTERS, Camille SIMON, Rogério LOPES DOS SANTOS, Valentina CAORSI, Sangsong WU, Jean-Francois JOANNY, Pierre SENS et Cecile SYKES. « Actin shells control buckling and wrinkling of biomembranes ». *Soft Matter* 15.47 (2019), p. 9647-9653 (cf. p. 5).
- [Labelle, 2012] Myriam LABELLE et Richard O HYNES. « The Initial Hours of Metastasis : The Importance of Cooperative Host-Tumor Cell Interactions during Hematogenous Dissemination ». *Cancer Discovery* 2.12 (2012), p. 1091-1099 (cf. p. 20).
- [Lambert, 2017] Arthur W. LAMBERT, Diwakar R. PATTABIRAMAN et Robert A. WEINBERG. « Emerging Biological Principles of Metastasis ». *Cell* 168.4 (2017), p. 670-691 (cf. p. 18).
- [Lammerding, 2006] Jan LAMMERDING, Loren G. FONG, Julie Y. JI, Karen REUE, Colin L. STEWART, Stephen G. YOUNG et Richard T. LEE. « Lamins A and C but Not Lamin B1 Regulate Nuclear Mechanics ». *Journal of Biological Chemistry* 281.35 (2006), p. 25768-25780 (cf. p. 3, 106, 114, 159).
- [Lander, 2001] Eric S. LANDER, Lauren M. LINTON, Bruce BIRREN, Chad NUSBAUM, Michael C. ZODY, Jennifer BALDWIN et al. « Initial sequencing and analysis of the human genome ». *Nature* 409.6822 (2001), p. 860-921 (cf. p. 29).
- [Lange, 2015] Janina R. LANGE, Julian STEINWACHS, Thorsten KOLB, Lena A. LAUTSCHAM, Irina HARDER, Graeme WHYTE et Ben FABRY. « Microconstriction Arrays for High-Throughput Quantitative Measurements of Cell Mechanical Properties ». *Biophysical Journal* 109.1 (2015), p. 26-34 (cf. p. 172).
- [Lapi, 2007] D. LAPI, P. L. MARCHIAFAVA et A. COLANTUONI. « Geometric characteristics of arterial network of rat pial microcirculation ». *Journal of Vascular Research* 45.1 (2007), p. 69-77 (cf. p. 122).
- [Laplaud, 2021] Valentin LAPLAUD, Nicolas LEVERNIER, Judith PINEAU, Mabel SAN ROMAN, Lucie BARBIER, Pablo J. S EZ, Ana Maria LENNON-DUM NIL, Pablo VARGAS, Karsten KRUSE, Olivia Du ROURE, Matthieu PIEL et Julien HEUVINGH. « Pinching the cortex of live cells reveals thickness instabilities caused by myosin II motors ». *Science Advances* 7.27 (2021), p. 1-11 (cf. p. 10).
- [Le Berre, 2014] Maël LE BERRE, Ewa ZLOTEK-ZLOTKIEWICZ, Daria BONAZZI, Franziska LAUTENSCHLAEGER et Matthieu PIEL. « Methods for Two-Dimensional Cell Confinement ». *Methods in Cell Biology.* T. 121. 2014, p. 213-229 (cf. p. 32).
- [Lee, 2018] Yin Loon LEE et Brian BURKE. « LINC complexes and nuclear positioning ». *Seminars in Cell & Developmental Biology* 82 (2018), p. 67-76 (cf. p. 4).
- [Levental, 2009] Kandice R LEVENTAL, Hongmei YU, Laura KASS, Johnathon N LAKINS, Mikala EGEBLAD, Janine T ERLER, Sheri F.T. FONG, Katalin CSISZAR, Amato GIACCIA, Wolfgang WENINGER, Mitsuo YAMAUCHI, David L GASSER et Valerie M WEAVER. « Matrix Crosslinking Forces Tumor Progression by Enhancing Integrin Signaling ». *Cell* 139.5 (2009), p. 891-906 (cf. p. 14).
- [Lewinska, 2017] Anna LEWINSKA, Diana BEDNARZ, Jagoda ADAMCZYK-GROCHALA et Maciej WNUK. « Phytochemical-induced nucleolar stress results in the inhibition of breast cancer cell proliferation ». *Redox Biology* 12.March (2017), p. 469-482 (cf. p. 114).

- [Li, 2008] Q.S. LI, G.Y.H. LEE, C.N. ONG et C.T. LIM. « AFM indentation study of breast cancer cells ». *Biochemical and Biophysical Research Communications* 374.4 (2008), p. 609-613 (cf. p. 12).
- [Lim, 2006] C.T. LIM, E.H. ZHOU et S.T. QUEK. « Mechanical models for living cells—a review ». *Journal of Biomechanics* 39.2 (2006), p. 195-216 (cf. p. 2).
- [Liu, 2015] Yan-Jun LIU, Maël LE BERRE, Franziska LAUTENSCHLAEGER, Paolo MAIURI, Andrew CALLAN-JONES, Mélina HEUZÉ, Tohru TAKAKI, Raphaël VOITURIEZ et Matthieu PIEL. « Confinement and Low Adhesion Induce Fast Amoeboid Migration of Slow Mesenchymal Cells ». *Cell* 160.4 (2015), p. 659-672 (cf. p. 32, 33, 161).
- [Loconte, 2023] Luisa LOCONTE, Davinia ARGUEDAS, Rojbin EL, Alix ZHOU, Anna CHIPONT, Lea GUYONNET, Coralie GUERIN, Ester PIOVESANA, José Luis VÁZQUEZ-IBAR, Alain JOLIOT, Clotilde THÉRY et Lorena MARTÍN-JAULAR. « Detection of the interactions of tumour derived extracellular vesicles with immune cells is dependent on EV-labelling methods ». *Journal of Extracellular Vesicles* 12.12 (2023) (cf. p. 136).
- [Loibl, 2024] S. LOIBL, F. ANDRÉ, T. BACHELOT, C.H. BARRIOS, J. BERGH, H.J. BURSTEIN, M.J. CARDOSO, L.A. CAREY, S. DAWOOD, L. DEL MASTRO, C. DENKERT, E.M. FALLENBERG, P.A. FRANCIS, H. GAMAL-ELDIN, K. GELMON, C.E. GEYER, M. GNANT, V. GUARNERI, S. GUPTA, S.B. KIM, D. KRUG, M. MARTIN, I. MEATTINI, M. MORROW, W. JANNI, S. PALUCH-SHIMON, A. PARTRIDGE, P. POORTMANS, L. PUSZTAI, M.M. REGAN, J. SPARANO, T. SPANIC, S. SWAIN, S. TJULANDIN, M. TOI, D. TRAPANI, A. TUTT, B. XU, G. CURIGLIANO et N. HARBECK. « Early breast cancer : ESMO Clinical Practice Guideline for diagnosis, treatment and follow-up ». *Annals of Oncology* 35.2 (2024), p. 159-182 (cf. p. 16).
- [Lomakin, 2020] A. J. LOMAKIN, C. J. CATTIN, D. CUVELIER, Z. ALRAIES, M. MOLINA, G. P. F. NADER, N. SRIVASTAVA, P. J. SÁEZ, J. M. GARCIA-ARCOS, I. Y. ZHITNYAK, A. BHARGAVA, M. K. DRISCOLL, E. S. WELF, R. FIOKKA, R. J. PETRIE, N. S. DE SILVA, J. M. GONZÁLEZ-GRANADO, N. MANEL, A. M. LENNON-DUMÉNIL, D. J. MÜLLER et M. PIEL. « The nucleus acts as a ruler tailoring cell responses to spatial constraints ». *Science* 370.6514 (2020), eaba2894 (cf. p. 32, 33, 91, 114, 161).
- [Lombardi, 2011] Maria L. LOMBARDI, Diana E. JAALOUK, Catherine M. SHANAHAN, Brian BURKE, Kyle J. ROUX et Jan LAMMERDING. « The Interaction between Nesprins and Sun Proteins at the Nuclear Envelope Is Critical for Force Transmission between the Nucleus and Cytoskeleton ». *Journal of Biological Chemistry* 286.30 (2011), p. 26743-26753 (cf. p. 4).
- [Lorenz, 2019] Charlotta LORENZ, Johanna FORSTING, Anna V. SCHEPERS, Julia KRAXNER, Susanne BAUCH, Hannes WITT, Stefan KLUMPP et Sarah KÖSTER. « Lateral Subunit Coupling Determines Intermediate Filament Mechanics ». *Physical Review Letters* 123.18 (2019), p. 188102 (cf. p. 22).
- [Lusk, 2020] C. Patrick LUSK et Nicholas R. ADER. « CHMPions of repair : Emerging perspectives on sensing and repairing the nuclear envelope barrier ». *Current Opinion in Cell Biology* 64.4 (2020), p. 25-33 (cf. p. 112).
- [Luzzi, 1998] Keith J. LUZZI, Ian C. MACDONALD, Eric E. SCHMIDT, Nancy KERKVLIE, Vincent L. MORRIS, Ann F. CHAMBERS et Alan C. GROOM. « Multistep Nature of Metastatic Inefficiency ». *The American Journal of Pathology* 153.3 (1998), p. 865-873 (cf. p. 20, 21, 24).
- [Lv, 2021] Jiadi LV, Yaoping LIU, Feiran CHENG, Jiping LI, Yabo ZHOU, Tianzhen ZHANG, Nannan ZHOU, Cong LI, Zhenfeng WANG, Longfei MA, Mengyu LIU, Qiang ZHU, Xiaohan LIU, Ke TANG, Jingwei MA, Huafeng ZHANG, Jing XIE, Yi FANG, Haizeng ZHANG, Ning WANG, Yuying LIU et Bo HUANG. « Cell softness regulates tumorigenicity and stemness of cancer cells ». *The EMBO Journal* 40 (2 2021), p. 1-14 (cf. p. 158).
- [Ma, 2017] Shijun MA, Afu FU, Geraldine Giap Ying CHIEW et Kathy Qian LUO. « Hemodynamic shear stress stimulates migration and extravasation of tumor cells by elevating cellular oxidative level ». *Cancer Letters* 388 (2017), p. 239-248 (cf. p. 121, 137).
- [Ma, 2014] Yujie MA, Julian THIELE, Loai ABDELMOHSEN, Jinge XU et Wilhelm T. S. HUCK. « Biocompatible macro-initiators controlling radical retention in microfluidic on-chip photo-polymerization of water-in-oil emulsions ». *Chem. Commun.* 50.1 (2014), p. 112-114 (cf. p. 143).
- [MacDonald, 1995] I. C. MACDONALD, S. AHARINEJAD, E. E. SCHMIDT et A. C. GROOM. *Luminal constrictions due to endothelial cells in capillaries of mouse exocrine pancreas*. 1995 (cf. p. iv, 23, 24, 159, 160).
- [Malashicheva, 2021] Anna MALASHICHEVA et Kseniya PEREPHELINA. « Diversity of Nuclear Lamin A/C Action as a Key to Tissue-Specific Regulation of Cellular Identity in Health and Disease ». *Frontiers in Cell and Developmental Biology* 9.October (2021), p. 1-18 (cf. p. 2).
- [Mandal, 2016] Kalpana MANDAL, Atef ASNACIOS, Bruno GOUD et Jean-Baptiste MANNEVILLE. « Mapping intracellular mechanics on micropatterned substrates ». *Proceedings of the National Academy of Sciences* 113.46 (2016), E7159-E7168 (cf. p. 9, 11, 12, 159).

## References

---

- [Mathieu, 2019] Samuel MATHIEU et Jean Baptiste MANNEVILLE. « Intracellular mechanics : connecting rheology and mechanotransduction ». *Current Opinion in Cell Biology* 56 (2019), p. 34-44 (cf. p. 6).
- [McGregor, 2016] Alexandra Lynn MCGREGOR, Chieh-Ren HSIA et Jan LAMMERDING. « Squish and squeeze — the nucleus as a physical barrier during migration in confined environments ». *Current Opinion in Cell Biology* 40.1 (2016), p. 32-40 (cf. p. 33).
- [Meng, 2004] Songdong MENG, Debasish TRIPATHY, Eugene P. FRENKEL, Sanjay SHETE, Elizabeth Z. NAFTALIS, James F. HUTH, Peter D. BEITSCH, Marilyn LEITCH, Susan HOOVER, David EUHUS, Barbara HALEY, Larry MORRISON, Timothy P. FLEMING, Dorothee HERLYN, Leon W. M. M. TERSTAPPEN, Tanja FEHM, Thomas F. TUCKER, Nancy LANE, Jianqiang WANG et Jonathan W. UHR. « Circulating Tumor Cells in Patients with Breast Cancer Dormancy ». *Clinical Cancer Research* 10.24 (2004), p. 8152-8162 (cf. p. 20, 121).
- [Miller, 2018] M. Craig MILLER, Peggy S. ROBINSON, Christopher WAGNER et Daniel J. O'SHANNESY. « The Parsortix™ Cell Separation System—A versatile liquid biopsy platform ». *Cytometry Part A* 93.12 (2018), p. 1234-1239 (cf. p. 26, 27).
- [Mitrossilis, 2010] Démosthène MITROSSILIS, Jonathan FOUCHARD, David PEREIRA, François POSTIC, Alain RICHERT, Michel SAINT-JEAN et Atef ASNACIOS. « Real-time single-cell response to stiffness ». *Proceedings of the National Academy of Sciences* 107.38 (2010), p. 16518-16523 (cf. p. 10).
- [Moeendarbary, 2013] Emad MOEENDARBARY, Léo VALON, Marco FRITZSCHE, Andrew R. HARRIS, Dale A. MOULDING, Adrian J. THRASHER, Eleanor STRIDE, L. MAHADEVAN et Guillaume T. CHARRAS. « The cytoplasm of living cells behaves as a poroelastic material ». *Nature Materials* 12.3 (2013), p. 253-261 (cf. p. 89).
- [Moore, 2023] Charles Paul MOORE, Julien HUSSON, Arezki BOUDAUD, Gabriel AMSELEM et Charles N. BAROUD. « Clogging of a Rectangular Slit by a Spherical Soft Particle ». *Physical Review Letters* 130.6 (2023), p. 064001 (cf. p. 85).
- [Morel, 2008] Anne-Pierre MOREL, Marjory LIÈVRE, Clémence THOMAS, George HINKAL, Stéphane ANSIEAU et Alain PUISIEUX. « Generation of Breast Cancer Stem Cells through Epithelial-Mesenchymal Transition ». *PLoS ONE* 3.8 (2008). Sous la dir. de Juha KLEFSTROM, e2888 (cf. p. 156).
- [Morgan, 2023] Eileen MORGAN, Melina ARNOLD, A. GINI, V. LORENZONI, C. J. CABASAG, Mathieu LAVERSANNE, Jerome VIGNAT, Jacques FERLAY, Neil MURPHY et Freddie BRAY. « Global burden of colorectal cancer in 2020 and 2040 : incidence and mortality estimates from GLOBOCAN ». *Gut* 72.2 (2023), p. 338-344 (cf. p. 17).
- [Morris, 2001] C.E. MORRIS et U. HOMANN. « Cell Surface Area Regulation and Membrane Tension ». *The Journal of Membrane Biology* 179.2 (2001), p. 79-102 (cf. p. 4, 6).
- [Müller, 2008] Bert MÜLLER, Sabrina LANG, Marco DOMINIETTO, Markus RUDIN, Georg SCHULZ, Hans DEYHLE, Marco GERMANN, Franz PFEIFFER, Christian DAVID et Timm WEITKAMP. « High-resolution tomographic imaging of microvessels ». *Developments in X-Ray Tomography VI*. Sous la dir. de Stuart R. STOCK. T. 7078. 2008. 2008, 70780B (cf. p. 23, 159).
- [Murrell, 2015] Michael MURRELL, Patrick W. OAKES, Martin LENZ et Margaret L. GARDEL. « Forcing cells into shape : the mechanics of actomyosin contractility ». *Nature Reviews Molecular Cell Biology* 16.8 (2015), p. 486-498 (cf. p. 5).
- [Nader, 2021a] Guilherme Pedreira de Freitas NADER, Sonia AGÜERA-GONZALEZ, Fiona ROUTET, Matthieu GRATIA, Mathieu MAURIN, Valeria CANCELILA, Clotilde CADART, Andrea PALAMIDESSI, Rodrigo Nalio RAMOS, Mabel SAN ROMAN, Matteo GENTILI, Ayako YAMADA, Alice WILLIART, Catalina LODILLINSKY, Emilie LAGOUTTE, Catherine VILLARD, Jean-Louis VIOVY, Claudio TRIPODO, Jérôme GALON, Giorgio SCITA, Nicolas MANEL, Philippe CHAVRIER et Matthieu PIEL. « Compromised nuclear envelope integrity drives TREX1-dependent DNA damage and tumor cell invasion ». *Cell* 184.20 (2021), 5230-5246.e22 (cf. p. 88, 93, 112).
- [Nader, 2021b] Guilherme Pedreira de Freitas NADER, Alice WILLIART et Matthieu PIEL. « Nuclear deformations, from signaling to perturbation and damage ». *Current Opinion in Cell Biology* 72 (2021), p. 137-145 (cf. p. 19, 31, 33, 112).
- [Najafi, 2019] Masoud NAJAFI, Bagher FARHOOD et Keywan MORTEZAEI. « Extracellular matrix (ECM) stiffness and degradation as cancer drivers ». *Journal of Cellular Biochemistry* 120.3 (2019), p. 2782-2790 (cf. p. 14).
- [Nassar, 2016] Dany NASSAR et Cédric BLANPAIN. « Cancer Stem Cells : Basic Concepts and Therapeutic Implications ». *Annual Review of Pathology : Mechanisms of Disease* 11.1 (2016), p. 47-76 (cf. p. 156).
- [Nath, 2019] Binita NATH, Anil P. BIDKAR, Vikash KUMAR, Amaresh DALAL, Mohit Kumar JOLLY, Siddhartha Sankar GHOSH et Gautam BISWAS. « Deciphering Hydrodynamic and Drug-Resistant Behaviors of Metastatic EMT Breast Cancer Cells Moving in a Constricted Microcapillary ». *Journal of Clinical Medicine* 8.8 (2019), p. 1194 (cf. p. 38).

- [Nath, 2018] Binita NATH, Asif RAZA, Vishal SETHI, Amaresh DALAL, Siddhartha Sankar GHOSH et Gautam BISWAS. « Understanding flow dynamics, viability and metastatic potency of cervical cancer (HeLa) cells through constricted microchannel ». *Scientific Reports* 8.1 (2018), p. 1-10 (cf. p. 37).
- [NCI, 2023] National Cancer Institute NCI. « Breast Cancer Treatment (PDQ) ». <https://www.cancer.gov/types/breast/patient/breast-treatment-pdq#section/all> (2023) (cf. p. 16).
- [Neelam, 2015] Srujana NEELAM, T. J. CHANCELLOR, Yuan LI, Jeffrey A. NICKERSON, Kyle J. ROUX, Richard B. DICKINSON et Tanmay P. LELE. « Direct force probe reveals the mechanics of nuclear homeostasis in the mammalian cell ». *Proceedings of the National Academy of Sciences of the United States of America* 112.18 (2015), p. 5720-5725 (cf. p. 114, 116).
- [Nematbakhsh, 2017] Yasaman NEMATBAKHS, Kuin Tian PANG et Chwee Teck LIM. « Correlating the viscoelasticity of breast cancer cells with their malignancy ». *Convergent Science Physical Oncology* 3.3 (2017), p. 034003 (cf. p. 9, 11, 12, 83, 159).
- [Normanno, 2017] Nicola NORMANNO, Marc G. DENIS, Kenneth S. THRESS, Marianne RATCLIFFE et Martin RECK. « Guide to detecting epidermal growth factor receptor ( EGFR ) mutations in ctDNA of patients with advanced non-small-cell lung cancer ». *Oncotarget* 8.7 (2017), p. 12501-12516 (cf. p. 155).
- [Olejarczyk, 2020] Wioletta OLEJARZ, Agnieszka DOMINIAK, Aleksandra ŻÓLNIEZAK, Grażyna KUBIAK-TOMASZEWSKA et Tomasz LORENC. « Tumor-Derived Exosomes in Immunosuppression and Immunotherapy ». *Journal of Immunology Research* 2020 (2020), p. 1-11 (cf. p. 137).
- [Omidvar, 2014] Ramin OMIDVAR, Mohammad TFAZZOLI-SHADPOUR, Mohammad Ali SHOKRGOZAR et Mostafa ROSTAMI. « Atomic force microscope-based single cell force spectroscopy of breast cancer cell lines : An approach for evaluating cellular invasion - Suppl.Infos ». *Journal of Biomechanics* 47.13 (2014), p. 3373-3379 (cf. p. 11, 12, 41, 83, 159).
- [Otsu, 1979] OTSU et N. « A threshold selection method from gray-level histograms ». *IEEE Transactions on Systems, Man and Cybernetics* 9.1 (1979), p. 62-66 (cf. p. 69, 152).
- [Otto, 2015] Oliver OTTO, Philipp ROSENDAHL, Alexander MIETKE, Stefan GOLFIER, Christoph HEROLD, Daniel KLAUE, Salvatore GIRARDO, Stefano PAGLIARA, Andrew EKPENYONG, Angela JACOBI, Manja WOBUS, Nicole TÖPFNER, Ulrich F. KEYSER, Jörg MANSFELD, Elisabeth FISCHER-FRIEDRICH et Jochen GUCK. « Real-time deformability cytometry : on-the-fly cell mechanical phenotyping ». *Nature Methods* 12.3 (2015), p. 199-202 (cf. p. 9, 10).
- [Pachenari, 2014] M. PACHENARI, S.M. SEYEDPOUR, M. JANMALEKI, S. Babazadeh SHAYAN, S. TARANEJOO et H. HOSSEINKHANI. « Mechanical properties of cancer cytoskeleton depend on actin filaments to microtubules content : Investigating different grades of colon cancer cell lines ». *Journal of Biomechanics* 47.2 (2014), p. 373-379 (cf. p. 12, 83, 88, 154).
- [Paget, 1889] S PAGET. « The distribution of secondary growths in cancer of the breast. 1889. » *Cancer metastasis reviews* 8.2 (1889), p. 98-101 (cf. p. 18).
- [Pajeroski, 2007] J. David PAJEROWSKI, Kris Noel DAHL, Franklin L. ZHONG, Paul J. SAMMAK et Dennis E. DISCHER. « Physical plasticity of the nucleus in stem cell differentiation ». *Proceedings of the National Academy of Sciences* 104.40 (2007), p. 15619-15624 (cf. p. 8, 9, 119).
- [Palmieri, 2015] V. PALMIERI, D. LUCCHETTI, A. MAIORANA, M. PAPI, G. MAULUCCI, F. CALAPÀ, G. CIASCA, R. GIORDANO, A. SGAMBATO et M. DE SPIRITO. « Mechanical and structural comparison between primary tumor and lymph node metastasis cells in colorectal cancer ». *Soft Matter* 11.28 (2015), p. 5719-5726 (cf. p. 88).
- [Paňková, 2010] K. PAŇKOVÁ, D. RÖSEL, M. NOVOTNÝ et Jan BRÁBEK. « The molecular mechanisms of transition between mesenchymal and amoeboid invasiveness in tumor cells ». *Cellular and Molecular Life Sciences* 67.1 (2010), p. 63-71 (cf. p. 20).
- [Pantel, 2016] K. PANTEL et M. R. SPEICHER. « The biology of circulating tumor cells ». *Oncogene* 35.10 (2016), p. 1216-1224 (cf. p. 156).
- [Pantel, 2019] Klaus PANTEL et Catherine ALIX-PANABIÈRES. « Liquid biopsy and minimal residual disease — latest advances and implications for cure ». *Nature Reviews Clinical Oncology* 16.7 (2019), p. 409-424 (cf. p. 25, 27).
- [Papaioannou, 2005] Theodors G. PAPAIOANNOU et Christodoulos STEFANADIS. « Vascular Wall Shear Stress : Basic Principles and Methods ». *Hellenic J Cardiol* 46 (2005), p. 9-15 (cf. p. 23).
- [Patteson, 2019] Alison E. PATTESON, Katarzyna POGODA, Fitzroy J. BYFIELD, Kalpana MANDAL, Zofia OSTROWSKA-PODHORODECKA, Elisabeth E. CHARRIER, Peter A. GALIE, Piotr DEPTUŁA, Robert BUCKI, Christopher A. MCCULLOCH et Paul A. JANMEY. « Loss of Vimentin Enhances Cell Motility through Small Confining Spaces ». *Small* 15.50 (2019), p. 1-10 (cf. p. 116).

## References

---

- [Patteson, 2020] Alison E. PATTESON, Amir VAHABIKASHI, Robert D. GOLDMAN et Paul A. JANMEY. « Mechanical and Non-Mechanical Functions of Filamentous and Non-Filamentous Vimentin ». *BioEssays* 42.11 (2020), p. 1-12 (cf. p. 5, 160).
- [Perea Paizal, 2021] Julia PEREA PAIZAL, Sam H. AU et Chris BAKAL. « Squeezing through the microcirculation : survival adaptations of circulating tumour cells to seed metastasis ». *British Journal of Cancer* 124.1 (2021), p. 58-65 (cf. p. 24, 158, 160).
- [Pinon, 2024] Léa PINON, Mélanie CHABAUD, Pierre NIVOIT, Jérôme WONG-NG, Tri Tho NGUYEN, Vanessa PAUL, Sylvie GOUSSARD, Emmanuel FRACHON, Dorian OBINO, Samy GOBAA et Guillaume DUMÉNIL. « Infection-on-Chip : an in vitro human vessel to study *Neisseria meningitidis* colonization 2 and vascular damages ». *bioRxiv* (2024) (cf. p. 136).
- [Pinon, 2022] Léa PINON, Nicolas RUYSSSEN, Judith PINEAU, Olivier MESDJIAN, Damien CUVELIER, Anna CHIPONT, Rachele ALLENA, Coralie L. GUERIN, Sophie ASNACIOS, Atef ASNACIOS, Paolo PIEROBON et Jacques FATTACCIOLI. « Phenotyping polarization dynamics of immune cells using a lipid droplet-cell pairing microfluidic platform ». *Cell Reports Methods* 2.11 (2022), p. 100335 (cf. p. 118).
- [Plodinec, 2012] Marija PLODINEC, Marko LOPARIC, Christophe A. MONNIER, Ellen C. OBERMANN, Rosanna ZANETTI-DALLENBACH, Philipp OERTLE, Janne T. HYOTYLA, Ueli AEBI, Mohamed BENTIREN-ALJ, Roderick Y. H. LIM et Cora-Ann SCHOENENBERGER. « The nanomechanical signature of breast cancer ». *Nature Nanotechnology* 7.11 (2012), p. 757-765 (cf. p. 12).
- [Prabhune, 2012] Meenakshi PRABHUNE, Gazanfer BELGE, Andreas DOTZAUER, Jörn BULLERDIEK et Manfred RADMACHER. « Comparison of mechanical properties of normal and malignant thyroid cells ». *Micron* 43.12 (2012), p. 1267-1272 (cf. p. 12).
- [Preira, 2013] Pascal PREIRA, Marie-Pierre VALIGNAT, José BICO et Olivier THÉODOLY. « Single cell rheometry with a microfluidic constriction : Quantitative control of friction and fluid leaks between cell and channel walls ». *Biomicrofluidics* 7.2 (2013), p. 024111 (cf. p. 85).
- [Raab, 2016] Matthew RAAB, Matteo GENTILI, H. DE BELLY, Hawa-Racine THIAM, Pablo VARGAS, A. J. JIMENEZ, F. LAUTENSCHLAEGER, Raphaël VOITURIEZ, Ana María LENNON-DUMÉNIL, Nicolas MANEL et Matthieu PIEL. « ESCRT III repairs nuclear envelope ruptures during cell migration to limit DNA damage and cell death ». *Science* 352.6283 (2016), p. 359-362 (cf. p. 34, 35, 112, 135, 161).
- [Rak, 2012] Janusz RAK et Abhijit GUHA. « Extracellular vesicles – vehicles that spread cancer genes ». *BioEssays* 34.6 (2012), p. 489-497 (cf. p. 131).
- [Regmi, 2017] Sagar REGMI, Afu FU et Kathy Qian LUO. « High Shear Stresses under Exercise Condition Destroy Circulating Tumor Cells in a Microfluidic System ». *Scientific Reports* 7.August 2016 (2017), p. 1-12 (cf. p. 25, 121, 137, 138, 161).
- [Regmi, 2018] Sagar REGMI, To Sing FUNG, Sierin LIM et Kathy Qian LUO. « Fluidic shear stress increases the anti-cancer effects of ROS-generating drugs in circulating tumor cells ». *Breast Cancer Research and Treatment* 172.2 (2018), p. 297-312 (cf. p. 139).
- [Remmerbach, 2009] Torsten W. REMMERBACH, Falk WOTTAWAH, Julia DIETRICH, Bryan LINCOLN, Christian WITTEKIND et Jochen GUCK. « Oral Cancer Diagnosis by Mechanical Phenotyping ». *Cancer Research* 69.5 (2009), p. 1728-1732 (cf. p. 12).
- [Ricci-Vitiani, 2007] Lucia RICCI-VITIANI, Dario G. LOMBARDI, Emanuela PILOZZI, Mauro BIFFONI, Matilde TODARO, Cesare PESCHLE et Ruggero DE MARIA. « Identification and expansion of human colon-cancer-initiating cells ». *Nature* 445.7123 (2007), p. 111-115 (cf. p. 156).
- [Riethdorf, 2007] Sabine RIETHDORF, Herbert FRITSCHKE, Volkmar MÜLLER, Thomas RAU, Christian SCHINDLBECK, Brigitte RACK, Wolfgang JANNI, Cornelia COITH, Katrin BECK, Fritz JÄNICKE, Summer JACKSON, Terrie GORNET, Massimo CRISTOFANILLI et Klaus PANTEL. « Detection of Circulating Tumor Cells in Peripheral Blood of Patients with Metastatic Breast Cancer : A Validation Study of the CellSearch System ». *Clinical Cancer Research* 13.3 (2007), p. 920-928 (cf. p. 26, 27).
- [Rizvi, 2013] Imran RIZVI, Umut A. GURKAN, Savas TASOGLU, Nermina ALAGIC, Jonathan P. CELLI, Lawrence B. MENSAH, Zhiming MAI, Utkan DEMIRCI et Tayyaba HASAN. « Flow induces epithelial-mesenchymal transition, cellular heterogeneity and biomarker modulation in 3D ovarian cancer nodules ». *Proceedings of the National Academy of Sciences* 110.22 (2013) (cf. p. 22).
- [Roh-Johnson, 2014] M ROH-JOHNSON, J J BRAVO-CORDERO, A PATSIALOU, V P SHARMA, P GUO, H LIU, L HODGSON et J CONDEELIS. « Macrophage contact induces RhoA GTPase signaling to trigger tumor cell intravasation ». *Oncogene* 33.33 (2014), p. 4203-4212 (cf. p. 20).

- [Rollin, 2023a] Romain ROLLIN. « Physical principles of size and density regulation in the cell and the cell nucleus ». Thèse de doct. 2023 (cf. p. 115).
- [Rollin, 2023b] Romain ROLLIN, Jean-François JOANNY et Pierre SENS. « Physical basis of the cell size scaling laws ». *eLife* 12 (2023), p. 1-43 (cf. p. 4).
- [Roy, 2021] Saynoi ROY, Raghava R. SUNKARA, Manan Y PARMAR, Saima SHAIKH et Sanjeev K. WAGHMARE. « EMT imparts cancer stemness and plasticity : new perspectives and therapeutic potential ». *Frontiers in Bioscience* 26.2 (2021), p. 4892 (cf. p. 156).
- [Sanger, 1977] F. SANGER, S. NICKLEN et A. R. COULSON. « DNA sequencing with chain-terminating inhibitors ». *Proceedings of the National Academy of Sciences* 74.12 (1977), p. 5463-5467 (cf. p. 29).
- [Schaedel, 2015] Laura SCHAEDEL, Karin JOHN, Jeremie GAILLARD, Maxence V. NACHURY, Laurent BLANCHOIN et Manuel THERY. « Microtubules self-repair in response to mechanical stress ». *Nature Materials* 14.11 (2015), p. 1156-1163 (cf. p. 6).
- [Schaedel, 2021] Laura SCHAEDEL, Charlotta LORENZ, Anna V. SCHEPERS, Stefan KLUMPP et Sarah KÖSTER. « Vimentin intermediate filaments stabilize dynamic microtubules by direct interactions ». *Nature Communications* 12.1 (2021) (cf. p. 6).
- [Senigagliaesi, 2022a] Beatrice SENIGAGLIESI, Diana E. BEDOLLA, Giovanni BIRARDA, Michele ZANETTI, Marco LAZZARINO, Lisa VACCARI, Pietro PARISSÉ et Loredana CASALIS. « Subcellular elements responsive to the biomechanical activity of triple-negative breast cancer-derived small extracellular vesicles ». *Biomolecular Concepts* 13.1 (2022), p. 322-333 (cf. p. 137).
- [Senigagliaesi, 2022b] Beatrice SENIGAGLIESI, Giuseppe SAMPERI, Nicola CEFARIN, Luciana GNEO, Sara PETROSI-NO, Mattia APOLLONIO, Federica CAPONNETTO, Riccardo SGARRA, Licio COLLAVIN, Daniela CESSSELLI, Loredana CASALIS et Pietro PARISSÉ. « Triple negative breast cancer-derived small extracellular vesicles as modulator of biomechanics in target cells ». *Nanomedicine : Nanotechnology, Biology and Medicine* 44 (2022), p. 102582 (cf. p. 137, 155).
- [Shao, 2018] Huilin SHAO, Hyungsoon IM, Cesar M. CASTRO, Xandra BREAKEFIELD, Ralph WEISSLEDER et Hakho LEE. *New Technologies for Analysis of Extracellular Vesicles*. T. 118. 4. 2018, p. 1917-1950 (cf. p. 136).
- [Shaw Bagnall, 2015] Josephine SHAW BAGNALL, Sangwon BYUN, Shahinoor BEGUM, David T. MIYAMOTO, Vivian C. HECHT, Shyamala MAHESWARAN, Shannon L. STOTT, Mehmet TONER, Richard O. HYNES et Scott R. MANALIS. « Deformability of Tumor Cells versus Blood Cells ». *Scientific Reports* 5.1 (2015), p. 18542 (cf. p. 24).
- [Sheetz, 2019] Michael SHEETZ. « A tale of two states : Normal and transformed, with and without rigidity sensing ». *Annual Review of Cell and Developmental Biology* 35 (2019), p. 169-190 (cf. p. 14, 20).
- [Sinha, 2011] Bidisha SINHA, Darius KÖSTER, Richard RUEZ, Pauline GONNORD, Michele BASTIANI, Daniel ABANKWA, Radu V. STAN, Gillian BUTLER-BROWNE, Benoit VEDIE, Ludger JOHANNES, Nobuhiro MORONE, Robert G. PARTON, Graça RAPOSO, Pierre SENS, Christophe LAMAZE et Pierre NASSOY. « Cells Respond to Mechanical Stress by Rapid Disassembly of Caveolae ». *Cell* 144.3 (2011), p. 402-413 (cf. p. 7).
- [Slatko, 2018] Barton E. SLATKO, Andrew F. GARDNER et Frederick M. AUSUBEL. « Overview of Next-Generation Sequencing Technologies ». *Current Protocols in Molecular Biology* 122.1 (2018), p. 1-11 (cf. p. 30).
- [Soler, 2018] Alexandra SOLER, Laure CAYREFOURCQ, Thibault MAZARD, Anna BABAYAN, Pierre Jean LAMY, Said ASSOÛ, Eric ASSEMAT, Klaus PANTEL et Catherine ALIX-PANABIÈRES. « Autologous cell lines from circulating colon cancer cells captured from sequential liquid biopsies as model to study therapy-driven tumor changes ». *Scientific Reports* 8.1 (2018), p. 1-12 (cf. p. 71, 144).
- [Spector, 1989] Ilan SPECTOR, Nava R. SHOCHET, Dina BLASBERGER et Yoel KASHMAN. « Latrunculins—novel marine macrolides that disrupt microfilament organization and affect cell growth : I. Comparison with cytochalasin D ». *Cell Motility* 13.3 (1989), p. 127-144 (cf. p. 91).
- [Stephens, 2017] Andrew D. STEPHENS, Edward J. BANIGAN, Stephen A. ADAM, Robert D. GOLDMAN et John F. MARKO. « Chromatin and lamin A determine two different mechanical response regimes of the cell nucleus ». *Molecular Biology of the Cell* 28.14 (2017). Sous la dir. de Dunn ALEX R., p. 1984-1996 (cf. p. 3, 93, 115, 119, 159).
- [Stephens, 2019] Andrew D. STEPHENS, Patrick Z. LIU, Viswajit KANDULA, Haimei CHEN, Luay M. ALMASSALHA, Cameron HERMAN, Vadim BACKMAN, Thomas O'HALLORAN, Stephen A. ADAM, Robert D. GOLDMAN, Edward J. BANIGAN et John F. MARKO. « Physicochemical mechanotransduction alters nuclear shape and mechanics via heterochromatin formation ». *Molecular Biology of the Cell* 30.17 (2019), p. 2320-2330 (cf. p. 4).
- [Stewart, 2014] Bernard W. STEWART et Christopher P. WILD. *World Cancer Report 2014*. International Agency for Research on Cancer, 2014 (cf. p. 18).

- [Stott, 2010] Shannon L STOTT, Richard J LEE, Sunitha NAGRATH, Min YU, David T. MIYAMOTO, Lindsey ULKUS, Elizabeth J INSERRA, Matthew ULMAN, Simeon SPRINGER, Zev NAKAMURA, Alessandra L MOORE, Dina I TSUKROV, Maria E KEMPNER, Douglas M. DAHL, Chin-lee WU, A John IAFRATE, Matthew R SMITH, Ronald G TOMPKINS, Lecia V SEQUIST, Mehmet TONER, Daniel A HABER et Shyamala MAHESWARAN. « Isolation and Characterization of Circulating Tumor Cells from Patients with Localized and Metastatic Prostate Cancer ». *Science Translational Medicine* 2.25 (2010) (cf. p. 20, 121).
- [Sung, 2021] Hyuna SUNG, Jacques FERLAY, Rebecca L. SIEGEL, Mathieu LAVERSANNE, Isabelle SOERJOMATARAM, Ahmedin JEMAL et Freddie BRAY. « Global Cancer Statistics 2020 : GLOBOCAN Estimates of Incidence and Mortality Worldwide for 36 Cancers in 185 Countries ». *CA : A Cancer Journal for Clinicians* 71.3 (2021), p. 209-249 (cf. p. 14, 15).
- [Svitkina, 1996] Tatyana M. SVITKINA, Alexander B. VERKHOVSKY et Gary G BORISY. « Plectin sidearms mediate interaction of intermediate filaments with microtubules and other components of the cytoskeleton. » *The Journal of cell biology* 135.4 (1996), p. 991-1007 (cf. p. 6).
- [Swift, 2013] Joe SWIFT, Irena L. IVANOVSKA, Amnon BUXBOIM, Takamasa HARADA, P. C. Dave P. DINGAL, Joel PINTER, J. David PAJEROWSKI, Kyle R. SPINLER, Jae-Won SHIN, Manorama TEWARI, Florian REHFELDT, David W. SPEICHER et Dennis E. DISCHER. « Nuclear Lamin-A Scales with Tissue Stiffness and Enhances Matrix-Directed Differentiation ». *Science* 341.6149 (2013), p. 1358-1375. eprint : [NIHMS150003](#) (cf. p. 13, 119).
- [Sznurkowska, 2022] Magdalena K. SZNURKOWSKA et Nicola ACETO. « The gate to metastasis : key players in cancer cell intravasation ». *The FEBS Journal* 289.15 (2022), p. 4336-4354 (cf. p. 20).
- [Tabatabaei, 2019] Mohammad TABATABAEI, Mohammad TAFAZZOLI-SHADPOUR et Mohammad Mehdi KHANI. « Correlation of the cell mechanical behavior and quantified cytoskeletal parameters in normal and cancerous breast cell lines ». *Biorheology* 56.4 (2019), p. 207-219 (cf. p. 11, 83, 88, 159).
- [Tabatabaei, 2021] Mohammad TABATABAEI, Mohammad TAFAZZOLI-SHADPOUR et Mohammad Mehdi KHANI. « Altered mechanical properties of actin fibers due to breast cancer invasion : parameter identification based on micropipette aspiration and multiscale tensegrity modeling ». *Medical & Biological Engineering & Computing* 59.3 (2021), p. 547-560 (cf. p. 12).
- [Tabibzadeh, 2020] Alireza TABIBZADEH, Fahimeh Safarnezhad TAMESHKEL, Yousef MORADI, Saber SOLTANI, Maziar MORADI-LAKEH, G. Hossein ASHRAFI, Nima MOTAMED, Farhad ZAMANI, Seyed Abbas MOTEVALIAN, Mahshid PANAHI, Maryam ESGHAEI, Hossein AJDARKOSH, Alireza MOUSAVI-JARRAHI et Mohammad Hadi Karbalaie NIYA. « Signal transduction pathway mutations in gastrointestinal (GI) cancers : a systematic review and meta-analysis ». *Scientific Reports* 10.1 (2020), p. 18713 (cf. p. 17).
- [Tapley, 2013] Erin C TAPLEY et Daniel A STARR. « Connecting the nucleus to the cytoskeleton by SUN-KASH bridges across the nuclear envelope ». *Current Opinion in Cell Biology* 25.1 (2013), p. 57-62 (cf. p. 4).
- [Tatischeff, 2023] Irène TATISCHEFF. « Extracellular Vesicle-DNA : The Next Liquid Biopsy Biomarker for Early Cancer Diagnosis ? » *Cancers* 15.5 (2023), p. 1456 (cf. p. 131).
- [Teng, 2018] Yao TENG, Kui ZHU, Chunyang XIONG et Jianyong HUANG. « Electrodeformation-Based Biomechanical Chip for Quantifying Global Viscoelasticity of Cancer Cells Regulated by Cell Cycle ». *Analytical Chemistry* 90.14 (2018), p. 8370-8378 (cf. p. 12, 117).
- [Théry, 2018] Clotilde THÉRY, Kenneth W. WITWER, Elena AIKAWA, Maria Jose ALCARAZ, Johnathon D. ANDERSON, Ramarosan ANDRIANTSITOHAINA et al. « Minimal information for studies of extracellular vesicles 2018 (MISEV2018) : a position statement of the International Society for Extracellular Vesicles and update of the MISEV2014 guidelines ». *Journal of Extracellular Vesicles* 7.1 (2018) (cf. p. 137).
- [Thiery, 2009] Jean Paul THIERY, Hervé ACLOQUE, Ruby Y.J. HUANG et M. Angela NIETO. « Epithelial-Mesenchymal Transitions in Development and Disease ». *Cell* 139.5 (2009), p. 871-890 (cf. p. 22, 156).
- [Thompson, 2023] Will THOMPSON et Eleftherios Terry PAPOUTSAKIS. « The role of biomechanical stress in extracellular vesicle formation, composition and activity ». *Biotechnology Advances* 66.January (2023), p. 108158 (cf. p. 131).
- [Tijore, 2018] Ajay TIJORE, Mingxi YAO, Yu-Hsiu WANG, Yasaman NEMATBAKSH, Anushya HARIHARAN, Chwee TECK LIM et Michael SHEETZ. « Mechanical Stretch Kills Transformed Cancer Cells ». *bioRxiv* (2018), p. 491746 (cf. p. 14).
- [Tinevez, 2017] Jean-Yves TINEVEZ, Nick PERRY, Johannes SCHINDELIN, Genevieve M. HOOPES, Gregory D. REYNOLDS, Emmanuel LAPLANTINE, Sebastian Y. BEDNAREK, Spencer L. SHORTE et Kevin W. ELICEIRI. « TrackMate : An open and extensible platform for single-particle tracking ». *Methods* 115.2016 (2017), p. 80-90 (cf. p. 68, 151).

- [Tosteson, 1960] D. C. TOSTESON et J. F. HOFFMAN. « Regulation of Cell Volume by Active Cation Transport in High and Low Potassium Sheep Red Cells ». *The Journal of General Physiology* 44.1 (1960), p. 169-194 (cf. p. 7).
- [Triantafillu, 2019] Ursula Lea TRIANTAFILLU, Seungjo PARK et Yonghyun KIM. « Fluid Shear Stress Induces Drug Resistance to Doxorubicin and Paclitaxel in the Breast Cancer Cell Line MCF7 ». *Advanced Therapeutics* 2.3 (2019), p. 1-8 (cf. p. 138, 139).
- [Turgay, 2017] Yagmur TURGAY, Matthias EIBAUER, Anne E. GOLDMAN, Takeshi SHIMI, Maayan KHAYAT, Kfir BEN-HARUSH, Anna DUBROVSKY-GAUPP, K. Tanuj SAPRA, Robert D. GOLDMAN et Ohad MEDALIA. « The molecular architecture of lamins in somatic cells ». *Nature* 543.7644 (2017), p. 261-264 (cf. p. 2, 3, 8).
- [Urbanska, 2020] Marta URBANSKA, Hector E. MUÑOZ, Josephine SHAW BAGNALL, Oliver OTTO, Scott R. MANALIS, Dino DI CARLO et Jochen GUCK. « A comparison of microfluidic methods for high-throughput cell deformability measurements ». *Nature Methods* 17.6 (2020), p. 587-593 (cf. p. 82, 83, 98, 159, 161).
- [Vahabikashi, 2022] Amir VAHABIKASHI, Suganya SIVAGURUNATHAN, Fiona Ann Sadsad NICDAO, Yu Long HAN, Chan Young PARK, Mark KITTISOPIKUL, Xianrong WONG, Joseph R. TRAN, Gregg G. GUNDERSEN, Karen L. REDDY, G. W. Gant LUXTON, Ming GUO, Jeffrey J. FREDBERG, Yixian ZHENG, Stephen A. ADAM et Robert D. GOLDMAN. « Nuclear lamin isoforms differentially contribute to LINC complex-dependent nucleocytoplasmic coupling and whole-cell mechanics ». *Proceedings of the National Academy of Sciences* 119.17 (2022), p. 1-12 (cf. p. 3).
- [Vaičekauskaite, 2020] Justina VAICEKAUSKAITE, Piotr MAZUREK, Sindhu VUDAYAGIRI et Anne Ladegaard SKOV. « Mapping the mechanical and electrical properties of commercial silicone elastomer formulations for stretchable transducers ». *Journal of Materials Chemistry C* 8.4 (2020), p. 1273-1279 (cf. p. 136).
- [Van Poznak, 2015] Catherine VAN POZNAK, Mark R. SOMERFIELD, Robert C. BAST, Massimo CRISTOFANILLI, Matthew P. GOETZ, Ana M. GONZALEZ-ANGULO, David G. HICKS, Elizabeth G. HILL, Minetta C. LIU, Wanda LUCAS, Ingrid A. MAYER, Robert G. MENNEL, William F. SYMMANS, Daniel F. HAYES et Lyndsay N. HARRIS. « Use of biomarkers to guide decisions on systemic therapy for women with metastatic breast cancer : American Society of Clinical Oncology clinical practice guideline ». *Journal of Clinical Oncology* 33.24 (2015), p. 2695-2704 (cf. p. 28).
- [Varotsos Vrynas, 2021] Angelos VAROTSOS VRYNAS, Julia PEREA PAIZAL, Chris BAKAL et Sam H. AU. « Arresting metastasis within the microcirculation ». *Clinical & Experimental Metastasis* 38.4 (2021), p. 337-342 (cf. p. 19, 21).
- [Vasseur, 2021] Antoine VASSEUR, Nicolas KIAVUE, François-Clément BIDARD, Jean-Yves PIERGA et Luc CABEL. « Clinical utility of circulating tumor cells : an update ». *Molecular Oncology* 15.6 (2021), p. 1647-1666 (cf. p. 27).
- [Vatandoust, 2015] Sina VATANDOUST. « Colorectal cancer : Metastases to a single organ ». *World Journal of Gastroenterology* 21.41 (2015), p. 11767 (cf. p. 155).
- [Venkova, 2022] Larisa VENKOVA, Amit Singh VISHEN, Sergio LEMBO, Nishit SRIVASTAVA, Baptiste DUCHAMP, Artur RUPPEL, Alice WILLIART, Stéphane VASSILOPOULOS, Alexandre DESLYS, Juan Manuel GARCIA ARCOS, Alba DIZ-MUÑOZ, Martial BALLAND, Jean François JOANNY, Damien CUVELIER, Pierre SENS et Matthieu PIEL. « A mechano-osmotic feedback couples cell volume to the rate of cell deformation ». *eLife* 11 (2022), p. 1-41 (cf. p. 7, 84, 86).
- [Venturini, 2020] Valeria VENTURINI, Fabio PEZZANO, Frederic CATALÀ CASTRO, Hanna-Maria HÄKKINEN, Senda JIMÉNEZ-DELGADO, Mariona COLOMER-ROSELL, Monica MARRO, Queralt TOLOSA-RAMON, Sonia PAZ-LÓPEZ, Miguel A VALVERDE, Julian WEGHUBER, Pablo LOZA-ALVAREZ, Michael KRIEG, Stefan WIESER et Verena RUPRECHT. « The nucleus measures shape changes for cellular proprioception to control dynamic cell behavior ». *Science* 370.6514 (2020), eaba2644 (cf. p. 32, 117).
- [Verhulsel, 2014] Marine VERHULSEL, Maéva VIGNES, Stéphanie DESCROIX, Laurent MALAQUIN, Danijela M. VIGNJEVIC et Jean-Louis VIOVY. « A review of microfabrication and hydrogel engineering for micro-organs on chips ». *Biomaterials* 35.6 (2014), p. 1816-1832 (cf. p. 31).
- [Vries, 2007] Anthony H B de VRIES, Bea E. KRENN, Roel van DRIEL, Vinod SUBRAMANIAM et Johannes S. KANGER. « Direct observation of nanomechanical properties of chromatin in living cells. » *Nano letters* 7.5 (2007), p. 1424-7 (cf. p. 3).
- [Wakatsuki, 2001] Tetsuro WAKATSUKI, Bill SCHWAB, Nathan C. THOMPSON et Elliot L. ELSON. « Effects of cytochalasin D and latrunculin B on mechanical properties of cells ». *Journal of Cell Science* 114.5 (2001), p. 1025-1036 (cf. p. 91).
- [Waks, 2019] Adrienne G. WAKS et Eric P. WINER. « Breast Cancer Treatment ». *JAMA* 321.3 (2019), p. 316 (cf. p. 16).

## References

---

- [Wan, 2022] Yuan WAN, Yi-Qiu XIA et Si-Yang ZHENG. « Extruded small extracellular vesicles : splinters of circulating tumour cells may promote cancer metastasis ? » *British Journal of Cancer* 127.7 (2022), p. 1180-1183 (cf. p. 131).
- [Wang, 2019] K. WANG, X. H. SUN, Y. ZHANG, T. ZHANG, Y. ZHENG, Y. C. WEI, P. ZHAO, D. Y. CHEN, H. A. WU, W. H. WANG, R. LONG, J. B. WANG et J. CHEN. « Characterization of cytoplasmic viscosity of hundreds of single tumour cells based on micropipette aspiration ». *Royal Society Open Science* 6.3 (2019), p. 181707 (cf. p. 90).
- [Wang, 2022] Mai WANG, Irena IVANOVSKA, Manasvita VASHISTH et Dennis E. DISCHER. « Nuclear mechano-protection : From tissue atlases as blueprints to distinctive regulation of nuclear lamins ». *APL Bioengineering* 6.2 (2022) (cf. p. 13).
- [Wei, 2016] Fanan WEI, Fei LAN, Bin LIU, Lianqing LIU et Guangyong LI. « Poroelasticity of cell nuclei revealed through atomic force microscopy characterization ». *Applied Physics Letters* 109.21 (2016) (cf. p. 115).
- [Weinberg, 2014] Robert A. WEINBERG. *The biology of cancer : second edition*. 2014, p. 282 (cf. p. 15).
- [Weiss, 1985] L. WEISS, D. S. DIMITROV et M. ANGELOVA. « The hemodynamic destruction of intravascular cancer cells in relation to myocardial metastasis. » *Proceedings of the National Academy of Sciences* 82.17 (1985), p. 5737-5741 (cf. p. 20, 138).
- [Weiss, 1990] Leonard WEISS. « Metastatic Inefficiency ». *Advances in Cancer Research*. T. 54. C. 1990, p. 159-211 (cf. p. 20, 121, 138, 159).
- [Wen, 2011] Qi WEN et Paul A. JANMEY. « Polymer physics of the cytoskeleton ». *Current Opinion in Solid State and Materials Science* 15.5 (2011), p. 177-182 (cf. p. 8).
- [Whitesides, 2006] George M. WHITESIDES. « The origins and the future of microfluidics ». *Nature* 442.7101 (2006), p. 368-373 (cf. p. 28).
- [WHO, 2020] World Health Organization WHO. « Global Health Estimates 2020 : Deaths by Cause, Age, Sex, by Country and by Region,2000-2019 ». <https://www.who.int/data/gho/data/themes/mortality-and-global-health-estimates/gh-e-leading-causes-of-death> (2020) (cf. p. 14).
- [Willis, 2008] Naomi D. WILLIS, Thomas R. COX, Syed F. RAHMAN-CASAÑS, Kim SMITS, Stefan A. PRZYBORSKI, Piet van den BRANDT, Manon van ENGELAND, Matty WEIJENBERG, Robert G. WILSON, Adriaan de BRUÏNE et Christopher J. HUTCHISON. « Lamin A/C Is a Risk Biomarker in Colorectal Cancer ». *PLoS ONE* 3.8 (2008). Sous la dir. de Kevin G. HARDWICK, e2988 (cf. p. 115).
- [Winkler, 2020] Juliane WINKLER, Abisola ABISOYE-OGUNNIYAN, Kevin J. METCALF et Zena WERB. « Concepts of extracellular matrix remodelling in tumour progression and metastasis ». *Nature Communications* 11.1 (2020), p. 5120 (cf. p. 13).
- [Woo, 2021] Xing Yi WOO, Jessica GIORDANO, Anuj SRIVASTAVA, Zi Ming ZHAO, Michael W. LLOYD, Roebi de BRUIJN et al. « Conservation of copy number profiles during engraftment and passaging of patient-derived cancer xenografts ». *Nature Genetics* 53.1 (2021), p. 86-99 (cf. p. 17, 88, 140).
- [Wu, 2018] Pei-Hsun WU, Dikla Raz-Ben AROUSH, Atef ASNACIOS, Wei-Chiang CHEN, Maxim E. DOKUKIN, Bryant L. DOSS, Pauline DURAND-SMET, Andrew EKPENYONG, Jochen GUCK, Natalia V. GUZ, Paul A. JANMEY, Jerry S. H. LEE, Nicole M. MOORE, Albrecht OTT, Yeh-Chuin POH, Robert ROS, Mathias SANDER, Igor SOKOLOV, Jack R. STAUNTON, Ning WANG, Graeme WHYTE et Denis WIRTZ. « A comparison of methods to assess cell mechanical properties ». *Nature Methods* 15 (7 2018), p. 491-498 (cf. p. 11).
- [Xia, 2018] Yiqiu XIA, Yuan WAN, Sijie HAO, Merisa NISIC, Ramdane A. HAROUAKA, Yizhu CHEN, Xin ZOU et Si Yang ZHENG. « Nucleus of Circulating Tumor Cell Determines Its Translocation Through Biomimetic Microconstrictions and Its Physical Enrichment by Microfiltration ». *Small* 14.44 (2018), p. 1-11 (cf. p. 38, 86).
- [Xia, 1998] Younan XIA et George M. WHITESIDES. « Soft Lithography ». *Angewandte Chemie International Edition* 37.5 (1998), p. 550-575 (cf. p. 28).
- [Xiao, 2016] Y. XIAO, Y. YU, L. NIU, M. QIAN, Z. DENG, W. QIU et H. ZHENG. « Quantitative evaluation of peripheral tissue elasticity for ultrasound-detected breast lesions ». *Clinical Radiology* 71.9 (2016), p. 896-904 (cf. p. 14).
- [Xie, 2019] Yongfang XIE, Mingling WANG, Min CHENG, Zhiqin GAO et Guohui WANG. « The viscoelastic behaviors of several kinds of cancer cells and normal cells ». *Journal of the Mechanical Behavior of Biomedical Materials* 91.February 2018 (2019), p. 54-58 (cf. p. 8).
- [Xu, 2012] Wenwei XU, Roman MEZENCEV, Byungkyu KIM, Lijuan WANG, John McDONALD et Todd SULCHEK. « Cell Stiffness Is a Biomarker of the Metastatic Potential of Ovarian Cancer Cells ». *PLoS ONE* 7.10 (2012). Sous la dir. de Surinder K. BATRA, e46609 (cf. p. 12).

- 
- [Yan, 2022] Zishen YAN, Xingyu XIA, William C. CHO, Dennis W. AU, Xueying SHAO, Chao FANG, Ye TIAN et Yuan LIN. « Rapid Plastic Deformation of Cancer Cells Correlates with High Metastatic Potential ». *Advanced Healthcare Materials* 11 (8 2022) (cf. p. 38).
- [Yang, 2020a] Bo YANG, Haguy WOLFENSON, Vin Yee CHUNG, Naotaka NAKAZAWA, Shuaimin LIU, Junqiang HU, Ruby Yun-Ju HUANG et Michael P. SHEETZ. « Stopping transformed cancer cell growth by rigidity sensing ». *Nature Materials* 19.2 (2020), p. 239-250 (cf. p. 14).
- [Yang, 2020b] Hui YANG, Yongyuan XU, Yanan ZHAO, Jing YIN, Zhiyi CHEN et Pintong HUANG. « The role of tissue elasticity in the differential diagnosis of benign and malignant breast lesions using shear wave elastography ». *BMC Cancer* 20.1 (2020), p. 930 (cf. p. 14).
- [Zagami, 2022] Paola ZAGAMI et Lisa Anne CAREY. « Triple negative breast cancer : Pitfalls and progress ». *npj Breast Cancer* 8.1 (2022), p. 95 (cf. p. 18).
- [Zeidman, 1950] Irving ZEIDMAN, Morton MCCUTCHEON et Dale Rex COMAN. « Factors Affecting the Number of Tumor Metastases Experiments with a Transplantable Mouse Tumor ». *Cancer Research* 10.6 (1950), p. 357-359 (cf. p. 20, 159).
- [Zhang, 2013] Lin ZHANG, Gang HUANG, Xiaowu LI, Yujun ZHANG, Yan JIANG, Junjie SHEN, Jia LIU, Qingliang WANG, Jin ZHU, Xiaobin FENG, Jiahong DONG et Cheng QIAN. « Hypoxia induces epithelial-mesenchymal transition via activation of SNAIL1 by hypoxia-inducible factor -1 $\alpha$  in hepatocellular carcinoma ». *BMC Cancer* 13.1 (2013), p. 108 (cf. p. 22).
- [Zilionis, 2017] Rapolas ZILIONIS, Juozas NAINYS, Adrian VERES, Virginia SAVOVA, David ZEMMOUR, Allon M. KLEIN et Linas MAZUTIS. « Single-cell barcoding and sequencing using droplet microfluidics ». *Nature Protocols* 12.1 (2017), p. 44-73 (cf. p. 118).

## RÉSUMÉ

---

Les métastases, responsables d'environ 90% des morts liées au cancer, sont formées par un processus complexe impliquant une phase intermédiaire de dissémination cancéreuse dans la circulation sanguine. Les cellules issues de la tumeur primaire y acquièrent alors le statut de cellules tumorales circulantes (CTCs). Les capillaires sanguins présentant un diamètre typique inférieur à celui de la cellule cancéreuse, et même de son noyau, les CTCs s'y retrouvent soumises à un stress hydrodynamique et à de fortes déformations. Nous nous interrogeons sur la façon dont ces cellules répondent mécaniquement à ces stress et déformations, et sur le lien entre ces réponses et le potentiel métastatique de ces cellules. Pour cela, nous avons développé deux dispositifs microfluidiques, qui constituent des modèles simplifiés in vitro de la microvasculature, et nous sommes intéressés à sept lignées cellulaires de cancer du sein et du colon. Le premier dispositif permet d'étudier la dynamique de déformation et de récupération à des temps courts à l'échelle de la cellule unique. Nous avons pu montrer que le temps d'arrêt des CTCs dans les constriction dépend en premier lieu de leur taille, puis de leur agressivité: à taille égale, les cellules issues d'un cancer plus agressif traversent plus rapidement les constriction. Nous avons aussi pu caractériser les propriétés rhéologiques des CTCs au cours de leur déformation et récupération morphologique. De façon intéressante, nous avons observé que le noyau des cellules les plus agressives récupèrent de façon quasiment instantanée. Cette récupération élastique semble être liée à la présence d'une cage de vimentine (filament intermédiaire) entourant le noyau, absente dans les cancers les moins agressifs. Le second dispositif permet, à l'échelle de la population de cellules, de suivre l'effet de déformations répétées sur la survie et l'agressivité des CTCs. Les cellules issues d'un cancer plus agressif semblent mieux survivre, car plus aptes à récupérer des déformations et dommages. Nous espérons, par la compréhension des mécanismes gouvernant la réponse des CTCs à des déformations rapides sous flux, pouvoir identifier des cibles thérapeutiques afin de perturber ces mécanismes et empêcher les CTCs de survivre à leur passage dans la circulation sanguine.

## MOTS CLÉS

---

Cellules Tumorales Circulantes, Méchanobiologie, Microfluidique, Noyau, Cytosquelette, Métastases.

## ABSTRACT

---

Metastases, which are responsible for about 90% of cancer-related deaths, are formed by a complex process involving an intermediate phase of cancerous dissemination in the bloodstream. There, cells from the primary tumor acquire the status of circulating tumor cells (CTCs). As blood capillaries display diameters typically smaller than both cancer cells and their nuclei, CTCs experience high shear stress and high deformations. We are investigating how these cells respond mechanically to these stresses and deformations, and how these responses relate to their metastatic potential. To this end, we have developed two microfluidic devices as simplified in vitro models of the blood microvasculature, and studied seven cell lines of breast and colon cancer. The first device allows us to decipher short-term dynamics of deformation and recovery at the single cell level. We were able to show that the arrest time of CTCs in constrictions depend firstly on their size, and then on their aggressiveness: for the same size, cells from a more aggressive cancer cross the constriction more quickly. We also characterized the rheological properties of CTCs during their deformation and morphological recovery. Interestingly, we observed that nuclei of more aggressive cells recover almost instantly. This elastic recovery may be linked to the presence of a vimentin (intermediate filament) cage-like structure around the nucleus, missing in the less aggressive cancers. The second device allows to monitor the effect of repeated deformation on CTCs survival and aggressiveness at the cell population level. Cells from a more aggressive cancer have a higher survival rate, as they are expected to better withstand deformations and damages. By understanding of mechanisms governing the response of CTCs to fast flow-induced deformations, we hope to identify new therapeutic targets to disrupt these mechanisms and prevent CTCs from surviving in the blood circulation.

## KEYWORDS

---

Circulating Tumor Cells, Mechanobiology, Microfluidic, Nucleus, Cytoskeleton, Metastasis.

